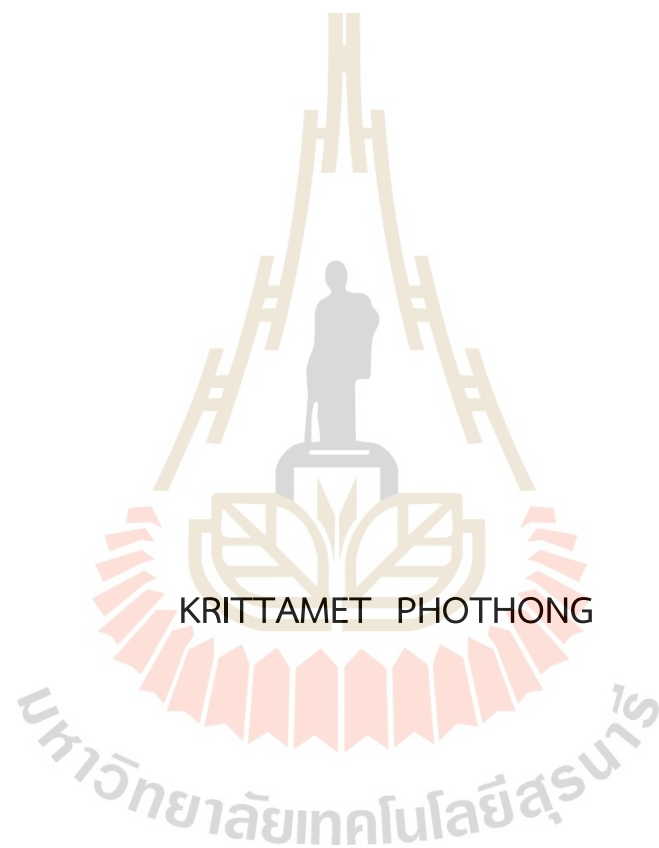


PORE DEVELOPMENT AND SURFACE FUNCTIONAL GROUPS  
FORMATION DURING CO<sub>2</sub> ACTIVATION OF BAMBOO-BASED  
ACTIVATED CARBON AND THE SIMULATION STUDY FOR WETTING  
BEHAVIOR OF FLUIDS ON A PLANAR CARBON SUBSTRATE



A Thesis Submitted in Partial Fulfillment of Requirements for the  
Degree of Doctor of Philosophy in Chemical Engineering  
Suranaree University of Technology  
Academic Year 2021

การพัฒนารูพรรณและการสร้างหมู่ฟุ้งซ่านกับถ่านกัมมันต์จากไม้ไผ่โดยวิธี  
กระตุ้นด้วยแก๊สคาร์บอนไดออกไซด์และการศึกษาโดยวิธีจำลองแบบของ  
พฤติกรรมการเป็ยกของของไหลบนพื้นผิวคาร์บอนแบบระนาบ

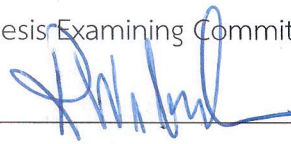


วิทยานิพนธ์นี้เป็นส่วนหนึ่งของการศึกษาตามหลักสูตรปริญญาวิศวกรรมศาสตรดุษฎีบัณฑิต  
สาขาวิชาวิศวกรรมเคมี  
มหาวิทยาลัยเทคโนโลยีสุรนารี  
ปีการศึกษา 2564

PORE DEVELOPMENT AND SURFACE FUNCTIONAL GROUPS  
FORMATION DURING CO<sub>2</sub> ACTIVATION OF BAMBOO-BASED  
ACTIVATED CARBON AND THE SIMULATION STUDY FOR WETTING  
BEHAVIOR OF FLUIDS ON A PLANAR CARBON SUBSTRATE

Suranaree University of Technology has approved this thesis submitted in partial fulfillment of the requirements for the Degree of Doctor of Philosophy.

Thesis Examining Committee



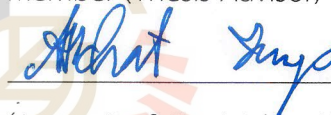
(Asst. Prof. Dr. Ratanawan Kiattikomol)

Chairperson



(Prof. Dr. Chaiyot Tangsathitkulchai)

Member (Thesis Advisor)



(Assoc. Prof. Dr. Atichat Wongkoblap)

Member



(Dr. Terasut Sookkumnerd)

Member

SUPUNNEE J.

(Dr. Supunnee Junpirom)

Member



(Assoc. Prof. Dr. Chatchai Jothityangkoon)

Vice Rector for Academic Affairs

and Quality Assurance



(Assoc. Prof. Dr. Pornsiri Jongkol)

Dean of Institute of Engineering

กฤตเมธ โปธิ์ทอง : การพัฒนารูพรุนและการสร้างหมู่ฟังก์ชันก่บนถ่านกัมมันต์จากไม้ไผ่โดยวิธี  
กระตุ้นด้วยแก๊สคาร์บอนไดออกไซด์และการศึกษาโดยวิธีจำลองแบบของพฤติกรรมการเปียก  
ของของไหลบนพื้นผิวคาร์บอนแบบระนาบ (PORE DEVELOPMENT AND SURFACE  
FUNCTIONAL GROUPS FORMATION DURING CO<sub>2</sub> ACTIVATION OF BAMBOO-BASED  
ACTIVATED CARBON AND THE SIMULATION STUDY FOR WETTING BEHAVIOR OF  
FLUIDS ON A PLANAR CARBON SUBSTRATE) อาจารย์ที่ปรึกษา :  
ศาสตราจารย์ ดร. ชัยยศ ตั้งสถิตย์กุลชัย, 238 หน้า.

คำสำคัญ : ไม้ไผ่/อุณหภูมิคาร์บอนในเซชัน/ถ่านกัมมันต์/การกระตุ้นเชิงกายภาพ/หมู่ฟังก์ชันก่บนผิว  
การดูดซับ/อาร์กอน/เอทิลีน/เอทานอล/แกรไฟต์/การเปลี่ยนแปลงของการเปียก

วิทยานิพนธ์ฉบับนี้ศึกษาการพัฒนาการรูพรุนและการเกิดหมู่ฟังก์ชันก่บนถ่านกัมมันต์ระหว่างการ  
กระตุ้นด้วยแก๊สคาร์บอนไดออกไซด์ การเพิ่มของปริมาณหมู่ฟังก์ชันก่บนผิวด้วยการออกซิไดส์ด้วยอากาศ  
และพฤติกรรมการเปียกของของไหลบนพื้นผิวคาร์บอนแบบระนาบ โดยงานวิจัยแบ่งเป็นส่วน  
งานวิจัยส่วนแรกศึกษาการพัฒนาการรูพรุนและการเกิดหมู่ฟังก์ชันก่บนผิวของถ่านกัมมันต์ที่สังเคราะห์จากไม้ไผ่  
โดยการกระตุ้นด้วยแก๊สคาร์บอนไดออกไซด์ จากผลการทดลองพบว่าถ่านกัมมันต์ที่เตรียมได้มีส่วน  
ของรูพรุนขนาดเล็กมากกว่า 85% ส่วนสมบัติความพรุน (พื้นที่ผิวและปริมาตรรูพรุน) ของถ่านกัม  
มันต์มีค่าเพิ่มขึ้นเมื่ออุณหภูมิของการกระตุ้นเพิ่มขึ้นในช่วงอุณหภูมิ 850 ถึง 950 องศาเซลเซียส  
ในขณะที่อุณหภูมิกระตุ้นที่ 950 ถึง 1000 องศาเซลเซียส สมบัติความพรุนมีค่าลดลง เนื่องจากการยุบ  
รวมของรูพรุนขนาดเล็กที่อยู่ใกล้กัน การเพิ่มขึ้นของเวลากระตุ้นในช่วง 60 ถึง 90 นาที ทำให้สมบัติ  
ความพรุนเพิ่มมากขึ้นในลักษณะเชิงเส้น แต่เมื่อเวลาของการกระตุ้นเพิ่มจาก 90 ถึง 120 นาที สมบัติ  
ความพรุนของถ่านกัมมันต์มีค่าลดลง นอกจากนั้นยังพบว่าอุณหภูมิคาร์บอนในเซชันมีผลต่อจำนวนของ  
จุดว่องไวต่อการเกิดปฏิกิริยาแก๊สซิฟิเคชันในขั้นตอนการกระตุ้นอีกด้วย ในส่วนของหมู่ฟังก์ชันก่บน  
ถ่านกัมมันต์นั้น ทั้งหมู่กรดและหมู่เบสได้เกิดการเปลี่ยนแปลงในระหว่างการกระตุ้นเช่นเดียวกัน  
อย่างไรก็ดี ปริมาณของหมู่ฟังก์ชันก่บนผิวมีแนวโน้มลดลงเมื่อถ่านถูกกระตุ้นที่อุณหภูมิสูงและใช้เวลานาน (>  
950 องศาเซลเซียสและ > 90 นาที) เพราะหมู่ฟังก์ชันก่บนผิวถูกทำลายภายใต้อุณหภูมิกระตุ้นที่สูง ข้อมูล  
สมบัติความพรุนของถ่านกัมมันต์และปริมาณหมู่ฟังก์ชันก่บนผิวได้ถูกนำมาสร้างเป็นความสัมพันธ์ทาง  
คณิตศาสตร์เพื่ออธิบายการเปลี่ยนแปลงสมบัติความพรุนและปริมาณหมู่ฟังก์ชันก่บนผิว โดยเป็นฟังก์ชันกับ  
อุณหภูมิคาร์บอนในเซชัน อุณหภูมิกระตุ้นและเวลากระตุ้นเช่นเดียวกัน

สำหรับงานในส่วนที่สอง ถ่านกัมมันต์สองตัวอย่างถูกเลือกจากงานในส่วนแรกเพื่อนำมาเพิ่ม  
ความเข้มข้นของหมู่ฟังก์ชันก่บนผิวในถ่านกัมมันต์โดยการออกซิไดส์ด้วยอากาศที่อุณหภูมิ 250 องศา  
เซลเซียสเป็นเวลาตั้งแต่ 240 ถึง 4320 นาที จากผลการทดลองพบว่าจำนวนของหมู่ฟังก์ชันก่บนผิวเพิ่มขึ้น

ตามการเพิ่มขึ้นของเวลาที่ใช้ออกซิไดส์ โดยรวมถ่านกัมมันต์ที่เตรียมจากชาร์ที่อุณหภูมิคาร์บอนไนซ์ 400 องศาเซลเซียส นาน 90 นาที มีการเรียงลำดับของปริมาณหมู่กรดที่เกิดขึ้นดังนี้ หมู่ฟีนอลิก > หมู่คาร์บอกซิลิก > หมู่แลคโตนิก สำหรับถ่านกัมมันต์ซึ่งเตรียมจากชาร์ที่อุณหภูมิ 500 องศาเซลเซียส นาน 90 นาที มีการเรียงลำดับดังนี้ หมู่คาร์บอกซิลิก > หมู่ฟีนอลิก > และหมู่แลคโตนิก ความแตกต่างของความเข้มข้นของหมู่กรดนี้อาจเกิดจากจำนวนของจุดว่องไวต่อการเกิดปฏิกิริยาสำหรับถ่านชาร์ที่ได้จากการคาร์บอนไนซ์ที่ 500 องศาเซลเซียสเป็นเวลา 90 นาทีนั้นมีมากกว่าของถ่านชาร์ที่ได้จากการคาร์บอนไนซ์ที่ 400 องศาเซลเซียสเป็นเวลา 90 นาที

ในส่วนที่สามของการศึกษาการดูดซับของเอทิลีนบนพื้นผิวคาร์บอนแบบเรียบ โดยใช้แบบจำลองโมเลกุลของเอทิลีนแบบไม่มีประจุและแบบที่มีประจุ พบว่าแบบจำลองของโมเลกุลเอทิลีนที่มีประจุสามารถอธิบายสมดุลวัฏภาคไอและของเหลว และการดูดซับของเอทิลีนบนพื้นผิวแกรไฟต์ได้ดีกว่าแบบจำลองที่ไม่มีประจุ จากนั้นแบบจำลองโมเลกุลที่มีประจุถูกนำไปสร้างแผนภูมิแบบเปียกของเอทิลีนในวัฏภาคการดูดซับบนพื้นผิวคาร์บอนแบบระนาบ ซึ่งแผนภูมินี้แสดงความสัมพันธ์ระหว่างอุณหภูมิที่ทำให้เกิดการเปียก และแรงดึงดูดของพื้นผิวคาร์บอน แผนภูมินี้ถูกแบ่งเป็นสามส่วนคือ สถานะไม่เปียก (Non-wetting) เปียกแบบไม่สมบูรณ์ (Incomplete wetting) และเปียกแบบสมบูรณ์ (Complete wetting) จากผลการจำลองพบว่า การเปลี่ยนแปลงการเปียกของเอทิลีนบนพื้นผิวคาร์บอนขึ้นอยู่กับตัวแปรสำคัญสามตัวคือ ค่าความร้อนการดูดซับที่ความหนาแน่นต่ำ แรงกระทำระหว่างโมเลกุลของเอทิลีน และความผันผวนทางความร้อนของระบบ

สำหรับงานในส่วนที่สี่ เป็นการจำลองการดูดซับของเอทานอลบนพื้นผิวแกรไฟต์ ผลการจำลองพบว่าที่อุณหภูมิ 190 เคลวิน เอทานอลดูดซับบนพื้นผิวแกรไฟต์ได้เพียง 1:4 ชั้นของเอทานอลที่ความดันอิ่มตัว เป็นเพราะว่าหมู่  $\text{CH}_3$  และ  $\text{CH}_2$  ในโมเลกุลเอทานอลเกาะติดแบบราบไปกับพื้นผิวแกรไฟต์ ในขณะที่หมู่  $\text{OH}$  นั้นยื่นขึ้นมาจากพื้นผิวแกรไฟต์เพื่อสร้างพันธะไฮโดรเจนระหว่างชั้นการดูดซับแรกและชั้นที่สอง จากนั้นเมื่ออุณหภูมิการดูดซับถูกเพิ่มขึ้นไปถึง 298 เคลวิน ทำให้โมเลกุลของเอทานอลสามารถหมุนตัวอย่างอิสระ ปรากฏการณ์นี้ทำให้เกิดการดูดซับมากกว่าสองชั้นบนพื้นผิวแกรไฟต์ที่ความดันอิ่มตัว เพราะว่าโมเลกุลของเอทานอลสามารถแบ่งปันพันธะไฮโดรเจนระหว่างชั้นที่หนึ่งและสอง และระหว่างชั้นที่สองและสาม ปรากฏการณ์การเปียกบนพื้นผิวแกรไฟต์ของเอทานอลนั้นพึ่งพาความผันผวนทางความร้อนค่อนข้างมาก เพราะแรงกระทำระหว่างเอทานอลและพื้นผิวแกรไฟต์นั้นมีค่าน้อยมาก

สาขาวิชาวิศวกรรมเคมี  
ปีการศึกษา 2564

ลายมือชื่อนักศึกษา Krittanet P.  
ลายมือชื่ออาจารย์ที่ปรึกษา Chanigt J.

KRITTAMET PHOTHONG : PORE DEVELOPMENT AND SURFACE FUNCTIONAL GROUPS FORMATION DURING CO<sub>2</sub> ACTIVATION OF BAMBOO-BASED ACTIVATED CARBON AND THE SIMULATION STUDY FOR WETTING BEHAVIOR OF FLUIDS ON A PLANAR CARBON SUBSTRATE. THESIS ADVISOR : PROF. CHAIYOT TANGSATHITKULCHAI, Ph.D., 238 PP.

Keywords : Bamboo/Carbonization temperature/Activated carbon/Physical activation/Surface functional groups/Adsorption/Argon/Ethylene Ethanol/Graphite/Wetting transition

This thesis aims to study the development of pore and the formation of surface functional groups during CO<sub>2</sub> activation, the increase in the amount of surface functional groups, and fundamental of the wetting behaviour of fluids on a planar carbon substrate. There are four parts for this thesis work. The first part is the study of pore development and formation of surface functional groups in activated carbon derived from bamboo by a two-step activation under CO<sub>2</sub>. The obtained results indicate that the activated carbon produced from bamboo contains mostly micropore (> 85%). The porous properties of activated carbon increased with the increase of activation temperature from 850 to 950°C, but tended to decrease at higher temperatures from 950 to 1000°C. The latter effect was due possibly by the merging of neighbouring micropores at increasing char burn-off. The increase in activation time from 60 to 90 min showed an increase in the porous properties of activated carbon but the porous properties dropped when the activation time increased from 90 to 120 min. It was also found that the carbonization temperature had a definite effect on the porous properties of activated carbon by the difference in the number of active sites for CO<sub>2</sub> activation during the activation process. The amount of surface functional groups (acidic and basic groups) varied during carbonization and activation processes. There was a tendency for the number of surface groups to decrease at high activation temperature and long activation time (> 950°C and > 90 min). The Empirical correlations were developed to predict the change in porous properties and the number of surface functional groups as functions of carbonization temperature, activation temperature, and activation time.

For the second part, the selected activated carbon samples from the preparation part were oxidized by air at a fixed temperature of 250°C with oxidizing times varying from 240 to 4320 min. The results showed that the number of surface groups increased with the increase of oxidizing time. The concentrations of acidic groups are in the following order: phenolic > carboxylic > lactonic for the activated carbons derived from char carbonized at 400°C and 90 min. For activated carbons prepared from char carbonized at 500°C and 90 min provided the amounts of acidic groups in the following order: carboxylic > phenolic > lactonic. The difference in the distribution of surface groups could be attributed to the differing amounts and compositions of the heteroatoms on the carbon surfaces.

The third part of this thesis is concerned with the presence of ethylene in the adsorbed phase on a planar carbon substrate. Two potential models of ethylene were employed to simulate the adsorption of ethylene on a planar substrate. The model which accounts for partial charges can correctly describe the experimental data. Then, the model containing partial charges was further utilized to construct the wetting map of ethylene on a planar carbon substrate. The wetting map shows the relationship between the wetting temperature ( $T_w$ ) of ethylene and the difference in substrate affinities ( $D^*$ ). The obtained wetting map can be separated into three zones, non-wetting, incomplete wetting, and complete wetting.

For the final part, the adsorption of ethanol on a graphite substrate was studied by the simulation. The results showed that at 190 K, there are only 1.4 layers of ethanol in the adsorbed phase on a graphite substrate at  $P_0$ . The  $\text{CH}_3$  and  $\text{CH}_2$  groups of ethanol in the first layer only lie flat to the graphite surface while the OH groups point away from the graphite surface to create the hydrogen bonding between the first and the second layer. When the temperature increases to 298 K, the adsorption of ethanol beyond two layers can be observed at  $P_0$ . The thermal fluctuation allows molecules of ethanol to rotate freely, thus allowing the hydrogen bonding between OH groups in the second and the third layer to be formed. The wetting transition of ethanol relies heavily upon the thermal fluctuation.

School of Chemical Engineering  
Academic Year 2021

Student's Signature Krittamet P.  
Advisor's Signature Chaiyot L.

## ACKNOWLEDGEMENTS

With the completion of my Ph.D. career, it is not admired as an individual work but rather as a group of nice people. First and foremost, I wish to sincerely thank my principal advisor, Prof. Dr. Chaiyot Tangsathitkulchai, for his distinguished encouragement, intense instruction, and unwavering dedication, without him, I would not have achieved this far, and my Ph.D. career would not have been completed. My sincere appreciation is also extended to my co-advisor, Assoc. Prof. Dr. Atichat Wongkoblak, his valuable suggestions have been highly valued. My special thanks also go to Prof. Dr. Duong D. Do, an excellent supervisor during my research time at The University of Queensland (UQ), Brisbane, Australia. He kept on constantly driving me through my limitation to ensure that this research would be a valuable asset for my future career. I also acknowledge the assistance from Prof. Dr. David Nicholson for his valuable suggestions in my research papers.

I would like to express my gratitude for their kind contribution to serve on my committees during my thesis examination, Dr. Terasut Sookkumnerd, Dr. Supunee Junpirom, and Asst. Prof. Dr. Ratanawan Kiattikomol. Their valuable comments and suggestions are also acknowledged.

I also appreciate the assistance from the technical staff at the School of Chemical Engineering's Laboratory, SUT, especially, Mr. Saran Dokmaikun and the technical staff of The Center for Scientific and Technological Equipment for their helping in my research works. My thanks go to Mrs. Amporn Ladnongkhun for her skill of the secretarial work of our school, for helping me with the countless paper works.

I sincerely give thanks to my colleagues in the Carbon and Adsorption Research (CAR) group, Mr. Suravit Naksusuk, Mr. Tarathorn Limsiri, Mr. Panuwat Lawtae, and Miss Prapatsorn Borisut for their helpful discussion, assistance, contribution to my research and for their wonderful and lasting friendship

My colleagues in the molecular adsorption group, Dr. Luisa Prasetyo, Dr. Shiliang Johnathan Tan, Dr. Hui Xu, Dr. Lumeng Liu, and Dr. Quang K. Loi also deserve my thanks for their extremely helpful, endless teaching me in the molecular simulation and encouraging throughout my journey at UQ.

I offer special gratitude to my friends when I was in the School of Chemical Engineering, UQ, Dr. Nur Hafizah, Dr. Pawarisa Luangthongkam, Mr. Ming Yao Lim, Mr. Nazmi Idros, Miss Kaili Li, and Mrs. Siti, for keeping our humour alive.

I gratefully acknowledge the financial support from the Thailand Research Fund (TRF) via the Royal Golden Jubilee Ph.D. (RJG) program, contract number PHD/0156/2557. The magnanimous allocation of computing resources from the UQ Research Computing Centre (RCC), the National e-Science Infrastructure Consortium in Thailand, and SUT HPCC of the Center for Computer Service are gratefully acknowledged.

Finally, I want to offer my genuine and infinite appreciation to my mother, Mrs. Praphasri Phothong, and my extended family, for their constant encouragement and dedication, they have never given up on me along this journey. I also want to show appreciation to my beloved girlfriend, Miss Chutima Suteejarupittaya for her unwavering support and endless love along with my Ph.D. career.

I would like to leave a quote from Mark Twain here.

*“The two most important days in your life are the day you are born and the day you find out why”*

The first important day that when my soul has discovered my physical body, and the second important day, where I believe, there are several days in my life, and the day that I have achieved my Ph.D. is one of them.

Krittamet Phothong

## TABLE OF CONTENTS

	Page
ABSTRACT (THAI).....	I
ABSTRACT (ENGLISH).....	III
ACKNOWLEDGEMENTS.....	V
TABLE OF CONTENTS.....	VII
LIST OF TABLES.....	XII
LIST OF FIGURES.....	XIII
SYMBOLS AND ABBREVIATIONS.....	XXIV
<b>CHAPTER</b>	
<b>I INTRODUCTION.....</b>	<b>1</b>
1.1 Background.....	1
1.2 Objectives.....	4
1.3 Scope and Limitation of Research.....	5
1.4 Output of Research.....	6
1.5 Thesis Structure.....	7
1.6 References.....	9
<b>II LITERATURE REVIEW AND THEORY.....</b>	<b>12</b>
2.1 Biomass.....	12
2.1.1 Structure of Biomass.....	12
2.1.2 Constituents of Biomass Cells.....	14
2.2 Activated Carbon.....	15
2.2.1 Structure.....	16
2.2.2 Surface Chemistry on Activated Carbon.....	17
2.2.3 Synthesis of Activated Carbon.....	25
2.2.4 Applications.....	29

## TABLE OF CONTENTS (Continued)

	Page
2.3 Adsorption.....	31
2.4 Adsorption Equilibrium.....	32
2.4.1 Adsorption Isotherms.....	32
2.4.2 Equations of Adsorption Isotherms.....	34
2.5 Adsorption Study via Computer Simulation.....	38
2.5.1 Simulation Method.....	38
2.5.2 Grand Canonical Ensemble (GC).....	39
2.5.3 Canonical Ensemble (NVT).....	40
2.5.4 Fluid-Fluid Potential.....	41
2.5.5 Solid-Fluid Potential.....	43
2.6 Wetting.....	44
2.6.1 Saturation Vapor Pressure.....	49
2.6.2 The Output Thermodynamic Properties.....	50
2.7 References.....	52
<b>III THE ANALYSIS OF PORE DEVELOPMENT AND SURFACE FUNCTIONAL GROUPS FORMATION DURING CO<sub>2</sub> ACTIVATION OF BAMBOO-BASED ACTIVATED CARBON.....</b>	<b>63</b>
Abstract.....	63
3.1 Introduction.....	64
3.2 Materials and Methods.....	66
3.2.1 Raw Materials.....	66
3.2.2 Char Preparation.....	66
3.2.3 Carbon Dioxide Activation.....	66
3.2.4 Characterization of Sample.....	67
3.3 Results and Discussion.....	70

## TABLE OF CONTENTS (Continued)

	Page
3.3.1 Precursor Characterization.....	70
3.3.2 N <sub>2</sub> Isotherms of the Prepared Activated Carbons.....	73
3.3.3 Porous Properties of the Prepared Activated Carbons.....	76
3.3.4 Correlations for Porous Properties of the Prepared Activated Carbons.....	86
3.3.5 Surface Chemistry of the Prepared Activated Carbon.....	93
3.3.6 Empirical Correlations for the Formation of the Surface Functional Groups.....	97
3.4 Conclusions.....	102
3.5 References.....	104
<b>IV PRELIMINARY STUDY ON THE FORMATION OF OXYGEN FUNCTIONAL GROUPS IN BAMBOO-BASED ACTIVATED CARBON BY AIR OXIDATION.....</b>	<b>110</b>
Abstract.....	110
4.1 Introduction.....	111
4.2 Materials and Methods.....	113
4.2.1 Raw Materials.....	113
4.2.2 Oxidation of Activated Carbon.....	113
4.2.3 Characterization of Products.....	115
4.3 Results and Discussion.....	117
4.3.1 Amount of Surface Groups.....	117
4.3.2 Textural Properties of the Activated Carbon.....	124
4.4 Conclusions.....	128

## TABLE OF CONTENTS (Continued)

	Page
4.5	References.....129
<b>V</b>	<b>WETTING TRANSITION OF ETHYLENE</b>
	<b>ON A PLANAR SUBSTRATE.....132</b>
	Abstract.....132
5.1	Introduction.....133
5.2	Simulation Model.....135
	5.2.1 Fluid-Fluid Potential.....135
	5.2.2 Solid-Fluid Potential.....136
5.3	Results and Discussion.....137
	5.3.1 Comparison of Potential Models.....137
	5.3.2 Adsorption on Graphite.....138
	5.3.3 Wetting Map.....144
5.4	Conclusion.....160
5.5	References.....161
<b>VI</b>	<b>INCOMPLETE WETTING OF ETHANOL</b>
	<b>ON A GRAPHITE SUBSTRATE.....167</b>
	Abstract.....167
6.1	Introduction.....168
6.2	Simulation Model.....170
	6.2.1 Fluid-Fluid Potential.....170
	6.2.2 Solid-Fluid Potential.....171
	6.2.3 Adsorption Measurement.....172
6.3	Results and Discussion.....172
	6.3.1 Possible Parameters that Influence Adsorption Behaviour.....176
	6.3.2 Adsorption of Ethanol on Graphite.....181

## TABLE OF CONTENTS (Continued)

	Page
6.3.3 Wetting Transition.....	185
6.3.4 Effect of Surface Affinity and Wetting Map.....	198
6.4 Conclusions.....	202
6.5 References.....	203
<b>VII CONCLUSIONS AND RECOMMENDATIONS.....</b>	<b>208</b>
7.1 Conclusions.....	208
7.2 Recommendations.....	211
<b>APPENDICES</b>	
APPENDIX A SUPPLEMENTARY INFORMATION.....	213
APPENDIX B LIST OF PUBLICATIONS.....	237
<b>VITA.....</b>	<b>238</b>

## LIST OF TABLES

Table	Page
2.1	Groups of biomasses and their subdivision.....13
2.2	Some IR spectra assignment of functional groups on activated carbon surface.....23
2.3	The amount of ash and elements in various adsorbents, they are presented in weight percentage.....24
2.4	Example of activated carbon used in the industries.....30
2.5	Potential parameters and coordinates of fluids used in this study.....43
3.1	Proximate and ultimate analyses of bamboo used in this work.....72
3.2	BET specific area of chars derived from CO <sub>2</sub> adsorption at 0°C (273.15 K) for chars prepared at different carbonization temperatures of 400, 500, and 600°C.....79
3.3	Distribution of pore volume for various pore sizes in activated carbon prepared under different preparation conditions.....85
3.4	Typical elemental analysis and surface chemistry of prepared chars and the prepared activated carbons. All activated carbon samples were derived from char carbonized at 400°C for 90 min.....97
4.1	Activated carbons used in this work.....115
4.2	The amount of surface groups in pristine activated carbons and the oxidized activated carbons.....120
4.3	Porous properties of pristine activated carbons and the oxidized samples...126
6.1	Exact values of temperature and bulk coexistence pressure used in the simulation.....175

## LIST OF FIGURES

Figure		Page
2.1	Major constituents of woody biomass.....	13
2.2	Molecular structure of (a) cellulose, (b) hemicellulose and (c) lignin.....	15
2.3	The structure of hexagonal graphite, which trigonal bonding within the graphene layers.....	17
2.4	Example of some oxygen surface functional groups on activated carbon: (a) and (b) carboxyl-carbonate; (c) carboxylic acid; (d) and (e) lactone; (f) ether bridge; (g) cyclic ethers; (h) and (i) cyclic anhydride; (j) quinone; (k) phenol; (l) alcohol; and (m) ketene.....	19
2.5	Example of some nitrogen surface functional groups on activated carbon: (a) nitroso; (b) nitrile; (c) pyridine-N-oxide; (d) pyridine; (e) pyridinium; (f) pyridine; and (g) amine.....	20
2.6	Physisorption isotherms.....	33
2.7	Illustration of (a) wetting and (b) non-wetting system.....	45
2.8	Several types of adsorption isotherms of simple gas on the homogeneous surface. To distinguish the wetting behaviour at different temperatures.....	47
2.9	Illustration of isotherms that fall into incomplete wetting region, usually at temperature below $T_R$ . The red line shows $T_{L,1}$ which is the wetting of the first layer at $P_0$ , while the blue line shows wetting of the second layer, $T_{L,2}$ . The dash line represents where the relative pressure is at unity.....	49
2.10	Illustration of the simulation box used in the determination of thermodynamic properties of the adsorbates.....	50
3.1	TG and DTG curves of bamboo biomass used in this work.....	72

## LIST OF FIGURES (Continued)

Figure	Page
3.2	Effects of carbonization temperature and activation time on N <sub>2</sub> adsorption isotherms of activated carbon prepared by CO <sub>2</sub> activation at (a) 950°C and 60 min (b) 950°C and 90 min.....74
3.3	Effects of activation temperature and activation time on N <sub>2</sub> adsorption isotherms of activated carbon prepared by CO <sub>2</sub> activation at (a) 850 to 1000°C and 90 min (b) 850 to 1000°C and 120 min. The activated carbons were derived from char carbonized at 500°C and 90 min.....74
3.4	Effects of activation time on N <sub>2</sub> adsorption isotherms of activated carbon prepared by CO <sub>2</sub> activation at (a) 900°C and (b) 950°C for 60, 90, and 120 min. The activated carbons were derived from char carbonized at 600°C and 90 min.....75
3.5	Effects of char burn-off on porous properties of the prepared activated carbons. (a) BET specific area, (b) total pore volume, (c) micropore volume, and (d) mesopore volume.....77
3.6	Effects of char burn-off on the percentage of micropore volume and mesopore volume. The blank symbols represent the micropore volume while the solid symbols represent the mesopore volume.....78
3.7	Effects of char burn-off on the average pore diameter of the prepared activated carbons.....80
3.8	Effects of activation temperature and activation time on BET specific area of activated carbon prepared from chars carbonized at different temperatures (400, 500, and 600°C) for (a) activation temperatures were varied from 850 to 1000°C while the activation time was kept constant at 60 min and (b) activation times were varied from 60 to 120 min while the activation temperature was kept constant at 900°C.....81

## LIST OF FIGURES (Continued)

Figure	Page
3.9      Variation of char reactivity during CO <sub>2</sub> gasification as a function of time for various chars and activation temperatures. Lines with black, blue, and red colors represent chars prepared at 400, 500, and 600°C, respectively, with each char being gasified at (a) 850°C, (b) 900°C, (c) 950°C, and (d) 1000°C for 120 min.....	82
3.10     Effects of activation temperature and activation time on the pore size distribution of produced activated carbon for (a) char C400-90 and activation time of 90 min and (b) for char C500-90 and activation temperature of 950°C.....	84
3.11     The relationship between the structural parameter and fractional conversion of char. Figure (a) - (c) refer to the activated carbon derived from char carbonized at 400, 500, and 600°C for 90 minutes, respectively.....	88
3.12     Correlations between (a) the constant C <sub>1</sub> and (b) the constant C <sub>2</sub> in Equation (3.7) and (3.8) and the carbonization temperature.....	89
3.13     The development of reaction surface with conversion according to RPM. The activated carbon products were derived from char carbonized at 400, 500, and 600°C for 90 minutes, respectively. The black solid line, blue dash line, and red dash-dot lines represent the predicted data derived from Equation (3.10). The black circles, blue triangles, and red diamonds indicate the experimental data points.....	90
3.14     The correlation between total pore volume ( $V_{tot}$ ) and BET specific area. The black solid line is predicted from Equation (3.13), while the blue circles are the experimental data.....	92
3.15     FTIR spectra of the prepared chars. The black solid line, blue dash line, and red dash-dot line refer to char carbonized at 400, 500, and 600°C for 90 min.....	94

## LIST OF FIGURES (Continued)

Figure	Page
3.16	FTIR spectra of the obtained activated carbon. The blue, red, green, and black solid lines refer to activated carbon prepared at 850, 900, 950, and 1000°C for 90 min. The black dash line is the char carbonized at 500°C. All carbon samples were derived from char carbonized at 500°C for 90 min.....96
3.17	Presentation of surface groups concentration in three different units of (a) mmol/g carbon, (b) mmol/g char, and (c) mmol/m <sup>2</sup> of BET specific area, as a function of percentage of char burn-off.....98
3.18	Surface response curves showing the effects of activation temperature and activation time on the amount of surface groups on activated carbon derived from char C400-90, (a) acidic groups and (b) basic groups 101
3.19	Surface response curves showing the effects of activation temperature and activation time on the amount of surface groups on activated carbon derived from char C500-90, (a) acidic groups and (b) basic groups....101
3.20	Surface response curves showing the effects of activation temperature and activation time on the amount of surface groups on activated carbon derived from char C600-90, (a) acidic groups and (b) basic groups....102
4.1	The effect of oxidation time on amount of surface functional groups. (a) samples were derived from char carbonized at 400°C for 90 min and (b) samples were derived from char carbonized at 500°C for 90 min.....118
4.2	The effect of oxidation time on the total amount of surface functional groups.....119
4.3	FTIR spectra of chars, pristine AC, and OAC samples. (a) The plots show the samples that derived from char C400-90, (b) the OAC sample oxidized at 2880 min and derived from char C400-90, and (c) the sample that derived from char C500-90.....123

## LIST OF FIGURES (Continued)

Figure	Page	
4.4	Effects of air oxidation in activated carbon on N <sub>2</sub> adsorption/desorption isotherms. (a) and (b) The OAC samples derived from char C400-90 while (c) and (d) derived from char C500-90.....	124
4.5	The amount of N <sub>2</sub> adsorption in carbon samples at the relative pressure of 0.3 for original activated carbons and the oxidized activated carbons. (a) Samples were derived from char carbonized at 400°C for 90 min and (b) samples were derived from char carbonized at 500°C for 90 min. The effects of oxidation time are presented.....	126
5.1	Schematic drawing of two ethylene models.....	136
5.2	Vapour-liquid coexistence densities curves for ethylene, blue squares represent TraPPE UA model, red circles are TraPPE UA2 model while the experimental data from NIST are shown as black solid lines. (a) Linear scale and (b) semi-log scale to emphasize at low density region.....	137
5.3	Saturated vapour pressure or bulk coexistence pressure for ethylene, blue squares represent TraPPE UA model, red circles are TraPPE UA2 while the experimental data from NIST are shown as black solid lines. (a) Linear scale and (b) semi-log scale to emphasize low temperature region.....	138
5.4	The adsorption isotherms of ethylene at 105 K on graphite. Blues squares represent TraPPE UA model, red circles are TraPPE UA2 model, and black solid line is the experimental data from Menaucourt <i>et al.</i> .....	140
5.5	The configurations of ethylene on graphite at 105 K, the pressure point is marked in <i>Figure 5.4</i> ( $P/P_0 = 0.1$ ). (a) TraPPE UA model and (b) TraPPE UA2 model.....	141

## LIST OF FIGURES (Continued)

Figure	Page	
5.6	The adsorption isotherms of ethylene at 193 K on graphite. (a) Plots are in linear scale and (b) log-log scale to emphasize the Henry's law region. Blue squares represent the TraPPE UA model, red circles are TraPPE UA2 model, and black solid line is the experimental data from Avgul and Kiselev.....	141
5.7	The isosteric heat of adsorption of ethylene at 105 K. (a) TraPPE UA model and (b) TraPPE UA2 model. The solid lines represent the heats obtained from the canonical ensemble, which provides information of the transition during the first-order transition. The heats of condensation (green dash-dot line) obtained from the canonical kMC scheme.....	143
5.8	The adsorbate-adsorbate (FF) contribution of isosteric heat and its dispersive (LJ) and electric interactions (Charges) contributions simulated with TraPPE UA2 model adsorption on graphite at 105 K.....	143
5.9	(a) The parametric map of the wetting temperature of argon as a function of surface affinity, $D^*$ and (b) the plots of heats of sublimation and condensation together with isosteric heats at zero loading calculated via Monte Carlo Integration at different surface affinities.....	145
5.10	(a) Adsorption isotherms of argon on substrate <b>A</b> at 30 K that has $D^*$ of 5.869 and (b) isosteric heat of adsorption with the contributions from adsorbate-adsorbate (FF) interactions and adsorbate-adsorbent (SF) interactions. The dash lines in heat plots obtained from the canonical ensemble to provide the evolution of heats during the first-order transition.....	148
5.11	(a) Adsorption isotherms of argon on graphite ( $D^*$ of 8.996) at 87 K and (b) snapshot of argon at 87 K and $P/P_0 \sim 0.99$ .....	149

## LIST OF FIGURES (Continued)

Figure	Page
5.12 (a) The parametric map of wetting temperature of ethylene as a function of surface affinity, $D^*$ and (b) the plots of heats of sublimation and condensation together with isosteric heats at zero loading calculated via Monte Carlo Integration at different surface affinities.....	151
5.13 Simulated adsorption isotherms of ethylene on graphite at various temperatures.....	152
5.14 The configurations snapshots of ethylene molecules on graphite at $P_0$ , the plots using centre of mass (COM) of ethylene molecules for temperatures (a) 50 K, (b) 82 K, (c) 100 K, and (d) 128 K.....	153
5.15 (a) Isosteric heat of adsorption of ethylene on graphite at 128 K, it is decomposed into adsorbate-adsorbate (FF) and adsorbent-adsorbate (SF) interactions. (b) Plots of heats in semi-log scale to emphasize the low loading region. The green dash line is heat of condensation at 128 K, calculated by canonical kMC scheme.....	153
5.16 (a) Adsorption isotherms of ethylene on a very weak substrate having $D^*$ of 1.643 and (b) the plots of heats of sublimation and condensation together with isosteric heat at zero loading calculated via Monte Carlo Integration at different surface affinities.....	155
5.17 Adsorption isotherms of ethylene at 230 K on substrate having $D^*$ of 1.643. The canonical isotherm gives the information during the transition from molecular clustering to adsorbed film on the substrate.....	156
5.18 The configuration snapshots of ethylene molecules on very weak substrate at point A to D as marked in canonical isotherm in <i>Figure 5.17</i> . The plots using centre of mass (COM) of ethylene molecules.....	156

## LIST OF FIGURES (Continued)

Figure	Page
5.19 (a) Isotheric heat of adsorption of ethylene on very weak substrate at 230 K, it is decomposed into adsorbate-adsorbate (FF) and adsorbent-adsorbate (SF) interactions. (b) Plots of heats in semi-log scale to emphasize the low loading region. The green dash line is heat of condensation at 230 K, calculated by canonical kMC scheme.....	158
6.1 Schematic drawing of the TraPPE UA ethanol molecule.....	171
6.2 The potential energy between ethanol, optimally oriented, and graphite as a function of the separation distance between the centre of geometry of ethanol and graphite (red squares), and the intermolecular potential energy as a function of the distance between the centres of geometry of two ethanol molecules, both of which are optimally oriented to maximize the interaction (blue circles)...	173
6.3 (a) The isosteric heat of adsorption at zero loading, $q_{st}^{(0)}$ , obtained via Monte Carlo Integration (MCI) for ethanol on graphite substrate (blue dash line) as a function of temperature. The simulated heat of condensation obtained from the canonical kMC scheme is also plotted on the same figure (red squares). (b) The ratio between $q_{st}^{(0)}$ and $\lambda_{cond}$ as a function of temperature.....	174
6.4 (a) The simulated coexistence density of ethanol (blue circles and red squares) obtained from VLE simulation and experimental data are in black dash line. (b) Plots are in semi-log scale to emphasize low density region.....	175
6.5 Experimental data and simulated adsorption isotherms of ethanol on homogeneous graphite surface at 190 K. Experimental data are in blue circles, while red squares are the simulated data. The green dash line is used to represent the statistical monolayer density of ethanol from the experimental data.....	176

## LIST OF FIGURES (Continued)

Figure	Page
6.6 Simulated adsorption isotherms of ethanol adsorption on graphite surface at 190 K, showing the contributions from first- (blue squares) and second layer (red diamonds) and total isotherm in black circles.....	177
6.7 Snapshot of ethanol adsorption on graphite at 190 K, at $P/P_0 = 0.65$ as marked in <i>Figure 6.6</i> , where blue, grey, red, and black represent $\text{CH}_2$ , $\text{CH}_3$ , O, and H atoms. The yellow molecules show ethanol in second layer.....	179
6.8 Control charts of ethanol adsorption on graphite at 190 K and bulk coexistence pressure. (a) and (b) for graphite dimension of $4.0 \times 4.0 \text{ nm}^2$ , while (c) and (d) for graphite dimension of $7.5 \times 7.5 \text{ nm}^2$ .....	180
6.9 Simulated adsorption isotherms for ethanol adsorption on graphite, plotted in terms of the surface excess density versus the reduced pressure; (a) 160 K to 298 K and (b) 325 K to 400 K.....	182
6.10 Simulated adsorption isotherms for ethanol adsorption on graphite, plotted in terms of the surface excess versus the reduced pressure in linear scales to highlight the high loading region, for a range of temperature from (a) 160 K to 298 K and (b) from 325 K to 400 K.....	183
6.11 (a) Experimental adsorption isotherms for ethanol on Carbopack F at various temperatures and (b) simulated adsorption isotherms for ethanol on graphite at various temperatures from 190 K to 298 K.....	185
6.12 Simulated isotherms and its contributions from the first and second layers for ethanol adsorption on graphite at 190 K.....	186
6.13 The configurations snapshots of ethanol molecules on graphite at 190 K (not to scale) for point P1, P2, P3, and P4 as marked in <i>Figure 6.12</i> . The black, red, blue, and grey circles refer to H atom, O atom, $\text{CH}_2$ group, and $\text{CH}_3$ group, respectively, for molecules in the first layer, the yellow circles refer to molecules in the second layer.....	186

## LIST OF FIGURES (Continued)

Figure	Page
6.14	Local density distribution (LDDs) of various sites in ethanol molecule on graphite at 190 K at points P1, P2, P3, and P4 as marked in <i>Figure 6.12</i> . The black, blue, red, and green solid lines represent CH <sub>2</sub> , CH <sub>3</sub> , H and O sites, respectively.....187
6.15	Illustration of ethanol configuration on graphite surface at 190 K. The configuration shows hydrogen bonding between first and second layer.....189
6.16	The simulated isosteric heat and its contributions from the adsorbate-adsorbate (FF) interactions and the adsorbent-adsorbate (SF) interactions for ethanol adsorption on graphite at 190 K. The horizontal dash line is the simulated heat of condensation from the canonical kMC scheme.....190
6.17	Simulated isotherms and its contributions from the first and second layers for ethanol adsorption on graphite at 298 K.....191
6.18	The configurations snapshots of ethanol molecules on graphite at 298 K (not to scale) for points P1, P2, and P3 as marked <i>Figure 6.17</i> . The black, red, blue, and grey circles refer to H atom, O atom, CH <sub>2</sub> group, and CH <sub>3</sub> group, respectively, for the molecules in the first layer, the yellow circles refer to molecules in the second layer.....192
6.19	The configurations snapshots of ethanol molecules on graphite at 298 K (not to scale) for points P4 and P5 as marked <i>Figure 6.17</i> . The black, red, blue, and grey circles refer to H atom, O atom, CH <sub>2</sub> group, and CH <sub>3</sub> group, respectively. For side view, we divided first, second, and third molecular layers using red, yellow, and brown molecules, respectively. The green dash circles are used to emphasize the hydrogen bonding between each layer.....193

## LIST OF FIGURES (Continued)

Figure	Page	
6.20	Local density distributions of various (LDDs) of various sites in ethanol molecules on graphite at 298 K at point P1, P3, P4, and P5 as marked in <i>Figure 6.17</i> . The black, blue, red, and green solid lines represent $\text{CH}_2$ , $\text{CH}_3$ , H and O sites, respectively.....	194
6.21	Illustration of ethanol configuration on graphite surface at 298 K. The configuration shows random rotation of ethanol molecules in second and third layers due to thermal fluctuation. The O and H atoms are pointing away from graphite surface, encourages the adsorption of ethanol beyond second layer.....	196
6.22	(a) The isosteric heat and its contributions from the adsorbate-adsorbate (FF) interactions and adsorbent-adsorbate (SF) interactions and (b) the simulated isosteric heat at low loading for ethanol adsorption on graphite at 298 K. The horizontal dash line is the simulated heat of condensation from the canonical kMC scheme.....	197
6.23	(a) The isosteric heat of adsorption of ethanol on Carbopack F and (b) plots are in semi-log scale to highlight low loading region.....	198
6.24	The wetting map for ethanol as a function of temperature and surface affinity, $D^*$ .....	199
6.25	Adsorption isotherms for ethanol on: (a) weak substrate having $D^*$ of 0.23 and (b) graphite substrate.....	200
6.26	The configurations snapshots of ethanol molecules on the weak substrate having $D^*$ of 0.23 at 455 K. The pressure points before and after the transition are marked in <i>Figure 6.25a</i> .....	201

## SYMBOLS AND ABBREVIATIONS

AC	Activated Carbon
BET	Brunauer-Emmett-Teller theory
C	Canonical ensemble
C	Carbonized char
$c$	Non-dimensional constant for Brunauer-Emmett-Teller ( <i>BET</i> ) equation
COM	Centre of Mass
$D^*$	Surface affinity
DA	Dubinin-Astakhov equation
$D_{avg}$	Average pore diameter (nm)
DR	Dubinin-Radushkevich equation
DTG	Derivative Thermogravimetric
$E_0$	Solid characteristic energy in DA and DR equations (kJ/mol)
EoS	Equation of State
FF	Fluid-Fluid (a.k.a. Adsorbate-Adsorbate)
FTIR	Fourier Transform Infrared Spectroscopy
GAC	Granular Activated Carbon
GC	Grand Canonical ensemble (a.k.a. $\mu VT$ ensemble)
GCMC	Grand Canonical Monte Carlo
GTCB	Graphitized Thermal Carbon Black
$H$	Pore width in the simulation (nm)
HOPG	Highly Oriented Pyrolytic Graphite
IUPAC	International Union of Pure and Applied Chemistry
$k_B$	Boltzmann constant ( $1.380649 \times 10^{-23}$ J/K)
kMC	Kinetic Monte Carlo
$k_{sf}$	Binary interaction parameter

## SYMBOLS AND ABBREVIATIONS (Continued)

LB	Lorentz-Berthelot mixing rule
LJ	Lennard-Jones
LDD	Local Density Distribution ( $\text{kmol/m}^3$ )
MC	Monte Carlo
MD	Molecular Dynamics
MMC	Metropolis Monte Carlo
$N$	Number of particles in the simulations box
$N_A$	Avogadro Number ( $6.02214076 \times 10^{23}$ molecule/mol)
NIST	National Institute of Standards and Technology
NVT	Number of particles, Volume, and Temperature (a.k.a. Canonical ensemble)
$P_0$	Bulk coexistence pressure (Pa) (a.k.a. Saturation vapour pressure)
$P/P_0$	Relative pressure
PBC	Periodic Boundary Condition
PPE	Personal Protective Equipment
PSD	Pore Size Distribution
$q$	Charges in the potential models (e)
$Q_{FF}$	The interaction energy between adsorbate-adsorbate molecules (kJ/mol)
$q_{st}$	Isosteric heat of adsorption (kJ/mol)
$q_{st}^{(0)}$	Isosteric heat at zero loading (kJ/mol)
$R$	Universal gas constant ( $8.314462 \text{ m}^3 \cdot \text{Pa} \cdot \text{K}^{-1} \cdot \text{mol}^{-1}$ )
$R_c$	Reactivity of char under $\text{CO}_2$ gasification (1/min)
RPM	Random Pore Model
$S_0$	Initial surface area per unit mass in the RPM equation ( $\text{m}^2/\text{g}$ )
$S_{BET}$	BET specific area ( $\text{m}^2/\text{g}$ )
SF	Solid-Fluid (a.k.a. Adsorbent-Adsorbate)
$T$	Temperature ( $^\circ\text{C}$ or K)
$t_{Act}$	Activation time (min)

## SYMBOLS AND ABBREVIATIONS (Continued)

$T_{Act}$	Activation temperature (°C)
$T_c$	Critical temperature (K)
$T_C$	Carbonization temperature (°C)
$T_{L,n}$	Layering temperature (K)
$T_R$	Roughening temperature (K)
$T_{tr}$	Bulk triple point temperature (K)
$T_W$	Wetting temperature (K)
TGA	Thermogravimetric Analysis
TraPPE	Transferable Potentials for Phase Equilibria
TVFM	Theory of Volume Filling Micropores
$U_{FF}$	The potential energy between adsorbate-adsorbate in the simulation (K)
$U_{SF}$	The potential energy between adsorbent-adsorbate in the simulation (K)
VLE	Vapour Liquid Equilibria
VSE	Vapour Solid Equilibria
$V_0$	The total (limiting) volume of micropore in DA and DR equations (cm <sup>3</sup> /g)
$V_{acc}$	Accessible volume of the simulation box (nm <sup>3</sup> )
$V_m$	Amount adsorbed in monolayer (mol/m <sup>2</sup> , mol/g, and cm <sup>3</sup> at STP/g)
$V_{mes}$	Mesopore volume (cm <sup>3</sup> /g)
$V_{mic}$	Micropore volume (cm <sup>3</sup> /g)
VOC	Volatile Organic Compound
$V_{tot}$	Total pore volume (cm <sup>3</sup> /g)
$X$	Fractional conversion of char
$\alpha$	Fractional conversion of char in the char reactivity equation
$\beta$	Affinity coefficient in DA and DR equations
$\Delta$	Interspacing between two graphene layers (0.3354 nm)
$\epsilon_0$	Vacuum permittivity of free space

## SYMBOLS AND ABBREVIATIONS (Continued)

$\mathcal{E}_{ff}$	Well depth of fluid (K)
$\mathcal{E}_{ss}$	Well depth of solid (K)
$\mathcal{E}_{sf}$	Cross-well depth of solid and fluid (K)
$\lambda_{sub/cond}$	Heat of phase change of the bulk fluid (sublimation or condensation) (kJ/mol)
$\Lambda$	de Broglie wavelength
$\mu$	Bulk chemical potential of the adsorbate
$\Omega$	The ratio between isosteric heat of adsorption and heat of phase change of bulk fluid
$\Psi$	Structural parameter in the RPM equation
$\rho_s$	Surface density of carbon (38.2 nm <sup>-2</sup> )
$\sigma$	Particle size parameter in the RPM equation
$\sigma_{ff}$	Collision diameter of fluid (nm)
$\sigma_m$	Projection area of the adsorbate molecule (nm <sup>2</sup> /molecule)
$\sigma_{ss}$	Collision diameter of solid (nm)
$\sigma_{sf}$	Cross-collision diameter between solid and fluid (nm)
$\tau$	Dimensionless time in the RPM equation

# CHAPTER I

## INTRODUCTION

### 1.1 Background

Activated carbon is a multipurpose material that can be used in separation and purification processes for both gas and liquid phases. Activated carbon is an amorphous carbon-based material that exhibits a high degree of porosity, an extended surface area, a microporous structure, high adsorption capacity as well as a high degree of surface reactivity. Typically, activated carbon can be synthesized from a variety of bio-based materials, *e.g.*, wood (López de Letona Sánchez *et al.*, 2006; Shahkarami *et al.*, 2015; Zhang *et al.*, 2014), barley straw (Pallarés *et al.*, 2018), cherry stone (Durán-Valle *et al.*, 2005), nutshell (Ahmadpour & Do, 1997) as well as agricultural residues (Zhang *et al.*, 2004). Carbonaceous materials also can be used to produce activated carbon, *e.g.*, coal, lignite, peat, and all family of coal (Ahmadpour & Do, 1996; Jawad *et al.*, 2018; Jiwalak *et al.*, 2005). There are two processes for the synthesis of activated carbon. The first process involves the two-step physical activation consisting of char preparation by carbonization of the raw material in an inert gas at a mid-high temperature (400 to 600°C), followed by the oxidizing of char using oxidizing agents such as CO<sub>2</sub> (Guo & Lua, 2000; Molina-Sabio *et al.*, 1996) or steam (Fan *et al.*, 2004; Pallarés *et al.*, 2018) at a relatively high temperature (800 to 1100°C). The second preparation process is achieved by a single-step carbonization of a precursor impregnated with inorganic chemical agents, *e.g.*, ZnCl<sub>2</sub> (Caturla *et al.*, 1991), NaOH (Yue *et al.*, 2006), H<sub>3</sub>PO<sub>4</sub> (Yorgun & Yıldız, 2015) and K<sub>2</sub>CO<sub>3</sub> (Hayashi *et al.*, 2002).

Generally, the adsorption capacity of activated carbon is mainly associated with the physical structure of activated carbon. The surface functionalities of activated carbon also partially enhance the adsorption capacity.

Surface chemistry of activated carbon are generally derived from heteroatoms present in the precursor and char, from which the surface functional groups are created during the activation process. Theoretically, the surface nature of activated carbon involves the hydrophilic surface functional groups and the hydrophobic graphene layers. Typically, the polar species, *e.g.*, water (Horikawa *et al.*, 2012), alcohol (Horikawa *et al.*, 2015) as well as a solution containing ions will interact with the surface functional groups, while the non-polar species or organic compounds are largely adsorbed on graphene layers. Generally, the surface of activated carbon can be modified by the oxidation reaction in the gas phase with air, O<sub>2</sub> and O<sub>3</sub> or in the liquid phase with HNO<sub>3</sub> (Khandaker *et al.*, 2017), H<sub>2</sub>SO<sub>4</sub> and H<sub>2</sub>O<sub>2</sub> (Heo & Park, 2018). Generally, the oxygen functional groups are formed on the edges of the graphene layers in the activated carbon.

Because of the abundant availability and fast growing of bamboo in Thailand, bamboo is considered as a potential precursor for producing activated carbon in this work. In 2009, around 500,000 tons of bamboo were produced in Thailand (Durst, 2009). Bamboo is generally used to produce food containers, handicrafts, flooring and ceilings (Durst, 2010) as well as scaffolding in construction sites and as a construction material itself (Daram, 2019; Sánchez Vivas *et al.*, 2020; Uthaiattrakoon, 2015). As to the production of activated carbon, information on the development of textural properties of activated carbon during the activation process is of prime importance for further application of activated carbon. During the activation process, however, the pore and surface functional groups are simultaneously developed on the carbon surface. Therefore, essential to trace the development of textural properties and the amount of surface functional groups in carbon during the activation process at different preparation conditions. This information about the development of pore and the amount of surface functional groups in carbon can be beneficial for producing a particular porous carbon to suit a certain application. Given these facts, this work aims to convert bamboo to a high-value product, which is activated carbon, by preparing bamboo-based activated carbon under various preparation conditions and investigating the effect of preparation conditions on the textural properties of produced carbons. Then the obtained results of textural properties are fitted with the correlations that

can be used to predict the porous properties of the carbon product. The formation of surface functional groups on char and activated carbons during the gasification reaction was also studied in this work. The correlations to predict the amount of surface functional groups formed in the char and activated carbon samples were also developed.

Apart from the synthesis of activated carbon, the application of activated carbon for the separation of a fluid mixture by an adsorption process is also important. The adsorption process occurs where the molecules of the concerning gases or liquids are exposed to a solid substrate that allows the adherence of fluid molecules on the solid substrate. Generally, activated carbon has been used in industries to separate valuable products from the bulk stream by the adsorption process. Examples of utilizing adsorption in the industries include water purification (Korotta-Gamage & Sathasivan, 2017), recovery of ethanol vapour from the bulk phase by activated carbon (Hashi *et al.*, 2010), removal of impurities from liquid or gas streams (Dabrowski, 2001), CO<sub>2</sub> recovery from flue gas by activated carbon (Na *et al.*, 2001), etc. Typically, four important parameters influencing the adsorption behaviour of a fluid on a solid substrate are adsorbate (*i.e.*, fluid), adsorbent (*i.e.*, solid substrate), temperature, and pressure. The effects of these parameters on the adsorption performance are crucial for the selection of the most suitable adsorbent for a specific application.

Recently, with the advance of technology, the adsorption mechanism of the concerning fluid on a solid substrate can also be studied by the computer simulation. Theoretically, when the potential parameters of the adsorbate and adsorbent are correctly described in the computer simulation, the output thermodynamic properties of the adsorption process can be properly predicted. There are several available techniques to study the adsorption behaviour by computer simulation such as Density Functional Theory (DFT), Molecular Dynamics (MD) simulation and Monte Carlo (MC) simulation. To study the equilibrium of adsorption, Monte Carlo simulation is a powerful tool to simulate the equilibrium properties of the fluid on the adsorbent as compared to DFT or MD techniques.

To emphasize the significance of computer simulation in adsorption study, the second part of this thesis work is therefore concerned with the application of the Monte Carlo (MC) technique (Metropolis *et al.*, 1953) in the grand canonical (GC) and canonical (C) ensembles (Allen & Tildesley, 2017) for investigating the wetting behaviour of the polar and non-polar fluids on a planar carbon substrate. First, the adsorption of argon on a planar carbon substrate is used as a reference adsorbate. Once the fundamental adsorption mechanism is derived from the argon adsorption system, ethylene and ethanol are employed to study the microscopic adsorption mechanism on a planar carbon substrate. The studied parameters are the temperature of the adsorption system and the strength of the planar substrate. The simulation results will be compared with the experimental data to validate the potential proposed models. Finally, the parametric map of wetting of ethylene and ethanol on planar substrates as a function of wetting temperatures are derived. These data should be of value for scientists and engineers in the synthesis of improved adsorbents for separating the fluids concerned.

## 1.2 Objectives

The primary aim of this thesis work was to study the pore development and formation of surface functional groups during the physical activation of activated carbon synthesis from bamboo. The variation in the amount of oxygen surface groups was also studied with the selected prepared activated carbons. The microscopic study of polar and non-polar species adsorption on a planar carbon substrate was also examined. To achieve this objective, we provided a systematical study by both the experiment and molecular simulation. The specific objectives of this work are listed as follows:

1.2.1 To prepare and characterize the char and activated carbon from bamboo by the two-step physical activation with CO<sub>2</sub>.

1.2.2 To develop the correlations for predicting the developed textural properties of the activated carbon during the CO<sub>2</sub> activation as a function of carbonization temperature and activation conditions.

1.2.3 To study the creation of surface functional groups during the activation and oxidation steps on the activated carbon surface.

1.2.4 To study the adsorption mechanism of argon, ethylene, and ethanol on a planar substrate at the microscopic scale.

1.2.5 To create the wetting map of ethylene and ethanol in terms of the relationship between the wetting temperatures and the affinities of substrates.

### **1.3 Scope and Limitation of the Research Work**

The scope of this work is separated into three parts: (1) preparation of activated carbon; (2) oxidation of the obtained activated carbons by air oxidation; and (3) a computer simulation of adsorption of polar and non-polar species on a planar carbon substrate.

#### **1.3.1 Preparation of Activated Carbon**

Bamboo wood was used to produce activated carbon at various preparation conditions, *i.e.*, carbonization temperature, activated temperature, and activation time. The prepared carbon products were characterized by N<sub>2</sub> adsorption/desorption at -195.8°C, Boehm's titration, Fourier Transform Infrared Spectroscopy, and an element analyzer. The obtained results were further used to develop the correlations describing the development of pores in activated carbon at different preparation conditions. The empirical correlations to predict the formation of surface functional groups were also proposed.

#### **1.3.2 Oxidation of the Prepared Activated Carbon**

The creation of oxygen functional groups on the prepared activated carbons was studied by oxidizing the carbons with air in a quartz tube reactor. The studied parameters were the type of virgin chars and oxidation time. The oxidized products were characterized by N<sub>2</sub> adsorption/desorption isotherms at -195.8°C, Boehm's titration, and Fourier Transform Infrared Spectroscopy.

### 1.3.3 Molecular Simulation

The graphite planar substrate was used in the simulation and argon, ethylene, and ethanol molecules were employed to represent the polar and non-polar species. Monte Carlo (MC) simulation in the grand canonical (GC) and canonical (C) ensembles was employed to study the vapour-liquid equilibria (VLE) and the adsorption of fluids on a graphite substrate. The simulation results were also compared against the experimental data. The microscopic structure, local density distribution and isosteric heat of adsorption were used to analyze the anatomy of adsorption on a perfect substrate. Lastly, the parametric maps of wetting ethylene and ethanol on different surface affinities were presented.

## 1.4 Output of Research

1.4.1 Ability to predict the porous properties and the concentration of surface functional groups of bamboo-based activated carbon as function of preparation conditions through the proposed empirical equations.

1.4.2 The kinetic data for the formation of surface functional groups on activated carbon from bamboo are derived.

1.4.3 The fundamental knowledge on the adsorption mechanism of polar and non-polar species on a planar substrate as a function of the temperature and the substrate affinity is gained.

1.4.4 Parametric maps of the wetting temperatures of ethanol and ethylene on a planar substrate with differences of substrate energies are derived.

## 1.5 Thesis Structure

This thesis consists of 7 chapters, 4 of which describe the work achieved during the candidature. The information for each chapter is briefly provided here.

### Chapter 1 Introduction

This chapter provides the introduction, objectives, scope and limitation, output of research, and the structure of thesis.

## **Chapter 2 Literature Review**

This chapter is concerned with a brief description of theory and literature that are related to the work in this thesis, including fundamentals of biomass, activated carbon, surface functional groups, theory of adsorption, the Monte Carlo (MC) simulation method, potential models. The outputs of the simulations are also reviewed.

## **Chapter 3 The Analysis of Pore Development and Surface Functional Groups Formation During CO<sub>2</sub> Activation of Bamboo-Based Activated Carbon**

This chapter presents the synthesis of activated carbon from bamboo, characterization methods, results, and the empirical correlations of the textural properties as a function of preparation conditions including carbonization temperature and activation conditions (time and temperature). The development of surface functional groups on activated carbon during the CO<sub>2</sub> activation are also systematically studied and the equations of concentration of oxygen functional groups were also produced.

## **Chapter 4 Preliminary Study on the Formation of Oxygen Functional Groups in Bamboo-Based Activated Carbon by Air Oxidation**

Some prepared activated carbons were selected and used to study the influence of air oxidation on the variation of surface functional groups in the activated carbons. Boehm's titration, Fourier Transform Infrared Spectroscopy and N<sub>2</sub> adsorption/desorption isotherms of the obtained oxidized activated carbon samples were employed to investigate the change in surface chemistry and the textural properties of the oxidized activated carbons.

## **Chapter 5 Wetting Transition of Ethylene on a Planar substrate**

Two potential models of ethylene, where one consists of charges and the other without charges were compared based on the vapour-liquid equilibria (VLE) and the adsorption isotherms of ethylene on a graphite substrate to investigate the influence of quadrupole moment using the Monte Carlo (MC) simulation in the grand canonical (GC) and canonical (C) ensembles. Then, the selected potential model that consists

of charges was further used to construct the parametric map of wetting of ethylene. The microscopic analysis of wetting of ethylene in the adsorbed phase on a planar substrate was studied to explore the physics behind the wetting process.

### **Chapter 6 Incomplete Wetting of Ethanol on a Graphite Substrate**

The Monte Carlo (MC) simulation in the grand canonical (GC) ensemble was employed to study the wetting behaviour of ethanol on a graphite substrate in this chapter. The studied parameters are temperature and the affinity of the substrate. The outcome of this chapter is the anatomy of ethanol adsorption on a graphite substrate on the microscopic scale and the parametric map of wetting (temperatures and surface affinities) of ethanol. The ethanol molecule in this chapter represents the associating fluid and the obtained results were compared with those of argon and ethylene adsorption on a planar substrate where the different wetting behaviour between ethanol, argon, and ethylene on a planar substrate is explored.

### **Chapter 7 Conclusions and Recommendations**

The final chapter summarizes the important results derived from the thesis work. The topics of future work are also proposed in this chapter

## 1.6 References

- Ahmadpour, A., & Do, D. D. (1996). The preparation of active carbons from coal by chemical and physical activation. **Carbon**. 34(4): 471-479.
- Ahmadpour, A., & Do, D. D. (1997). The preparation of activated carbon from macadamia nutshell by chemical activation. **Carbon**. 35(12): 1723-1732.
- Allen, M. P., & Tildesley, D. J. (2017). **Computer Simulation of Liquids** (2nd ed.). Oxford: Oxford University Press.
- Caturla, F., Molina-Sabio, M., & Rodríguez-Reinoso, F. (1991). Preparation of activated carbon by chemical activation with ZnCl<sub>2</sub>. **Carbon**. 29(7): 999-1007.
- Dabrowski, A. (2001). Adsorption — from theory to practice. **Advances in Colloid and Interface Science**. 93(1): 135-224.
- Daram, S. (2019). The Analysis of Safety Factor for Bamboo used in Construction. **Journal of Architecture, Design and Construction**. 1(3): 9-24.
- Durán-Valle, C. J., Gómez-Corzo, M., Pastor-Villegas, J., & Gómez-Serrano, V. (2005). Study of cherry stones as raw material in preparation of carbonaceous adsorbents. **Journal of Analytical and Applied Pyrolysis**. 73(1): 59-67.
- Durst, P. B. (2009). **Thailand Forestry Outlook Study** Bangkok: Asia-Pacific Forestry Sector Outlook Study II.
- Durst, P. B. (2010). **The Second Asia-Pacific Forestry Sector Outlook Study**. Bangkok: Food and Agriculture Organization of the United Nations.
- Fan, M., Marshall, W., Daugaard, D., & Brown, R. C. (2004). Steam activation of chars produced from oat hulls and corn stover. **Bioresource Technology**. 93(1): 103-107.
- Guo, J., & Lua, A. C. (2000). Preparation of activated carbons from oil-palm-stone chars by microwave-induced carbon dioxide activation. **Carbon**. 38(14): 1985-1993.
- Hashi, M., Tezel, F. H., & Thibault, J. (2010). Ethanol Recovery from Fermentation Broth via Carbon Dioxide Stripping and Adsorption. **Energy & Fuels**. 24(9): 4628-4637.
- Hayashi, J. i., Horikawa, T., Muroyama, K., & Gomes, V. G. (2002). Activated carbon from chickpea husk by chemical activation with K<sub>2</sub>CO<sub>3</sub>: preparation and characterization. **Microporous and Mesoporous Materials**. 55(1): 63-68.

- Heo, Y.-J., & Park, S.-J. (2018). H<sub>2</sub>O<sub>2</sub>/steam activation as an eco-friendly and efficient top-down approach to enhancing porosity on carbonaceous materials: the effect of inevitable oxygen functionalities on CO<sub>2</sub> capture. **Green Chemistry**. 20(22): 5224-5234.
- Horikawa, T., Sakao, N., Sekida, T., Hayashi, J. i., Do, D. D., & Katoh, M. (2012). Preparation of nitrogen-doped porous carbon by ammonia gas treatment and the effects of N-doping on water adsorption. **Carbon**. 50(5): 1833-1842.
- Horikawa, T., Takenouchi, M., Do, D. D., Sotowa, K.-I., Alcántara-Avila, J. R., & Nicholson, D. (2015). Adsorption of Water and Methanol on Highly Graphitized Thermal Carbon Black and Activated Carbon Fibre %J Australian Journal of Chemistry. 68(9): 1336-1341.
- Jawad, A. H., Ismail, K., Ishak, M. A. M., & Wilson, L. D. (2018). Conversion of Malaysian low-rank coal to mesoporous activated carbon: Structure characterization and adsorption properties. **Chinese Journal of Chemical Engineering**.
- Jiwalak, N., Tangsathitkulchai, C., & Tangsathitkulchai, M. (2005). Activated carbon from lignite coal by chemical activation with potassium hydroxide. **Suranaree Journal of Science and Technology**. 13(3): 207-218.
- Khandaker, S., Kuba, T., Kamida, S., & Uchikawa, Y. (2017). Adsorption of cesium from aqueous solution by raw and concentrated nitric acid-modified bamboo charcoal. **Journal of Environmental Chemical Engineering**. 5(2): 1456-1464.
- Korotta-Gamage, S. M., & Sathasivan, A. (2017). A review: Potential and challenges of biologically activated carbon to remove natural organic matter in drinking water purification process. **Chemosphere**. 167: 120-138.
- López de Letona Sánchez, M., Macías-García, A., Díaz-Díez, M. A., Cuerda-Correa, E. M., Gañán-Gómez, J., & Nadal-Gisbert, A. (2006). Preparation of activated carbons previously treated with hydrogen peroxide: Study of their porous texture. **Applied Surface Science**. 252(17): 5984-5987.
- Metropolis, N., Rosenbluth, A. W., Rosenbluth, M. N., Teller, A. H., & Teller, E. (1953). Equation of State Calculations by Fast Computing Machines. **The Journal of Chemical Physics**. 21(6): 1087-1092.

- Molina-Sabio, M., Gonzalez, M. T., Rodriguez-Reinoso, F., & Sepúlveda-Escribano, A. (1996). Effect of steam and carbon dioxide activation in the micropore size distribution of activated carbon. **Carbon**. 34(4): 505-509.
- Na, B.-K., Koo, K.-K., Eum, H.-M., Lee, H., & Song, H. K. (2001). CO<sub>2</sub> recovery from flue gas by PSA process using activated carbon. **Korean Journal of Chemical Engineering**. 18(2): 220-227.
- Pallarés, J., González-Cencerrado, A., & Arauzo, I. (2018). Production and characterization of activated carbon from barley straw by physical activation with carbon dioxide and steam. **Biomass and Bioenergy**. 115: 64-73.
- Sánchez Vivas, L., Costello, K., Mobley, S., Mihelcic, J. R., & Mullins, G. (2020). Determination of safety factors for structural bamboo design applications. **Architectural Engineering and Design Management**. 1-12.
- Shahkarami, S., Dalai, A. K., Soltan, J., Hu, Y., & Wang, D. (2015). Selective CO<sub>2</sub> Capture by Activated Carbons: Evaluation of the Effects of Precursors and Pyrolysis Process. **Energy & Fuels**. 29(11): 7433-7440.
- Uthaiattrakoon, T. (2015). *Bamboo Design and Construction in Thailand : Bamboo Art Gallery at Arsomsilp Institute of the Arts*. Paper presented at the 10th World Bamboo Congress, Korea.
- Yorgun, S., & Yıldız, D. (2015). Preparation and characterization of activated carbons from Paulownia wood by chemical activation with H<sub>3</sub>PO<sub>4</sub>. **Journal of the Taiwan Institute of Chemical Engineers**. 53: 122-131.
- Yue, Z., Economy, J., & Bordson, G. (2006). Preparation and characterization of NaOH-activated carbons from phenolic resin. **Journal of Materials Chemistry**. 16(15): 1456-1461.
- Zhang, T., Walawender, W. P., Fan, L. T., Fan, M., Daugaard, D., & Brown, R. C. (2004). Preparation of activated carbon from forest and agricultural residues through CO<sub>2</sub> activation. **Chemical Engineering Journal**. 105(1): 53-59.
- Zhang, Y.-J., Xing, Z.-J., Duan, Z.-K., Meng, L., & Wang, Y. (2014). Effects of steam activation on the pore structure and surface chemistry of activated carbon derived from bamboo waste. **Applied Surface Science**. 315(Supplement C): 279-286.

## CHAPTER II

### LITERATURE REVIEW AND THEORY

#### 2.1 Biomass

Biomass is referred to as any organic materials that are derived from plants or animals, although a generally accepted definition is difficult to identify. However, the United Nations Framework Convention of Climate Change (UNFCCC, 2005) gives a unified definition of biomass as:

*“Non-fossilized and biodegradable organic materials originating from plants, animals and micro-organism. This shall also include products, by-products, residues and waste from agriculture, forestry, and related industries as well as the non-fossilized and biodegradable organic functions of industrial and municipal wastes”*

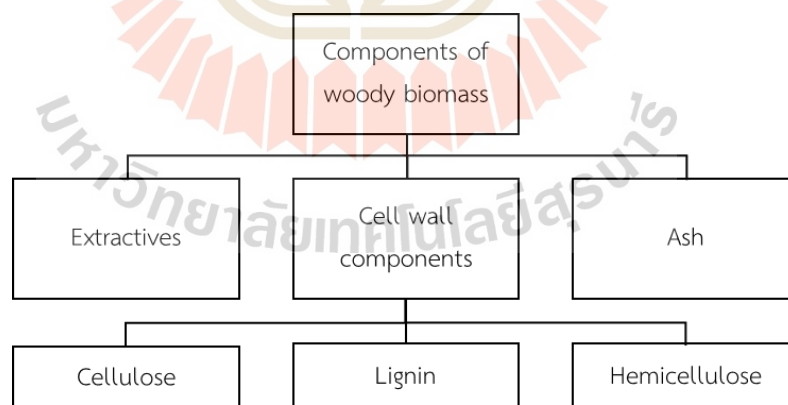
Table 2.1 shows that biomass originates from a variety of sources. Broadly speaking, the mentioned sources include all plants, plant-derived materials as well as livestock manures. Pristine or virgin biomass comes directly from plants or animals, whereas waste or derived biomass comes from different biomass-derived products.

##### 2.1.1 Structure of Biomass

Biomass is a complex structure of organic materials, e.g., carbohydrates, fats, and proteins, along with a small amount of minerals, e.g., sodium, phosphorus, calcium, and iron. The main components of woody biomass can be separated into three main parts, which are extractives, fibre or cell wall, and ash. The components can be summarized in *Figure 2.1*.

**Table 2.1** Groups of biomasses and their subdivision (Basu, 2013).

Pristine	Terrestrial biomass	Forest, grasses, energy crops, and cultivated crops
	Aquatic biomass	Algae and water plants
Waste	Municipal waste	Municipal solid waste, biosolids, sewage, and landfill gas
	Agricultural solid waste	Livestock, manures, and agricultural crop residues
	Forestry residues	Bark, leaves and floor residues
	Industrial waste	Demolition wood, sawdust, and waste oil of fat

**Figure 2.1** Major constituents of woody biomass.

*Extractives:* Substances present in vegetable or animal fibre that can be separated by solvents and recovered using the evaporation of the solutions. They are oil, protein, starch, sugar, etc.

*Cell wall:* It is made from carbohydrates and lignin. Carbohydrates are mainly cellulose or hemicellulose fibers that provide strength to the plant structure, while lignin holds fibre together.

*Ash:* The inorganic compounds of biomass.

### 2.1.2 Constituents of Biomass Cells

Normally, there are three major polymeric compositions of biomass: cellulose, hemicellulose, and lignin. They are briefly described here.

*Cellulose:* Cellulose is the most common organic compound on Earth, it is the primary structural component of cell walls in biomass. The organic formula is  $(C_6H_{10}O_5)_n$ . Cellulose is a long-chain polymer with a high degree of polymerization (~10,000) and a large number of molecular weight (~50,000). Many glucose molecules form up together and make the crystalline structure of cellulose. This structure gives a very high strength, allowing it to provide the skeletal structure of the earthy biomass (Klass, 1998). Cellulose is a major component of wood which constitutes about 40 – 45% by weight on a dry basis of wood.

*Hemicellulose:* This is another constituent of the cell wall of plants. Most of the woods consist of 20 – 30% by weight on a dry basis. It has a random amorphous structure with little strength. It is a group of carbohydrates and a branched-chain structure with lower a degree of polymerization (~100 – 200). The chemical formula  $(C_5H_8O_4)_n$  can be used to present the hemicellulose structure (Klass, 1998). The molecular arrangement of cellulose and hemicellulose are presented in *Figure 2.2a* and *b*, respectively. Typically, there is a variation in the composition of hemicellulose among different biomasses. Most hemicellulose contains some simple sugar as well, e.g., d-xylose, d-glucose, d-galactose, l-arabinose, d-glucuronic acid, and d-mannose.

*Lignin:* This is a complex branched polymer of phenylpropane and is an integral part of the cell wall of plants. It is primarily a three-dimensional polymer of 4-propenylphenol, 4-propenyl-2-methoxyphenol and 4-propenyl-2,5-dimethoxyphenol (Diebold & Bridgwater, 1997). This is one of the highest organic polymers on Earth. Typically, hardwood contains about 18 – 25%, while softwood contains 25 – 35% on

a dry basis. Lignin is the cementing agent for cellulose fibres to hold cells together. The notable monomeric units are benzene rings in the polymer structure.

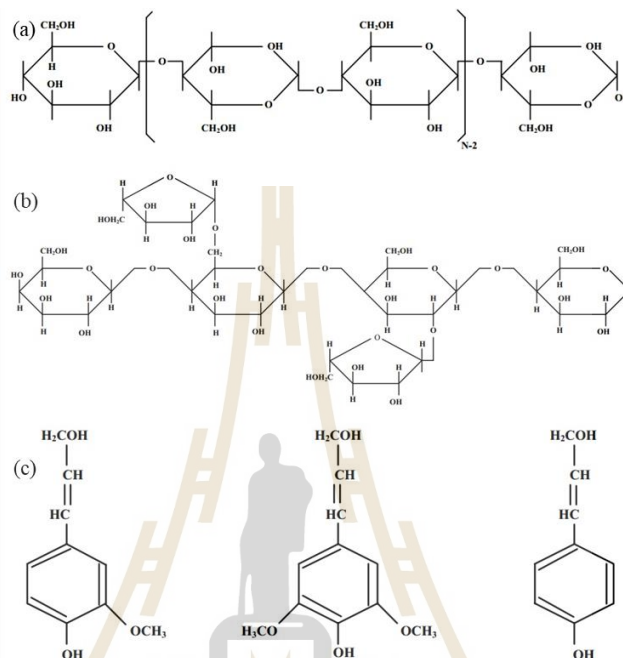


**Figure 2.2** Molecular structure of (a) cellulose, (b) hemicellulose and (c) lignin (Ngernyen, 2007).

## 2.2 Activated Carbon

Activated carbon is an amorphous carbon-based material. It is prepared to exhibit a high degree of porosity and a large internal surface area. Activated carbon can be obtained by activation of char under oxidizing agents of various carbonaceous materials, e.g., peat, wood, lignite, coal, fruit pits and shells, and biomass (pristine and waste). The materials can be either powder or granular form. The powder form gives a large pore diameter with a small internal surface area, whereas the granular form consists of a large internal surface area with a smaller pore diameter. Typically, activated carbon contains hydrophobic graphene layers and hydrophilic functional groups. Consequently, it can be used to adsorb a wide range of molecules in either gas or liquid phases.

Activated carbon was firstly used around 1500 B.C. as an adsorbent for medicinal purposes and as a purifying agent by The Egyptians (Bansal *et al.*, 1988). The ancient Hindus in India filtered drinking water by charcoal. In the 18<sup>th</sup> century, there were two published works to explain the study of gas uptake using charcoal (Fontana, 1777; Scheele, 1780). Then in 1785, the purification of solution using charcoal to remove the colour from solution was discovered (Lovits, 1955). Later in 1900, charcoal was introduced to the industry for use in the sugar refining process, previously they used bone char. Then, during World War I, charcoal derived from coconut shell was used as an adsorbent in the gas mask to protect the troopers from poisonous gases, e.g., chlorine, phosgene, and mustard gas in trench warfare (Marsh & Rodriguez-Reinoso, 2006; Tarkovskaya, 1990). Since, the activated carbon filter has been in use until now for the personal protective equipment (PPE) in the industry, laboratory, hospital, etc.

The world demand for activated carbon is about 2 million metric tons in 2020, which are divided for each continent as follows: 520,000 tons in North America, 130,000 tons in Central and South America, 270,000 tons in Western Europe, 140,000 tons in Eastern Europe, 110,000 tons in Africa and the Middle East, and 830,000 tons in the Asia Pacific (FILTNEWS, 2016).

### 2.2.1 Structure of Activated Carbon

Activated carbon has one of the most complex structures of porous solids. Activated carbon structure consists of the amorphous structure of the graphite microcrystallines. Within the hexagonal graphite, the layer is known as the graphene layer. Each layer lies above and below each other, however, it does not displace. They form an ABABAB sequence (see *Figure 2.3*). The density of hexagonal graphite is about 2.25 g/cm<sup>3</sup>. The interspacing between each graphene layer is 0.3354 nm and the distance between two carbon atoms is 0.142 nm. Considering the graphene layer, the bonding is trigonal sp<sup>2</sup>-hybrid  $\sigma$ -bonds with delocalized  $\pi$ -bonds within the layer. The interspacing between layers of 0.3354 nm is larger than the 0.142 nm of the C-C atoms, indicating no chemical bonding between the layers. So, the interaction force is mainly the van der Waals force.

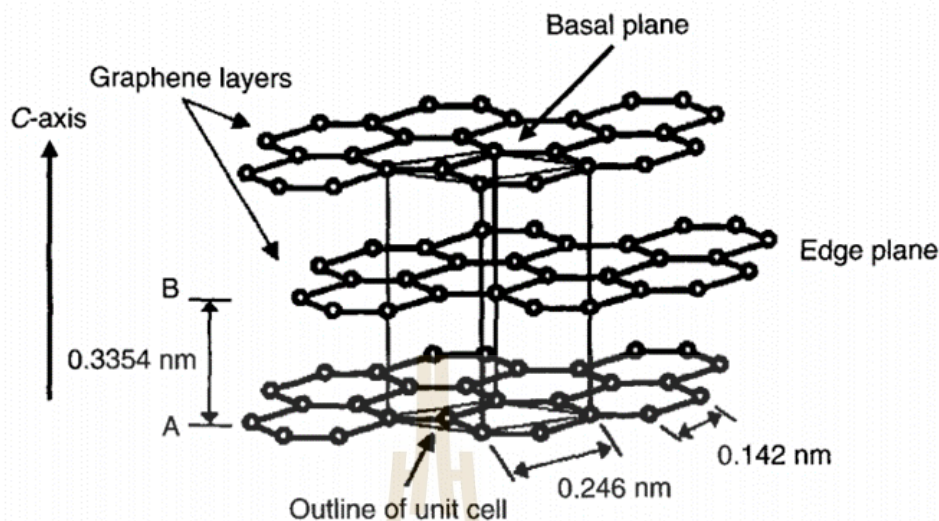


**Figure 2.3** The structure of hexagonal graphite, which trigonal bonding within the graphene layers (Marsh & Rodriguez-Reinoso, 2006).

### 2.2.2 Surface Chemistry of Activated Carbon

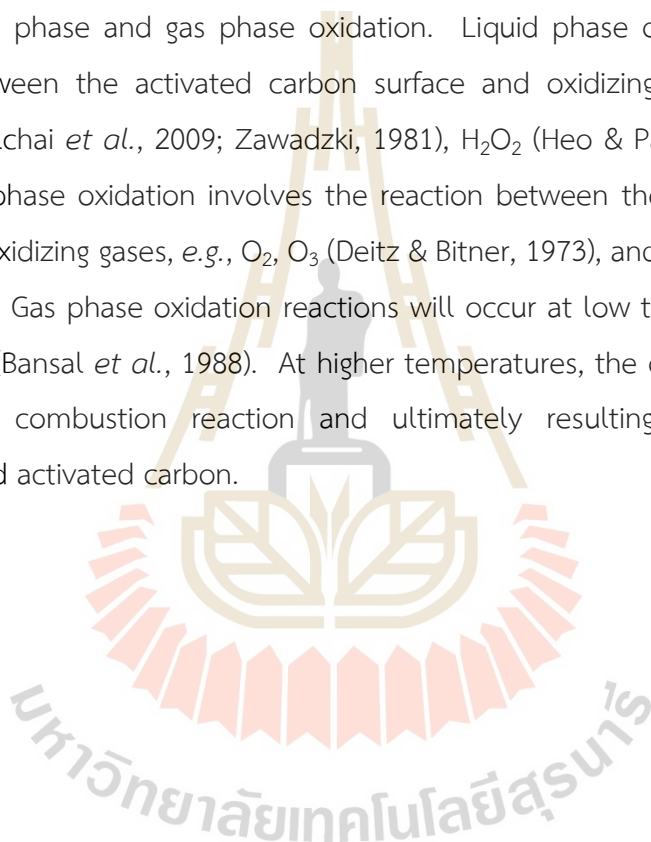
Due to the hydrophobic character of activated carbon, it can be used as a good adsorbent for non-polar compounds. However, the defects in microcrystalline structure and the presence of ash compounds and heteroatom, activated carbon can also be used to adsorb polar molecules (Marsh *et al.*, 1997). The heteroatoms are usually presented in the pristine materials, *e.g.*, oxygen, hydrogen, nitrogen, sulfur, phosphorous, and halogens, and once they were carbonized and activated, they become a part of the chemical structure of the activated carbon. These heteroatoms are also bonded at the edges and also at in-ring (Marsh *et al.*, 1997) of the graphene sheets and become surface compounds (Bansal *et al.*, 1988). These atoms form acidic, basic as well as natural functional groups and somehow, they are similar to those in organic chemistry (Boehm, 1966b, 1994).

#### *Oxygen Functional Groups*

The most significant functional groups on activated carbon are the oxygen functional groups, because of their abundant quantities as compared to other surface functional groups. They also have strong effects on the adsorption properties of

activated carbon. The chemical structure of some oxygen surface functional groups is presented in *Figure 2.4*. Carboxylic, lactone, and hydroxyl groups are considered as weakly acidic groups (Boehm, 1994), while the rest, *e.g.*, pyrone, chromene, and quinone are normally basic (Boehm, 1994; Garten & Weiss, 1957).

All types of carbon are metastable against oxygen-containing gases or oxidizing agents (Marsh *et al.*, 1997). There are two ways to modify the surface of activated carbon, that is, liquid phase and gas phase oxidation. Liquid phase oxidation involves the reaction between the activated carbon surface and oxidizing solution, *e.g.*,  $\text{HNO}_3$  (Tangsathitkulchai *et al.*, 2009; Zawadzki, 1981),  $\text{H}_2\text{O}_2$  (Heo & Park, 2018),  $\text{H}_2\text{SO}_4$ , and  $\text{HClO}_4$ . Gas phase oxidation involves the reaction between the surface of activated carbon and oxidizing gases, *e.g.*,  $\text{O}_2$ ,  $\text{O}_3$  (Deitz & Bitner, 1973), and air (Tangsathitkulchai *et al.*, 2009). Gas phase oxidation reactions will occur at low temperatures at about 200 – 300°C (Bansal *et al.*, 1988). At higher temperatures, the oxidation reaction will turn into a combustion reaction and ultimately resulting in ash instead of functionalized activated carbon.



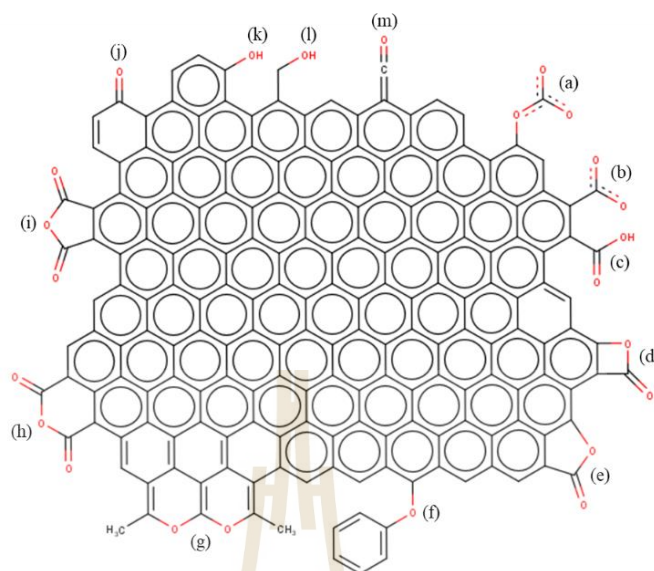


**Figure 2.4** Examples of some oxygen surface functional groups on activated carbon: (a) and (b) carboxyl-carbonates; (c) carboxylic acid; (d) and (e) lactone; (f) ether bridge; (g) cyclic ethers; (h) and (i) cyclic anhydride; (j) quinone; (k) phenol; (l) alcohol; and (m) ketene (Fanning & Vannice, 1993).

#### Nitrogen Functional Groups

Nitrogen functional groups integrate the adsorptive and catalytic properties of activated carbon (Bagreev & Bandosz, 2002; Pels *et al.*, 1995) and they are incorporated into activated carbon surface by  $\text{NH}_3$  treatment (Lahaye, 1998). The nitrogen functional groups on the activated carbon surface can increase the adsorption capacity of phenol and acidic gases, *e.g.*,  $\text{SO}_2$  and  $\text{H}_2\text{S}$  (Wenzhong *et al.*, 2008). During the surface modification process, using a high temperature in the furnace leads to a more stable structure of the nitrogen functional groups on the carbon surface (Bagreev & Bandosz, 2002) and produce more stable basic functional groups. Some structures of nitrogen-containing surface groups are shown in *Figure 2.5*.

Bagreev and co-workers (Bagreev *et al.*, 2004) have created nitrogen functional groups on activated carbon using impregnation with the melamine and urea solution at ambient temperature, followed by carbonization at 650 – 850°C. The obtained char

was then used to adsorb  $\text{H}_2\text{S}$ . Chen and co-workers (Chen *et al.*, 2005) used  $\text{NH}_3$  to create nitrogen functional groups on bituminous granular activated carbon (GAC) at 500 – 800°C for 60 minutes. The prepared char was then employed to adsorb perchlorate solution at an ambient temperature. It was found that  $\text{NH}_3$  treatment appears to be an effective method to improve the adsorption of perchlorate in an aqueous solution.

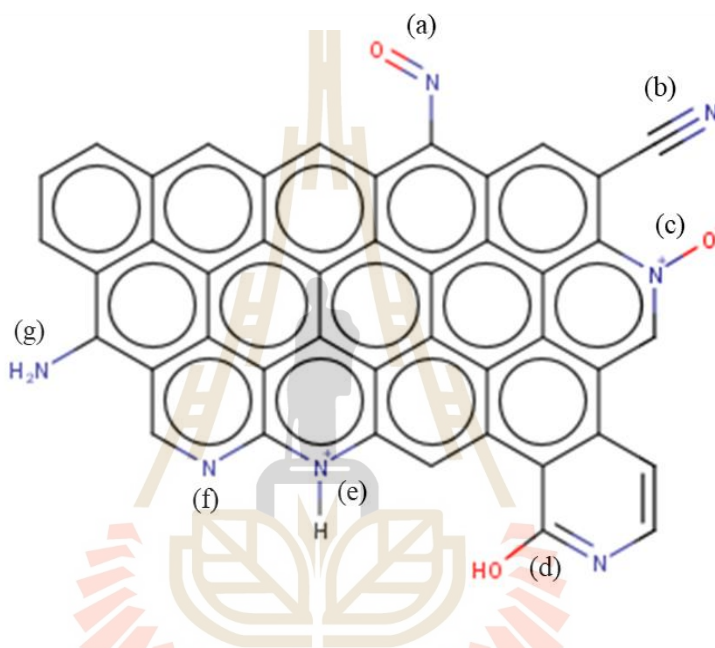


**Figure 2.5** Examples of some nitrogen surface functional groups on activated carbon: (a) nitroso; (b) nitrile; (c) pyridine-N-oxide; (d) pyridine; (e) pyridinium; (f) pyrrole; and (g) amine (Ngernyen, 2007).

#### *Other Surface Functional Groups*

The HCl treatment process on activated carbon produced chemisorbed chlorine on the activated carbon surface, and at the same time, chlorine caused a reduction in micropore volume (Bansal *et al.*, 1988). The treatment process using HF does not create fluorine on the carbon surface. This can be attributed to the HCl which is a strong acid with  $\text{p}K_a = -7$ , while HF is a weak acid with a  $\text{p}K_a$  of 2.95, at 25°C (Moreno-castilla *et al.*, 1998).

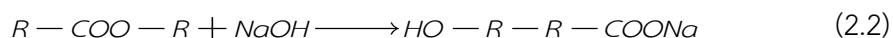
Chlorine is distributed on the external and internal surfaces of activated carbon. It is bonded using covalent bond to the carbon atoms as well (Pérez-Cadenas *et al.*, 2003). Bromine on the surface of activated carbon can be introduced by chemisorption, however, the bonds are not as strong as those of chlorine and carbon (Boehm, 1994).

### 2.2.2.1 Methods to Characterize Surface Functional Groups

There are several ways to analyze surface functional groups on activated carbon, *e.g.*, acid-base titration, Fourier Transform Infrared Spectroscopy (FTIR), X-Ray Photoelectron Spectroscopy (XPS), Temperature Programmed Desorption (TPD), and elemental analysis. Here, details of certain methods that are related to the present work are given.

#### *Acid-Base Titration*

Acid-base titration was firstly proposed by Boehm in 1966 (Boehm, 1966b). Boehm titration is one of the most widely used methods to determine the amounts of surface chemistry of activated carbon. The theory is based on acid and base in aqueous solutions being neutralized with a variety of basic and acidic functional groups on the surface of activated carbon. The principle of titration is briefly described here. Carboxylic, lactonic, and phenolic groups on activated carbon surfaces can be determined by sodium hydroxide solution (NaOH). The reactions of NaOH with these functional groups are shown in Equations (2.1) to (2.3), respectively (Boehm, 1966a; Li, 2012; Seung Kim & Rae Park, 2016).



Hydrogen ions in carboxylic and phenolic groups were replaced by sodium cation from NaOH solution, forming sodium carboxylates and sodium phenolates. For the reaction of NaOH with lactonic groups, sodium carboxylates and phenolic groups are formed.

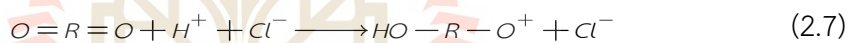
Typically, sodium carbonate ( $\text{Na}_2\text{CO}_3$ ), which is a weak acid and weaker than that of  $\text{NaOH}$ , can only neutralize the carboxylic group and lactonic groups. The reaction mechanisms involved are presented in Equations (2.4) to (2.5), respectively.



Another weak acid, which is sodium bicarbonate ( $\text{NaHCO}_3$ ) reacts only with carboxylic groups on the activated carbon surface., resulting in sodium carboxylates due to its weakest basic property among the three basic solutions mentioned previously. Equation (2.6) presents the reaction mechanism.



On the other hand, to determine the basic surface functional groups, hydrochloric acid ( $\text{HCl}$ ) is employed to neutralize the basic surface functional groups. The reaction is shown in Equation (2.7).



In conclusion, the basic solutions and acid solutions can be employed to identify the quantities of surface functional groups on activated carbon. Boehm titration is a practical way to yield the preliminary results of surface functional groups.

#### *Fourier Transform Infrared Spectroscopy (FTIR)*

At the beginning of the 20<sup>th</sup> century, FTIR was rapidly developed due to the rapid development of technologies on computers. The combination of Michelson interferometer with computer technology gives FTIR analysis works very well. It has so many advantages, e.g., short time of measurement, high resolution and sensibility, and a broad range of measurement spectrum. FTIR is applied to determine the samples with scattering property and strong adsorption capacity, especially activated carbon. The principle of FTIR is described as follows.

Infrared adsorption spectra of molecules are a vibrational or rotational spectrum of compounds that are based on the adsorption resulting from the transition of vibrational

or rotational energy level of molecules. Compared with the standard spectrum, the information of functional groups molecules on activated carbon can be determined by the frequency of the adsorption band. The wavelength regions that associate with surface functional groups on activated carbon are summarized in *Table 2.2*.

**Table 2.2** Some IR spectra assignment of functional groups on activated carbon surface (Fanning & Vannice, 1993).

Functional Groups	Wavenumber (cm <sup>-1</sup> )		
	1000 – 1500	1500 – 2050	2050 – 3700
C-O in ethers (stretching)	1000 – 1300		
Alcohols	1049 – 1276		3200 – 3640
Phenolic groups			
C-OH stretch	1000 – 122		
Phenolic groups			
O-H bend/stretch	1160 – 1200		2500 – 3620
Carbonates			
Carboxyl-carbonate	1100 – 1500	1590 – 1600	
Aromatic C=C stretching		1585 – 1600	
Quinones		1550 – 1680	
Carboxylic acids (-COOH)	1120 – 1200	1665 – 1760	2500 – 3300
Lactones	1160 – 1370	1675 – 1790	
Carboxylic anhydrides	980 – 1300	1740 – 1880	
C-H stretch			2600 – 3000
N-H, C=N		1560 – 1570	
C-N aromatic ring	1000, 1250, 1355		
C-N	1190		2040 – 2070
C=C=N			
N-O-	1000 – 1300		

### Elemental Analysis

Perhaps the elemental contents of carbonized char and prepared activated carbon can be used to indirectly determine the type of element in surface functional groups. Li and co-workers examined the amount of ash and elements in their adsorbent by the element analyzer (Li *et al.*, 2009). The element analyzer (Varia EL, Elementar, Analysensysteme GmbH) was employed to investigate carbon (C), hydrogen (H), nitrogen (N), and oxygen (O) was calculated by difference, while sulfur (S) was determined by the sulfur analyzer (SC-132, LECO). The results are presented in *Table 2.3*.

**Table 2.3** The amount of ash and elements in various adsorbents, they are presented in weight percentage (Li *et al.*, 2009).

Sample	Ash	C	H	N	S	O
AC	8.32	88.47	0.50	0.43	0.46	1.82
ACO1	7.11	86.89	2.11	0.83	0.38	2.67
ACO2	7.04	86.36	2.04	0.77	0.36	3.49
ACD	0.53	93.40	1.76	0.58	0.42	1.95

Four adsorbents used are activated carbon prepared with different conditions as shown in *Table 2.3*. Among the four samples, normal AC has highest ash content of 8.32 wt. %. After it was treated with  $\text{HNO}_3$  and resulting in ACO1 and ACO2 (the treatment times are 4 hours and 6 hours, respectively) the resulting carbons possess lower ash content. The  $\text{HNO}_3$  treatment removed some ash from the normal AC. Then the final sample, ACD has the lowest ash content (0.53 wt. %) which was treated by HCl and HF, giving most of the ash content being removed. The results of samples AC, ACO1, and ACO2 indicate that the elements H, N, and O were increased by  $\text{HNO}_3$  treatment. From the results, it can be concluded that the role of  $\text{HNO}_3$  treatment is to modify the surface chemistry of activated carbon.

### *Temperature Programmed Desorption (TPD)*

This is one of the useful temperature-programmed techniques to investigate the structures and properties of catalysts and interaction between reaction molecules. They are also frequently used to identify surface functional groups on activated carbon, especially oxygen-containing groups via chemical mass spectrometer or adsorption/desorption apparatus (Li, 2012).

The decomposition of oxygen-containing surface groups on activated carbon depends on temperature. After the decomposition process, CO and CO<sub>2</sub> will be desorbed from the samples at different temperatures (Brender *et al.*, 2012; Salame & Bandosz, 2001). Hence, it could be concluded that certain oxygen-containing surface groups could decompose at a specific temperature. Typical desorption temperatures of some surface functional groups are as follows: the production of CO<sub>2</sub> at a temperature ranging from 200 – 250°C could result from the decomposition of carboxylic acid (Otake & Jenkins, 1993; Zhuang *et al.*, 1994). The formation of CO<sub>2</sub> at about 627 – 650°C could be related to the decomposition of lactone (Marchon *et al.*, 1988; Zhuang *et al.*, 1994). The desorption of CO at temperatures ranging of 600 – 700°C accounts for the decomposition of the phenolic group (Zielke *et al.*, 1996), and at 700 – 980°C is related to the desorption of quinones and carbonyl groups (Marchon *et al.*, 1988). The temperature from ambient up to 1000°C is high enough to desorb all the functional groups on the carbon surface. However, some reports point out the desorption of the extremely stable oxygen compounds above 1200°C, which are pyrone-like compounds (Fritz & Hüttinger, 1993) and the C-O-C bonds with the atoms of C on the edge between two crystallites in nuclear graphite (Pan & Yang, 1992).

### **2.2.3 Synthesis of Activated Carbon**

Commonly, two methods are used to produce activated carbon, which are physical activation and chemical activation. Physical activation has a purpose to enhance or develop the porosity in carbonized char by gasifying with oxidizing gases (*e.g.*, CO<sub>2</sub>) or steam under very high temperatures (*i.e.*, 850 – 1100°C). The chemical activation can be achieved by carbonization of the impregnated precursors with a

chemical agent (e.g.,  $\text{H}_3\text{PO}_4$ ,  $\text{ZnCl}_2$ ) at lower temperatures, between 500 – 900°C. The details of carbonization, physical activation, and chemical activation are given below.

#### 2.2.3.1 Precursor

Activated carbon can be produced from most carbon containing organic materials. For commercial production, coalified matter (e.g., peat, lignite, coal) or the biomass (e.g., nutshell, coconut shell, corncob, palm stone) (Ahmadpour & Do, 1997; El-Hendawy *et al.*, 2001; Guo & Lua, 2000) can be used. The mentioned raw materials give high carbon yield for the production of activated carbon are inexpensive, especially from coal origin (Linares-Solano *et al.*, 2000). However, the precursors from biomass tend to give high volatile organic compounds (VOCs) and low fixed carbon as compared to coal origin, basically due to the polymeric structure of the biomass.

#### 2.2.3.2 Carbonization

The noncarbon compounds will be thermally eliminated in this process. It is usually carried out at a temperature between 400 – 800°C. The obtained product consists of high fixed carbon called char. The purpose of carbonization is to produce carbon structure, create initial porosity, and remove of volatile organic compounds (VOCs).

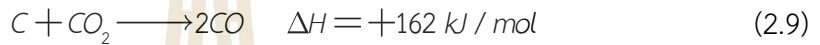
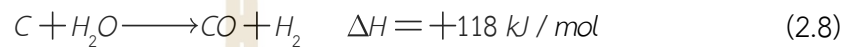
The important parameters that determine the quality and the yield of the derived char are the heating rate, the final temperature, the holding time at the carbonization temperature, and the nature and physical state of the precursors.

#### 2.2.3.3 Physical Activation

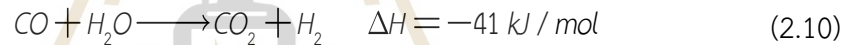
The obtained char from the carbonization step is further activated in the second step to produce activated carbon. The obtained char has low internal surface area due to the blockage of the pores by tars, and then the porous structure has not fully developed (Rodríguez-Reinoso & Molina-Sabio, 1998). The oxidizing agents are then employed for the activation step (e.g.,  $\text{CO}_2$  or steam) to form the reaction between the gas and char which produces activated carbon with a high degree of porosity (Rodríguez-Reinoso & Molina-Sabio, 1998). To develop the porosity in char, the oxidizing agent penetrates through the initial pores and then the reaction

between the oxidizing agent and carbon atoms takes place on the internal surface. This results in the creation of new pores, opening the blocked pores, and widening the rudimentary pores (Rodríguez-Reinoso, 2002).

The gasification reactions between steam and carbon (water-gas reaction) and  $\text{CO}_2$  with carbon are endothermic (Bansal *et al.*, 1988). They are usually carried out at 800 – 1000°C (Rodríguez-Reinoso, 2002). The reactions involved are presented as follows:



The reactions are endothermic, so the heat sources are required (*e.g.*, furnace) to drive the reactions and maintain the temperature. For steam activation, two further reactions are the reaction of steam with carbon accompanied by the water-gas formation reaction, which is catalyzed by the carbon surface as:



This reaction is exothermic, but the heterogeneous water-gas reaction is dominant, so the overall process is endothermic.

Oxygen is one of the oxidizing agents that can be used as well. The reaction of oxygen and carbon atom can be written as follows:



The reaction is exothermic, therefore it is difficult to control the reaction between  $\text{O}_2$  and char due to the carbon burning reaction. Since the extent of reaction is difficult to control, therefore this method is rarely used (Bansal *et al.*, 1988).

The burn-off parameter indicates the gasification level, which is dependent on the properties of char and the activating conditions including activation temperature, activation time as well as the composition and flow rate of an oxidizing agent, etc. The burn-off can be mathematically expressed as:

$$\text{Burn-off} \% = \frac{W_{char} - W_{ac}}{W_{char}} \times 100 \quad (2.12)$$

where  $W_{char}$  and  $W_{ac}$  are the initial weight of char and the obtained weight of activated carbon after the activation process, respectively.

Activation of char by  $\text{CO}_2$  develops micropores (Marsh *et al.*, 1997), while steam activation can cause the pore widening of the developed micropores, resulting in mesopores and macropores development (Rodríguez-Reinoso & Molina-Sabio, 1998; Zhang *et al.*, 2014).

#### 2.2.3.4 Chemical Activation

Chemical activation is usually employed when the precursor comes from biomass or of wood origin. The precursor is usually impregnated with an activating agent which is normally an inorganic chemical solution that results in the degradation of cellulose fibre in the precursor. Then, the impregnated precursor is carbonized under an inert gas at about  $400 - 600^\circ\text{C}$  (Bansal *et al.*, 1988). The derived activated carbon product is cooled in the furnace until it reaches ambient temperature. It is then collected and washed thoroughly with water to eliminate the leftover activating agent. Finally, the product is dried in the oven to remove the excess moisture. During the activation process, the activating agent dehydrates the precursor, resulting in charring and aromatization of the carbon skeleton and the formation of porous structure (Bansal *et al.*, 1988).

The commonly used activating agents are metal compounds (*e.g.*,  $\text{ZnCl}_2$ ,  $\text{AlCl}_3$ ), alkali and alkaline earth metal compounds (*e.g.*,  $\text{KOH}$ ,  $\text{K}_2\text{CO}_3$ ,  $\text{NaOH}$ ,  $\text{Na}_2\text{CO}_3$ , and  $\text{MgCl}_2$ ) as well as acid substances (*e.g.*,  $\text{H}_3\text{PO}_4$ ,  $\text{HNO}_3$ , and  $\text{H}_2\text{SO}_4$ ). The common feature of these activating agents is that they are dehydrating agents which interrupt the formation of tar and influence the pyrolytic decomposition (Bansal *et al.*, 1988; Marsh *et al.*, 1997). They also decrease the acetic acid, methanol and increase the yield of activated carbon (Bansal *et al.*, 1988).

Generally, the characteristics of the activated carbon product depend on the ratio of impregnation with a chemical agent (*i.e.*, the mass ratio of the chemical agent to wood or biomass), carbonization temperature in the furnace, and holding temperature and time.

Activated carbon produced from the chemical activation method can yield a relatively high BET specific area of over 3,000 m<sup>2</sup>/g, calculated based on the N<sub>2</sub> adsorption/desorption isotherms at -196°C (77.4 K). It was produced from KOH chemical activation using petroleum coke and carbonized at 700°C (Otowa *et al.*, 1997). The development of porosity by KOH activation is suggested by the reduction of KOH to potassium atoms (K). Then these metallic atoms penetrate between graphene layers, resulting in a larger space between graphene layers. Finally, in the carbonization process, the free metallic atoms are thermally removed from the graphene layers and the space between layers is the microporosity (Marsh & Rodriguez-Reinoso, 2006).

However, chemical activation always deals with the hazardous chemical compounds and environmental concerns associated with chemical substances. This method should be performed carefully and economically to avoid the environmental impact as much as possible (*i.e.*, recover and reuse chemicals agent from the activation process).

#### 2.2.4 Applications

Activated carbons are versatile and unique adsorbents because of their high specific area, microporous structure, high adsorption capacity, and a high degree of surface reactivity. Their practical applications are the removal of colour from sugar syrup (Mudoga *et al.*, 2008), gas separation and storage (Caldwell *et al.*, 2015; Sircar *et al.*, 1996), solvent recovery (Chinn & King, 1999; Staggs *et al.*, 2017), wastewater treatment (Lo *et al.*, 2012; Peng *et al.*, 2015), and air pollution control (Ferraz, 1988). *Table 2.4* summarizes the applications of activated carbon for both gas- and liquid-systems.

**Table 2.4** Example of activated carbon used in the industries (Marsh & Rodriguez-Reinoso, 2006).

Process	Applications
Gas phase	<ol style="list-style-type: none"> <li>1. Off-gas purification, removal of SO<sub>2</sub>, H<sub>2</sub>S, CS<sub>2</sub>, etc.</li> <li>2. Effluent gas purification</li> <li>3. Petroleum refineries</li> <li>4. Sewage and geothermal plants</li> <li>5. Solvent recovery</li> <li>6. Natural gas storage</li> <li>7. Adsorption of radionuclides</li> <li>8. Separation of gas mixtures</li> <li>9. Organic and inorganic process catalysis, both are support material and as a catalyst</li> <li>10. Cigarette filters</li> <li>11. Industrial gas masks</li> <li>12. Chemical warfare agent protection, including clothing, gas masks, and atmospheres in a warship, submarines, tanks, and aircrafts</li> <li>13. Odour control</li> <li>14. Removal of VOCs</li> </ol>
Liquid phase	<ol style="list-style-type: none"> <li>1. Drinking water purification, removal of chlorine compounds and other VOCs</li> <li>2. Removal of heavy metal ions from groundwater</li> <li>3. Treatment of both industrial and municipal wastewater</li> <li>4. Metallic ion adsorption (gold and other metals)</li> <li>5. Sugar and sweetener industries need decolourization agents</li> <li>6. Food, beverage, and vegetable oil industries for removal of colours and unacceptable tastes</li> </ol>

**Table 2.4** Example of activated carbon used in the industries (Marsh & Rodriguez-Reinoso, 2006). (Continued)

Process	Applications
Liquid phase	7. Pharmaceutical industry 8. Drug detoxification in the body 9. Inorganic compounds removal (As, Cd, F, Cu, Se, Pb, etc.) 10. Organic, halogenated organics, oxygenated organics, etc. removal

### 2.3 Adsorption

The adhesion of atoms, molecules, and ions from the bulk gas or liquid on a surface is called “*adsorption*”. The adsorption process produces film layers of the fluid which is called “*adsorbate*” on the substrate or surface, which is called “*adsorbent*”. The adsorbent can be either surface (2D) or pore (3D). The adsorption process is used to separate the selected gases or liquids component from the bulk phase by porous solids. So, the key parameters in the adsorption process are the porous solid, temperature, and pressure. Moreover, desorption is the reverse process of adsorption.

There are two major types of adsorptions, the first is the physical adsorption or physisorption, and the second is chemisorption. The difference between these two types is how the adsorbate molecules interact with adsorbents. In physisorption, the gas or liquid molecules have a relatively weak force between adsorbate and adsorbent, e.g., London force or van der Waals force. On the other hand, chemisorption creates the exchange of electrons between the adsorbate and adsorbent, resulting in the strong bonding between the fluid and a solid substrate. Chemisorption also involves the chemical reaction between fluid and a solid substrate as well.

## 2.4 Adsorption Equilibrium

The information of adsorption equilibrium is one of the most important pieces of information which can lead us to the understanding of the adsorption process. The adsorption equilibrium of the process always starts with the pure component with the solid adsorbent. No matter how many components are in the system, the data of pure components can lead us to the understanding of kinetic and equilibrium for both single component and multicomponent systems (Do, 1998).

### 2.4.1 Adsorption Isotherms

The adsorption isotherm is the phrase that is used to call the relationship between “*amount adsorbed*” and “*adsorbate concentration*” in the fluid phase at a fixed temperature and that system is in equilibrium. The adsorption isotherm data can be used to determine useful information of adsorbent and the interaction between adsorbate-adsorbent as well. There is several information that can be interpreted from the adsorption isotherm, e.g., the determination of the internal surface area of adsorbent, pore volume, average pore size, pore size distribution, capacity of the solid adsorbent at the equilibrium pressure, etc.

For a gas system, the amount adsorbed is denoted by  $n$ , which depends on the temperature of the system,  $T$ , and the pressure,  $P$ . Thus, for a given adsorbent-adsorbate system, the adsorption isotherm can be mathematically expressed as:

$$n = f(P, T) \quad (2.13)$$

or it can be written in terms of relative pressure, which is usually scaled by the saturation pressure,  $P_0$  of the concerning fluid at a given temperature. We can write:

$$n = f\left(\frac{P}{P_0}, T\right) \quad (2.14)$$

There are six types of physisorption isotherms for gas adsorption clarified by the IUPAC (Sing, 1985). However, the new types of isotherms have been recently studied and identified. The updated version of these isotherms is shown in *Figure 2.6*, and the details of isotherms are given below.

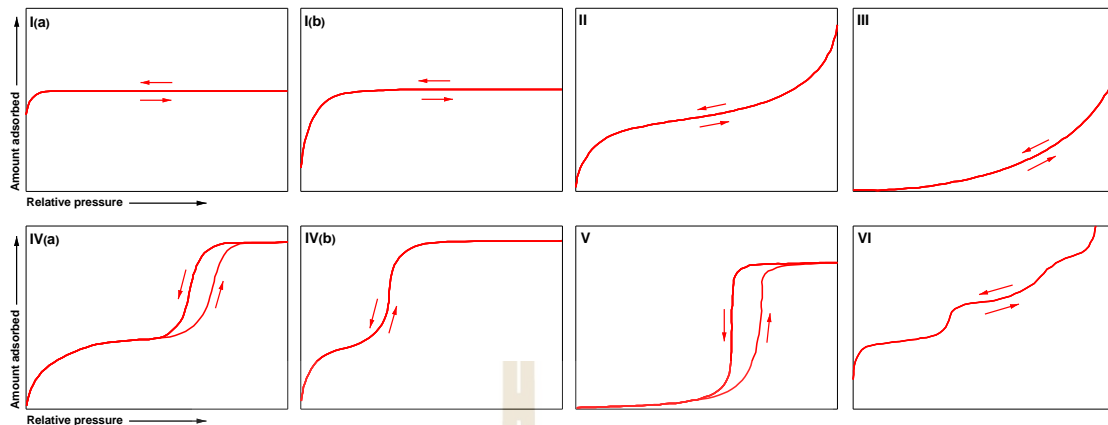


Figure 2.6 Physisorption isotherms (Thommes *et al.*, 2015).

**Type I:** This is an isotherm for microporous solid showing monolayer adsorption. The limiting uptake is dominated by the micropore volume. A steep uptake can be seen at very low relative pressures ( $P/P_0$ ) and the completion of monolayer density can be observed at  $\sim 0.3P/P_0$ . Type I(a) is the solid with a narrow micropore ( $< \sim 1$  nm), while Type I(b) is the solid with a wider range of pore size distribution ( $< \sim 2.5$  nm).

**Type II:** This isotherm is typified by the physisorption of gas on a nonporous or microporous solid. It involves a multilayer adsorption (Brunauer *et al.*, 1938). Point B is usually the completion of the monolayer capacity, and the beginning of the multilayer adsorption.

**Type III:** This isotherm shows a very weak interaction energy between adsorbate and adsorbent, which results in low capacity at low  $P/P_0$ . An example of this system is water adsorption on activated carbon (Horikawa *et al.*, 2010). The adsorbed amount remains finite at  $P/P_0 = 1$ .

**Type IV:** In this case, the monolayer and multilayer adsorption on pore walls occur, following by the condensation in pores. This happens in the mesoporous solid (e.g., industrial adsorbent, molecular sieve). Pore condensation is the condition that a gas in the pore condenses into a liquid-like state at a pressure less than  $P_0$  (Thommes & Cychosz, 2014). Type IV(a) shows the capillary condensation which occurs when the

pore width exceeds the critical width, it depends on the adsorption system and temperature. Type IV(b) can be obtained from a conical or cylindrical mesopore with the apex being closed (Thommes *et al.*, 2015).

**Type V:** This type is similar to Type III, where the clustering of molecules in pores occur and is followed by the pore filling. An example of this isotherm is water adsorption in slit pores (Liu *et al.*, 2019).

**Type VI:** This is a layer-by-layer adsorption isotherm on a very uniform surface. An example of this type is the argon adsorption on a graphite substrate at a low temperature, which is much lower than the bulk triple point temperature of argon (Prasetyo, Xu, *et al.*, 2019).

#### 2.4.1.1 Classification of Pore Size

In physisorption, the pore size in a solid adsorbent can be classified according to IUPAC as (Sing, 1985):

- pores diameters exceed about 50 nm are *macropores*.
- pores diameters between 2 nm and 50 nm are *mesopores*.
- pores diameters smaller than about 2 nm are *micropores*.

#### 2.4.2 Equations of Adsorption Isotherms

Several isotherm equations have been developed in the field of adsorption since which can be found in several references (Bansal & Goyal, 2005; Brunauer *et al.*, 1938; Dubinin, 1967; Freundlich, 1907; Freundlich, 1932; Langmuir, 1918). Here, we present some of the basic and practical isotherms that are related to this work.

##### 2.4.2.1 Langmuir Equation

This equation was derived by Langmuir (Langmuir, 1918) using the adsorption of gases on a planar substrate of glass, mica, and platinum. The assumptions of this equation are:

- Homogeneous surface with adsorption energy being constant all over the surface.
- Each adsorption site accommodates one adsorbed molecule only.
- Adsorbate molecules are adsorbed at definite, localized sites.

The most basic isotherm equation of Langmuir can be written as:

$$\frac{P}{V} = \frac{1}{V_m b} + \frac{P}{V_m} \quad (2.15)$$

where  $P$  is pressure (for adsorption in the gas phase),  $V$  is adsorbed amount, and  $V_m$  is the monolayer adsorbed amount. The parameter  $b$  is the affinity constant which indicates how strong the adsorbate molecule is attracted onto an adsorbent surface (Do, 1998).

#### 2.4.2.2 Brunauer, Emmett, and Teller (BET) Equation

This isotherm equation is the most famous equation in adsorption science. It was derived based on multilayer adsorption of a gas on a flat surface (Brunauer *et al.*, 1938). The assumptions of the BET theory basically are based on Langmuir isotherm, however, there are three more assumptions for the multilayer adsorption (Junpirom, 2006).

- Multilayer adsorption is unlimited.
- The adsorption and desorption only occur at the sites exposing to the bulk phase.
- The adsorption energy in the second and higher layers are equal to the enthalpy of liquefaction.

The famous BET equation can be written in the linear form as:

$$\frac{P}{V(P_0 - P)} = \frac{1}{V_m c} + \frac{c-1}{V_m c} \frac{P}{P_0} \quad (2.16)$$

where  $P_0$  is the saturation pressure at the corresponding temperature, the fitting parameter  $c$  indicates that the larger value of  $c$ , the sooner of multilayer will form and the convexity of isotherm can increase toward low pressure range (Do, 1998).

Alternatively, the BET equation can be written in a number of moles,  $n$ , as

$$\frac{P}{n P_0 - P} = \frac{1}{n_m c} + \frac{c-1}{n_m c} \frac{P}{P_0} \quad (2.17)$$

The relationship between  $P/n P_0 - P$  and  $P/P_0$  gives  $n_m$  and  $c$ , which can be further employed to determine the “BET specific area” per unit mass of adsorbent,  $S_{BET}$ . That is,

$$S_{BET} = n_m N_A \sigma_m / m \quad (2.18)$$

where  $n_m$  is the monolayer adsorbed amount in mol/g,  $N_A$  is the Avogadro number,  $\sigma_m$  is the projection area of the adsorbate molecule ( $\text{nm}^2/\text{molecule}$ ) and  $m$  is the mass of adsorbent.

Usually, the BET plot is restricted to the limited part of the full isotherm, *i.e.*,  $P/P_0 \sim 0.05$  to  $0.30$  for Type II and Type IV isotherms. The choice of adsorptive gases to determine BET specific area can be varied. Nitrogen adsorption isotherm at  $77.4 \text{ K}$  ( $-195.8^\circ\text{C}$ ) is used to obtain  $S_{BET}$  using  $\sigma_m$  of  $0.162 \text{ nm}^2/\text{molecule}$ . However, due to the quadrupole moment of the nitrogen molecule, the orientation of nitrogen molecules depends on the adsorbent and surface chemistry. This can lead to the hesitation in  $\sigma_m$  of nitrogen (Thommes *et al.*, 2015). Argon adsorption isotherm at  $87.3 \text{ K}$  ( $-185.8^\circ\text{C}$ ) can be an alternative choice, using  $\sigma_m$  of  $0.142 \text{ nm}^2/\text{atom}$ . Due to no quadrupole moment of argon atom and high temperature ( $87.3 \text{ K}$ ), argon especially offers advantages for micropore analysis (Rouquerol *et al.*, 2013).

### 2.4.2.3 Dubinin-Radushkevich (DR) Equation

This theory has been developed by Dubinin and Radushkevich in 1947 (Dubinin, 1975). It has been used to describe the adsorption of gases and vapours in many microporous solids, especially activated carbon. The equation is based on the adsorption potential theory of Polanyi (Polanyi, 1914, 1932, 1963) and

the adsorption process of the Theory of Volume Filling of Micropores (TVFM). The DR equation can be represented as:

$$V = V_0 \left[ -\frac{1}{\beta E_0^2} \left( RT \ln \frac{P}{P_0} \right)^2 \right] \quad (2.19)$$

where  $V_0$  is the total (limiting) volume of micropore (Bansal & Goyal, 2005),  $E_0$  is the solid characteristic energy towards a reference adsorbate where benzene is usually used as the reference adsorbate (Do, 1998).  $\beta$  is called “*affinity coefficient*”, which is a function of the adsorbate, and it can be calculated from the molar volume in the liquid state at 293.15 K. For benzene, the  $\beta$  is 1.0. Values of  $\beta$  for other gases and vapours can be found in references by Dubinin (Dubinin, 1975) and Bansal & Goyal (Bansal & Goyal, 2005).

#### 2.4.2.4 Dubinin-Astakhov (DA) Equation

The DR equation can be employed to explain the adsorption of gases and vapours in micropores fairly well for the activated carbon at a low degree of burn-off (%). But in practice, the activated carbon with a high degree of burn-off will exhibit a high degree of surface heterogeneity and a wider range of pore size distribution. Dubinin and Astakhov (Dubinin, 1975) have developed the isotherm equation to account for this surface heterogeneity effect of the solid adsorbent. The equation derived is similar to Equation (2.19), but with the introduction of  $n$  parameter to describe the surface heterogeneity.

$$V = V_0 \left[ -\frac{1}{\beta E_0^n} \left( RT \ln \frac{P}{P_0} \right)^n \right] \quad (2.20)$$

It is found that if  $n = 3.0$ , the equation can describe the adsorption for a narrow micropore size distribution. Normally, the  $n$  values of activated carbon lie between 1.2 to 1.8 and for zeolite with extremely narrow micropore size,  $n$  values are between 3.0 to 6.0 (Do, 1998).

## 2.5 Adsorption Study via Computer Simulation

In sections 2.4.1 and 2.4.2, the adsorption equilibrium isotherms and isotherms equation have been described. In this section, the computer simulation method is presented to study the adsorption equilibrium of polar and non-polar species on a planar solid substrate and in pores. The simulation results can lead us to a better understanding of the physics of adsorption using the analysis at the microscopic scale, which cannot be studied by the experiment.

### 2.5.1 Simulation Method

To study the adsorption of fluid on a substrate using molecular simulation, two approaches can be employed. The first is the Molecular Dynamics (MD) simulation (Alder & Wainwright, 1959) and the second is the Metropolis Monte Carlo (MMC or MC) simulation (Metropolis *et al.*, 1953). MD is based on the movement of atoms or molecules that can interact with a solid substrate over a fixed period, resulting in the evolution of the adsorption state as a function of time. While the idea of MC said, the adsorption equilibrium can be addressed by the estimation of possible outcomes and then solved by a sampling experiment from all possible outcomes. More details of MD and MC can be found in the documentation of Frenkel and Smit (Frenkel & Smit, 2002) and Allen and Tildesley (Allen & Tildesley, 2017).

In the adsorption study, the equilibrium of the system for each pressure at a fixed temperature can be obtained by generating a sequence of configurations of the Markov chain (Prasetyo, 2019). The classic Metropolis procedure (MC) are summarized as the following steps (Prasetyo, 2019):

1. Specify the thermodynamic properties to initiate the system, *e.g.*, the chemical potential of the adsorbate,  $\mu$ , the volume of the system,  $x$ -,  $y$ - and  $z$ - directions, and temperature,  $T$ . These properties are set for the grand canonical ensemble, while for the canonical ensemble, the number of particles,  $N$  is specified in place of  $\mu$ .
2. The cumulative properties of the system should be set at zero.

3. Create the trial move randomly with equal probability. The trial move could be displacement, rotation, volume change, and insertion or deletion. It depends on the ensemble.
4. Calculate the energy of the system before the event takes place, this is called  $U$ .
5. Execute that event and calculate the energy of the system after the execution, this is the new configuration and called,  $U'$ .
6. The obtained configuration is now considered to be rejected or accepted, depending on the probability.
7. If that event is accepted, the new configuration is updated. However, if the event is rejected, the previous configuration is recovered. For every accepted move, the number of each move is counted for  $N$  move, the properties of the configuration are summed up, which can be mathematically expressed as:  $x = \sum_{i=1}^N x_i$ ,  $x_i$  is the properties at  $i$ -th configuration.
8. The simulation of trial moves should be carried out for a number of configurations to ensure that the system reaches equilibrium. Once the equilibration stage is finished, the program will repeat steps 2 to 7 for the sampling stage to determine the thermodynamic properties.
9. Once the sampling stage is finished, the average thermodynamic properties of the system are then calculated, that is:

$$\langle x \rangle = \frac{\sum_{i=1}^N x_i}{N} \quad (2.21)$$

### 2.5.2 Grand Canonical Ensemble (GC)

There are different types of the ensembles in MC simulation, *e.g.*, isobaric isothermal (NPT), grand canonical (GC or  $\mu$ VT), canonical (C or NVT), and Gibbs ensembles.

For the GC ensemble or the  $\mu$ VT ensemble, the chemical potential of the adsorbate ( $\mu$ ), temperature ( $T$ ), and volume of the simulation box ( $V$ ) are fixed and the number

of particles in the system can be varied. This ensemble exactly mimics the experimental setup of the adsorption of a fluid in an adsorbent. The pressure, temperature, are known and they can be employed to calculate the equilibrium concentration of the fluid in the adsorbent (Frenkel & Smit, 2002). Thus, the MC simulation in the GC ensemble is the most practical tool that is widely used to study the adsorption of a fluid in an adsorbent.

The trial moves of GC ensemble involve three types of moves, *i.e.*, displacement, insertion, and deletion of particles in the simulation box.

**The displacement of particle:** A particle is selected randomly and migrated to the new position. The probability to accept the displacement is given by:

$$P^{acc} = \min \left[ 1, \exp \left[ -\beta (U' - U) \right] \right] \quad (2.22)$$

**The insertion and deletion of particles:** A new particle is inserted randomly, or a selected particle is removed randomly from the system. The probability to accept the insertion is:

$$P^{acc} = \min \left[ 1, \frac{V}{\Lambda^3} \frac{1}{N+1} \exp \left[ -\beta (\mu - U' + U) \right] \right] \quad (2.23)$$

and the removal is accepted with the probability:

$$P^{acc} = \min \left[ 1, \frac{\Lambda^3 N}{V} \exp \left[ -\beta (\mu + U' - U) \right] \right] \quad (2.24)$$

where  $\beta$  is the reciprocal temperature,  $1/k_B T$ ,  $k_B$  is the Boltzmann's constant.  $U'$  and  $U$  are the potential energies after and before trial moves, respectively.  $\Lambda = \sqrt{h^2 / 2\pi m k_B T}$  is the thermal de Broglie wavelength.  $N$  is the number of particles in the system.

### 2.5.3 Canonical Ensemble (C or NVT)

For the canonical ensemble or NVT, the number of particles ( $N$ ), volume of the system ( $V$ ), and temperature ( $T$ ) are fixed. Then, only a particle can move to a

new position each time. So, the NVT ensemble proceeds by random displacement move to minimize the potential energy of the system (Prasetyo, 2019). The output properties from this ensemble are chemical potential,  $\mu$ , (*i.e.*, pressure). The probability to accept the displacement move is similar to Equation (2.22) in the GC ensemble.

In this study, the C and GC ensembles were employed to study the adsorption of a fluid in an adsorbent. We provide the equal probability for the three trial moves, *i.e.*, displacement, insertion, and deletion for each cycle, and 1,000 steps were tried for each cycle. In the equilibration stage, the displacement was initially set as 2.0 nm and adjusted at the end of each cycle to give an acceptance ratio of 20% (Mountain & Thirumalai, 1994). The simulation box was modelled as 20 times of the first collision diameter of the corresponding fluid in the *x*- and *y*-direction, while the length in the *z*-direction was kept at 10.0 nm. The top of the simulation box is a hard wall, and a planar substrate is placed at the bottom of the box. The cut-off radius was 5 times of the collision diameter of the first LJ site of the concerning fluid. The simulations were performed at least  $5.0 \times 10^6$  cycles in the equilibration and the sampling stages to ensure that the equilibrium had been achieved. The equation of state (EoS) by Johnson *et al.* (Johnson *et al.*, 1993) was employed to determine the chemical potential of the adsorbate in the simulation for a given temperature and pressure.

#### 2.5.4 Fluid-Fluid Potential

To obtain the fluid-fluid interaction energy, the famous model of Lennard-Jones 12-16 was employed. This model is very simple, and the parameters of the fluids are widely available. The interaction energy between two fluid molecules with the same type can be calculated with Lennard-Jones 12-16 potential (Lennard-Jones, 1931, 1932) as follows:

$$\varphi_{ff}(r) = 4\varepsilon_{ff} \left[ \left( \frac{\sigma_{ff}}{r} \right)^{12} - \left( \frac{\sigma_{ff}}{r} \right)^6 \right] \quad (2.25)$$

where  $r$  is the distance between the two molecules,  $\varepsilon_{ff}$  is the well-depth of the interaction energy, and  $\sigma$  is the collision diameter of the fluid.

For the pairwise fluid-fluid energy between two molecules  $i$  and  $j$  with partial charges, the interaction energy is given by the combination of Lennard-Jones 12-6 and the Coulomb electrostatic interactions (Tipler, 1999):

$$\varphi_{i,j} = \sum_{c=1}^C \sum_{d=1}^D 4\varepsilon_{ij}^{cd} \left[ \left( \frac{\sigma_{ij}^{cd}}{r_{ij}^{cd}} \right)^{12} - \left( \frac{\sigma_{ij}^{cd}}{r_{ij}^{cd}} \right)^6 \right] + \sum_{a=1}^A \sum_{b=1}^B \frac{q_i^a q_j^b}{4\pi\varepsilon_0 r_{ij}^{ab}} \quad (2.26)$$

where  $A$  and  $B$  are the number of partial charges,  $C$  and  $D$  are the numbers of LJ sites on molecules  $i$  and  $j$ , respectively.  $\varepsilon_0$  is the vacuum permittivity of free space.  $r_{i,j}^{c,d}$  is the separation distance between LJ sites  $c$  of molecule  $i$  and LJ site  $d$  of molecule  $j$  with a cross-well depth,  $\varepsilon_{i,j}^{c,d}$  and a cross-collision diameter,  $\sigma_{i,j}^{c,d}$ .  $r_{i,j}^{a,b}$  is the separation distance between charge  $a$  having  $q_i^a$  on molecule  $i$  with charge  $b$  having  $q_j^b$  on molecule  $j$ . The cross-collision diameter and cross-well depth can be determined using Lorentz (Lorentz, 1881) and Berthelot (Berthelot, 1898) mixing rules as follows:

$$\sigma_{ij}^{cd} = \frac{1}{2} \sigma_i^c + \sigma_j^d \quad (2.27)$$

$$\varepsilon_{ij}^{cd} = \sqrt{\varepsilon_i^c \varepsilon_j^d} \quad (2.28)$$

In this work, the polar and non-polar fluids were studied, *i.e.*, argon, nitrogen, ethylene, and ethanol. Argon was modelled as a simple LJ fluid, this model is proposed by Michels *et al.* (Michels *et al.*, 1949). Nitrogen was also modelled as a single LJ fluid by Ravikovitch *et al.* (Ravikovitch *et al.*, 2000). Ethylene was described by the TraPPE-UA model (Wick *et al.*, 2000) and the TraPPE-UA2 model (Shah *et al.*, 2017). The TraPPE-UA consists of two LJ sites, while the TraPPE-UA2 consists of two LJ sites and accounts for four sites of partial charges, this is due to the quadrupole moment of the real ethylene molecule (Buckingham *et al.*, 1968). Ethanol was modelled as TraPPE-UA (Chen *et al.*, 2001), it consists of three LJ sites, which are, one methylene group, one methyl group, and oxygen. While hydrogen atom has no LJ site, only partial charge exists. The partial charges also lie on the methylene group and oxygen. Another ethanol model was also used here to test the vapour-liquid equilibria (VLE) and adsorption on a graphite substrate. This model was developed by Schnabel *et al.*

(Schnabel *et al.*, 2005). It is called the new rigid model. The potential parameters and coordinates of the fluids used in this study are presented in *Table 2.5*.

**Table 2.5** Potential parameters and coordinates of fluids used in this study.

Fluid	Site	$\sigma$ (nm)	$\epsilon/k_B$ (K)	$q$ (e)	$x$ (nm)	$y$ (nm)	$z$ (nm)
Ar	Ar	0.3045	119.8	-	0	0	0
N <sub>2</sub>	N <sub>2</sub>	0.3615	101.5	-	0	0	0
C <sub>2</sub> H <sub>4</sub> UA	CH <sub>2</sub>	0.3675	85	-	-0.0665	0	0
	CH <sub>2</sub>	0.3675	85	-	0.0665	0	0
C <sub>2</sub> H <sub>4</sub> UA2	CH <sub>2</sub>	0.3575	99.8	+0.320	-0.085	0	0
	CH <sub>2</sub>	0.3575	99.8	+0.320	0.085	0	0
	Charge	-	-	-0.320	0	0.065	0
	Charge	-	-	-0.320	0	-0.065	0
C <sub>2</sub> H <sub>5</sub> OH (UA)	CH <sub>3</sub>	0.375	98	-	-0.1280	-0.0856	0
	CH <sub>2</sub>	0.395	46	+0.265	0	0	0
	O	0.302	93	-0.700	0.1146	-0.0856	0
	H	-	-	+0.435	0.1922	-0.0318	0
C <sub>2</sub> H <sub>5</sub> OH (rigid)	CH <sub>3</sub>	0.36072	120.15	-	-0.1984	0	0
	CH <sub>2</sub>	0.34612	86.291	+0.25560	0	0	0
	O	0.31496	85.053	-0.69711	0.002846	0.17156	0
	H	-	-	+0.44151	0.094477	0.196828	0

### 2.5.5 Solid-Fluid Potential

The interaction energy between a particle  $i$  and the homogeneous solid substrate with infinite in the  $x$ - and  $y$ -direction of a distance  $z$  was calculated by the Steele 10-4-3 equation (Steele, 1973).

$$\varphi_{i,s} = 2\pi\rho_s\epsilon_{sf}\sigma_{sf}^2 \left[ \frac{2}{5} \left( \frac{\sigma_{sf}}{z} \right)^{10} - \left( \frac{\sigma_{sf}}{z} \right)^4 - \frac{\sigma_{sf}^4}{3\Delta \cdot 0.61\Delta + z^3} \right] \quad (2.29)$$

where surface density,  $\rho_s = 38.2 \text{ nm}^{-2}$ ,  $\epsilon_{sf}$  and  $\sigma_{sf}$  are the cross-well depth and cross-collision diameter, they are calculated from LB mixing rules. The interspacing between

two graphene layers,  $\Delta = 0.3354$  nm. A collision diameter of carbon atom in graphite,  $\sigma_{ss} = 0.34$  nm with the well depth,  $\epsilon_{ss}/k_B = 28$  K.

## 2.6 Wetting

Typically, the wetting and non-wetting phenomena can be commonly seen in our daily life, e.g., water droplets on a leaf in your garden in the morning or water droplets on your waxed boots, where water does not wet the waxed layer of the boots. Another good example is when the drops of mercury can move freely on the glass surface. However, once the surface is changed to silver, the mercury can spread easily and cover almost the entire silver surface at the ambient temperature (Be'er *et al.*, 2007). So, the mercury and a silver surface can be considered as a wetting system. In general, wetting on a surface is the creation of liquid film on the substrate (similar to adsorption of a fluid on a substrate), by bringing in the vapour from the bulk phase to the adsorbed phase on the substrate. Once the substrate is full of the adsorbed film, the system then can turn from two-dimensional of thin liquid film to three-dimensional thick liquid film. On the other hand, non-wetting is where the adsorbate only forms clusters on the substrate, indicating that the interaction energy between the adsorbate and the adsorbate is stronger than the interaction energy between adsorbate and adsorbent. However, the non-wetting system can be changed to wetting by the external disturbance, e.g., temperature. The illustration of wetting and non-wetting on the substrate is shown in *Figure 2.7*.

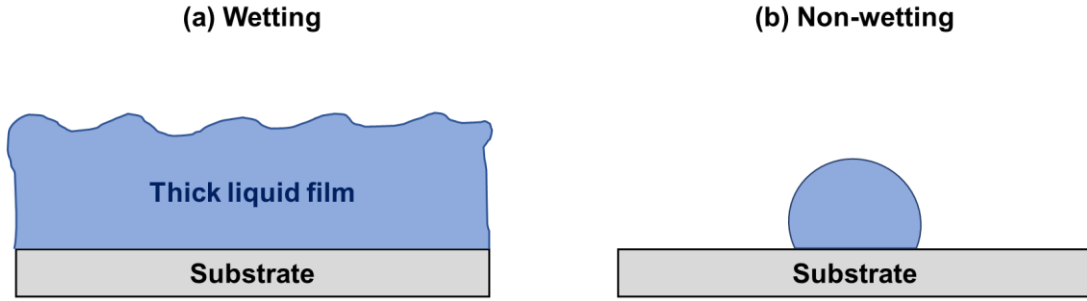


**Figure 2.7** Illustration of (a) wetting and (b) non-wetting system.

The wetting, incomplete wetting, and non-wetting behaviour of a fluid on a substrate have attracted research interests over the last few decades due to its importance in many applications, *e.g.*, biomaterials (Wu *et al.*, 2010), coating on nanomaterials, sensor (Reisch *et al.*, 2009), as well as microparticles production (Sung *et al.*, 2008). These interests resulting in the wetting behaviour has been studied experimentally and theoretically (Drir *et al.*, 1986; Meichel *et al.*, 1990; Nham & Hess, 1989; Patra *et al.*, 2015; Tan *et al.*, 2019; Xu *et al.*, 2019; Youn & Hess, 1990).

Generally, in the colloidal science, the wettability of a fluid on a substrate is determined by the contact angle between the fluid and the substrate (Saam, 2009), while in the adsorption science, the adsorption isotherms can be employed to indicate the wetting behaviour (Steele, 2008) of a concerning fluid on a planar substrate. In this simulation study, wetting is indicated by the interaction energy between the ratio of the depth of the minimum in the solid-fluid potential energy,  $|u_{SF}|_{\min}$  to the depth of the minimum in the fluid-fluid potential energy,  $|u_{FF}|_{\min}$ , symbolized by  $D^*$ . Hence,

$$D^* = \frac{|u_{SF}|_{\min}}{|u_{FF}|_{\min}} \quad (2.30)$$

where parameter  $D^*$  can be employed to indicate the wetting behaviour of the system. For a system with large value of  $D^*$ , *e.g.*, argon on a graphite substrate (L. Prasetyo *et al.*, 2018), we always see at least monolayer coverage of argon on a graphite substrate even the temperature is at 0 K. On the other hand, the systems with low  $D^*$ , *e.g.*, argon on a caesium substrate (Gatica & Cole, 2009), and methanol on a graphite substrate

(Prasetyo, Horikawa, *et al.*, 2019). These systems tend to show clusters of adsorbate molecules on the surface instead of layering at a low temperature. They require a high temperature to wet the substrate. The other parameter that can be employed to indicate the wetting behaviour of a fluid on a substrate at a very low adsorbed amount (Henry's law region) is the ratio between isosteric heat at zero loading,  $q_{st}^0$  to the heat of phase change in the bulk (condensation or sublimation),  $\lambda_{sub/cond}$  at the corresponding temperature (L. Prasetyo *et al.*, 2018). That is,

$$\Omega^0 = \frac{q_{st}^0}{\lambda_{sub/cond}} \quad (2.31)$$

from which if the  $\Omega^0$  is equal or more than one, the wetting can occur. For  $\Omega^0$  smaller than one, it is difficult to observe wetting in that system (it does not mean the system cannot wet). However, the energy from adsorbate-adsorbate ( $Q_{FF}$ ) interactions can make up the system, then wetting can occur. Take Equation (2.32) for considering the wetting behaviour.

To measure the wetting of an adsorbate on a substrate, Equation (2.31) is developed to account for the adsorbate-adsorbate interactions ( $Q_{FF}$ ), and the new equation can be simply written as:

$$\Omega = \frac{q_{st}^0 + Q_{FF}}{\lambda_{sub/cond}} \quad (2.32)$$

where  $Q_{FF}$  is the heat from the interactions between adsorbate-adsorbate molecules during the course of adsorption. This value can compensate the numerator in Equation (2.32), thus the ratio of  $\Omega$  is equal to or more than one.

The wetting behaviour of a fluid on a substrate can also be determined using adsorption isotherms, where the plots between surface density,  $\Gamma$ , versus relative pressure,  $P/P_0$ , are shown in *Figure 2.8*.

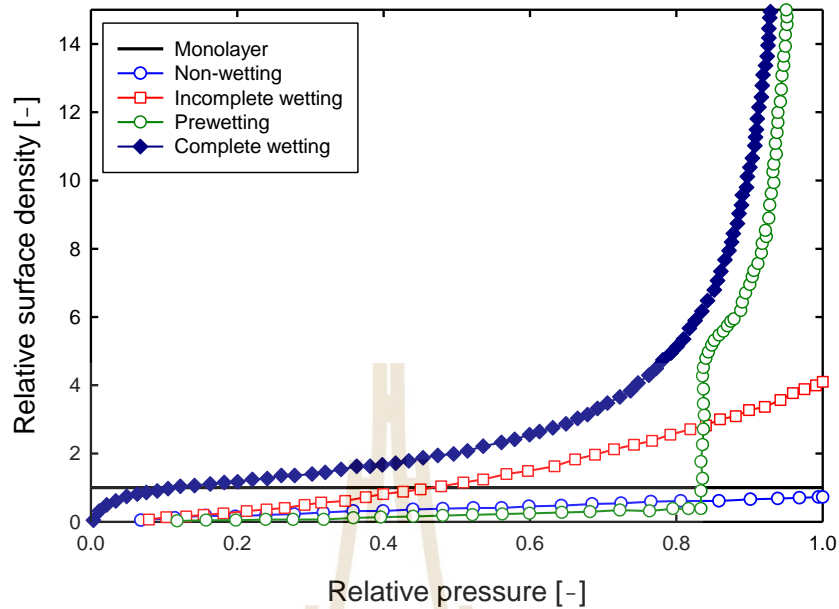


**Figure 2.8** Several types of adsorption isotherms of simple gas on the homogeneous surface. To distinguish the wetting behaviour at different temperatures (Steele, 2008).

Figure 2.8 shows the following:

- Black solid line indicates the monolayer coverage density on the substrate.
- Next, the isotherm with blue circles indicates the system with non-wetting or drying. The density of fluid on the substrate is less than the monolayer capacity. This system shows that the fluid molecules are more favorable to form mobile clusters on the substrate without layering, but once the temperature is high enough, the clusters can coalesce and form a monolayer.
- Incomplete wetting or partial wetting (red squares), the adsorbed molecules form finite layers (or finite adsorbed density) on the substrate at the bulk coexistence pressure,  $P_0$ .
- Complete wetting (or sometimes called wetting) is shown as dark blue diamonds, usually complete wetting occurs when the adsorbed amount

can complete monolayer coverage, then the number of layers tend to infinite as the pressure approaches  $P_0$ . This is the BET multilayers adsorption isotherm.

- Prewetting (green circles) is the thin-to-thick film of the adsorbate on the substrate, then we see a vertical jump and the adsorbed density goes to infinity as the pressure approaches  $P_0$ . This system happens when the  $D^*$  value is very small, and more details on prewetting using a computer simulation study was explained by Prasetyo *et al.* (Luisa Prasetyo *et al.*, 2018).

Additional parameters used to identify the wetting behaviour of a fluid on a substrate are:

- Roughening temperature,  $T_R$ . This temperature indicates that when the system is at this temperature and higher, the adsorbate on the top that exposes to the bulk gas is undulated enough and the complete wetting occurs. This temperature also demarcates between the incomplete wetting region and the complete wetting region in the wetting map.
- Layering temperature,  $T_{L,n}$ . At this temperature where the first-order transition in isotherm can be seen at the bulk coexistence pressure,  $P_0$ . For example,  $T_{L,1}$  means the isotherm show first-order transition of the monolayer density at  $P_0$ . Usually,  $T_{L,n}$  falls in the incomplete wetting region, lower than the roughening temperature,  $T_R$  (see *Figure 2.9* for the illustration).
- Wetting temperature,  $T_w$ . At this temperature, the complete wetting occurs at  $P_0$ , and wetting is continuous.
- Bulk coexistence pressure,  $P_0$ . This is the saturation vapour pressure at temperature above bulk triple point temperature ( $T_{tr}$ ) and below the critical temperature ( $T_c$ ) of the adsorbate and is obtained from the vapour-liquid equilibria (VLE). If the temperature is below  $T_{tr}$  then  $P_0$

is called sublimation vapour pressure, which is obtained from the vapour-solid equilibria (VSE).

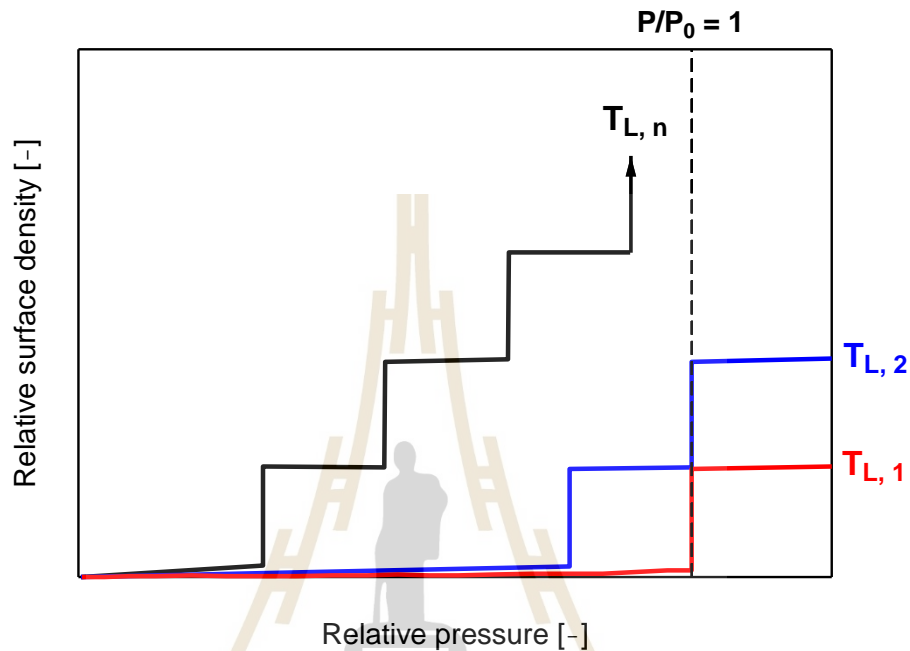


**Figure 2.9** Illustration of isotherms that fall into the incomplete wetting region, usually at a temperature below  $T_R$ . The red line shows  $T_{L,1}$  which is the wetting of the first layer at  $P_0$ , while the blue line shows wetting of the second layer,  $T_{L,2}$ . The dash line represents where the relative pressure is at unity (Loi, 2021).

### 2.6.1 Saturation Vapour Pressure

To address the problem of wetting, one important parameter is saturation vapour pressure, or in this study called bulk coexistence pressure ( $P_0$ ), as mentioned in section 2.4.3.6.  $P_0$  is used in the plot of isotherm in terms of surface density versus relative pressure, so it is essential to determine the appropriate value of  $P_0$ . In this study, the kinetic Monte Carlo (kMC) in the canonical ensemble (NVT) (Nguyen *et al.*, 2016) was employed to determine the bulk coexistence pressure from the vapour-liquid equilibria (VLE) using adsorbate potential models previously mentioned in section 2.4.3.4.

The simulation box used to determine VLE for each adsorbate is set up as in *Figure 2.10*. The x- and y-direction were 20 times, while the z-direction was 60 times that of the collision diameter of the first LJ site of the concerning fluid. The box size was large enough to ensure that the output thermodynamic properties are reliable. Initially, the liquid slab of the adsorbate was placed at the centre of the box, and each molecule was given a random orientation. The simulation was carried out for  $5.0 \times 10^8$  configurations in the equilibration and the sampling stages. All molecules in the box were shifted to the middle of the box for every 100 configurations in the z-direction to maintain the centre of mass of the system and the coordinates of molecules were translated correspondingly. Periodic boundary conditions (PBC) were applied in all directions.

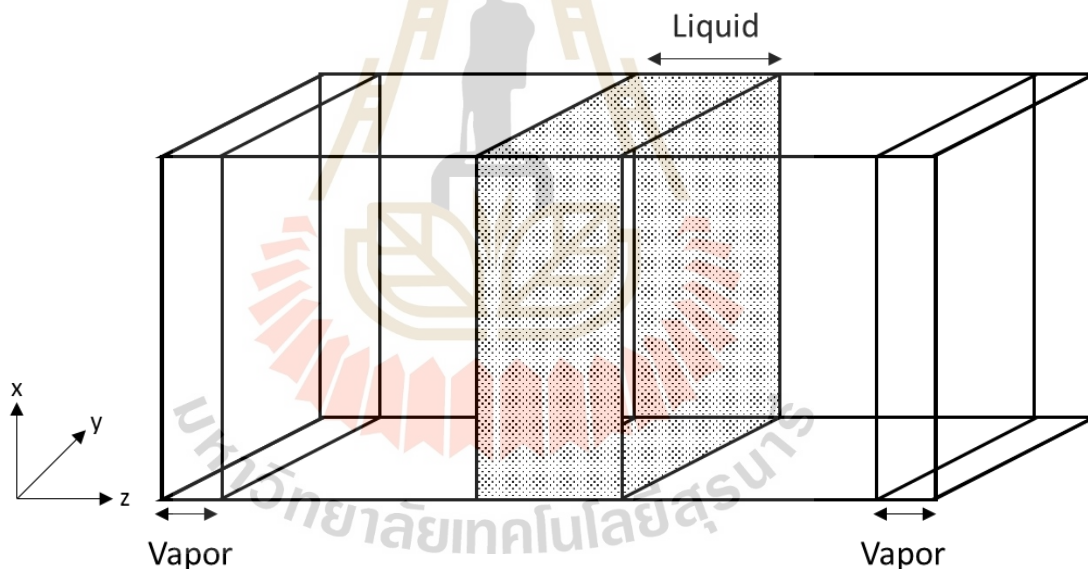


**Figure 2.10** Illustration of the simulation box used in the determination of thermodynamic properties of the adsorbates.

### 2.6.2 The Output Thermodynamic Properties

*Surface Excess* – The adsorption isotherm is expressed as excess density on the surface as a function of pressure, it is defined as:

$$\Gamma_{excess} = \frac{N_{excess}}{L_x L_y} = \frac{\langle N \rangle - V_{acc} \rho_{gas}}{L_x L_y} \quad (2.33)$$

where  $\langle N \rangle$  is the ensemble average of the number of molecules in the simulation box,  $\rho_{gas}$  is the bulk gas density,  $V_{acc}$  is the accessible volume of the simulation box (defined as the volume that is accessible to the centre of a molecule whose adsorbate-adsorbent (SF) potential energy is non-positive) (Herrera *et al.*, 2010).  $L_x$  and  $L_y$  are the length of the simulation box in the x- and y-direction, respectively.

*Isosteric Heat* – In the GC ensemble, the isosteric heat of adsorption is calculated using fluctuation theory (Nicholson & Parsonage, 1982), and is written as:

$$q_{st} = k_B T - \frac{\langle UN \rangle - \langle U \rangle \langle N \rangle}{\langle N^2 \rangle - \langle N \rangle \langle N \rangle} \quad (2.34)$$

where  $N$  is the number of molecules in the simulation box,  $U$  is the summation of the potential energies of interaction between adsorbate-adsorbate molecules ( $U_{FF}$ ) and between adsorbate-adsorbent ( $U_{SF}$ ).  $k_B$  is the Boltzmann constant and  $T$  is the temperature of the system,  $\langle \ \rangle$  which represents the ensemble average.

*Local Density Distribution (LDD)* – The variation of the local density with the distance of the centre of mass (COM) of the molecule from the surface is calculated with the local density distribution:

$$\rho_z = \frac{\langle \Delta N_{z,z+\Delta z} \rangle}{L_x L_y \Delta z} \quad (2.35)$$

where  $\langle \Delta N_{z,z+\Delta z} \rangle$  is the ensemble average of the number of molecules whose COM is located in the region bound between  $z$  and  $z + \Delta z$ .  $\Delta z$  is the width of the bin in the z-direction.

## 2.7 References

- Ahmadpour, A., & Do, D. D. (1997). The preparation of activated carbon from macadamia nutshell by chemical activation. **Carbon**. 35(12): 1723-1732.
- Alder, B. J., & Wainwright, T. E. (1959). Studies in Molecular Dynamics. I. General Method. **The Journal of Chemical Physics**. 31(2): 459-466.
- Allen, M. P., & Tildesley, D. J. (2017). **Computer Simulation of Liquids** (2nd ed.). Oxford: Oxford University Press.
- Bagreev, A., Angel Menendez, J., Dukhno, I., Tarasenko, Y., & Bandosz, T. J. (2004). Bituminous coal-based activated carbons modified with nitrogen as adsorbents of hydrogen sulfide. **Carbon**. 42(3): 469-476.
- Bagreev, A., & Bandosz, T. J. (2002). A Role of Sodium Hydroxide in the Process of Hydrogen Sulfide Adsorption/Oxidation on Caustic-Impregnated Activated Carbons. **Industrial & Engineering Chemistry Research**. 41(4): 672-679.
- Bansal, R. C., Donnet, J. B., & Stoeckli, F. (1988). **Active Carbon**. New York City, New York: Marcel Dekker.
- Bansal, R. C., & Goyal, M. (2005). **Activated Carbon Adsorption**. Florida: CRC Press.
- Basu, P. (2013). **Biomass Gasification, Pyrolysis and Torrefaction: Practical Design and Theory** (2nd ed.). San Diego: Academic Press.
- Be'er, A., Lereah, Y., Frydman, A., & Taitelbaum, H. (2007). Spreading of mercury droplets on thin silver films at room temperature. **Physical Review E**. 75(5): 051601.
- Berthelot, D. (1898). Sur le mélange des gaz. **Comptes rendus de l'Académie des sciences**. 126: 1703-1885.
- Boehm, H. P. (1966a). Chemical Identification of Surface Groups. In D. D. Eley, H. Pines, & P. B. Weisz (Eds.), *Advances in Catalysis* (Vol. 16, pp. 179-274): Academic Press.
- Boehm, H. P. (1966b). Functional Groups on the Surfaces of Solids. **Angewandte Chemie International Edition in English**. 5(6): 533-544.
- Boehm, H. P. (1994). Some aspects of the surface chemistry of carbon blacks and other carbons. **Carbon**. 32(5): 759-769.

- Brender, P., Gadiou, R., Rietsch, J.-C., Fioux, P., Dentzer, J., Ponche, A., & Vix-Guterl, C. (2012). Characterization of Carbon Surface Chemistry by Combined Temperature Programmed Desorption with in Situ X-ray Photoelectron Spectrometry and Temperature Programmed Desorption with Mass Spectrometry Analysis. **Analytical Chemistry**. 84(5): 2147-2153.
- Brunauer, S., Emmett, P. H., & Teller, E. (1938). Adsorption of Gases in Multimolecular Layers. **Journal of the American Chemical Society**. 60(2): 309-319.
- Buckingham, A. D., Disch, R. L., & Dunmur, D. A. (1968). Quadrupole moments of some simple molecules. **Journal of the American Chemical Society**. 90(12): 3104-3107.
- Caldwell, S. J., Al-Duri, B., Sun, N., Sun, C.-g., Snape, C. E., Li, K., & Wood, J. (2015). Carbon Dioxide Separation from Nitrogen/Hydrogen Mixtures over Activated Carbon Beads: Adsorption Isotherms and Breakthrough Studies. **Energy & Fuels**. 29(6): 3796-3807.
- Chen, B., J. Potoff, J., & Siepmann, J. I. (2001). Monte Carlo Calculations for Alcohols and Their Mixtures with Alkanes. Transferable Potentials for Phase Equilibria. 5. United-Atom Description of Primary, Secondary, and Tertiary Alcohols. **The Journal of Physical Chemistry B**. 105: 3093-3104.
- Chen, W., Cannon, F. S., & Rangel-Mendez, J. R. (2005). Ammonia-tailoring of GAC to enhance perchlorate removal. II: Perchlorate adsorption. **Carbon**. 43(3): 581-590.
- Chinn, D., & King, C. J. (1999). Adsorption of Glycols, Sugars, and Related Multiple -OH Compounds onto Activated Carbons. 2. Solvent Regeneration. **Industrial & Engineering Chemistry Research**. 38(10): 3746-3753.
- Deitz, V. R., & Bitner, J. L. (1973). Interaction of ozone with adsorbent charcoals. **Carbon**. 11(4): 393-401.
- Diebold, J. P., & Bridgwater, A. V. (1997). Overview of Fast Pyrolysis of Biomass for the production of Liquid Fuels. In *Developments in Thermochemical Biomass Conversion*: Blackie A&P.
- Do, D. D. (1998). **Adsorption Analysis: Equilibria and Kinetics**. London: Imperial College Press.

- Drir, M., Nham, H. S., & Hess, G. B. (1986). Multilayer adsorption and wetting: Ethylene on graphite. **Physical Review B**. 33(7): 5145-5148.
- Dubinin, M. M. (1967). Adsorption in micropores. **Journal of Colloid and Interface Science**. 23(4): 487-499.
- Dubinin, M. M. (1975). Physical Adsorption of Gases and Vapors in Micropores. In D. A. Cadenhead, J. F. Danielli, & M. D. Rosenberg (Eds.), *Progress in Surface and Membrane Science* (Vol. 9, pp. 1-70): Elsevier.
- El-Hendawy, A.-N. A., Samra, S. E., & Girgis, B. S. (2001). Adsorption characteristics of activated carbons obtained from corncobs. **Colloids and Surfaces A: Physicochemical and Engineering Aspects**. 180(3): 209-221.
- Fanning, P. E., & Vannice, M. A. (1993). A DRIFTS study of the formation of surface groups on carbon by oxidation. **Carbon**. 31(5): 721-730.
- Ferraz, M. C. A. (1988). Preparation of activated carbon for air pollution control. **Fuel**. 67(9): 1237-1241.
- FILTNEWS. (2016). **Demand for activated carbon to approach 2 million metric tons [Online]**. <http://www.filtnews.com/demand-activated-carbon-approach-2-million-metric-tons/>: Available.
- Fontana, A. F. (1777). **Memorie Mat. Fis. Soc. Ital. Sci.** 1: 679.
- Frenkel, D., & Smit, B. (2002). **Understanding Molecular Simulation: From Algorithms to Applications**. London: Academic Press.
- Freundlich, H. (1907). Über die Adsorption in Lösungen. **Zeitschrift für Physikalische Chemie**. 57U(1): 385-470.
- Freundlich, H. (1932). Of the adsorption of gases. Section II. Kinetics and energetics of gas adsorption. Introductory paper to section II. **Transactions of the Faraday Society**. 28(0): 195-201.
- Fritz, O. W., & Hüttinger, K. J. (1993). Active sites and intrinsic rates of carbon-gas reactions—a definite confirmation with the carbon-carbon dioxide reaction. **Carbon**. 31(6): 923-930.
- Garten, V. A., & Weiss, D. E. (1957). A new interpretation of the Acidic and Basic structures in Carbons. II. The Chromene-carbonium ion couple in Carbon. **Australian Journal of Chemistry**. 10(3): 309-328.

- Gatica, S. M., & Cole, M. W. (2009). To Wet or Not to Wet: That Is the Question. **Journal of Low Temperature Physics**. 157(3): 111.
- Guo, J., & Lua, A. C. (2000). Preparation of activated carbons from oil-palm-stone chars by microwave-induced carbon dioxide activation. **Carbon**. 38(14): 1985-1993.
- Heo, Y.-J., & Park, S.-J. (2018). H<sub>2</sub>O<sub>2</sub>/steam activation as an eco-friendly and efficient top-down approach to enhancing porosity on carbonaceous materials: the effect of inevitable oxygen functionalities on CO<sub>2</sub> capture. **Green Chemistry**. 20(22): 5224-5234.
- Herrera, L., Do, D. D., & Nicholson, D. (2010). A Monte Carlo integration method to determine accessible volume, accessible surface area and its fractal dimension. **Journal of Colloid and Interface Science**. 348(2): 529-536.
- Horikawa, T., Kitakaze, Y., Sekida, T., Hayashi, J. i., & Katoh, M. (2010). Characteristics and humidity control capacity of activated carbon from bamboo. **Bioresource Technology**. 101(11): 3964-3969.
- Johnson, J. K., Zollweg, J. A., & Gubbins, K. E. (1993). The Lennard-Jones equation of state revisited. **Molecular Physics**. 78(3): 591-618.
- Junpirom, S. (2006). **Activated Carbon from Longan Seed: Its Activation Model and Adsorption of Water Vapor and Benzene**. Doctor of Philosophy. Ph.D. Dissertation. Suranaree University of Technology, Nakhon Ratchasima, Thailand.
- Klass, D. L. (1998). **Biomass for renewable energy, fuels, and chemicals**. San Diego: Academic Press.
- Lahaye, J. (1998). The chemistry of carbon surfaces. **Fuel**. 77(6): 543-547.
- Langmuir, I. (1918). THE ADSORPTION OF GASES ON PLANE SURFACES OF GLASS, MICA AND PLATINUM. **Journal of the American Chemical Society**. 40(9): 1361-1403.
- Lennard-Jones, J. E. (1931). Cohesion. **Proceedings of the Physical Society**. 43(5): 461-482.
- Lennard-Jones, J. E. (1932). Processes of adsorption and diffusion on solid surfaces. **Transactions of the Faraday Society**. 28(0): 333-359.
- Li, B. (2012). Characterization of Pore Structure and Surface Chemistry of Activated Carbons – A Review. In M. S. Salih (Ed.), *Fourier Transform - Materials Analysis*: IntechOpen.

- Li, B., Lei, Z., & Huang, Z. (2009). Surface-Treated Activated Carbon for Removal of Aromatic Compounds from Water. **Chemical Engineering & Technology**. 32(5): 763-770.
- Linares-Solano, A., Martín-Gullón, I., Salinas-Martínez de Lecea, C., & Serrano-Talavera, B. (2000). Activated carbons from bituminous coal: effect of mineral matter content. **Fuel**. 79(6): 635-643.
- Liu, L., Zeng, Y., Tan, S. J., Xu, H., Do, D. D., Nicholson, D., & Liu, J. (2019). On the mechanism of water adsorption in carbon micropores – A molecular simulation study. **Chemical Engineering Journal**. 357: 358-366.
- Lo, S.-F., Wang, S.-Y., Tsai, M.-J., & Lin, L.-D. (2012). Adsorption capacity and removal efficiency of heavy metal ions by Moso and Ma bamboo activated carbons. **Chemical Engineering Research and Design**. 90(9): 1397-1406.
- Loi, Q. K. (2021). **Fundamental study of physical adsorption and wetting phenomena on homogeneous and heterogeneous solids**. Doctor of Philosophy. Ph.D. Dissertation The University of Queensland, Brisbane, Australia.
- Lorentz, H. A. (1881). Ueber die Anwendung des Satzes vom Virial in der kinetischen Theorie der Gase. **Annalen der Physik**. 248(1): 127-136.
- Lovits, T. E. (1955). **Izbrannye trudy po khimii i khimicheskoi tekhnologii (Selected Works on Chemistry and Chemical Technology)**. Moscow: Izd-vo Akademii nauk SSSR.
- Marchon, B., Carrazza, J., Heinemann, H., & Somorjai, G. A. (1988). TPD and XPS studies of O<sub>2</sub>, CO<sub>2</sub>, and H<sub>2</sub>O adsorption on clean polycrystalline graphite. **Carbon**. 26(4): 507-514.
- Marsh, H., Heintz, E. A., & Rodriguez-Reinoso, F. (1997). **Introduction to Carbon Technologies**. Alicante: Universidad de Alicante.
- Marsh, H., & Rodriguez-Reinoso, F. (2006). **Activated Carbon**. London: Elsevier.
- Meichel, T., Dawson, P. T., Morrison, J. A., Sullivan, D. E., & Koga, Y. (1990). Adsorption of ethylene on graphite near saturation: wetting transition/capillary condensation. **Langmuir**. 6(10): 1579-1584.

- Metropolis, N., Rosenbluth, A. W., Rosenbluth, M. N., Teller, A. H., & Teller, E. (1953). Equation of State Calculations by Fast Computing Machines. **J. Chem. Phys.** 21(6): 1087-1092.
- Michels, A., Wijker, H., & Wijker, H. (1949). Isotherms of argon between 0°C and 150°C and pressures up to 2900 atmospheres. **Physica.** 15(7): 627-633.
- Moreno-castilla, C., Carrasco-marín, F., Maldonado-hódar, F. J., & Rivera-utrilla, J. (1998). Effects of non-oxidant and oxidant acid treatments on the surface properties of an activated carbon with very low ash content. **Carbon.** 36(1): 145-151.
- Mountain, R. D., & Thirumalai, D. (1994). Quantative measure of efficiency of Monte Carlo simulations. **Physica A: Statistical Mechanics and its Applications.** 210(3): 453-460.
- Mudoga, H. L., Yucel, H., & Kincal, N. S. (2008). Decolorization of sugar syrups using commercial and sugar beet pulp based activated carbons. **Bioresour Technol.** 99(9): 3528-3533.
- Ngernyen, Y. (2007). **Wood-Based Activated Carbon: Preparation, Surface Modification, and Adsorption Study.** Doctor of Philosophy. Suranaree University of Technology, Nakhon Ratchasima.
- Nguyen, V. T., Tan, S. J., Do, D. D., & Nicholson, D. (2016). Application of kinetic Monte Carlo method to the vapour-liquid equilibria of associating fluids and their mixtures. **Molecular Simulation.** 42(8): 642-654.
- Nham, H. S., & Hess, G. B. (1989). Ellipsometric study of krypton, methane, and argon films on graphite: how complete is wetting? **Langmuir.** 5(3): 575-582.
- Nicholson, D., & Parsonage, G. (1982). **Computer simulation and the statistical mechanics of adsorption.** London: Academic Press.
- Otake, Y., & Jenkins, R. G. (1993). Characterization of oxygen-containing surface complexes created on a microporous carbon by air and nitric acid treatment. **Carbon.** 31(1): 109-121.
- Otowa, T., Nojima, Y., & Miyazaki, T. (1997). Development of KOH activated high surface area carbon and its application to drinking water purification. **Carbon.** 35(9): 1315-1319.

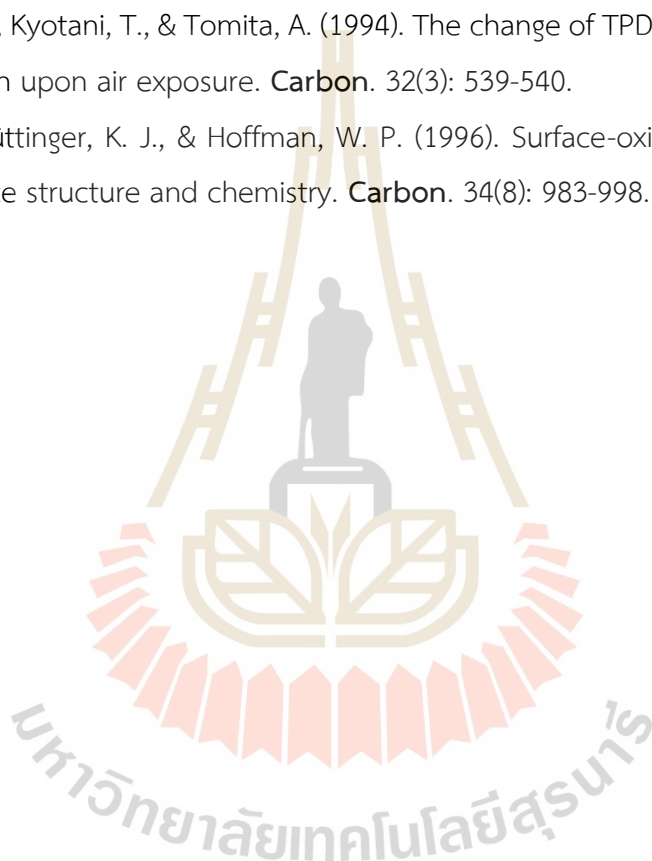
- Pan, Z., & Yang, R. T. (1992). Strongly bonded oxygen in graphite: detection by high-temperature TPD and characterization. **Industrial & Engineering Chemistry Research**. 31(12): 2675-2680.
- Patra, T. K., Khan, S., Srivastava, R., & Singh, J. K. (2015). Understanding Wetting Transitions Using Molecular Simulation. In Y. M. Joshi & S. Khandekar (Eds.), *Nanoscale and Microscale Phenomena: Fundamentals and Applications* (pp. 139-166). New Delhi: Springer India.
- Pels, J. R., Kapteijn, F., Moulijn, J. A., Zhu, Q., & Thomas, K. M. (1995). Evolution of nitrogen functionalities in carbonaceous materials during pyrolysis. **Carbon**. 33(11): 1641-1653.
- Peng, X., Hu, F., Lam, F. L. Y., Wang, Y., Liu, Z., & Dai, H. (2015). Adsorption behavior and mechanisms of ciprofloxacin from aqueous solution by ordered mesoporous carbon and bamboo-based carbon. **Journal of Colloid and Interface Science**. 460(Supplement C): 349-360.
- Pérez-Cadenas, A., Maldonado-Hódar, F. J., & Moreno-Castilla, C. (2003). On the nature of surface acid sites of chlorinated activated carbons. **Carbon**. 41(3): 473-478.
- Polanyi, M. (1914). **Verhandl. Dtsch. Phys. Ges.** 16: 1012.
- Polanyi, M. (1932). Section III.—Theories of the adsorption of gases. A general survey and some additional remarks. Introductory paper to section III. **Transactions of the Faraday Society**. 28(0): 316-333.
- Polanyi, M. (1963). The Potential Theory of Adsorption. **Science**. 141(3585): 1010.
- Prasetyo, L. (2019). **Fundamental Study of Adsorption of Non-Polar and Polar Fluids on Hydrophobic Ordered Solids**. Doctor of Philosophy. Ph.D. Dissertation. The University of Queensland, Brisbane, Australia.
- Prasetyo, L., Horikawa, T., Takashima, N., Do, D. D., & Nicholson, D. (2019). On the transition from partial wetting to complete wetting of methanol on graphite. **Physical Chemistry Chemical Physics**. 21(47): 26219-26231.
- Prasetyo, L., Loi, Q. K., Tan, S. J., Do, D. D., & Nicholson, D. (2018). Effects of temperature on the transition from clustering to layering for argon adsorption on substrates of different strength - Parametric map of wetting, pre-wetting and non-wetting. **Microporous and Mesoporous Materials**.

- Prasetyo, L., Tan, S., Akram, A., Do, D. D., & Nicholson, D. (2018). Cluster growth and coalescence of argon on weakly adsorbing substrates: The origin of the thin-to-thick film transition. **Colloids and Surfaces A: Physicochemical and Engineering Aspects**. 554: 169-179.
- Prasetyo, L., Xu, H., Fan, C., Do, D. D., & Nicholson, D. (2019). On the coexistence pressure between the bulk and adsorbed argon on substrates of different strength – Temperature dependence of the characteristics of the adsorbate. **Chemical Engineering Journal**. 378: 122214.
- Ravikovitch, P. I., Vishnyakov, A., Russo, R., & Neimark, A. V. (2000). Unified approach to pore size characterization of microporous carbonaceous materials from N<sub>2</sub>, Ar, and CO<sub>2</sub> adsorption isotherms. **Langmuir**. 16(5): 2311-2320.
- Reisch, A., Voegel, J.-C., Gonthier, E., Decher, G., Senger, B., Schaaf, P., & Mésini, P. J. (2009). Polyelectrolyte Multilayers Capped with Polyelectrolytes Bearing Phosphorylcholine and Triethylene Glycol Groups: Parameters Influencing Antifouling Properties. **Langmuir**. 25(6): 3610-3617.
- Rodríguez-Reinoso, F. (2002). Production and Applications of Activated Carbons. In *Handbook of Porous Solids* (pp. 1766-1827).
- Rodríguez-Reinoso, F., & Molina-Sabio, M. (1998). Textural and chemical characterization of microporous carbons. **Advances in Colloid and Interface Science**. 76: 271-294.
- Rouquerol, J., Rouquerol, F., Llewellyn, P., Maurin, G., & Sing Kenneth, S. W. (2013). **Adsorption by Powders and Porous Solids** (2nd Ed.): Academic Press.
- Saam, W. F. (2009). Wetting, Capillary Condensation and More. **Journal of Low Temperature Physics**. 157(3): 77-100.
- Salame, II, & Bandosz, T. J. (2001). Surface Chemistry of Activated Carbons: Combining the Results of Temperature-Programmed Desorption, Boehm, and Potentiometric Titrations. **J Colloid Interface Sci**. 240(1): 252-258.
- Scheele, C. W. (1780). **Chemical Observation and Experiments on Air and Fire**: Complutense University of Madrid.

- Schnabel, T., Vrabec, J., & Hasse, H. (2005). Henry's law constants of methane, nitrogen, oxygen and carbon dioxide in ethanol from 273 to 498 K: Prediction from molecular simulation. **Fluid Phase Equilibria**. 233(2): 134-143.
- Seung Kim, Y., & Rae Park, C. (2016). Chapter 13 - Titration Method for the Identification of Surface Functional Groups. In M. Inagaki & F. Kang (Eds.), *Materials Science and Engineering of Carbon* (pp. 273-286): Butterworth-Heinemann.
- Shah, M. S., Siepmann, J. I., & Tsepatis, M. (2017). Transferable potentials for phase equilibria. Improved united-atom description of ethane and ethylene. **AIChE Journal**. 63(11): 5098-5110.
- Sing, K. S. W. (1985). Reporting physisorption data for gas/solid systems with special reference to the determination of surface area and porosity (Recommendations 1984). **Pure and Applied Chemistry**. 57(4): 603-619.
- Sircar, S., Golden, T. C., & Rao, M. B. (1996). Activated carbon for gas separation and storage. **Carbon**. 34(1): 1-12.
- Staggs, K. W., Qiang, Z., Madathil, K., Gregson, C., Xia, Y., Vogt, B., & Nielsen, D. R. (2017). High Efficiency and Facile Butanol Recovery with Magnetically Responsive Micro/Mesoporous Carbon Adsorbents. **ACS Sustainable Chemistry & Engineering**. 5(1): 885-894.
- Steele, W. A. (1973). The physical interaction of gases with crystalline solids: I. Gas-solid energies and properties of isolated adsorbed atoms. **Surface Science**. 36(1): 317-352.
- Steele, W. A. (2008). Chapter Eight - Wetting Phenomena. In E. J. Bottani & J. M.D. Tascón (Eds.), *Adsorption by Carbons* (pp. 167-185). Amsterdam: Elsevier.
- Sung, K. E., Vanapalli, S. A., Mukhija, D., McKay, H. A., Mirecki Millunchick, J., Burns, M. A., & Solomon, M. J. (2008). Programmable Fluidic Production of Microparticles with Configurable Anisotropy. **Journal of the American Chemical Society**. 130(4): 1335-1340.
- Tan, S. J., Prasetyo, L., Do, D. D., & Nicholson, D. (2019). Interplay between Wetting and Filling of Argon Adsorption in Slit Pores with Different Surface Energies Transition from Filling in Micropores to Capillary Condensation in Mesopores. **Industrial & Engineering Chemistry Research**. 58(51): 23294-23303.

- Tangsathitkulchai, C., Ngernyen, Y., & Tangsathitkulchai, M. (2009). Surface modification and adsorption of eucalyptus wood-based activated carbons: Effects of oxidation treatment, carbon porous structure and activation method. **Korean Journal of Chemical Engineering**. 26(5): 1341-1352.
- Tarkovskaya, I. A. (1990). **Sto professii aktivnogo uglya (A Hundred of Jobs of Activated Carbons)**. Kiev: Naukova Dumka.
- Thommes, M., & Cychoz, K. A. (2014). Physical adsorption characterization of nanoporous materials: progress and challenges. **Adsorption**. 20(2): 233-250.
- Thommes, M., Kaneko, K., Neimark Alexander, V., Olivier James, P., Rodriguez-Reinoso, F., Rouquerol, J., & Sing Kenneth, S. W. (2015). Physisorption of gases, with special reference to the evaluation of surface area and pore size distribution (IUPAC Technical Report). In *Pure and Applied Chemistry* (Vol. 87, pp. 1051).
- Tipler, P. A. (1999). **Physics for Scientists and Engineers** (4th ed.). New York: W.H. Freeman & Company.
- UNFCCC. (2005). Clarification on Definition of Biomass and Consideration of Changes in Carbon Pools due to a CDM Project Activity. **EB-20**. Annex 8.
- Wenzhong, S., Zhijie, L., & Yihong, L. (2008). Surface Chemical Functional Groups Modification of Porous Carbon. **Recent Patents on Chemical Engineering**. 1(1): 27-40.
- Wick, C. D., Martin, M. G., & Siepmann, J. I. (2000). Transferable Potentials for Phase Equilibria. 4. United-Atom Description of Linear and Branched Alkenes and Alkylbenzenes. **The Journal of Physical Chemistry B**. 104(33): 8008-8016.
- Wu, C., Chen, M., & Xing, C. (2010). Molecular Understanding of Conformational Dynamics of a Fibronectin Module on Rutile (110) Surface. **Langmuir**. 26(20): 15972-15981.
- Xu, H., Zeng, Y., Do, D. D., & Nicholson, D. (2019). On the Nonwetting/Wetting Behavior of Carbon Dioxide on Graphite. **The Journal of Physical Chemistry C**. 123(14): 9112-9120.
- Youn, H. S., & Hess, G. B. (1990). Wetting and melting behavior of oxygen films on graphite. **Physical Review Letters**. 64(4): 443-446.

- Zawadzki, J. (1981). IR spectroscopy investigations of acidic character of carbonaceous films oxidized with HNO<sub>3</sub> solution. **Carbon**. 19(1): 19-25.
- Zhang, Y.-J., Xing, Z.-J., Duan, Z.-K., Meng, L., & Wang, Y. (2014). Effects of steam activation on the pore structure and surface chemistry of activated carbon derived from bamboo waste. **Applied Surface Science**. 315(Supplement C): 279-286.
- Zhuang, Q. L., Kyotani, T., & Tomita, A. (1994). The change of TPD pattern of O<sub>2</sub>-gasified carbon upon air exposure. **Carbon**. 32(3): 539-540.
- Zielke, U., Hüttinger, K. J., & Hoffman, W. P. (1996). Surface-oxidized carbon fibers: I. Surface structure and chemistry. **Carbon**. 34(8): 983-998.



# CHAPTER III

## THE ANALYSIS OF PORE DEVELOPMENT AND SURFACE FUNCTIONAL GROUPS FORMATION DURING CO<sub>2</sub> ACTIVATION OF BAMBOO-BASED ACTIVATED CARBON

### Abstract

Pore development and the formation of oxygen functional groups were studied for activated carbon prepared from bamboo (*Bambusa bambos*) using a two-step activation with CO<sub>2</sub>, as functions of carbonization temperature and activation conditions (time and temperature). Results show that activated carbon produced from bamboo contains mostly micropores in the pore size range of 0.65 to 1.4 nm. All porous properties of activated carbons increased with the increase in the activation temperature over the range from 850 to 950°C, but decreased in the temperature range of 950 to 1000°C, due principally to the merging of neighboring pores. The increase in the activation time also increased porous properties linearly from 60 to 90 minutes, which then dropped from 90 to 120 minutes. It was found that the carbonization temperature played an important role in determining the number and distribution of active sites for CO<sub>2</sub> gasification during the activation process. Empirical equations were proposed to conveniently predict all important porous properties of the prepared activated carbons in terms of carbonization temperature, activation temperature, and activation time. Oxygen functional groups formed during the carbonization and activation steps of activated carbon synthesis and their contents were dependent on the preparation conditions employed. Using Boehm's titration technique, only phenolic and carboxylic groups were detected for the acid functional groups in both the chars and activated carbons in varying amounts. Empirical equations were also developed to estimate the total contents of the acid and basic groups in activated carbons in terms of the carbonization temperature, activation temperature, and activation time.

### 3.1 Introduction

Activated carbon is one of the most widely used solid adsorbents for separation and purification processes in both gas (González-García, 2018) and liquid (Deng *et al.*, 2015) systems. Activated carbon is an amorphous carbon-based material which exhibits a high degree of porosity, an extended surface area, microporous structure, high adsorption capacity and a high degree of surface reactivity (Bansal *et al.*, 1988). Typically, activated carbon can be synthesized from a variety of carbonaceous materials including cherry stone (Durán-Valle *et al.*, 2005), sugar cane bagasse (Erlich *et al.*, 2006), palm stone (Guo & Lua, 2000), agricultural waste (Blachnio *et al.*, 2020), hemp stem hemicellulose (Y. Wang *et al.*, 2015), and bamboo (Mi *et al.*, 2019; Y. X. Wang *et al.*, 2015) or coal (Jawad *et al.*, 2018), lignite (Toles *et al.*, 1996), and peat (Khadiran *et al.*, 2015). Sewage sludge, the residual material produced as a by-product from sewage treatment plants and which contains large amounts of organic matter, could be another potential source for activated carbon production, since the biochar produced from the sewage sludge showed a reasonably high carbon content and surface area of 47% and 152 m<sup>2</sup>/g, respectively (de Souza Souza *et al.*, 2021; Konczak *et al.*, 2019). The elementary structures of activated carbon are graphene layers and quasi-graphitic fragments that are composed together, which are referred to as microcrystalline structures. The microcrystalline structures randomly connect together forming a porous activated carbon. Consequently, the disorganized structure of activated carbon produces certain unique properties for the adsorbent, e.g., high surface area and porosity, a wide range of surface functional groups and a distribution of pore sizes (Pallarés *et al.*, 2018). These characteristics increase the flexibility of activated carbon in adsorbing a wide variety of adsorbate molecules.

The pore structure of activated carbon is distinguished by the volume distribution of various pore sizes (micropores, mesopores and macropores). This pore size distribution and pore connectivity have a direct influence on the diffusion rate of an adsorbate to the adsorption sites, while the adsorption capacity for an adsorbate is determined by the specific surface area and pore volume of activated carbon. In addition to the pore structure effect on the adsorption kinetics and equilibrium, the nature of surface chemistry also affects the selectivity or specificity for a given

adsorbate by activated carbon. Activated carbon contains heteroatoms, for example, oxygen, nitrogen, hydrogen, sulfur, etc. and these atoms can react with the oxidizing agent during the activation process, leading to the formation of various surface functionalities on the carbon surface.

Commercial activated carbon is often produced by a two-step physical activation method, consisting of a char preparation step by the carbonization of a precursor in an inert atmosphere at a mid-high temperature (400 to 600°C) (Bansal *et al.*, 1988) and followed by a char activation step at a relatively high temperature (800 to 1100°C) to increase the internal porosity by gasification with an oxidizing agent such as steam, CO<sub>2</sub>, H<sub>2</sub>O<sub>2</sub>, and O<sub>2</sub> (Bouchelta *et al.*, 2008; Heo & Park, 2018; Lawtae & Tangsathikulchai, 2021; Marsh & Rodriguez-Reinoso, 2006; Molina-Sabio *et al.*, 1996). Porous properties and surface chemistry of the resulting activated carbon depend on the type of raw materials, the carbonization conditions (time and temperature) and activation conditions (time and temperature) (Chang *et al.*, 2000; Katesa *et al.*, 2013; Shahkarami *et al.*, 2015). It is of prime importance to have detailed knowledge, both quantitatively and qualitatively, concerning the effect of the aforementioned preparation conditions on the pore development and the formation of surface functional groups, which in turn will benefit the selection of the most suitable activated carbon to meet a specific application.

It is therefore the purpose of this work to produce activated carbon from a bamboo precursor by the conventional two-step activation process using carbon dioxide as the activating agent and the variables studied were carbonization temperature, activation time and activation temperature. Porous properties of the prepared activated carbon samples were measured and correlated mathematically with the preparation variables. The mechanism of pore development as a function of the extent of gasification reaction was proposed to gain a better understanding of the influence of the activated carbon preparation conditions. The type and amount of oxygen functional groups during char activation were also determined and appropriate empirical equations were proposed to correlate the concentration of the surface functional groups with the conditions of activated carbon synthesis.

## 3.2 Materials and Methods

### 3.2.1 Raw Materials

Bamboo (*Bambusa Bambos*) was used as the starting raw material in this study. The as-received bamboo was chopped and cut into square pieces and sieved to obtain an average particle size of 2.03 mm (8 × 12 mesh). Next, the raw material was rinsed thoroughly with DI water to eliminate all dirt and contaminants, and then it was dried at 110°C for 24 h in an electric oven to remove excess moisture. The obtained sample was kept in a desiccator for further analysis and the preparation of char.

### 3.2.2 Char Preparation

A dried bamboo sample weighing about 30 g was loaded into an alumina ceramic boat and placed in a horizontal ceramic tube furnace (CTF 12/75/700, Carbolite, Staffordshire, UK) of diameter 75 mm with N<sub>2</sub> gas (99.995% of purity, Thai Special Gas, Rayong, Thailand) flowing through at the rate of 100 cm<sup>3</sup>/min. The carbonization was programmed by heating the furnace from the ambient temperature to 400°C at a heating rate of 10°C/min and then it was held at this temperature for 90 min. Then, the furnace was switched off and the product was cooled down inside the horizontal tube furnace to the ambient temperature under a constant flow of N<sub>2</sub>. Finally, the char produced was removed from the furnace and kept in a desiccator for further activation in CO<sub>2</sub>. The carbonization temperatures studied were 400, 500 and 600°C and the carbonization time was kept constant at 90 min for all runs. The weights of the dried bamboo and that of the derived char were recorded to determine the yield of the char product.

### 3.2.3 Carbon Dioxide Activation

The activation of carbonized char was carried out in the same tube furnace that was set in a vertical position. A quartz tube was inserted into the furnace to use as a reactor for char gasification. A total of 20 g of carbonized char were loaded into the quartz tube. The top and bottom of the furnace were insulated with ceramic fiber blankets to prevent heat losses to the surrounding area. The heating temperature was programmed to increase from the ambient temperature to the desired activation temperature at a heating rate of 10°C/min under the flow of N<sub>2</sub> at 100 cm<sup>3</sup>/min. When

the desired activation temperature was reached, N<sub>2</sub> was stopped and CO<sub>2</sub> (99.995% of purity, Thai Special Gas, Rayong, Thailand) was immediately admitted into the quartz tube reactor at a constant flow rate of 100 cm<sup>3</sup>/min. After the char was activated with CO<sub>2</sub> for the required period of time, the CO<sub>2</sub> valve was closed and N<sub>2</sub> was then allowed to flow into the quartz tube at the rate of 100 cm<sup>3</sup>/min. The furnace was then switched off and the product was cooled down in the furnace to the ambient temperature under a constant flow of N<sub>2</sub>. The obtained activated carbon product was kept in a desiccator for further characterization. The activation conditions studied were 850, 900, 950 and 1000°C and the holding times were 60, 90 and 120 min for each activation temperature. As an example, the prepared activated carbon was designated as C400-90 AC850-60 to denote that this activated carbon product was derived from the activation temperature of 850°C for 60 min and using the char prepared at 400°C for 90 min.

The degree of char burn-off or char conversion in weight% was computed from the following equation,

$$\text{Burn-off \%} = \frac{W_{char} - W_{ac}}{W_{char}} \times 100 \quad (3.1)$$

The yield of activated carbon product was calculated from the following equation:

$$\text{Activated Carbon Yield \%} = 100 - \text{Burn-off \%} \quad (3.2)$$

where  $w_{char}$  and  $w_{ac}$  are the weights of char before activation and the obtained activated carbon, respectively.

### 3.2.4 Characterization of Sample

#### 3.2.4.1 Bamboo Characterization

The prepared bamboo was analyzed by a thermogravimetric analyzer (TGA/DSC-1 Star System, Mettler-Toledo, Greifensee, Switzerland) for the proximate analysis using ASTM method (D7582-15, 2015) to determine moisture, volatile matter, fixed carbon, and ash content (Basu, 2013). The ultimate analysis was performed by a CHN analyzer (CHN 628, Leco Corporation, St. Joseph, Michigan, USA). The results obtained were weight percent of carbon, hydrogen, and nitrogen. The weight percent of oxygen was determined by mass balance, that is, %O = 100 - [%C+%H+%N].

### 3.2.4.2 Porous Properties of Products

The porous properties of the derived activated carbon were determined from the adsorption/desorption isotherm data of N<sub>2</sub> (99.9999% of purity, Linde Thailand, Rayong, Thailand) at -195.8°C, measured with a high-performance adsorption analyzer (ASAP 2010, Micromeritics, Norcross, Georgia, USA). The sample was first loaded into a sample tube and degassed at 300°C under a vacuum pressure of below 10 µmHg for 12 hrs. Then, the sample tube was transferred to the analysis port to perform the adsorption/desorption of N<sub>2</sub> at -195.8°C for a pressure range of up to 760 mmHg. The Brunauer-Emmett-Teller (BET) equation (Brunauer *et al.*, 1938) was applied to calculate the specific surface area ( $S_{BET}$ ) using the N<sub>2</sub> adsorption isotherm data for the relative pressures ( $P/P_0$ ) of 0.05 to 0.25 (Thommes *et al.*, 2015). The total pore volume ( $V_{tot}$ ) was determined from the volume of N<sub>2</sub> adsorbed at a relative pressure of 0.98 and converted to the volume of N<sub>2</sub> in a liquid state at -195.8°C, assuming that the adsorbed N<sub>2</sub> is in the liquid-like state at the temperature of adsorption. The micropore volume ( $V_{mic}$ ) for pore sizes smaller than 2.0 nm was determined from the Dubinin-Radushkevich (DR) equation (Dubinin, 1975), while the volume of mesopores ( $V_{mes}$ ) was derived from the difference between the total pore volume ( $V_{tot}$ ) and the micropore volume. The average pore diameter was also determined using the relation  $4V_{tot}/S_{BET}$ , where  $V_{tot}$  is the total pore volume and  $S_{BET}$  is the BET surface area. The pore size distribution (PSD) of the prepared activated carbon was computed based on the Monte Carlo (MC) simulation technique of which a brief theory is provided in section 3.2.4.5.

### 3.2.4.3 Surface Chemistry

Boehm titration (Boehm, 1994, 2002) is one of the most widely used methods to determine the quantity of oxygen functional groups on the surface of activated carbon. Based on this method, it is assumed that the acidic groups on the surface of activated carbon are neutralized with bases of varying strength: (1) carboxylic group in a NaHCO<sub>3</sub> solution, (2) carboxylic and lactonic groups in a Na<sub>2</sub>CO<sub>3</sub> solution and (3) a combination of carboxylic, lactonic and phenolic groups in a NaOH solution. To determine the basic group contents on the activated carbon surface, HCl solution was employed to neutralize the basic groups. The titration procedures were mentioned

elsewhere (Seung Kim & Rae Park, 2016). In brief, the following steps were employed: (1) About 4 g of activated carbon were crushed in a mortar and sieved with a 20-mesh screen (850  $\mu\text{m}$ ). The under-size particles ( $\sim 850 \mu\text{m}$ ) weighing about 1 g were collected and loaded into each of the four conical flasks (the exact weight of carbon in each conical flask was recorded). (2) Each of the first three conical flasks was mixed with 50  $\text{cm}^3$  of 0.1 M solutions of HCl, NaOH and  $\text{NaHCO}_3$ , respectively. The last conical flask was mixed with 50  $\text{cm}^3$  of 0.05 M solution of  $\text{Na}_2\text{CO}_3$ . (3) All flasks were sealed and shaken at 150 rpm for 24 hrs at the ambient temperature and after that the mixture was filtered. A total of 10  $\text{cm}^3$  of the respective filtered solutions of NaOH,  $\text{Na}_2\text{CO}_3$  and  $\text{NaHCO}_3$  were titrated with 0.1 M HCl solution, while the filtered solution of HCl was titrated with 0.1 M NaOH solution. (4) The volumes of titrants of the various bases and acids were used to calculate the number of various oxygen functional groups on the surface of the activated carbon.

#### 3.2.4.4 FTIR Spectra

Fourier Transform Infrared (FTIR) spectroscopy (Vertex 70 FT-IR, Bruker, Billerica, Massachusetts, USA) was employed to identify the functional groups present on the surface of the prepared char and activated carbon. The infrared spectra from a light source were ascertained over the wave number from 4000 to 400  $\text{cm}^{-1}$ . For each sample run, 64 scans were performed with a resolution value of 4  $\text{cm}^{-1}$ .

#### 3.2.4.5 Pore Size Distribution (PSD) using Computer Simulation

A brief description of the Monte Carlo simulation for determining the pore size distribution of activated carbon is presented in this section. In this work, Monte Carlo (MC) simulation (Metropolis *et al.*, 1953) in the grand canonical (GC) ensemble (Allen & Tildesley, 2017) was employed to obtain the kernel of reference adsorption isotherms. Pores were modelled as perfect slit pores with pore widths,  $H$ , ranging from 0.65 to 4.0 nm. The distance in the  $x$ - and  $y$ -directions was  $6.0 \times 6.0 \text{ nm}^2$ , while the pore width,  $H$ , was in the  $z$ -direction. Periodic boundary conditions (PBC) were applied in the  $x$ - and  $y$ -directions and the cut-off radius was chosen to be 5 times the collision diameter of the fluid. The pore wall was modelled using the homogeneous graphite surface proposed by Steele (Steele, 1978) with the following values of the pertinent parameters are listed in Chapter II.

Nitrogen was modelled as a single LJ molecule as proposed by Ravikovitch *et al.* (Ravikovitch *et al.*, 2000). The reduced well depth of the fluid was  $\varepsilon_{ff}/k_B = 101.5$  K, and a collision diameter was  $\sigma_{ff} = 0.3615$  nm.

A family of nitrogen adsorption isotherms at  $-195.8^\circ\text{C}$  were determined using computer simulation and  $10^5$  cycles were executed in the equilibration stage, and the same number in the sampling stage. In each cycle, there were 1,000 trial moves of local displacement, insertion, and deletion with equal probabilities. In the equilibration stage, the maximum displacement length was initially set as one half of the largest dimension of the simulation box and was adjusted at the end of each cycle to give an acceptance ratio of 20% (Mountain & Thirumalai, 1994). The chemical potential for a given temperature and pressure, used as input in the simulation, was calculated using the equation of state (EoS) of Johnson *et al.* (Johnson *et al.*, 1993). The adsorbed density was expressed as the absolute adsorbed density in slit pore per unit accessible volume (Herrera *et al.*, 2010) as a function of pressure.

The experimental  $\text{N}_2$  isotherms at  $-195.8^\circ\text{C}$  of activated carbon and the theoretical isotherms from the simulation are then paired and optimized using Solver in Microsoft Excel to minimize the sum square error between the experimental and simulated isotherms. The pore size distribution (PSD) of activated carbon can then be derived as the relationship between the differential pore volume per unit pore width and the average pore width.

### 3.3 Results and Discussion

#### 3.3.1 Precursor Characterization

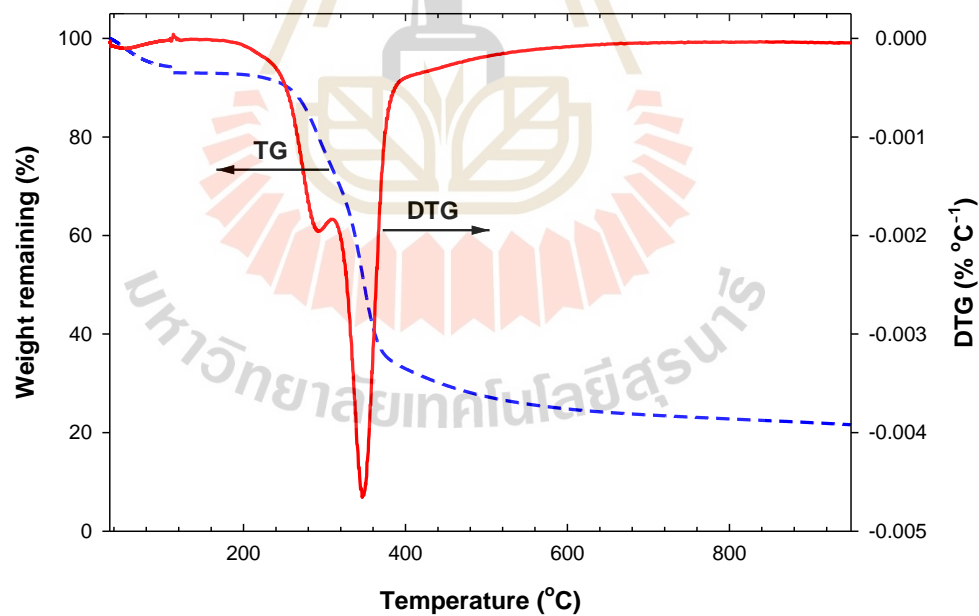
Table 3.1 shows the proximate and ultimate analyses of the precursor used in this work. The results indicate that bamboo wood has a high content of volatile matter (73.02%) and low composition of ash. The fixed carbon of bamboo is 19.91% which is comparable to other biomass materials, e.g., 18.27% for oil palm fiber (Lua & Guo, 1998), 19.08% for eucalyptus, 17.15% for wattle wood (Ngernyen *et al.*, 2006), 16.74% for palm kernel, 11.83% for cassava pulp (Weerachanchai *et al.*, 2011), 19.6% for longan seed (Junpirom *et al.*, 2010), and 26.6% for bamboo (Zhang *et al.*, 2014).

For the ultimate analysis, carbon and oxygen were the major elements since they are parts of the biomass structure which consists of cellulose, hemicellulose, and lignin.

The thermogravimetric analysis was employed to investigate the thermal decomposition behavior of bamboo in a nitrogen atmosphere and the results are shown in *Figure 3.1*, for the TG and DTG curves. The TG curve shows the weight remaining versus the heating temperature, while the DTG curve gives the first derivative of the TG curve or the decomposition rate. The first detected small peak of the DTG curve at the temperature below 110°C is attributed to the vaporization of residual moisture from the bamboo wood, which gives a weight loss of about 7%. Next, there are two observed peaks of the DTG curve that are related to the devolatilization process. The first peak occurs over the temperature range of 180 to 300°C and the second peak from 300 to 390°C. The maximum devolatilization rate of bamboo wood occurs at 345°C for the second peak whereas the first small peak occurs at 290°C. Lignin usually decomposes first at a low temperature around 150°C and continues to decompose up to the temperature of 900°C (Yang *et al.*, 2007). The first peak of the DTG curve from 180 to 300°C should represent the decomposition of hemicellulose, since the range of the decomposition temperature agrees with that of the decomposition of the commercial hemicellulose (Yang *et al.*, 2007). Finally, the thermal decomposition of cellulose has been reported to occur over a higher temperature range from 315 to 400°C (Yang *et al.*, 2007). Therefore, the appearance of the second DTG peak (300–390°C) should be attributed to the decomposition of the cellulose component.

**Table 3.1** Proximate and ultimate analyses of bamboo used in this work.

Analysis method	
Proximate analysis	wt%
Moisture	6.97
Volatile compounds	73.02
Fixed carbon	19.91
Ash	0.10
Ultimate analysis	
	wt%
C	45.33
H	6.13
N	0.40
O	48.14

**Figure 3.1** TG and DTG curves of bamboo biomass used in this work.

### 3.3.2 N<sub>2</sub> Isotherms of the Prepared Activated Carbons

Effects of carbonization temperature, activation temperature and activation time on the nitrogen isotherms at  $-195.8^{\circ}\text{C}$  (77.4 K) of the prepared bamboo activated carbons are typically shown in *Figure 3.2-3.4*, respectively. Obviously, the shape of the isotherm curves is dictated by the pore structure and pore size distribution of the adsorbent. The results indicate that two types of isotherm curves can be identified depending on the preparation conditions. They are Type I isotherm of the IUPAC classification (Thommes *et al.*, 2015) with a very small hysteresis loop and Type II isotherm (Thommes *et al.*, 2015) with a larger size of the hysteresis loop. Type I isotherm with a small hysteresis loop indicates the adsorption in micropores by a pore filling mechanism, followed by multilayer adsorption in small numbers of mesopores. This type of isotherm was found in activated carbon prepared at a relatively low activation temperature, as demonstrated in *Figure 3.3* for samples AC850-90 and AC850-120. Type II isotherm with a larger hysteresis loop indicates the adsorption in micropores and adsorption in mesopores of proportionally larger volume, thus changing the isotherm shape from a flat plateau region for Type I isotherm to an isotherm with a linear increase in the adsorbed amount with an increase in the relative pressures. This type of isotherm is typified by activated carbon prepared at activation temperatures higher than  $850^{\circ}\text{C}$ .

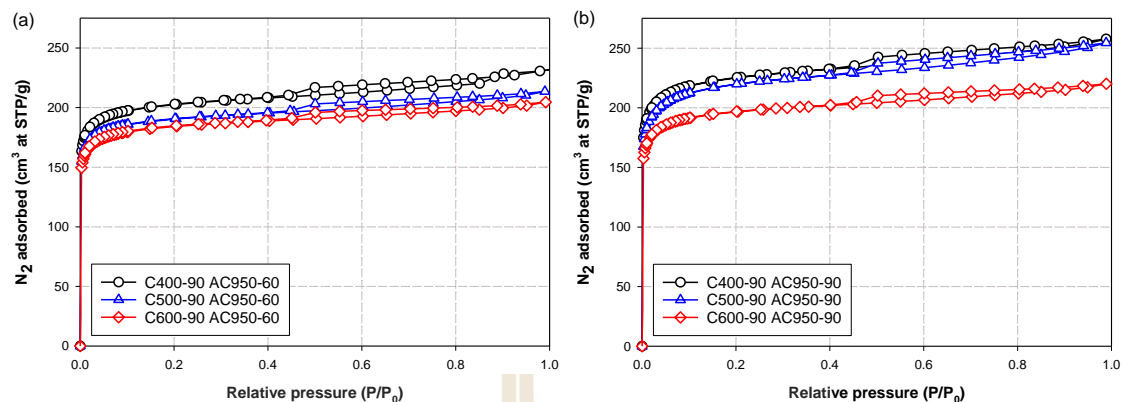


**Figure 3.2** Effects of carbonization temperature and activation time on N<sub>2</sub> adsorption isotherms of activated carbon prepared by CO<sub>2</sub> activation at (a) 950°C and 60 min (b) 950°C and 90 min.

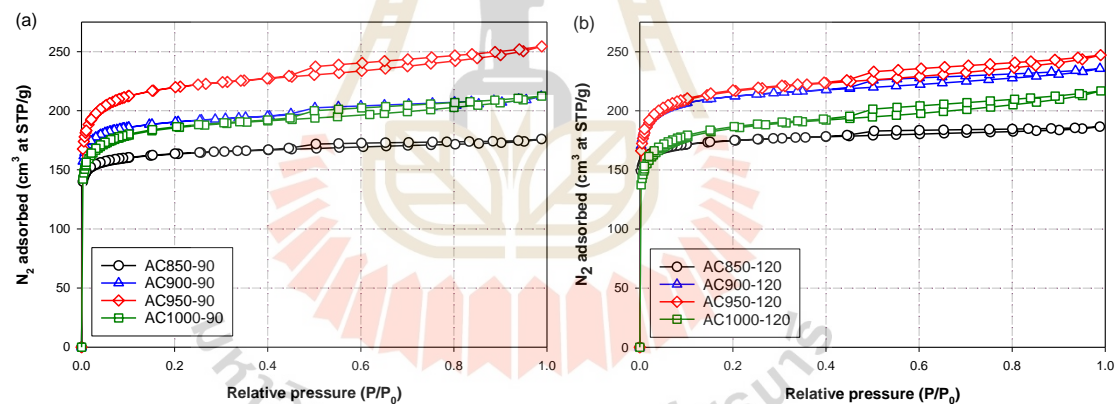


**Figure 3.3** Effects of activation temperature and activation time on N<sub>2</sub> adsorption isotherms of activated carbon prepared by CO<sub>2</sub> activation at (a) 850 to 1000°C and 90 min (b) 850 to 1000°C and 120 min. The activated carbons were derived from char carbonized at 500°C and 90 min.

It is further observed from the adsorption isotherms in *Figure 3.2* that the amount of N<sub>2</sub> adsorbed tended to decrease for activated carbon prepared at a higher carbonization temperature. This behavior should be attributed to the difference in the char reactivity which affects the rate of CO<sub>2</sub> gasification during the activation

step, thus producing differences in the porous properties of the derived activated carbon. A detailed discussion on this aspect is presented in the next section.

The effect of activation temperature on  $N_2$  isotherms of activated carbon is displayed in *Figure 3.3* at two activation times of 90 and 120 min, for activated carbon prepared from char carbonized at  $500^\circ\text{C}$  for 90 min. It was observed that increasing the activation temperature from  $850$  to  $950^\circ\text{C}$  increased the nitrogen isotherms which resulted from the increasing gasification rate that consumed more carbon atoms, thus providing an increase in the porous properties of the activated carbon. However, further increase in the activation temperature to  $1000^\circ\text{C}$  gave rise to a decrease in  $N_2$  adsorption. This can possibly be ascribed to the reduction in the surface area of the activated carbon caused by either the coalescence of a number of adjacent pores arising at a high degree of char burn-off or the enlargement of the existing small pores at such a high activation temperature (El-Hendawy *et al.*, 2001).

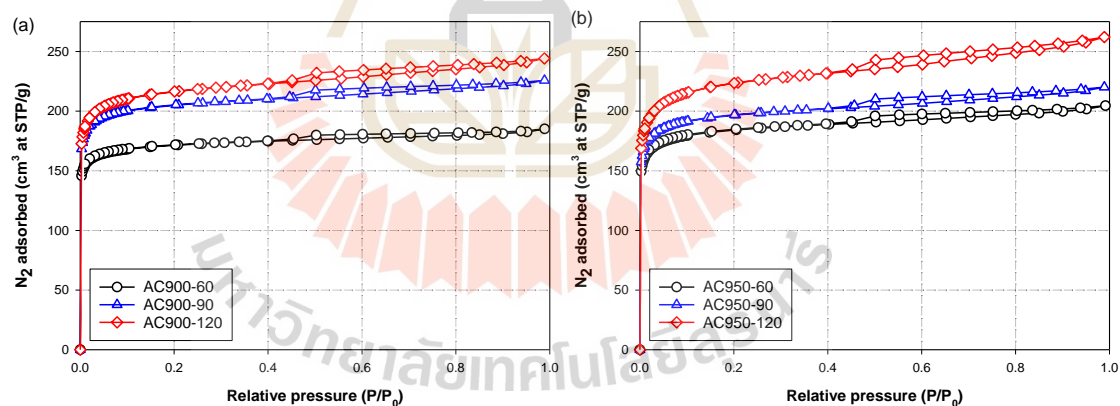


**Figure 3.4** Effects of activation time on  $N_2$  adsorption isotherms of activated carbon prepared by  $\text{CO}_2$  activation at (a)  $900^\circ\text{C}$  and (b)  $950^\circ\text{C}$  for 60, 90, and 120 min. The activated carbons were derived from char carbonized at  $600^\circ\text{C}$  and 90 min.

*Figure 3.4a* and *b* depict the effect of activation time on nitrogen isotherms for the activated carbon prepared from char carbonized at  $600^\circ\text{C}$  for 90 min at the activation temperature of  $900$  and  $950^\circ\text{C}$ , respectively. The amount of  $N_2$

adsorbed increased with the increase in activation time. Increasing activation time will allow more CO<sub>2</sub> molecules to diffuse to different reaction sites and/or increase the probability of molecular collision for a successful gasification reaction.

### 3.3.3 Porous Properties of the Prepared Activated Carbons

The effects of preparation conditions on the porous properties of the derived activated carbons are tabulated in *Table S1* (see Appendix A). To ease the discussion, the results of porous properties of the activated carbon produced are presented graphically, as shown in *Figure 3.5*, to show the effects of char burn-off and the carbonization temperature. The char burn-off is a parameter that incorporates the effects of activation time and temperature of the activation step. It was observed that the BET specific area, the micropore volume and the total pore volume appeared to increase with the increase in char burn-off and passed through a maximum at a critical char burn-off. The decrease in these porous properties is hypothesized to result from either the enlargement of the existing pores or the consolidation of neighboring pores, or possibly from both mechanisms. If these hypotheses are plausible, it indicates that the reactivity and the distribution of the reaction sites on the carbon surfaces for the gasification reaction could exert a considerable influence on the pore development of the resulting activated carbon. On the other hand, there was a tendency for the mesopore volume to increase continuously with the increase in char burn-off. However, the maximum percentage of mesopore volume for the maximum char burn-off of 65% is only 20% of the total pore volume, as shown in *Figure 3.6*. Results from *Table S1* (see Appendix A) also indicate that the maximum char burn-off is only about 65%, even the chars were activated at a very high activation temperature (1000°C) and with a long activation time (120 min). This is possibly attributable to the dense and tenacious cellulosic structure of the bamboo which causes the production of activated carbon from bamboo to contain mostly micropores.

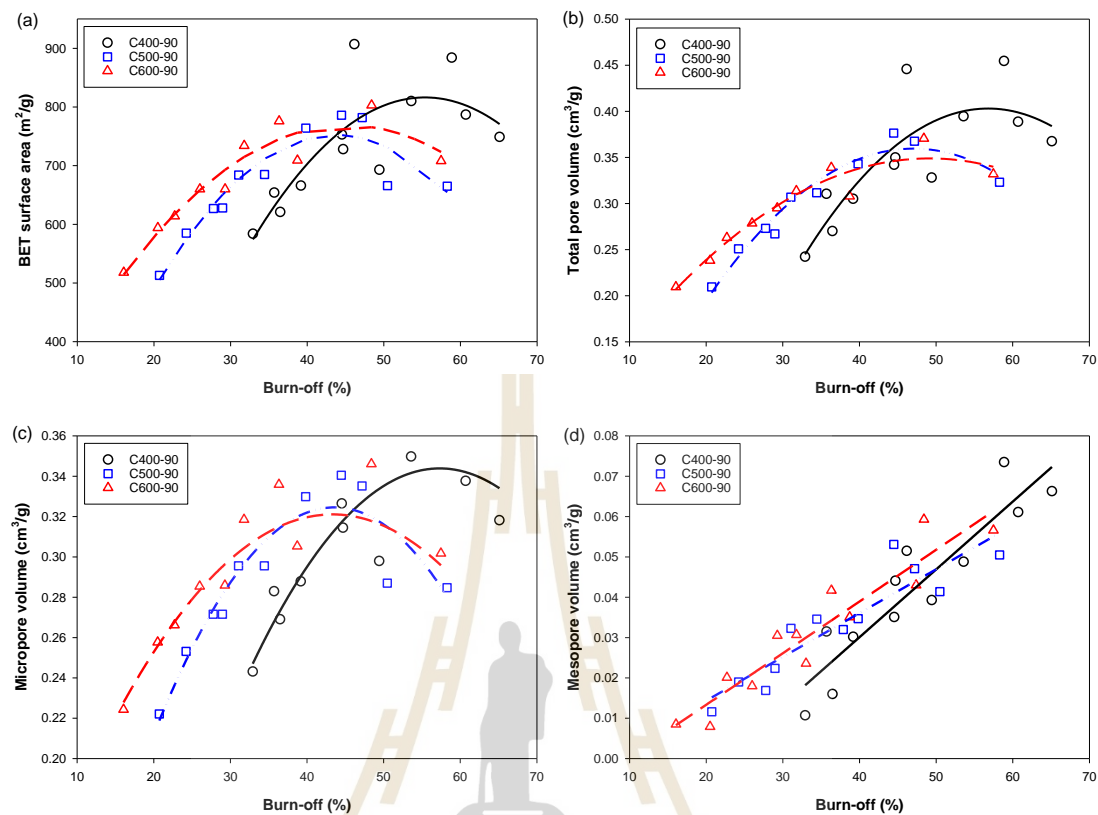
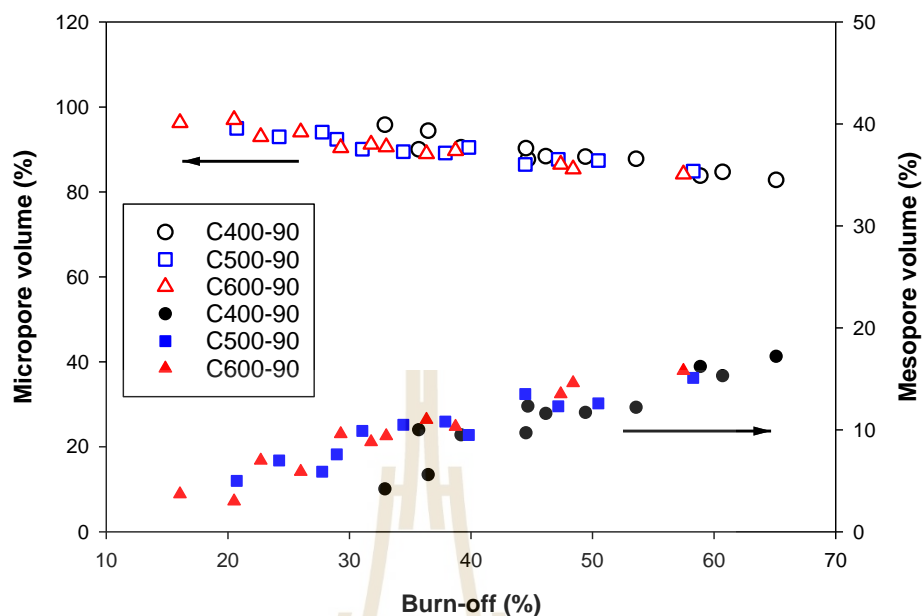


Figure 3.5 Effects of char burn-off on porous properties of the prepared activated carbons. (a) BET specific area, (b) total pore volume, (c) micropore volume, and (d) mesopore volume.



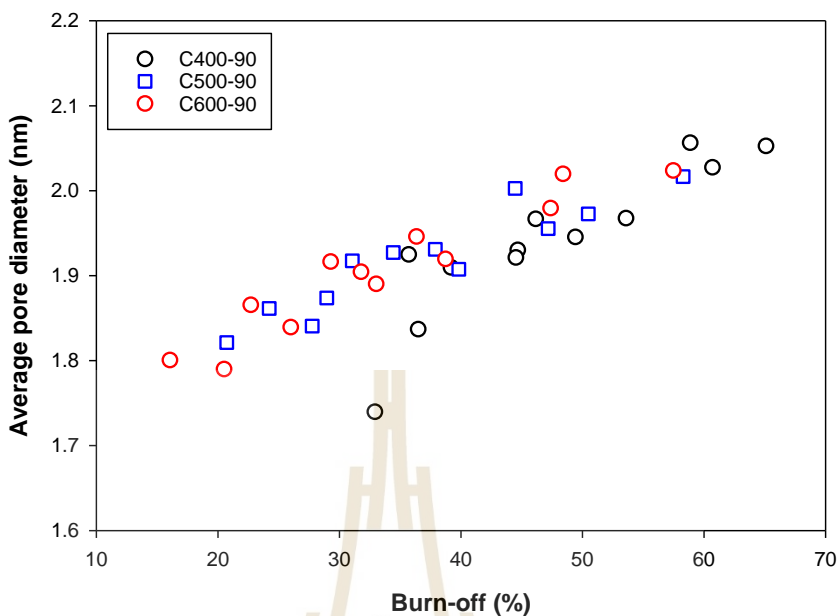
**Figure 3.6** Effects of char burn-off on the percentage of micropore volume and mesopore volume. The blank symbols represent the micropore volume while the solid symbols represent the mesopore volume.

It is interesting to note from *Table S1* (see Appendix A) that the maximum surface area of  $907 \text{ m}^2/\text{g}$  was obtained for bamboo-activated carbon under moderate preparation conditions for char carbonized at  $400^\circ\text{C}$  and 90 min and activation conditions of  $900^\circ\text{C}$  and 120 min with about 46.2% char burn-off for the two-step activation in  $\text{CO}_2$ . Apart from the conventional two-step physical activation (carbonization/activation), the one-step gasification in an oxidizing gas by heating a precursor from room temperature to the desired activation temperature can also be utilized for the production of activated carbon. As an example, Liu *et al.* (Liu *et al.*, 2018) synthesized activated char briquette from the pine sawdust briquette at the maximum gasification temperature of  $800^\circ\text{C}$  under 100%  $\text{CO}_2$  using the one-step heating that produced the activated biochar with reasonable BET specific area of around  $478 \text{ m}^2/\text{g}$ . However, the application of the two-step activation is more advantageous for the reason that it could effectively remove tarry materials during the first carbonization step, giving better quality char for the following activation step.

Next, *Figure 3.5* shows that for up to 50% of char burn-off, the porous properties of activated carbon increased with the increase in carbonization temperature. This is the result of char being carbonized at a higher temperature having a higher initial surface area (see *Table 3.2*). Therefore, for a given char burn-off, the new area formed by gasification for each char must be equal, thus making the char with a higher initial surface area (higher carbonization temperature) possess a higher total surface area after the activation process. *Figure 3.7* shows the effect of char burn-off on the average pore diameter ( $D_{avg}$ ) of activated carbon. The average pore diameter varied over a narrow range with the value increasing roughly in the range from 1.74 to 2.05 nm when the char burn-off increased from 16.9 to 65.1%, and the carbonization temperature appeared to have no significant effect on the average pore size.

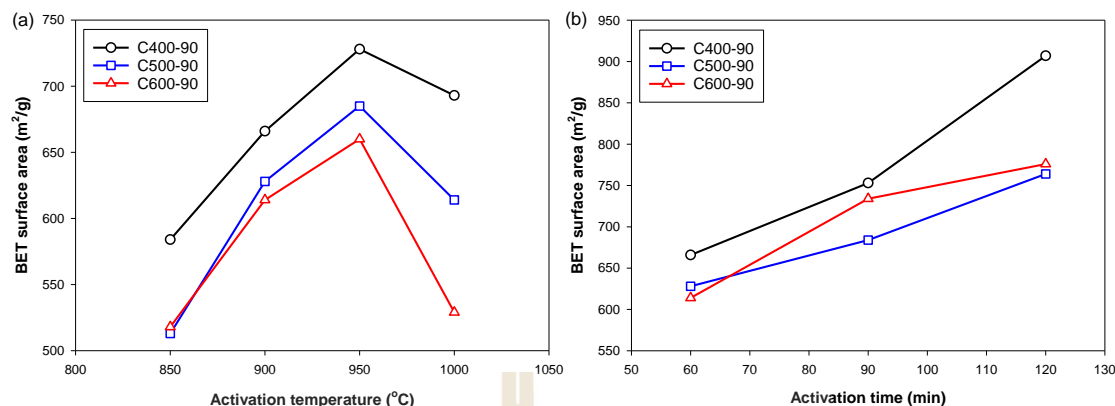
**Table 3.2** BET specific area of chars derived from CO<sub>2</sub> adsorption at 0°C (273.15 K) for chars prepared at different carbonization temperatures of 400, 500, and 600°C.

Char sample	BET specific area, $S_0$ , (m <sup>2</sup> /g)
C400-90	144
C500-90	178
C600-90	219



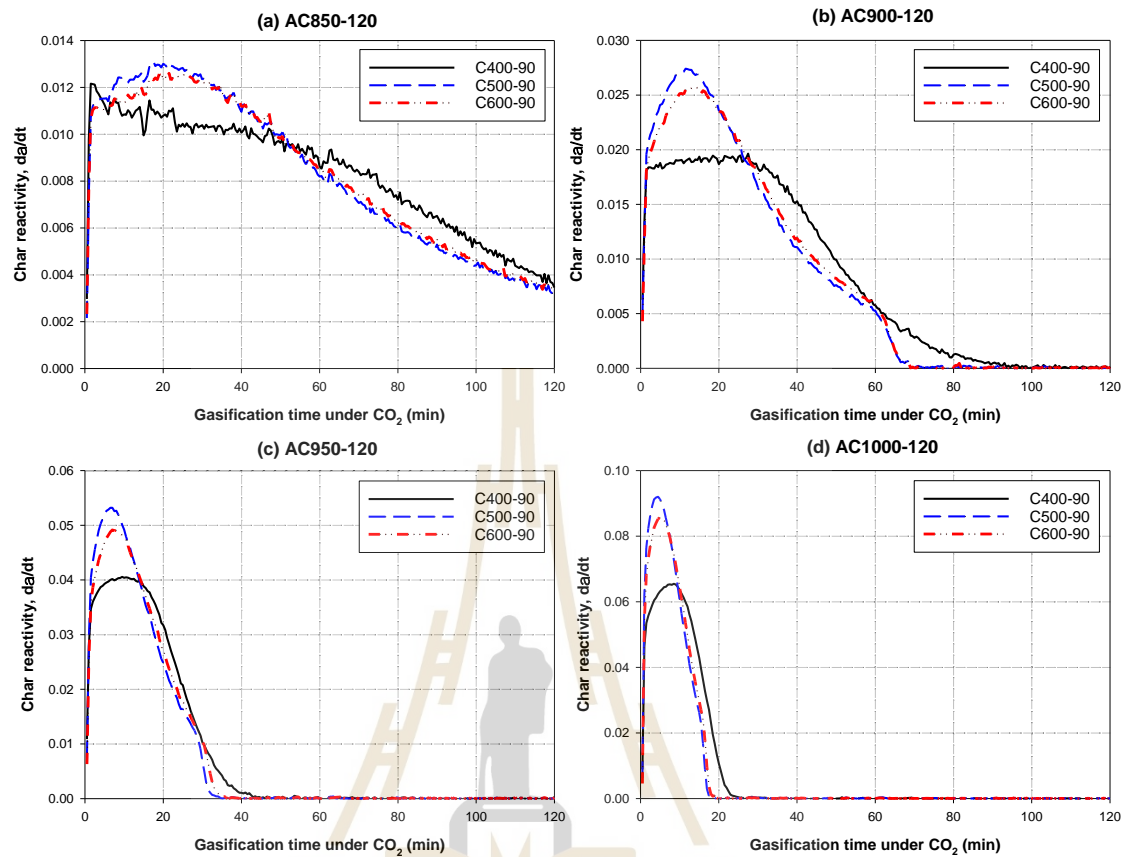
**Figure 3.7** Effects of char burn-off on the average pore diameter of the prepared activated carbons.

Figure 3.8 shows the effects of activation temperature and time on one of the important porous properties of activated carbon, the BET specific area, as a function of carbonization temperature. For activated carbon prepared from each carbonization temperature in the range from 400 to 600°C, the specific surface area increased approximately linearly over the increase in activation temperature from 850 to 950°C, but showed a rapid decrease from 950 to 1000°C. The increase in the surface area is due mainly to the increase in the gasification rate with the increase in the reaction temperature, while the decrease in surface area above 950°C is possibly the result of pore enlargement. This instance could occur when a considerable amount of carbon is consumed by the reaction, giving an increase in the average pore size of activated carbon and hence a consequent decrease in the surface area. Figure 3.8b shows that the increase in the activation time increased the activated carbon-specific area in an almost linear fashion. Increasing the activation time would increase the frequency of molecular collision for a successful reaction to occur or allow more time for CO<sub>2</sub> to diffuse to the reaction sites, hence more carbon atoms in the graphene layers may have been removed for pore development.



**Figure 3.8** Effects of activation temperature and activation time on BET specific area of activated carbon prepared from chars carbonized at different temperatures (400, 500, and 600°C) for (a) activation temperatures were varied from 850 to 1000°C while the activation time was kept constant at 60 min and (b) activation times were varied from 60 to 120 min while the activation temperature was kept constant at 900°C.

As to the effect of carbonization temperature, it is obvious that the surface area decreased with the increase in the carbonization temperature in the range of 400 to 600°C, although the specific area of char prior to activation increases with increasing carbonization temperature (see *Table 3.2*). This signifies that activated carbon prepared at the lowest carbonization of 400°C might be most reactive for CO<sub>2</sub> gasification. To prove this hypothesis, bamboo chars prepared at 400, 500 and 600°C in the tube furnace were subjected to CO<sub>2</sub> gasification in a thermogravimetric analyzer (TGA/DSC-1 Star System, Mettler-Toledo, Greifensee, Switzerland) under conditions simulating the actual activation conditions. The char reactivity was defined here as the rate of fractional weight loss according to Equation (3.3) and were computed from the TGA data and plotted with respect to the gasification time, as shown in *Figure 3.9*.



**Figure 3.9** Variation of char reactivity during  $CO_2$  gasification as a function of time for various chars and activation temperatures. Lines with black, blue, and red colors represent chars prepared at 400, 500, and 600°C, respectively, with each char being gasified at (a) 850°C, (b) 900°C, (c) 950°C, and (d) 1000°C for 120 min.

The char reactivity for  $CO_2$  gasification ( $R_c$ ) can be defined as

$$R_c = d\alpha/dt \quad (3.3)$$

where the fractional conversion of char,  $\alpha = (w_0 - w_t) / (w_0 - w_\infty)$ , and  $w_0$ ,  $w_t$ , and  $w_\infty$  are the weights of initial char, activated carbon at time  $t$  and the remaining ash, respectively.

Figure 3.9 shows the effect of gasification time on the values of char reactivity as functions of activation temperature (850 to 1000°C) and carbonization temperature. The reactivity curves showed a characteristic rising and falling with

reference to the increase in reaction time and demonstrated that the reactivity of char carbonized at the lowest temperature of 400°C gave the lowest reactivity, but the char carbonized at the intermediate temperature of 500°C produced the highest reactivity. This evidence suggests that although the char prepared at 400°C (sample C400-90) had the lowest reactivity for the gasification, it could have had more reactive sites, which enabled the increase in the reaction rate and hence producing a larger developed surface area. Therefore, it is likely that carbonization temperature could have a profound effect on the number and distribution of reactive sites available during the activation step, which will control the resulting porous structure of the prepared activated carbon. This emphasizes the significance of carbonization temperature in determining the reactivity of char for the gasification reaction and the subsequent pore development in activated carbon.

We now turn to the effect of the preparation conditions on the pore size distribution of the produced activated carbon, which was computed based on the MC simulation procedure. *Table 3.3* summarizes the distribution of pore sizes for all the prepared activated carbons, and the data are exemplified in *Figure 3.10* to illustrate the effects of the activation conditions on the distribution of pore sizes. The pores developed in bamboo-based activated carbon show the characteristics of multimodal size distribution, which covers the micropore size range from 0.65 to 2.0 nm and mesopores from 2.0 to 4.0 nm. Most of the pores produced (> 80% of total pore volume) were concentrated in the micropore size range of 0.65 to 1.4 nm. Some super-micropores (1.4–2.0 nm) were observed but no ultra-micropores (< 1.4 nm) were detected in any of the activated carbons. *Table 3.3* also shows that the mesopores were produced only in the size range of 3.0 to 4.0 nm with much smaller proportions as compared to the volume of the generated micropores. *Figure 3.10* further shows that the increase in activation temperature from 850 to 950°C increased the volume of the micropores in the size range from 0.65 to 1.4 nm, but the volume decreased slightly at the activation temperature of 1000°C, corresponding to the creation of more mesopores. Again, this might explain the creation of mesopores at the expense of micropores at a high activation temperature by the mechanism of pore enlargement, as previously outlined.

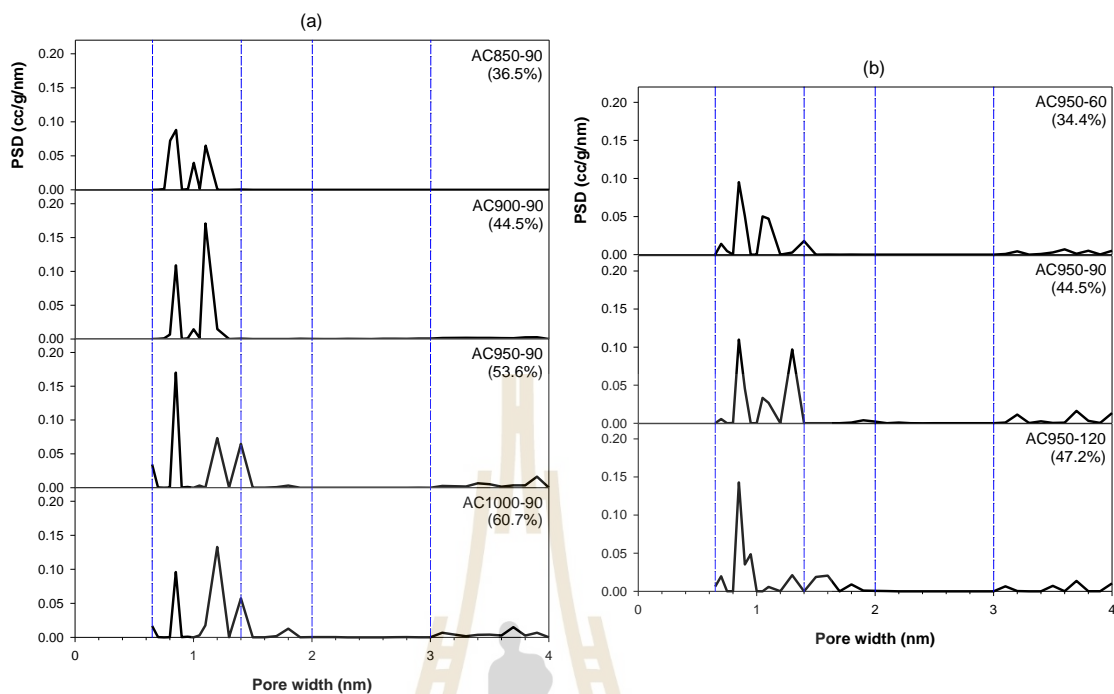


**Figure 3.10** Effects of activation temperature and activation time on the pore size distribution of produced activated carbon for (a) char C400-90 and activation time of 90 min and (b) for char C500-90 and activation temperature of 950°C.

**Table 3.3** Distribution of pore volume for various pore sizes in activated carbon prepared under different preparation conditions.

Run no.	Sample	Pore volume for pore width (cm <sup>3</sup> /g)				V <sub>tot</sub> (cm <sup>3</sup> /g)
		0.65–1.4 nm	1.4–2.0 nm	2.0–3.0 nm	3.0–4.0 nm	
from C400-90						
1	AC850-60	0.2344	0.0072	0.000	0.0006	0.2539
2	AC900-60	0.2757	0.0122	0.000	0.0171	0.3181
3	AC950-60	0.3155	0.0012	0.000	0.0332	0.3586
4	AC1000-60	0.2934	0.0074	0.000	0.0274	0.3373
5	AC850-90	0.2700	0.0001	0.000	0.000	0.2851
6	AC900-90	0.3206	0.0008	0.000	0.0205	0.3616
7	AC950-90	0.3479	0.004	0.000	0.0427	0.3986
8	AC1000-90	0.3254	0.015	0.000	0.0483	0.3988
9	AC850-120	0.2834	0.0001	0.000	0.0270	0.3145
10	AC900-120	0.3577	0.0176	0.000	0.0768	0.4458
11	AC950-120	0.3292	0.0442	0.000	0.0762	0.4546
12	AC1000-120	0.2484	0.0507	0.000	0.0684	0.3845
from C500-90						
13	AC850-60	0.2095	0.0001	0.000	0.000	0.2337
14	AC900-60	0.2535	0.0003	0.000	0.0133	0.294
15	AC950-60	0.2832	0.0005	0.000	0.028	0.3302
16	AC1000-60	0.2551	0.0011	0.000	0.0275	0.2964
17	AC850-90	0.2425	0.0004	0.000	0.0079	0.2722
18	AC900-90	0.2807	0.0024	0.000	0.0236	0.3279
19	AC950-90	0.3183	0.0072	0.000	0.0509	0.3936
20	AC1000-90	0.2624	0.0138	0.000	0.0364	0.3284
21	AC850-120	0.2682	0.0017	0.000	0.0032	0.2885
22	AC900-120	0.2939	0.029	0.000	0.0202	0.3646
23	AC950-120	0.2795	0.0498	0.000	0.0383	0.3823
24	AC1000-120	0.2193	0.0582	0.000	0.0457	0.3353
from C600-90						
25	AC850-60	0.2084	0.0011	0.000	0.000	0.2328
26	AC900-60	0.2466	0.0031	0.000	0.0132	0.2863
27	AC950-60	0.2639	0.0106	0.000	0.0205	0.3164
28	AC1000-60	0.1997	0.0168	0.000	0.013	0.2501
29	AC850-90	0.2377	0.0006	0.000	0.000	0.2656
30	AC900-90	0.2750	0.0174	0.000	0.0213	0.3492
31	AC950-90	0.2537	0.027	0.000	0.0272	0.3404
32	AC1000-90	0.2135	0.0381	0.000	0.0407	0.3178
33	AC850-120	0.2732	0.0017	0.000	0.0037	0.3034
34	AC900-120	0.2691	0.0349	0.000	0.0349	0.3776
35	AC950-120	0.249	0.0665	0.000	0.055	0.4054
36	AC1000-120	0.208	0.0703	0.000	0.0536	0.3584

The effect of activation time on the pore size distribution was similar to that of the activation temperature. The increase in activation time from 60 to 90 min increased the micropore volume but again it declined slightly at the longest time of 120 min, concomitant with the increase in the mesopore volume. Overall, it can be deduced that the number and distribution of reactive sites available for the CO<sub>2</sub> gasification of the carbonized chars play a significant role in the formation of different pore sizes as well as the pore connectivity during the activation process for the synthesis of activated carbon from bamboo biomass.

### 3.3.4 Correlations for Porous Properties of the Prepared Activated Carbons

In general, the fluid-solid reaction models can be classified into two schemes: (1) the reaction taking place on the surfaces of nonporous grains, and (2) the reaction that occurs on the pore surface within the solid (Bhatia & Perlmutter, 1980; Szekeley & Evans, 1970). Of these models, the Random Pore Model (RPM) developed by Bhatia and Perlmutter (Bhatia & Perlmutter, 1980) has been widely used in describing the gasification kinetics for porous solids, since it takes into account the effects of pore creation and the coalescence of neighboring pores at a high degree of char burn-off, thus showing a consequent decrease in the porous properties. Therefore, this model was adopted in this study to predict the development of porous properties of the obtained activated carbon from bamboo biomass. The final form of the random pore model (RPM) in terms of the developed surface area of solid can be written as:

$$\frac{S}{S_0} = \frac{1-X}{1-\frac{\tau}{\sigma}} \sqrt{1-\psi \ln \left[ \frac{1-X}{1-\frac{\tau}{\sigma}} \right]} \quad (3.4)$$

where  $S$  is the reaction surface area per unit mass,  $S_0$  is the initial surface area per unit mass (the specific area of original char),  $X$  is the fractional conversion,  $\sigma$  is the particle size parameter,  $\tau$  is the dimensionless time and  $\psi$  is the structural parameter. From Equation (3.4), it is convenient to assume  $\sigma \rightarrow \infty$  since the particle external surface

area can be negligible in comparison with the magnitude of the internal surface area.

This gives:

$$\frac{S}{S_0} = 1 - X \sqrt{1 - \psi \ln 1 - X} \quad (3.5)$$

The structural parameter ( $\psi$ ) was first calculated as a function of conversion based on Equation (3.5) using the surface area data of activated carbon ( $S$ ), as shown in *Table S1* (see Appendix A) and  $S_0$  for the surface area of the starting char which was estimated from  $\text{CO}_2$  isotherm data at  $0^\circ\text{C}$ , as shown in *Table 3.2*. It is obvious that the structural parameter should depend on the conversion ( $X$ ) because of the consequent change in the pore structure of the solid with the progression of reaction. It should be noted that the effect of activation time and temperature on the surface area ( $S$ ) is accounted for by the char conversion ( $X$ ). The relationship between the structural parameter and the char conversion can be approximated by the following power-law equation,

$$\psi = C_1 X^{C_2} \quad (3.6)$$

The fitting of the structural parameter as a function of char conversion is illustrated in *Figure 3.11*.

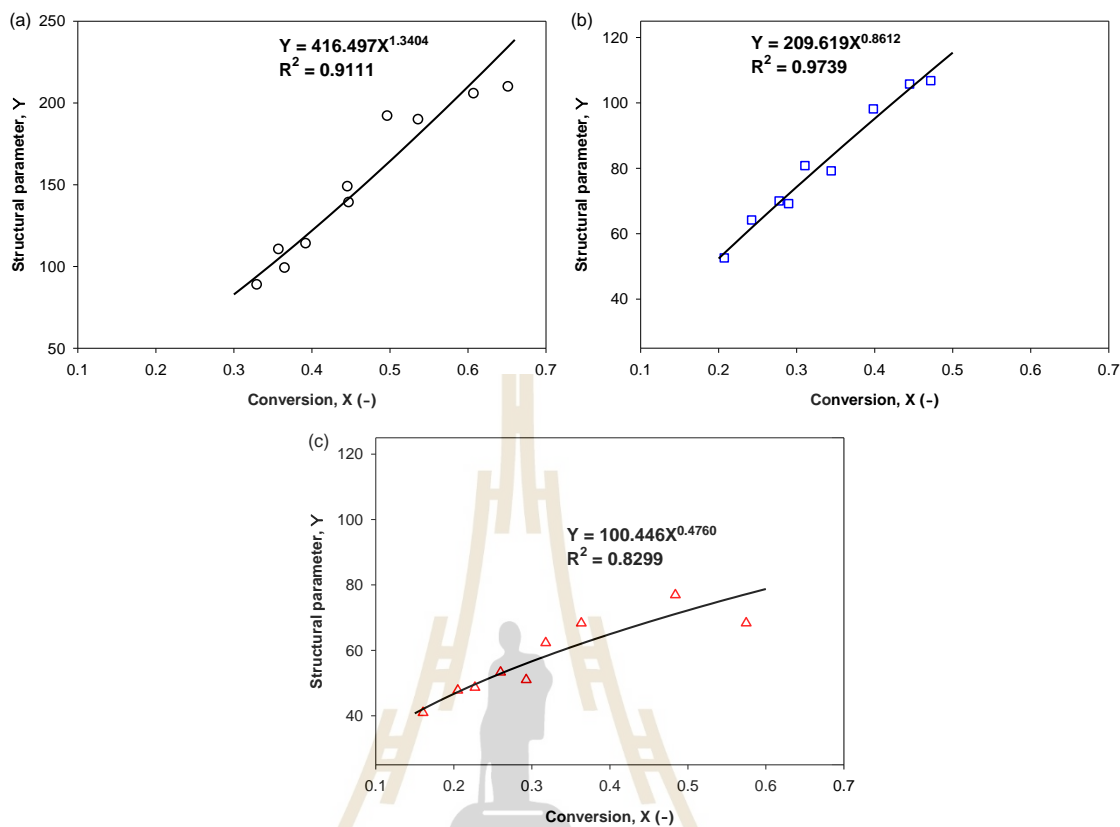


**Figure 3.11** The relationship between the structural parameter and fractional conversion of char. Figure (a)-(c) refer to the activated carbon derived from char carbonized at 400, 500, and 600°C for 90 minutes, respectively.

Next, the constants  $C_1$  and  $C_2$  were correlated with the carbonization temperature ( $T_c$ ) according to the power-law equation, as shown in the following equations,

$$C_1 = C_3 T_c^{C_4} \quad (3.7)$$

$$C_2 = C_5 T_c^{C_6} \quad (3.8)$$

and *Figure 3.12* shows the fitting results.

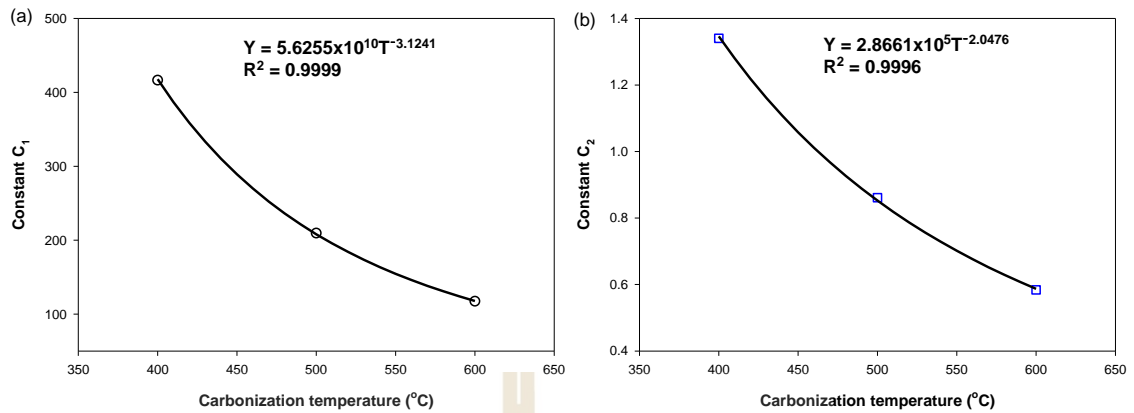


**Figure 3.12** Correlations between (a) the constant  $C_1$  and (b) the constant  $C_2$  in Equations (3.7) and (3.8) and the carbonization temperature.

Combining Equations (3.5) to (3.8) finally gives

$$\frac{S}{S_0} = 1 - X \sqrt{1 - C_1 T_c^{C_2} X^{C_3 T_c^{C_4}} \ln 1 - X} \quad (3.9)$$

Equation (3.9) was used to fit the measured surface area ( $S/S_0$ ) and the constants in the equation ( $C_1$ ,  $C_2$ ,  $C_3$ , and  $C_4$ ) were evaluated by the non-linear regression. The final derived equation reads

$$\frac{S}{S_0} = 1 - X \sqrt{1 - 5.6255 \times 10^{10} T_c^{-3.1241} X^{2.8661 \times 10^5 T_c^{-2.0476}} \ln 1 - X} \quad (3.10)$$

The coefficient of determination,  $R^2$ , derived from fitting Equation (3.10) to the experimental data is 0.9788 with the standard error of 0.1826. *Figure 3.13* compares the experimental and computed surface area results at three carbonization temperatures. Overall, the prediction capability of the random pore model (RPM) is satisfactory up to the maximum char conversion of about 0.65.

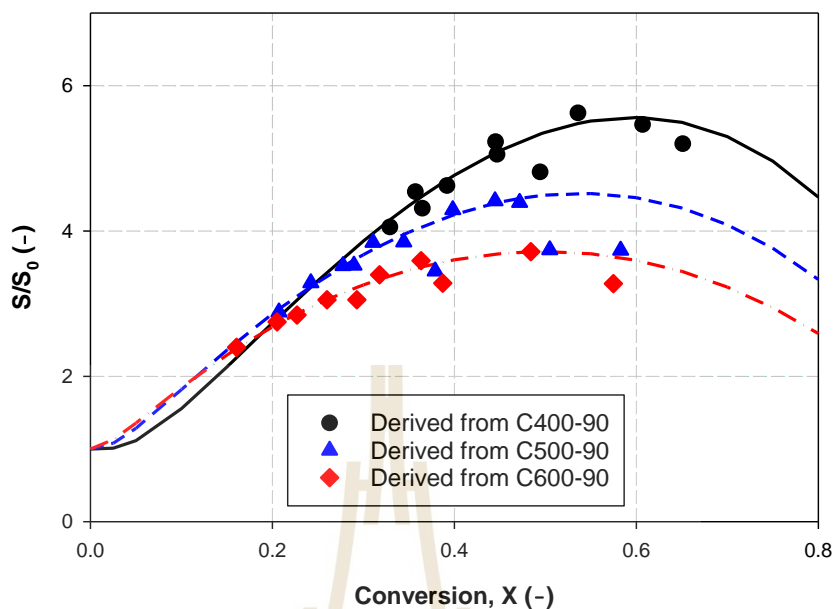


**Figure 3.13** The development of reaction surface with conversion according to the RPM. The activated carbon products were derived from chars carbonized at 400, 500, and 600°C for 90 minutes, respectively. The black solid line, blue dash line, and red dash-dot lines represent the predicted data derived from Equation (3.10). The black circles, blue triangles, and red diamonds indicate the experimental data points.

It appeared that there was an optimum char conversion or char burn-off that produced activated carbon with a maximum surface area and this optimum conversion depended on the carbonization temperature, being 0.597, 0.539 and 0.499 for the carbonization temperature of 400, 500 and 600°C, respectively. The difference in the optimum char conversion with the change in the carbonization temperature should result from the difference in the char reactivity for the CO<sub>2</sub> gasification, caused by the decomposition of cellulosic components of the precursor at different carbonization temperatures. The decrease in surface area at the conversion larger than the optimum one is possibly due to the association of adjacent pores into larger size pores. The fractional char conversion (X) is related to the activation conditions (time and temperature) by the following proposed equation.

$$\begin{aligned}
X = & -3.9708 \times 10^{-1} - 5.131 \times 10^{-3} T_C + 4.1554 \times 10^{-3} T_{Act} - 1.2122 \times 10^{-2} t_{Act} + 4.63 \times 10^{-7} T_C T_{Act} \\
& + 5.7333 \times 10^{-6} T_C t_{Act} + 1.5213 \times 10^{-5} T_{Act} t_{Act} + 3.5213 \times 10^{-6} T_C^2 - 2.2256 \times 10^{-6} T_{Act}^2 - 1.4583 \times 10^{-5} t_{Act}^2
\end{aligned}
\quad (3.11)$$

where  $X$  is the fractional conversion of char,  $T_C$  is the carbonization temperature in °C,  $T_{Act}$  is the activation temperature in °C, and  $t_{Act}$  is the activation time in minutes, with  $R^2$  and standard error of estimate being 0.9923 and 0.0122, respectively.

It should be noted that Equations (3.10) and (3.11) can be used to estimate the surface area of activated carbon from bamboo precursor, knowing the carbonization temperature, activation temperature and activation time in the range of 400 to 600°C, 850 to 1000°C and 60 to 120 min, respectively.

Next, an attempt was made to develop an equation for estimating the total pore volume of activated carbon as a function of preparation conditions. It was found that the total pore volume ( $V_{tot}$ ) in cm<sup>3</sup>/g correlates approximately well with the BET specific area of activated carbon, according to the following power-law model:

$$V_{tot} = a S_{BET}^b \quad (3.12)$$

where  $a$  and  $b$  are the constants of the equation and  $S_{BET}$  is the BET specific area in m<sup>2</sup>/g of the obtained activated carbon. After fitting Equation (3.12) with the experimental data, the following final equation is derived.

$$V_{tot} = 1.314 \times 10^{-4} S_{BET}^{1.199} \quad (3.13)$$

Figure 3.14 shows the agreement between the total pore volume determined from the N<sub>2</sub> adsorption isotherms and that predicted by Equation (3.13), as a function of BET specific area. The coefficient of determination,  $R^2$ , is 0.9738. This correlation can be employed to determine the total pore volume of the activated carbon from the corresponding BET specific area. The limitation of this correlation is that it can be used to predict the total pore volume in activated carbon obtained from bamboo precursor only and under the synthesis conditions used in the study.

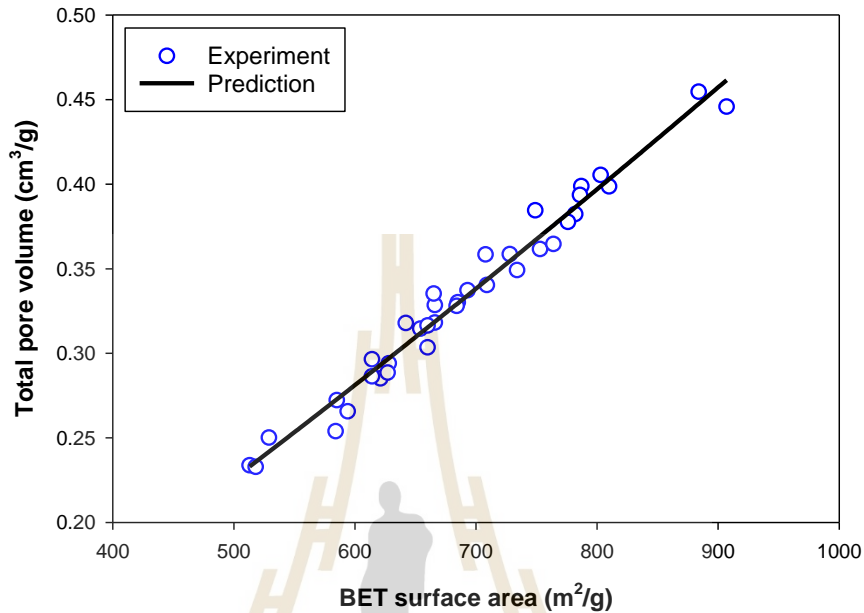


**Figure 3.14** The correlation between total pore volume ( $V_{tot}$ ) and BET specific area. The black solid line is predicted from Equation (3.13), while the blue circles are the experimental data.

Further work was devoted to the development of an empirical equation to correlate the micropore volume with the preparation conditions for activated carbon production. The following final equation was proposed.

$$\begin{aligned}
 V_{mic} = & -8.5823 - 7.5308 \times 10^{-4} T_C + 1.9081 \times 10^{-2} T_{Act} + 3.5284 \times 10^{-3} t_{Act} - 1.3147 \times 10^{-6} T_C T_{Act} \\
 & + 6.4792 \times 10^{-7} T_C t_{Act} - 1.6811 \times 10^{-6} T_{Act} t_{Act} + 1.7525 \times 10^{-6} T_C^2 - 9.7544 \times 10^{-6} T_{Act}^2 - 7.4861 \times 10^{-6} t_{Act}^2
 \end{aligned}
 \quad (3.14)$$

where  $V_{mic}$  is the volume of micropore of activated carbon in  $\text{cm}^3/\text{g}$ ,  $T_C$  is the carbonization temperature in  $^\circ\text{C}$ ,  $T_{Act}$  is the activation temperature in  $^\circ\text{C}$ , and  $t_{Act}$  is the activation time in min. The  $R^2$  is 0.9241 with the standard error of 0.0134.

Finally, the equation for estimating the amount of mesopore volume ( $V_{mes}$ ) can be obtained from the difference between the total pore volume ( $V_{tot}$ ) and the micropore volume ( $V_{mic}$ ). That is,

$$V_{mes} \text{ cm}^3/\text{g} = V_{tot} \text{ cm}^3/\text{g} - V_{mic} \text{ cm}^3/\text{g} \quad (3.15)$$

where  $V_{tot}$  and  $V_{mic}$  are computed from Equations (3.13) and (3.14), respectively.

In conclusion, all the important porous properties of activated carbon produced from bamboo by the two-step activation with  $\text{CO}_2$ , including BET specific area, the total pore volume, the micropore volume, and the mesopore volume can be readily estimated from the developed equations as functions of the carbonization temperature (400 to 600°C), activation temperature (850 to 1000°C), and activation time (60 to 120 min).

### 3.3.5 Surface Chemistry of the Prepared Activated Carbons

Fourier Transform Infrared Spectroscopy (FTIR) and elemental analysis were employed to analyze the development of surface functionality on the surface of activated carbon during the carbonization and the activation steps. First, three samples of char were selected for the analysis, which are char carbonized at 400, 500 and 600°C for 90 min and the FTIR results are shown in *Figure 3.15*. The aromatic rings are characterized by the intense band at about  $1590 \text{ cm}^{-1}$ ; this is assigned to rings vibration in large condensed aromatic carbon (Burg *et al.*, 2002). This band is typically found in carbonaceous materials (Bouwman & Freriks, 1980; Fujii *et al.*, 1970). The small band at about  $1360 \text{ cm}^{-1}$  for the C400-90 sample corresponds to the existence of  $\text{CH}_3$  groups (CH-bending vibration) (Bouwman & Freriks, 1980). The weak band located at about  $1170 \text{ cm}^{-1}$  can be assigned to the C-O stretching vibration of phenol and aromatic ring of ether (Brown, 1955; Zhang *et al.*, 2014). The broad band between  $1220$  to  $1430 \text{ cm}^{-1}$  of the C400-90 sample is attributed to nitrate, carboxyl and carboxylate groups (Zielke *et al.*, 1996). The strong band at  $1080 \text{ cm}^{-1}$  was observed for all char samples, and this band is assigned to C-O stretching vibration of primary alcohols (Zielke *et al.*, 1996). Lastly, the C-H out-of-plane bend at  $740 \text{ cm}^{-1}$  indicates the presence of aromatic ring in activated carbon (Nandiyanto *et al.*, 2019).

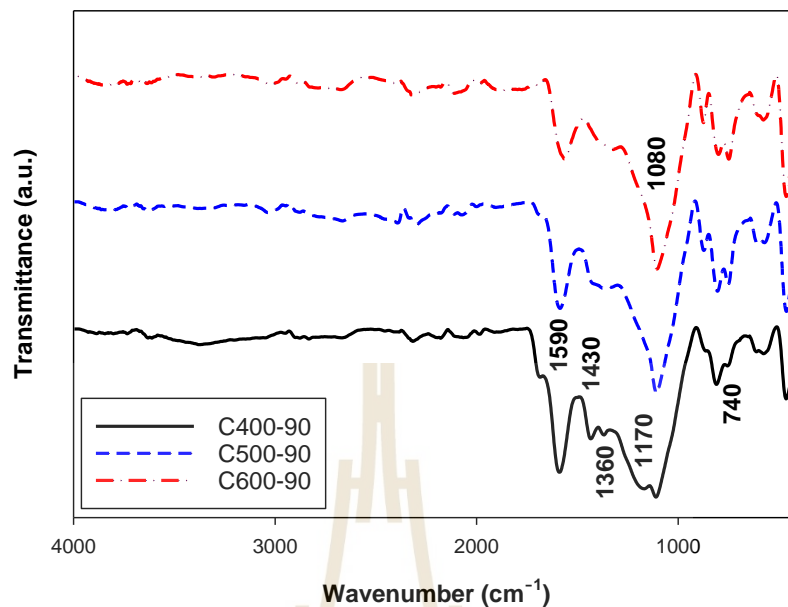
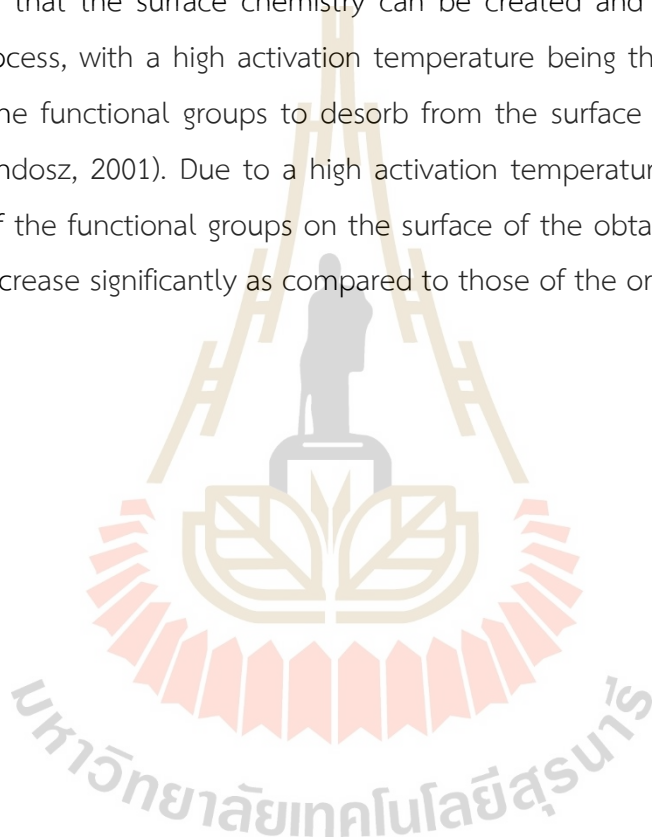


**Figure 3.15** FTIR spectra of the prepared chars. The black solid line, blue dash line, and red dash-dot line refer to char carbonized at 400, 500, and 600°C for 90 min.

The presence of the surface chemistry in the carbonized chars indicates that the different surface functional groups can be created during the carbonization step of the bamboo precursor. Next, we explore the surface chemistry of the activated carbon derived from the prepared char.

FTIR spectra of activated carbon prepared at 850, 900, 950 and 1000°C with the activation time of 90 min are typically shown in *Figure 3.16*. Here, we use char carbonized at 500°C for 90 min as the starting char. The intense adsorption band at 1080  $\text{cm}^{-1}$  was observed in the char sample, while the intensity of this band decreased for the activated carbon samples. This implies a decrease in C-O of primary alcohol structure. The weak band at about 1560  $\text{cm}^{-1}$  was found in all activated carbon samples, however, the adsorption band continued to decrease in intensity when the activation temperature was increased. This indicates that the amount of large condensed aromatic frame decreases during the activation at a high temperature, corresponding to the consumption of carbon atoms in the graphene layers by the gasification reaction. The stretching vibration of C-H was observed as weak bands at

about 2850 to 3000  $\text{cm}^{-1}$ , mostly in activated carbon samples but was not found in the char sample. The adsorption bands at about 2850 and 2920  $\text{cm}^{-1}$  are referred to the symmetric and asymmetric stretching vibration of  $\text{CH}_2$  and  $\text{CH}_3$  groups (Burg *et al.*, 2002; Gomez-Serrano *et al.*, 1996). The intensity of these bands tended to decrease when the activation temperature was increased, indicating the removal of hydrogen content during the activation process (Liu *et al.*, 2010). The FTIR results of activated carbon imply that the surface chemistry can be created and destroyed during the activation process, with a high activation temperature being the key parameter that encourages the functional groups to desorb from the surface (Brender *et al.*, 2012; Salame & Bandosz, 2001). Due to a high activation temperature and long activation time, most of the functional groups on the surface of the obtained activated carbon tended to decrease significantly as compared to those of the original char.



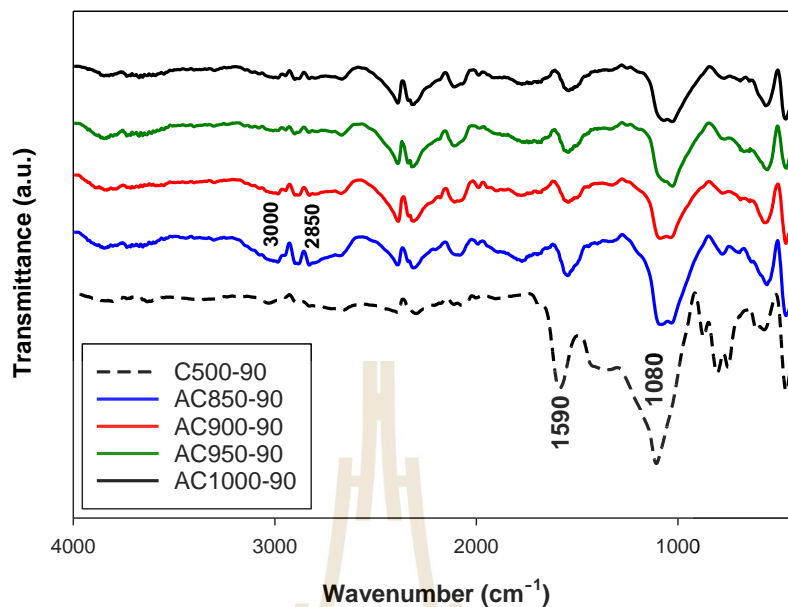


**Figure 3.16** FTIR spectra of the obtained activated carbon. The blue, red, green, and black solid lines refer to activated carbon prepared at 850, 900, 950, and 1000°C for 90 min. The black dash line is the char carbonized at 500°C. All carbon samples were derived from char carbonized at 500°C for 90 min.

To substantiate quantitatively the creation and removing of surface groups during the carbonization and physical activation, the Boehm titration technique was used to quantify the change of surface functional groups. The weight fraction of elements in the char and activated carbon samples and the amounts of surface functional groups obtained from the Boehm titration are listed in *Table 3.4*. For the char sample, as the carbonization temperature increased, the basic groups appeared to increase. On the other hand, the acidic groups decreased while the carbonization temperature was increased. These results are attributed to the thermal instability of acidic and basic groups with respect to the change in the carbonization temperature; at a higher carbonization temperature most of the acid groups are destroyed, whereas the basic groups are developed (Sato et al., 2007). The decrease in the acidic groups is as well confirmed by the decrease in the weight fraction of oxygen contents from the element analysis, as shown in *Table 3.4*.

**Table 3.4** Typical elemental analysis and surface chemistry of prepared chars and the prepared activated carbons. All activated carbon samples were derived from char carbonized at 400°C for 90 min.

Sample	Elemental analysis (wt%)				Amount of surface functional groups (mmol/g)				
	C	H	N	O	Carboxylic	Lactonic	Phenolic	Total acidic	Total basic
C400-90	56.0	3.8	0.5	39.7	0.37	0.00	0.40	0.77	0.21
C500-90	50.4	3.1	0.4	46.1	0.44	0.00	0.11	0.55	0.38
C600-90	52.5	2.4	0.4	44.6	0.32	0.00	0.00	0.32	0.44
AC850-120	60.0	1.8	0.5	37.7	0.04	0.00	0.35	0.39	0.71
AC900-120	60.0	1.7	0.6	37.7	0.01	0.00	0.45	0.46	0.82
AC950-120	57.9	1.5	0.6	40.0	0.06	0.00	0.43	0.49	0.87
AC1000-120	53.2	1.6	0.4	44.8	0.08	0.00	0.43	0.51	0.82

For activated carbon samples, it was found that the total acidic groups increased with the increase in activation temperature, with about 31% increase over the range of temperature from 850 to 1000°C. The total basic group also showed an increase of 22% when the activation temperature increased from 850 to 950°C, but tended to drop at the higher temperature of 1000°C. It is understandable that the acidic surface groups are created and destroyed in parallel along with the development of porous properties during the gasification reactions under CO<sub>2</sub>, with a higher activation temperature creating more oxygen functional groups (Bansal & Goyal, 2005). As noticed from *Table 3.4*, the carboxylic group is the major surface group in bamboo char, while in the prepared activated carbon the phenolic group showed the highest content. The lactonic groups were not detected in all the analyzed samples.

### 3.3.6 Empirical Correlations for the Formation of the Surface Functional Groups

This section is devoted to the development of empirical equations for correlating the number of surface functional groups with the preparation conditions for the production of activated carbon. We commenced by examining the relationship between the concentration of the surface groups and the percentage of char burn-off. Three possible concentration units for the functional groups, mmol/g AC, mmol/g char and mmol/m<sup>2</sup> of AC surface area, were tried and the plots of functional group concentration versus burn-off are shown in *Figure 3.17*. Only the surface concentration in the unit of mmol/g char yielded a clearer relationship. Thus, the data on the amount of surface functional groups in the unit of mmol/g char were used for developing the

mathematical correlation between the surface group concentration (acidic and basic groups) and the preparation conditions (carbonization temperature, and activation time and temperature) used in this study.

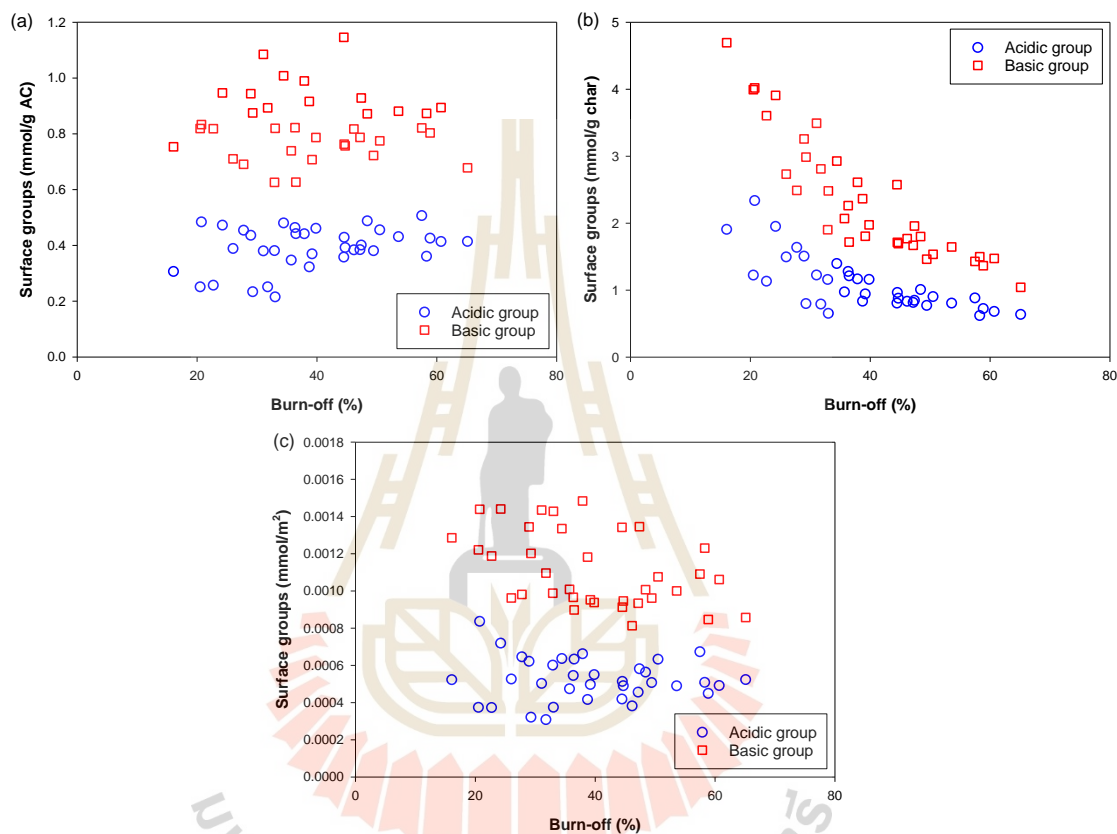


**Figure 3.17** Presentation of surface groups concentration in three different units of (a) mmol/g carbon, (b) mmol/g char, and (c) mmol/m<sup>2</sup> of BET specific area, as a function of percentage of char burn-off.

We started by defining various variables involved. For independent variables,  $x_1$  is given as the carbonization temperature (°C),  $x_2$  is the activation temperature (°C) and  $x_3$  is the activation time (minutes). The dependent variable  $Y$  represents the response or the concentration of surface functional groups in mmol/g char being obtained from the experimental data. The following relationship can then be written,

$$Y = f(x_1, x_2, x_3) + \varepsilon \quad (3.16)$$

where  $\varepsilon$  is the error or interference that occurs in a system that affects the magnitude of the response.

The experimental data were then fitted with the following second-order polynomial equation of the form,

$$Y = \beta_0 + \sum_{i=1}^2 \beta_i x_i + \sum_{i=1}^2 \beta_{ii} x_i^2 + \sum_{i < j}^2 \sum_{j=1}^2 \beta_{ij} x_i x_j + \varepsilon \quad (3.17)$$

where  $Y$  is the predicted response,  $\beta_0$  is a constant,  $\beta_i$  is a linear term coefficient,  $\beta_{ii}$  is a quadratic term coefficient and  $\beta_{ij}$  is a cross product term coefficient.

It is convenient to first put the dependent and independent variables in normalized forms, that is,

$$x_{i,norm} = \frac{x_i - x_{min}}{x_{diff}} \quad (3.18)$$

$$Y_{i,norm} = \frac{Y_i - Y_{min}}{Y_{diff}} \quad (3.19)$$

where  $x_{i,norm}$  and  $Y_{i,norm}$  are the normalized values of the independent variable,  $x_i$  and  $Y_i$  dependent variables,  $x_{min}$  and  $Y_{min}$  are the minimum values of  $x_i$  and  $Y_i$ , and  $x_{diff}$  and  $Y_{diff}$  are the difference between the maximum and minimum values of  $x_i$  and  $Y_i$ , respectively. Equation (3.17) was used to fit the normalized values of  $Y$  and  $x$  from experiments and a non-linear regression was applied to obtain the values of constants in the equation by minimizing the overall error. The final equations in normalized forms with the fitted constants were first derived from data fitting and then they were converted back to the normal forms of the dependent and independent variables. The final derived equations are the following.

$$Y_{acid} = 26.3872 + 4.1162 \times 10^{-2} T_C - 6.6906 \times 10^{-2} T_{Act} - 5.3928 \times 10^{-2} t_{Act} - 1.0685 \times 10^{-5} T_C T_{Act} \\ + 1.5745 \times 10^{-5} T_C t_{Act} + 2.5878 \times 10^{-5} T_{Act} t_{Act} - 3.1749 \times 10^{-5} T_C^2 + 3.5153 \times 10^{-5} T_{Act}^2 + 1.0291 \times 10^{-4} t_{Act}^2 \quad (3.20)$$

$$Y_{base} = -12.7457 + 9.9663 \times 10^{-2} T_C - 1.6788 \times 10^{-2} T_{Act} + 3.7510 \times 10^{-2} t_{Act} - 4.1479 \times 10^{-5} T_C T_{Act} \\ - 1.0268 \times 10^{-4} T_C t_{Act} + 2.3321 \times 10^{-5} T_{Act} t_{Act} - 4.6442 \times 10^{-5} T_C^2 + 1.4370 \times 10^{-5} T_{Act}^2 - 1.3059 \times 10^{-4} t_{Act}^2 \quad (3.21)$$

where  $Y_{acid}$  and  $Y_{basic}$  are the amounts of acid and basic surface groups in mmol/g char, respectively.  $T_C$  is the carbonization temperature (400 to 600°C),  $T_{Act}$  is the activation

temperature (850 to 1000°C), and  $t_{Act}$  is the activation time (60 to 120 min). The  $R^2$  of Equations (3.20) and (3.21) are 0.821 and 0.9254, with standard error of 0.1203 and 0.0784, respectively.

Next, Equations (3.20) and (3.21) were used to determine the optimum conditions that give the highest amounts of acid and basic surface groups on activated carbon by plotting a surface response of the dependent variable (amount of surface groups) as a function of the independent variables (preparation conditions), as typically shown in *Figure 3.18–20*. The optimum conditions for creating the acidic surface groups were found to be 520°C and 90 min for carbonization conditions and activation temperature of 850°C with 60 min of activation time. For the formation of maximum basic groups, the optimum conditions are 600°C and 90 min for carbonization conditions and the activation conditions of 850°C and 60 min. These conditions are reasonable, considering the fact that a too high activation temperature and long activation time used during the activation process could destroy the number of surface groups formed in the activated carbon.



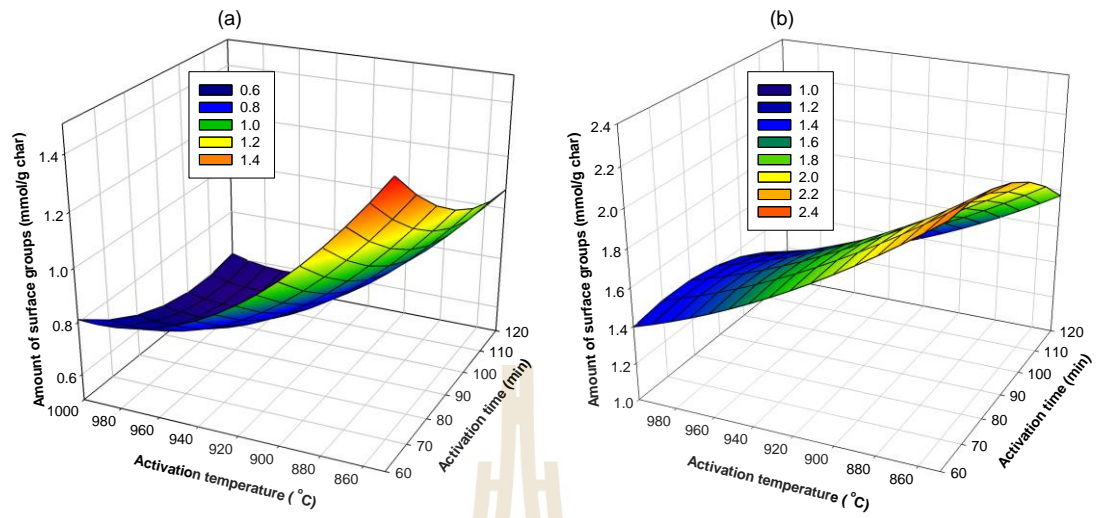


**Figure 3.18** Surface response curves showing the effects of activation temperature and activation time on the amount of surface groups on activated carbon derived from char C400-90, (a) acidic groups and (b) basic groups.

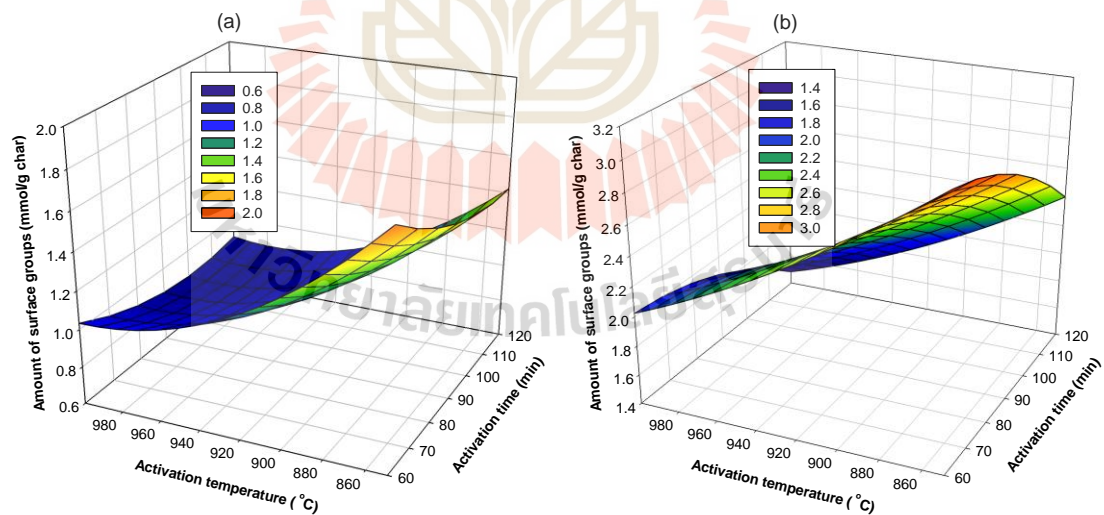


**Figure 3.19** Surface response curves showing the effects of activation temperature and activation time on the amount of surface groups on activated carbon derived from char C500-90, (a) acidic groups and (b) basic groups.

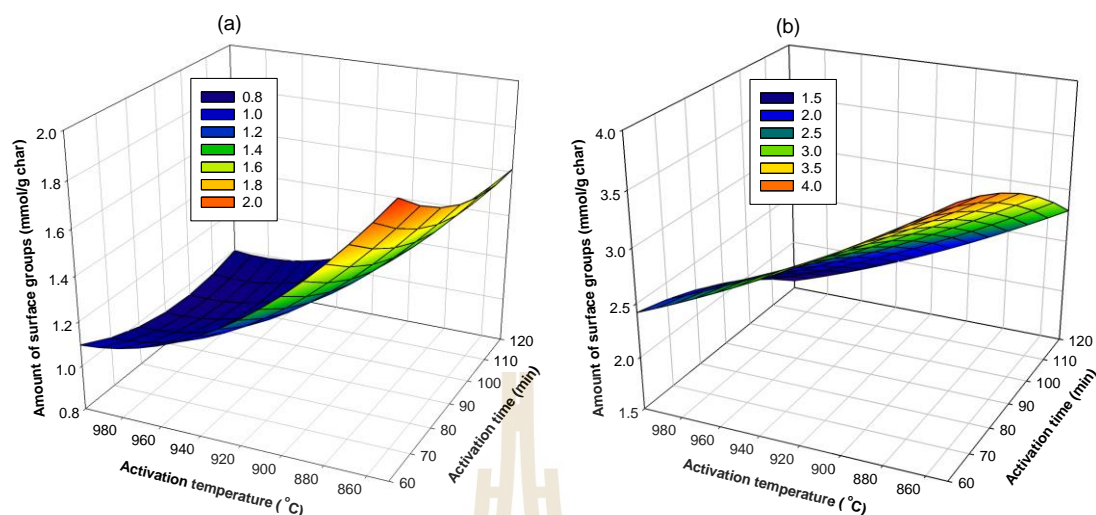


**Figure 3.20** Surface response curves showing the effects of activation temperature and activation time on the amount of surface groups on activated carbon derived from char C600-90, (a) acidic groups and (b) basic groups.

### 3.4 Conclusions

Bamboo was used as a precursor for the synthesis of activated carbon by the two-step physical activation with carbon dioxide and the effects of carbonization temperature (400 to 600°C), activation temperature (850 to 1000°C) and activation time (60 to 120 min) on the pore development and the formation of oxygen functional groups were investigated. Increasing activation conditions promoted the porous properties of produced activated carbons, but at a relatively high degree of char burn-off the surface area and micropore volume decreased with the corresponding increase in mesopore volume. Under the preparation conditions investigated, the activated carbon prepared from bamboo contained mostly micropores (> 85% of total pore volume). The maximum surface area of 907 m<sup>2</sup>/g and total pore volume of 0.446 cm<sup>3</sup>/g were obtained at carbonization temperature of 400°C and 90 min, activation temperature of 900°C and 120 min. Under the same activation conditions, activated carbon prepared from the char carbonized at the lowest temperature of 400°C gave the highest porous properties, presumably because of having a larger number of active sites for the CO<sub>2</sub> gasification. The results of pore size distribution of produced activated

carbons indicate that most pores were developed in the micropore size range of 0.65 to 1.4 nm. Empirical correlations were proposed to predict all the important porous properties of the bamboo-based activated carbons as functions of carbonization temperature and activation conditions. It is obvious that the creation of surface functional groups by the oxidation of CO<sub>2</sub> takes place in parallel with the development of carbon pores. It was found that the amounts of acidic surface functional groups in the char samples decreased with the increase in carbonization temperature, while the opposite effect occurred for the contents of the basic groups. When the activation temperature increased, both the contents of acid and basic groups tended to increase. Empirical equations were developed to estimate the amounts of the total acid and basic surface groups in bamboo-activated carbons in terms of carbonization temperature and activation conditions. The knowledge of the concentration of oxygen functional groups of activated carbon as a function of preparation conditions would be beneficial to the selection of experimental conditions for oxidizing activated carbon, by air or an acid, with the purpose being to effectively increase the contents of surface functional groups.



### 3.5 References

- Allen, M. P., & Tildesley, D. J. (2017). **Computer Simulation of Liquids** (2nd ed.). Oxford: Oxford University Press.
- Bansal, R. C., Donnet, J. B., & Stoeckli, F. (1988). **Active Carbon**. New York City, New York: Marcel Dekker.
- Bansal, R. C., & Goyal, M. (2005). **Activated Carbon Adsorption**. Florida: CRC Press.
- Basu, P. (2013). **Biomass Gasification, Pyrolysis and Torrefaction: Practical Design and Theory** (2nd ed.). San Diego: Academic Press.
- Bhatia, S. K. B., & Perlmutter, D. D. (1980). A random pore model for fluid-solid reactions: I. Isothermal, kinetic control. **AIChE Journal**. 26(3): 379-386.
- Blachnio, M., Derylo-Marczewska, A., Charmas, B., Zienkiewicz-Strzalka, M., Bogatyrov, V., & Galaburda, M. (2020). Activated Carbon from Agricultural Wastes for Adsorption of Organic Pollutants. **Molecules**. 25(21): 5105.
- Boehm, H. P. (1994). Some aspects of the surface chemistry of carbon blacks and other carbons. **Carbon**. 32(5): 759-769.
- Boehm, H. P. (2002). Surface oxides on carbon and their analysis: a critical assessment. **Carbon**. 40(2): 145-149.
- Bouchelta, C., Medjram, M. S., Bertrand, O., & Bellat, J.-P. (2008). Preparation and characterization of activated carbon from date stones by physical activation with steam. **Journal of Analytical and Applied Pyrolysis**. 82(1): 70-77.
- Bouwman, R., & Freriks, I. L. C. (1980). Low-temperature oxidation of a bituminous coal. Infrared spectroscopic study of samples from a coal pile. **Fuel**. 59(5): 315-322.
- Brender, P., Gadiou, R., Rietsch, J.-C., Fioux, P., Dentzer, J., Ponche, A., & Vix-Guterl, C. (2012). Characterization of Carbon Surface Chemistry by Combined Temperature Programmed Desorption with in Situ X-ray Photoelectron Spectrometry and Temperature Programmed Desorption with Mass Spectrometry Analysis. **Analytical Chemistry**. 84(5): 2147-2153.
- Brown, J. K. (1955). The infrared spectra of coals. **Journal of the Chemical Society (Resumed)**. (0): 744-752.
- Brunauer, S., Emmett, P. H., & Teller, E. (1938). Adsorption of Gases in Multimolecular Layers. **Journal of the American Chemical Society**. 60(2): 309-319.

- Burg, P., Fydrych, P., Cagniant, D., Nanse, G., Bimer, J., & Jankowska, A. (2002). The characterization of nitrogen-enriched activated carbons by IR, XPS and LSER methods. **Carbon**. 40(9): 1521-1531.
- Chang, C.-F., Chang, C.-Y., & Tsai, W.-T. (2000). Effects of Burn-off and Activation Temperature on Preparation of Activated Carbon from Corn Cob Agrowaste by CO<sub>2</sub> and Steam. **Journal of Colloid and Interface Science**. 232(1): 45-49.
- D7582-15, A. (2015). Standard Test Methods for Proximate Analysis of Coal and Coke by Macro Thermogravimetric Analysis.
- de Souza Souza, C., Bomfim, M. R., Conceição de Almeida, M. d., Alves, L. d. S., de Santana, W. N., da Silva Amorim, I. C., & Santos, J. A. G. (2021). Induced changes of pyrolysis temperature on the physicochemical traits of sewage sludge and on the potential ecological risks. **Scientific Reports**. 11(1): 974.
- Deng, S., Nie, Y., Du, Z., Huang, Q., Meng, P., Wang, B., . . . Yu, G. (2015). Enhanced adsorption of perfluorooctane sulfonate and perfluorooctanoate by bamboo-derived granular activated carbon. **Journal of Hazardous Materials**. 282: 150-157.
- Dubinin, M. M. (1975). Physical Adsorption of Gases and Vapors in Micropores. In D. A. Cadenhead, J. F. Danielli, & M. D. Rosenberg (Eds.), *Progress in Surface and Membrane Science* (Vol. 9, pp. 1-70): Elsevier.
- Durán-Valle, C. J., Gómez-Corzo, M., Pastor-Villegas, J., & Gómez-Serrano, V. (2005). Study of cherry stones as raw material in preparation of carbonaceous adsorbents. **Journal of Analytical and Applied Pyrolysis**. 73(1): 59-67.
- El-Hendawy, A.-N. A., Samra, S. E., & Girgis, B. S. (2001). Adsorption characteristics of activated carbons obtained from corncobs. **Colloids and Surfaces A: Physicochemical and Engineering Aspects**. 180(3): 209-221.
- Erlich, C., Björnbohm, E., Bolado, D., Giner, M., & Fransson, T. H. (2006). Pyrolysis and gasification of pellets from sugar cane bagasse and wood. **Fuel**. 85(10): 1535-1540.
- Fujii, S., Ōsawa, Y., & Sugimura, H. (1970). Infra-red spectra of Japanese coal: The absorption bands at 3030, 2920 and 1600 cm<sup>-1</sup>. **Fuel**. 49(1): 68-75.

- Gomez-Serrano, V., Pastor-Villegas, J., Perez-Florindo, A., Duran-Valle, C., & Valenzuela-Calahorro, C. (1996). FT-IR study of rockrose and of char and activated carbon. **Journal of Analytical and Applied Pyrolysis**. 36(1): 71-80.
- González-García, P. (2018). Activated carbon from lignocellulosics precursors: A review of the synthesis methods, characterization techniques and applications. **Renewable and Sustainable Energy Reviews**. 82: 1393-1414.
- Guo, J., & Lua, A. C. (2000). Preparation of activated carbons from oil-palm-stone chars by microwave-induced carbon dioxide activation. **Carbon**. 38(14): 1985-1993.
- Heo, Y.-J., & Park, S.-J. (2018). H<sub>2</sub>O<sub>2</sub>/steam activation as an eco-friendly and efficient top-down approach to enhancing porosity on carbonaceous materials: the effect of inevitable oxygen functionalities on CO<sub>2</sub> capture. **Green Chemistry**. 20(22): 5224-5234.
- Herrera, L., Do, D. D., & Nicholson, D. (2010). A Monte Carlo integration method to determine accessible volume, accessible surface area and its fractal dimension. **Journal of Colloid and Interface Science**. 348(2): 529-536.
- Jawad, A. H., Ismail, K., Ishak, M. A. M., & Wilson, L. D. (2018). Conversion of Malaysian low-rank coal to mesoporous activated carbon: Structure characterization and adsorption properties. **Chinese Journal of Chemical Engineering**.
- Johnson, J. K., Zollweg, J. A., & Gubbins, K. E. (1993). The Lennard-Jones equation of state revisited. **Molecular Physics**. 78(3): 591-618.
- Junpirom, S., Tangsathitkulchai, C., & Tangsathitkulchai, M. (2010). Thermogravimetric analysis of longan seed biomass with a two-parallel reactions model. **Korean Journal of Chemical Engineering**. 27(3): 791-801.
- Katesa, J., Junpirom, S., & Tangsathitkulchai, C. (2013). Effect of carbonization temperature on properties of char and activated carbon from coconut shell. **Suranaree Journal of Science and Technology**. 20(4): 269-278.
- Khadiran, T., Hussein, M. Z., Zainal, Z., & Rusli, R. (2015). Activated carbon derived from peat soil as a framework for the preparation of shape-stabilized phase change material. **Energy**. 82: 468-478.

- Konczak, M., Oleszczuk, P., & Różyło, K. (2019). Application of different carrying gases and ratio between sewage sludge and willow for engineered (smart) biochar production. **Journal of CO2 Utilization**. 29: 20-28.
- Lawtae, P., & Tangsathikulchai, C. (2021). A New Approach for Controlling Mesoporosity in Activated Carbon by the Consecutive Process of Air Oxidation, Thermal Destruction of Surface Functional Groups, and Carbon Activation (the OTA Method). **Molecules**. 26(9): 2758.
- Liu, Q.-S., Zheng, T., Wang, P., & Guo, L. (2010). Preparation and characterization of activated carbon from bamboo by microwave-induced phosphoric acid activation. **Industrial Crops and Products**. 31(2): 233-238.
- Liu, Z., Zhang, F., Liu, H., Ba, F., Yan, S., & Hu, J. (2018). Pyrolysis/gasification of pine sawdust biomass briquettes under carbon dioxide atmosphere: Study on carbon dioxide reduction (utilization) and biochar briquettes physicochemical properties. **Bioresource Technology**. 249: 983-991.
- Lua, A. C., & Guo, J. (1998). Preparation and characterization of chars from oil palm waste. **Carbon**. 36(11): 1663-1670.
- Marsh, H., & Rodriguez-Reinoso, F. (2006). **Activated Carbon**. London: Elsevier.
- Metropolis, N., Rosenbluth, A. W., Rosenbluth, M. N., Teller, A. H., & Teller, E. (1953). Equation of State Calculations by Fast Computing Machines. **The Journal of Chemical Physics**. 21(6): 1087-1092.
- Mi, B., Wang, J., Xiang, H., Liang, F., Yang, J., Feng, Z., . . . Fei, B. (2019). Nitrogen Self-Doped Activated Carbons Derived from Bamboo Shoots as Adsorbent for Methylene Blue Adsorption. **Molecules**. 24(16): 3012.
- Molina-Sabio, M., Gonzalez, M. T., Rodriguez-Reinoso, F., & Sepúlveda-Escribano, A. (1996). Effect of steam and carbon dioxide activation in the micropore size distribution of activated carbon. **Carbon**. 34(4): 505-509.
- Mountain, R. D., & Thirumalai, D. (1994). Quantative measure of efficiency of Monte Carlo simulations. **Physica A: Statistical Mechanics and its Applications**. 210(3): 453-460.

- Nandiyanto, A., Oktiani, R., & Ragadhita, R. (2019). How to Read and Interpret FTIR Spectroscopy of Organic Material. **Indonesian Journal of Science and Technology**. 4: 97-118.
- Ngernyen, Y., Tangsathitkulchai, C., & Tangsathitkulchai, M. (2006). Porous properties of activated carbon produced from Eucalyptus and Wattle wood by carbon dioxide activation. **Korean Journal of Chemical Engineering**. 23(6): 1046-1054.
- Pallarés, J., González-Cencerrado, A., & Arauzo, I. (2018). Production and characterization of activated carbon from barley straw by physical activation with carbon dioxide and steam. **Biomass and Bioenergy**. 115: 64-73.
- Ravikovitch, P. I., Vishnyakov, A., Russo, R., & Neimark, A. V. (2000). Unified approach to pore size characterization of microporous carbonaceous materials from N<sub>2</sub>, Ar, and CO<sub>2</sub> adsorption isotherms. **Langmuir**. 16(5): 2311-2320.
- Salame, Il, & Bandoz, T. J. (2001). Surface Chemistry of Activated Carbons: Combining the Results of Temperature-Programmed Desorption, Boehm, and Potentiometric Titrations. **J Colloid Interface Sci**. 240(1): 252-258.
- Sato, S., Yoshihara, K., Moriyama, K., Machida, M., & Tatsumoto, H. (2007). Influence of activated carbon surface acidity on adsorption of heavy metal ions and aromatics from aqueous solution. **Applied Surface Science**. 253(20): 8554-8559.
- Seung Kim, Y., & Rae Park, C. (2016). Chapter 13 - Titration Method for the Identification of Surface Functional Groups. In M. Inagaki & F. Kang (Eds.), *Materials Science and Engineering of Carbon* (pp. 273-286): Butterworth-Heinemann.
- Shahkarami, S., Dalai, A. K., Soltan, J., Hu, Y., & Wang, D. (2015). Selective CO<sub>2</sub> Capture by Activated Carbons: Evaluation of the Effects of Precursors and Pyrolysis Process. **Energy & Fuels**. 29(11): 7433-7440.
- Steele, W. A. (1978). The interaction of rare gas atoms with graphitized carbon black. **The Journal of Physical Chemistry**. 82(7): 817-821.
- Szekely, J., & Evans, J. W. (1970). A structural model for gas-solid reactions with a moving boundary. **Chemical Engineering Science**. 25(6): 1091-1107.
- Thommes, M., Kaneko, K., Neimark Alexander, V., Olivier James, P., Rodriguez-Reinoso, F., Rouquerol, J., & Sing Kenneth, S. W. (2015). Physisorption of gases, with

- special reference to the evaluation of surface area and pore size distribution (IUPAC Technical Report). In *Pure and Applied Chemistry* (Vol. 87, pp. 1051).
- Toles, C., Rimmer, S., & Hower, J. C. (1996). Production of activated carbons from a washington lignite using phosphoric acid activation. **Carbon**. 34(11): 1419-1426.
- Wang, Y., Yang, R., Li, M., & Zhao, Z. (2015). Hydrothermal preparation of highly porous carbon spheres from hemp (*Cannabis sativa* L.) stem hemicellulose for use in energy-related applications. **Industrial Crops and Products**. 65: 216-226.
- Wang, Y. X., Ngo, H. H., & Guo, W. S. (2015). Preparation of a specific bamboo based activated carbon and its application for ciprofloxacin removal. **Sci Total Environ**. 533: 32-39.
- Weerachanchai, P., Tangsathitkulchai, C., & Tangsathitkulchai, M. (2011). Characterization of products from slow pyrolysis of palm kernel cake and cassava pulp residue. **Korean Journal of Chemical Engineering**. 28(12): 2262-2274.
- Yang, H., Yan, R., Chen, H., Lee, D. H., & Zheng, C. (2007). Characteristics of hemicellulose, cellulose and lignin pyrolysis. **Fuel**. 86(12): 1781-1788.
- Zhang, Y.-J., Xing, Z.-J., Duan, Z.-K., Meng, L., & Wang, Y. (2014). Effects of steam activation on the pore structure and surface chemistry of activated carbon derived from bamboo waste. **Applied Surface Science**. 315(Supplement C): 279-286.
- Zielke, U., Hüttinger, K. J., & Hoffman, W. P. (1996). Surface-oxidized carbon fibers: I. Surface structure and chemistry. **Carbon**. 34(8): 983-998.

**CHAPTER IV**  
**PRELIMINARY STUDY ON THE FORMATION OF OXYGEN**  
**FUNCTIONAL GROUPS IN BAMBOO-BASED ACTIVATED CARBON**  
**BY AIR OXIDATION**

**Abstract**

Two prepared activated carbon samples with different porous textures derived from bamboo were used to prepare oxidized activated carbon by air oxidation in this work. The oxidation temperature was fixed at 250°C, while the oxidation times were varied from 240 to 4320 min. It was observed that the porous properties of the oxidized activated carbons increased with the increase of oxidation time. As well, the percentage of mesopores increased from 16% to 27% by volume. Boehm titration results showed that the number of acid groups in the oxidized activated carbon increased after the increase of oxidation time. These results were also confirmed by FTIR analysis. The numbers of acidic groups formed were in the following decreasing order: phenolic > carboxylic > lactonic for the activated carbon samples derived from char carbonized at 400°C for 90 min, while the samples obtained from char carbonized at 500°C for 90 min showed the following order: carboxylic > phenolic > lactonic. These differences could be attributed to the different reactivity of the original char obtained from different carbonization temperatures. However, the lactonic group was not detected in all the carbon samples.

## 4.1 Introduction

Activated carbon is a unique porous material with a large surface area, high surface heterogeneity, and a high degree of surface reactivity (Bansal *et al.*, 1988). Activated carbon structure consists of carbon basal planes and attached surface functional groups. Generally, the functional groups are located at the edge of the graphene layers (Arafat *et al.*, 1999). Ash also exists in the activated carbon, this is the inorganic residue from the production process of the activated carbon. The basal planes of activated carbon are hydrophobic in nature, while the surface functional groups are usually hydrophilic, thus enabling the activated carbon to adsorb an array of organic compounds. The textural properties of activated carbon and the concentration of surface functional groups on activated carbon, which influence the adsorption performance, depends on the starting precursors as well as the conditions (*e.g.*, physical, or chemical activation) used for the preparation.

The most important and dominant chemical structure in the activated carbon is oxygen surface groups (Bansal *et al.*, 1988). During the pyrolysis and activation process, the heteroatoms (*e.g.*, oxygen, hydrogen, chlorine, sulfur, etc.) that originally associated with the starting material have become part of the chemical structure of activated carbon, in form of surface functional groups (Bansal *et al.*, 1988). The concentration of surface functional groups could be either increase or decrease by further treatment after the activation process.

The surface of activated carbon can be modified by treatment with oxidizing agents in gas or liquid systems. The oxidizing agents in the gas phase consist of gases or vapours that mostly consist of oxygen-based, *e.g.*, O<sub>2</sub>, O<sub>3</sub>, air, and steam (Santiago *et al.*, 2005), while in the liquid phase, the examples of oxidizing agents are HNO<sub>3</sub>, H<sub>2</sub>O<sub>2</sub>, (NH<sub>4</sub>)<sub>2</sub>S<sub>2</sub>O<sub>8</sub> (Heo & Park, 2018; Tangsathitkulchai *et al.*, 2009). For the treatment in the liquid phase, the activated carbon is soaked in a solution for a required time, or it can be boiled in the oxidizing solution using a reflux method, followed by the process of washing and drying. After the treatment with oxidizing agents, the obtained oxidized activated carbon will contain both acidic and basic groups. Since the functional groups containing oxygen are polar in nature, they can efficiently attract polar fluids. Examples

are formaldehyde adsorption in the functionalized carbon slit pores (Liu, Liu, *et al.*, 2019) and water adsorption in carbon slit pores that consist of hydroxyl groups (Liu, Zeng, *et al.*, 2019). Another example is a good polar interaction between surface functional groups in the modified activated carbon and heavy metal ions such as  $\text{Cd}^{2+}$ ,  $\text{Zn}^{2+}$  (Sato *et al.*, 2007),  $\text{Pb}^{2+}$  (El-Hendawy, 2003),  $\text{Cu}^{2+}$  (Biniak *et al.*, 1999), and  $\text{Cr}^{6+}$  (Liu *et al.*, 2007).

Previous works on the oxidation of activated carbon have illustrated that the oxidation condition during treatment of activated carbon could affect the concentration of surface groups. For example, Pradhan and Sandle (Pradhan & Sandle, 1999) oxidized granular activated carbon by  $\text{HNO}_3$ ,  $\text{H}_2\text{O}_2$ , and  $(\text{NH}_4)_2\text{S}_2\text{O}_8$  and found that the activated carbon oxidized by  $\text{HNO}_3$  showed the highest concentration of acidic groups, while the activated carbon oxidized by  $\text{H}_2\text{O}_2$  gave the lowest number of acidic groups. This should arise from the fact that  $\text{HNO}_3$  is a strong acid, thus giving the highest acidic group formation in the activated carbon. Tamon and Okazaki (Tamon & Okazaki, 1996) have illustrated that the concentration of oxidizing agents could affect the amounts of surface functional groups in activated carbon. The activated carbon was oxidized by wet oxidation at different concentrations of  $\text{HNO}_3$  of 1.1, 6.6, and 13.2 N. As expected, the activated carbon that was oxidized with 13.2 N of  $\text{HNO}_3$  provided the largest amount of acidic groups. However, the BET specific area and micropore volume of this sample were lower than those of the original activated carbon. This could arise from the presence of surface functional groups that are formed at the entrance of the pores, hence resulting in micropore blocking. Also, a very high concentration of  $\text{HNO}_3$ , could destroy the porous structure of activated carbon, thus giving in low micropore volume and BET specific area. The effect of oxidation temperature was also studied and the results indicated that a higher number of acidic groups was achieved at a higher treatment temperature (Bandosz *et al.*, 1993). Lastly, the influence of oxidation time on the adsorption efficiency was investigated, where the activated carbon was treated under ozone at 10 min and 120 min, respectively. The treated sample with a longer oxidation time enhanced the adsorption of Cr(III) in an aqueous solution. This was attributed to the increase of acidic groups (mainly carboxylic group) that could attract more metallic ions in solution (Rivera-Utrilla &

Sánchez-Polo, 2003). Apart from the mentioned oxidation conditions, the origin of activated carbon and its porous properties should also influence the amount of produced surface functional groups. It should be noted that most of the oxidation methods were performed via wet oxidation, which poses a serious problem for the residual high-concentrated acid solutions. Therefore, this work is aimed to study the formation of surface groups in bamboo-based activated carbon using a more environmentally friendly method by oxidizing the carbon in the air at different oxidation times.

Consequently, this chapter reports on the formation of surface groups by studying the effects of oxidation conditions, *e.g.*, oxidation time and the type of precursors. The characterization tools used in this work were Boehm's titration to determine the number of surface groups in carbon, Fourier Transform Infrared Spectroscopy (FTIR) for qualitative characterization of surface functional groups, and the N<sub>2</sub> adsorption/desorption isotherms of the oxidized activated carbons at -196°C (77 K) to characterize the textural properties of the original activated carbons and the oxidized activated carbons.

## 4.2 Materials and Method

### 4.2.1 Raw Materials

Two samples of activated carbons were prepared from chars carbonized at 400°C and 500°C for 90 minutes, using activation temperature of 950°C and 90 min. These activated carbon samples were designated as C4 AC950-90 and C5 AC950-90.

### 4.2.2 Oxidation of Activated Carbon

About 10 grams (exact weight was recorded) of pristine activated carbon were loaded into a quartz reactor. The quartz tube reactor was then placed in a vertical ceramic tube furnace (CTF 12/75/700, Carbolite, Staffordshire, UK). The gaps between the quartz reactor and the ceramic tube furnace at the top and bottom were sealed by ceramic fibre blankets to prevent heat losses to the ambient. The experimental procedure was as follows. (1) Heating the furnace from an ambient temperature to the desired oxidation temperature at a rate of 10°C/min under the flow

of N<sub>2</sub> gas (99.995% of purity, Thai Special Gas, Rayong, Thailand) at the flowrate of 100 cm<sup>3</sup>/min; (2) once the desired final temperature was reached, N<sub>2</sub> was stopped and air (99.995% of purity, Linde Thailand, Rayong, Thailand) was allowed to flow into the quartz reactor at the same flow rate, and the final temperature was held for the desired oxidation time. (3) After that, the air valve was switched off and N<sub>2</sub> was again admitted to the reactor at the flow rate of 100 cm<sup>3</sup>/min, and then the furnace was switched off to prevent further oxidation reaction. The oxidized carbon product was allowed to cool down inside the furnace to the ambient temperature. Then it was removed and kept in a desiccator for further analysis. The oxidation temperature was kept constant at 250°C and the oxidation times used were 240, 480, 720, 1,440, 2,880, and 4,320 min. The oxidized carbon samples were designated as OACX–Y, where OAC means the oxidized activated carbon, X is the oxidation temperature and Y is the oxidation time. For example, OAC250–240 indicates that this product was oxidized by air at 250°C for 240 min. The description for each tested sample is shown in *Table 4.1*. It should be noted why the oxidation temperature was fixed at 250°C here. The oxidations were tested at 260 and 275°C before, these oxidation temperatures caused the combustion of activated carbon in the reactor, giving ash in the final product. Thus, the oxidation temperature was fixed at 250°C in this work in order to avoid the fast combustion reactions.

**Table 4.1** Activated carbons used in this work.

Sample	Description
C400-90	Char carbonized at 400°C for 90 min.
C500-90	Char carbonized at 500°C for 90 min.
C4 AC950-90	Activated carbon was obtained at an activation temperature of 950°C for 90 min, derived from char C400-90.
C5 AC950-90	Activated carbon was obtained at an activation temperature of 950°C for 90 min, derived from char C500-90.
C4 OAC250-240	Oxidized activated carbon at 250°C for 240 min under air, derived from activated carbon sample AC950-90 and carbonized char sample C400-90. The oxidation times were 240, 480, 720, 1440, 2880, and 4320 min, respectively.
C5 OAC250-240	Oxidized activated carbon at 250°C for 240 min under air, derived from activated carbon sample AC950-90 and carbonized char sample C500-90. The oxidation times were 240, 480, 720, 1440, 2880, and 4320 min, respectively.

### 4.2.3 Characterization of Products

#### 4.2.3.1 Porous Properties of Activated Carbon

The obtained OAC samples were determined for their porous properties using N<sub>2</sub> adsorption/desorption isotherms measured at -196°C by a high-performance adsorption analyzer (ASAP 2020 Plus, Micromeritics, Norcross, Georgia, USA). First, the OAC sample was degassed at 300°C at a vacuum pressure of 10 µmHg for 12 hrs to remove any remaining contaminants in the sample. Then the sample was analyzed by collecting N<sub>2</sub> (99.9999% of purity, Linde Thailand, Rayong, Thailand) adsorption/desorption isotherms as a function of pressure up to 760 mmHg. The

obtained isotherms data were analyzed for BET specific area ( $S_{BET}$ ) using Brunauer-Emmett-Teller theory (Brunauer *et al.*, 1938). The total pore volume ( $V_{tot}$ ) was calculated from the adsorbed amount of  $N_2$  at the relative pressure ( $P/P_0$ ) of 0.98 and converted it to the volume of  $N_2$  in the liquid state at the adsorbed temperature. The Dubinin-Radushkevich (DR) equation (Dubinin, 1975) was employed to determine the micropore volume ( $V_{mic}$ ), while the volume of mesopore was determined by subtracting the micropore volume from the total pore volume. Finally, the average pore diameter ( $D_{avg}$ ) was calculated by the equation  $4V_{tot}/S_{BET}$ , assuming cylindrical pore shape.

#### 4.2.3.2 Determination of Surface Chemistry

Boehm titration (Boehm, 1994) was employed to study the surface chemistry of the OAC products. It was performed by the following steps: (1) About 4 grams of OAC was crushed in a mortar, then it was sieved using sieve number 20-mesh (850  $\mu\text{m}$ ), and the undersize particles ( $<850 \mu\text{m}$ ) was collected and loaded into four conical flasks for about 1 gram each (exact weight was recorded); (2) flasks number 1 and 2 were loaded with 50  $\text{cm}^3$  of 0.1 M NaOH and 0.1 M HCl, while flasks number 3 and 4 were filled with 0.05 M  $\text{Na}_2\text{CO}_3$  and 0.1 M  $\text{NaHCO}_3$ ; (3) all four flasks were sealed and shaken at 150 rpm for 24 hrs at the ambient temperature; (4) flasks number 1 and 2 were filtered using a filter paper to separate the solid carbon from solutions, then 10  $\text{cm}^3$  of the filtered solutions were titrated with 0.1 M HCl and 0.1 M NaOH to determine total acidic groups and total basic groups. (5) Flasks number 3 and 4 were filtered, pipetted, and back titrated to determine the total of carboxylic and lactonic groups (flask number 3), while flask number 4 was used to determine the carboxylic group only. The amount of surface groups on OAC samples can then be calculated and presented in the unit of mmol of surface groups per gram of carbon.

#### 4.2.3.3 FTIR Spectra

The Fourier Transform Infrared Spectroscopy (FTIR) was employed to identify the type of surface functional groups on the pristine activated carbons and OAC samples. About 0.025 grams of activated carbon were placed on a sample holder of a FTIR spectra (Vertex 70 FT-IR, Bruker, Billerica, MA, USA), using the

attenuated total reflection (ATR) method. This method allows a direct measurement of surface functional groups on the surface of samples by FTIR. The IR spectra were collected in the mid-IR spectrum, ranging from 400 to 4000  $\text{cm}^{-1}$  with the scan resolution of 4  $\text{cm}^{-1}$ , with each run containing 64 scans.

## 4.3 Results and Discussion

### 4.3.1 Amount of Surface Groups

#### 4.3.1.1 Boehm's Titration

The carbonized chars were activated under  $\text{CO}_2$  at 950°C for 90 min, giving two sample of activated carbons, C4 AC950-90 and C5 AC950-90. The amount of surface functional groups on these two samples are shown in *Figure 4.1* and *Table 4.2*. These two samples of original activated carbon show low amount of acidic surface groups as compared to the original chars (see *Table 4.2*). This is because at high activation temperature and long activation time, the thermal process disrupts the bonds between surface functional groups and carbon layers. While the amount of basic groups are relatively high, it should be reminded that the  $\text{O}_2$  in  $\text{CO}_2$  during the activation process and nitrogen containing groups in the original char can cause the basicity in activated carbon (Shafeeyan *et al.*, 2010).

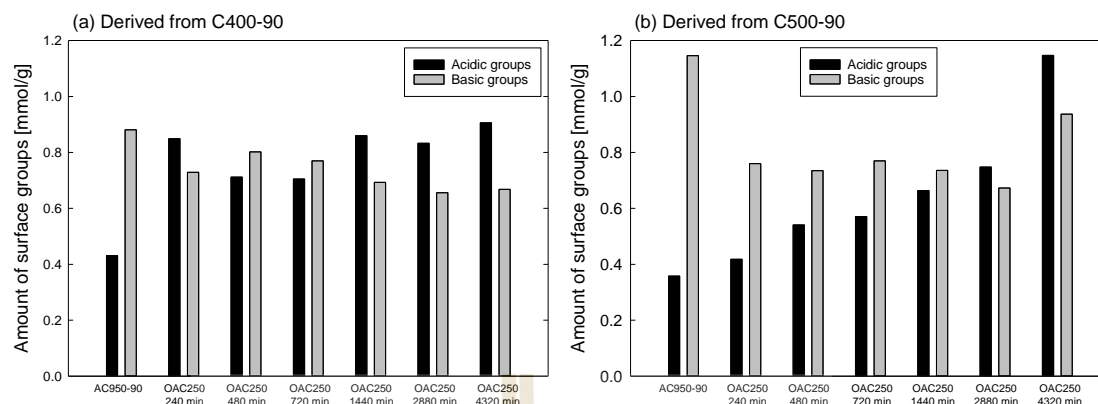


**Figure 4.1** The effects of oxidation time on amount of surface functional groups. (a) samples were derived from char carbonized at 400°C for 90 min and (b) samples were derived from char carbonized at 500°C for 90 min.

Now we turn into the gas phase oxidation of activated carbons using air. The results are present in bar graph in *Figure 4.1*. These appear a tendency for the total amount of acidic groups to increase with the increase in the oxidation time, especially for the sample derived from char carbonized at 500°C for 90 min (see *Figure 4.1b*). Longer reaction time should increase the probability for successful reaction between  $O_2$  and heteroatoms on the carbon surfaces. On the other hand, the amount of basic groups seemed to decrease when the oxidation time was increased, although the affect was not so pronounced for carbonized char at 500°C for 90 min. It should be noted that some of the oxygen-containing groups could act as basic sites, or some of the basic sites could be oxygen-free type (Contescu *et al.*, 1998; Moreno-Castilla *et al.*, 2000). Therefore, the amount of basic groups could be influenced by the electron donor/acceptor of acidic groups (Tangsathitkulchai *et al.*, 2009). Thus, the present of surface basicity in the OAC samples is not only from the basic groups in the sample, but probably from the oxygen-containing groups as well. This is supported by the total amount of surface functional groups present in *Figure 4.2*, showing that the amount of surface groups increased with the increase of oxidation time.

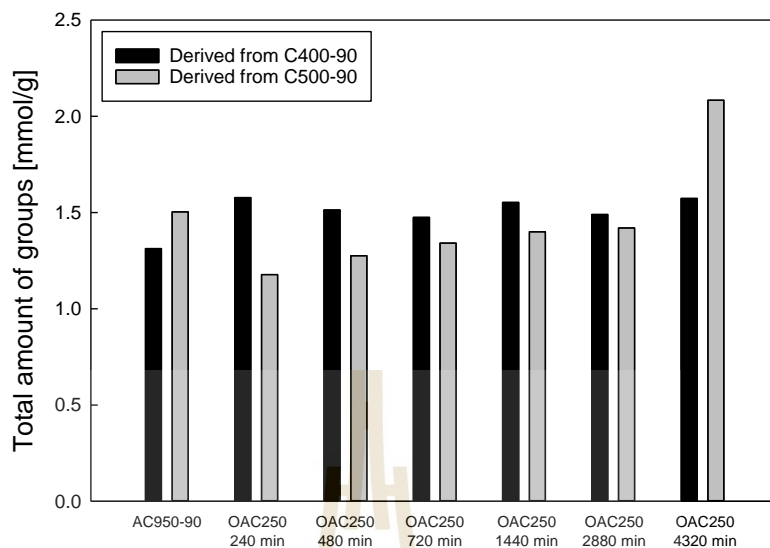


**Figure 4.2** The effect of oxidation time on the total amount of surface functional groups.

Figure 4.2 show the effect of carbonization temperature on the total amount of oxygen functional groups. It appeared that higher carbonization temperature gave higher amount of oxygen surface groups. However, the difference became less as the oxidation time increased. The difference could result from the difference in the number of active sites for air oxidation. According to the results, it could be deduced that char prepared at a higher temperature of 500°C could have a larger number of active sites than that of char prepared at 400°C.

Another hypothesis that could explain the gas phase oxidation using air can be drawn here. The oxidation process of carbon and air is intensely dependent on diffusion of  $O_2$  into the interconnected pores. In 1956 Puri and his co-worker (Puri *et al.*, 1956) studied the creation of oxygen complex groups on several charcoal samples. They found that if the pure oxygen was used to oxidize the samples, the process is very fast, and it can be completed in less than 12 hrs. While using air (21% of  $O_2$  and 79% of  $N_2$ ), it could take up to 3 months to complete the process. Moreover, the oxygen containing groups in activated carbon can be destroyed as well under the atmosphere of inert gas (Laine *et al.*, 1963), which is  $N_2$  in this case, although at the low oxidation temperature of 250°C. This results in the creation and destruction

of the surface groups at the same time during the oxidation process. It should be noted that even under the oxidation process using air at a low temperature, some of the carbons could be consumed by slow combustion process that could affect the amount of surface groups as well as the porous properties of carbons.

**Table 4.2** The amount of surface groups in pristine activated carbons and the oxidized activated carbons.

Sample	Carboxylic (mmol/g)	Lactonic (mmol/g)	Phenolic (mmol/g)	Total acidic groups (mmol/g)	Total basic groups (mmol/g)	Total groups (mmol/g)
Derived from char C400-90						
C400-90	0.372	0.000	0.395	0.768	0.205	0.973
C4 AC950-90	0.479	0.000	0.000	0.431	0.881	1.313
OAC250-240	0.266	0.000	0.583	0.849	0.729	1.578
OAC250-480	0.338	0.000	0.374	0.712	0.802	1.514
OAC250-720	0.352	0.000	0.353	0.705	0.770	1.475
OAC250-1440	0.373	0.000	0.487	0.860	0.693	1.553
OAC250-2880	0.346	0.000	0.487	0.833	0.656	1.490
OAC250-4320	0.336	0.000	0.570	0.906	0.668	1.574
Derived from char C500-90						
C500-90	0.436	0.000	0.112	0.548	0.383	0.931
C5 AC950-90	0.358	0.000	0.000	0.358	1.146	1.504
OAC250-240	0.418	0.000	0.000	0.418	0.760	1.178
OAC250-480	0.490	0.000	0.051	0.541	0.735	1.276
OAC250-720	0.507	0.000	0.064	0.571	0.770	1.342
OAC250-1440	0.477	0.000	0.187	0.664	0.736	1.400
OAC250-2880	0.490	0.000	0.258	0.748	0.673	1.420
OAC250-4320	N/A	N/A	N/A	1.147	0.937	2.084

Comparing gas-phase and liquid-phase oxidation, Ngernyen reported that wet oxidation of eucalyptus-based activated carbon in  $H_2O_2$  or  $HNO_3$  gave higher amount of oxygen functional groups about 200% higher than the oxidation in air (Ngernyen, 2007). However, for the gas phase oxidation, the process is cleaner, simple to handle, and no need to deal with the remaining oxidizing agent, although the yield of functional groups formation is lower by almost two-fold.

Lastly, it was discovered that the acidic lactonic groups were not detected for all carbon samples, including the char products. This could be related

to the difference of chemical composition and structure of bamboo used in this work. Another likely reason is that lactonic group is thermally desorbed at a relatively low temperature, between 130 to 630°C (Marchon *et al.*, 1988). It is therefore likely that the lactonic groups formed, if any, could have been destroyed during the carbonization process at 400 or 500°C.

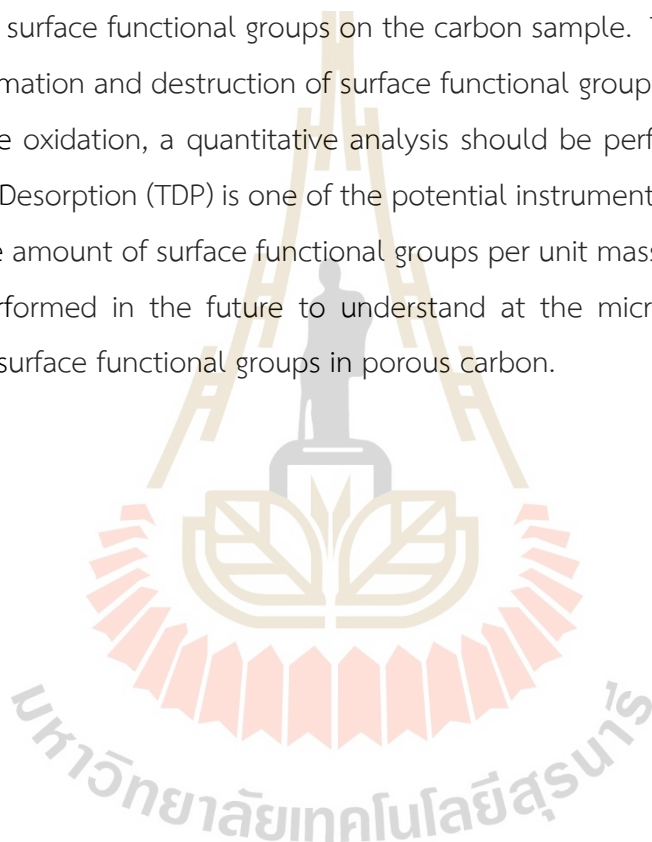
#### 4.3.1.2 FTIR Studies

The chemical structure of pristine activated carbon and the oxidized activated carbon samples can be qualitatively studied using the information of FTIR. The typical FTIR results of pristine AC and OAC samples are shown in *Figure 4.3*. The aromatic rings were indicated by the intense band at about 1590  $\text{cm}^{-1}$ , and this is generally found in the carbonaceous materials that are derived from biomass. However, the intensity of this band decreased in the activated carbon (C4 AC950-90) as compared with char (C400-90). This indicates that some of the aromatic rings were destroyed during the activation step under a high temperature. The band at about 1430  $\text{cm}^{-1}$  implies that the samples consist of nitrate, carboxyl, and carboxylate groups. This is consistent with the finding of the carboxylic group by Boehm's titration. Next, the band located at 1170  $\text{cm}^{-1}$  can be assigned to the existing phenol and aromatic ring of ether (Zhang *et al.*, 2014). In addition, the strong band at about 1080  $\text{cm}^{-1}$  are observed for all samples, this band indicates the C-O stretching vibration of the primary alcohols (Coates, 2006).

Apart from the typical surface functional that was found in the early discussion, we now turn into the discussion of not so common compounds in the activated carbon as shown in *Figure 4.3b*. The strong band at about 2100  $\text{cm}^{-1}$  is assigned to the triple-bonded between carbon and carbon of the acetylenic compounds. Typically, the nitrogen compounds show an intense absorption band at about 2280 to 2200  $\text{cm}^{-1}$  which is consistent with the finding in *Figure 4.3b*. So, the band at about 2280  $\text{cm}^{-1}$  can be assigned to the formation of cyanide and nitrile compounds. Perhaps the nitrogen from the bamboo precursor and in the gas phase oxidation could affect the concentration of nitrogen functional groups in the samples. This is confirmed by the weight fraction of nitrogen contents from the elemental

analysis of the bamboo precursor, as shown in *Table 3.1* (see Chapter III). Lastly, the small band at about  $3650\text{ cm}^{-1}$  implies that there is an O-H stretching vibration of phenol groups in the sample. It is supported by the band at  $1170\text{ cm}^{-1}$  as mentioned earlier. *Figure 4.3c* shows FTIR spectra of the samples derived from char C500-90. Most of the results are similar to the samples derived from char C400-90.

It should be noted that FTIR spectra only give the qualitative results of the surface functional groups on the carbon sample. To investigate in more detail the formation and destruction of surface functional groups during the activation and gas-phase oxidation, a quantitative analysis should be performed. Temperature Programmed Desorption (TDP) is one of the potential instruments that can provide the change of the amount of surface functional groups per unit mass of the samples. This could be performed in the future to understand at the microscopic scale for the formation of surface functional groups in porous carbon.



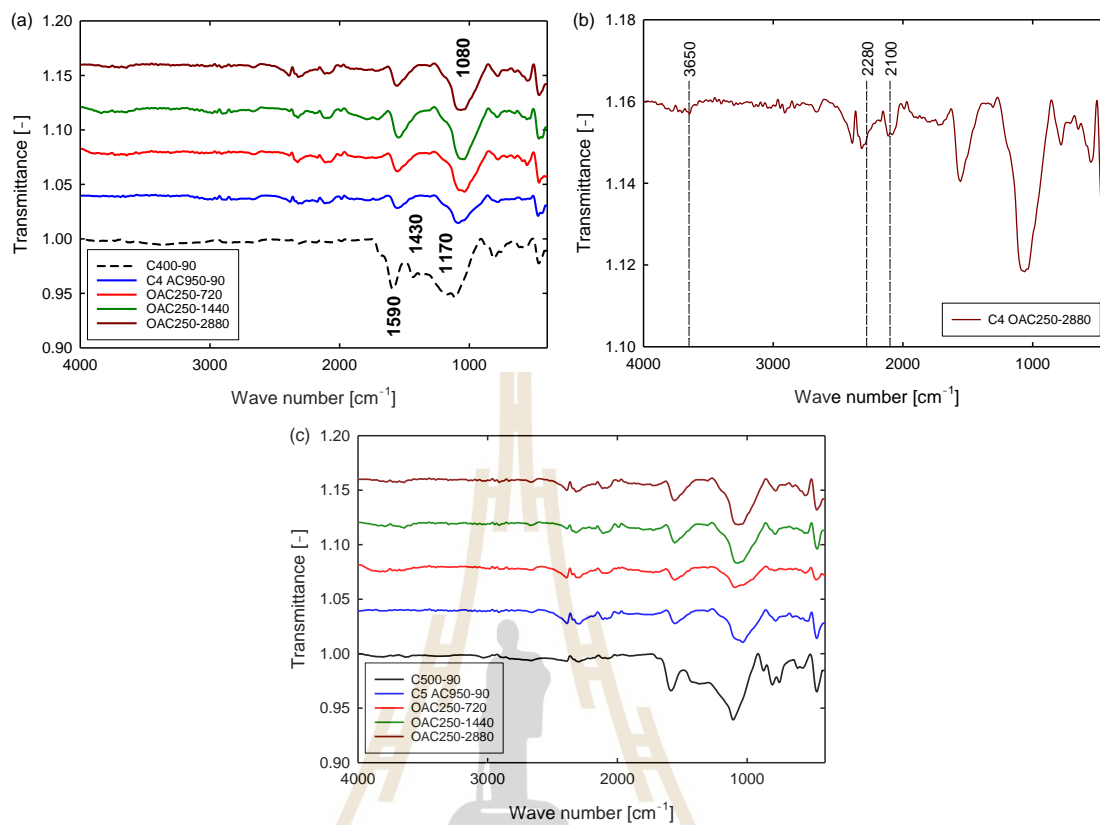


**Figure 4.3** FTIR spectra of the chars, pristine AC, and OAC samples. (a) The plots show the samples that derived from char C400-90, (b) the OAC sample oxidized at 2880 min and derived from char C400-90, and (c) the samples that derived from char C500-90.

### 4.3.2 Textural Properties of the Activated Carbon

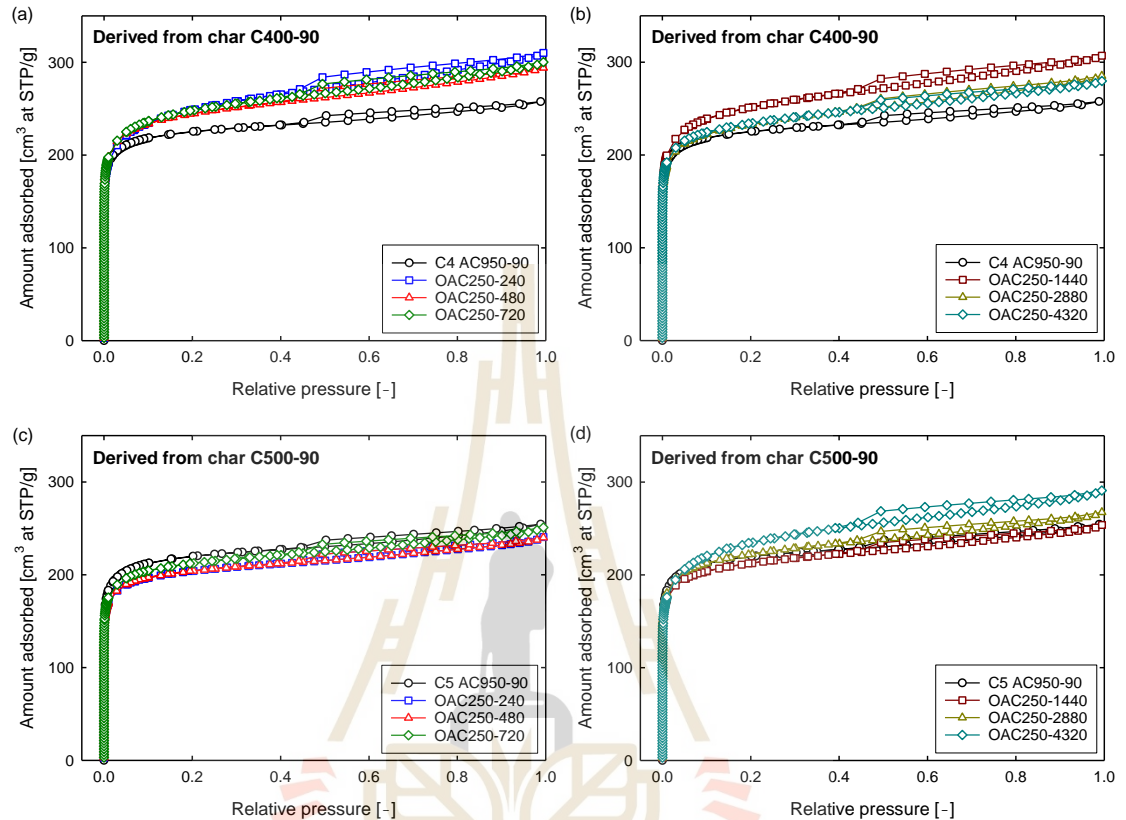


**Figure 4.4** Effects of air oxidation in activated carbon on  $N_2$  adsorption/desorption isotherms. (a) and (b) The OAC samples derived from char C400-90 while (c) and (d) derived from char C500-90.

The  $N_2$  adsorption/desorption isotherms at  $-196^\circ\text{C}$  for the original activated carbons and the oxidized activated carbons are presented in *Figure 4.4*. It is observed that the shape of isotherms of all activated carbons showed a rapid increase of  $N_2$  adsorption at low pressure over a narrow range, followed by a gradually continuous increase at high pressures. These characteristic curves indicate that the activated carbons contain mostly micropores with some mesopores. It can be said that the isotherms show the adsorption behaviour between Type I and Type II, according to the IUPAC classification (Thommes *et al.*, 2015).

Since the effect of oxidation time on the  $N_2$  isotherms is difficult to perceive, it was decided to present the results in term of the amount adsorbed at one selected relative pressure ( $P/P_0$ ) of 0.30, as shown in *Figure 4.5*. It is clear that the oxidation time and type of original activated carbons had a definite effect on the amount of  $N_2$  adsorbed. For activated carbon series prepared from carbonized char at 400°C and 90 min, all oxidized samples gave higher amounts of  $N_2$  adsorbed than that of the non-oxidized sample, on the average by about 15%. This seems to indicate a corresponding change in the porous properties of the carbon samples due to the effect of oxidation time. There was almost no significant change in the amount adsorbed for the increase of oxidation time from 240 to 1440 min. However, for the increasing the oxidation time from 1440 to 4320 min, a drop in the amount of  $N_2$  adsorbed is clearly seen.

On the other hand, the behaviour of  $N_2$  adsorption for the oxidized carbon samples prepared from carbonized char at 500°C and 90 min appears to be different. Overall, the amounts of  $N_2$  adsorbed of the oxidized samples were lower than that of the original carbon, except for the sample oxidized at the longest period of 4320 min. Among the oxidized samples, it is obvious that increasing oxidation time from 240 to 4320 min increased the amount adsorbed.

From these results, it is noted that even at a relatively low oxidation temperature of 250°C, oxidation time could affect, to a certain extent, the adsorption behaviour of  $N_2$  probe molecules, and hence the carbon porous properties.

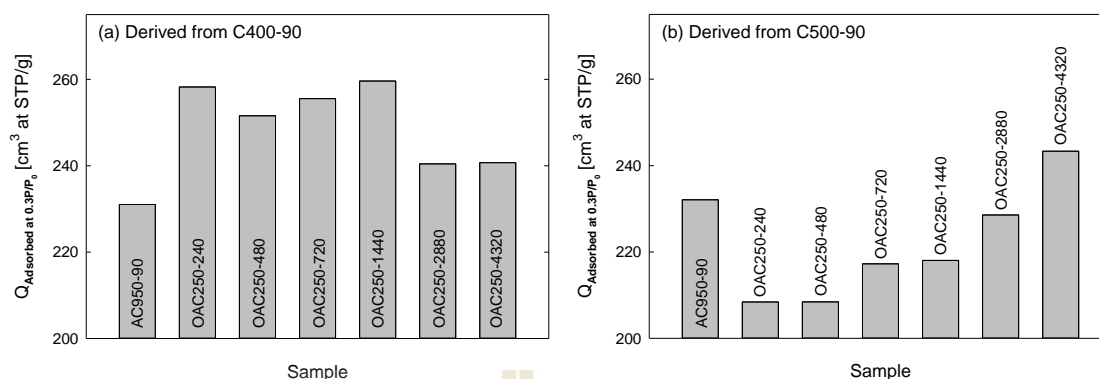


**Figure 4.5** The amount of  $N_2$  adsorption in carbon samples at the relative pressure of 0.3 for original activated carbons and the oxidized activated carbons. (a) Samples were derived from char carbonized at  $400^\circ\text{C}$  for 90 min and (b) samples were derived from char carbonized at  $500^\circ\text{C}$  for 90 min. The effects of oxidation time are presented.

**Table 4.3** Porous properties of pristine activated carbons and the oxidized samples.

Sample	$S_{BET}$ ( $\text{m}^2/\text{g}$ )	$V_{tot}$ ( $\text{cm}^3/\text{g}$ )	$V_{mic}$ ( $\text{cm}^3/\text{g}$ )	$V_{mes}$ ( $\text{cm}^3/\text{g}$ )	Micropore (%)	Mesopore (%)	$D_{avg}$ (nm)
Derived from C400-90							
AC950-90	810	0.399	0.352	0.046	88.4	11.6	1.968
OAC250-240	889	0.475	0.358	0.117	75.3	24.7	2.137
OAC250-480	870	0.451	0.353	0.098	78.3	21.7	2.073
OAC250-720	884	0.460	0.365	0.096	79.2	20.8	2.324
OAC250-1440	895	0.471	0.358	0.113	76.0	24.0	2.105
OAC250-2880	830	0.437	0.346	0.091	79.3	20.7	2.347
OAC250-4320	832	0.429	0.340	0.089	79.2	20.8	2.065
Derived from C500-90							
AC950-90	786	0.394	0.339	0.054	86.2	13.8	2.003
OAC250-240	725	0.368	0.309	0.059	84.0	16.0	2.280
OAC250-480	725	0.367	0.299	0.068	81.5	18.5	2.027
OAC250-720	756	0.388	0.318	0.070	81.9	18.1	2.302
OAC250-1440	756	0.384	0.307	0.077	80.1	19.9	2.031
OAC250-2880	790	0.409	0.329	0.080	80.4	19.6	2.310
OAC250-4320	841	0.440	0.320	0.120	72.8	27.2	2.093

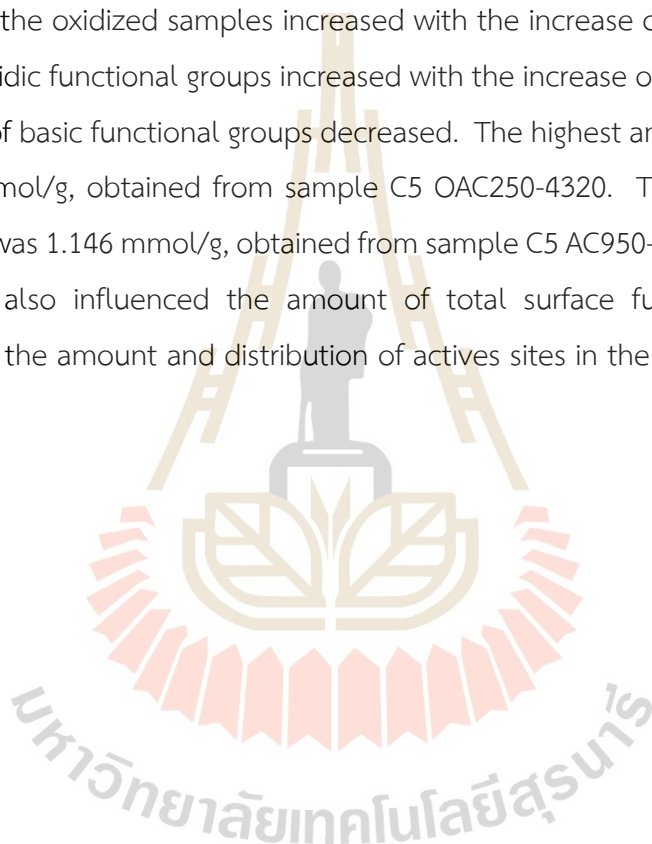
Table 4.3 summarizes the porous properties of two types of treated activated carbons. The activated carbon produced from carbonized char at  $400^\circ\text{C}$  and 90 min is highly microporous (88.4% micropores and 11.6% mesopores, by volume).

When it is oxidized with air, all porous properties ( $S_{BET}$ ,  $V_{tot}$ ,  $V_{mic}$ , and  $V_{mes}$ ) increased but not so pronounced. It is likely that apart from the formation of functional groups during the oxidation process, some of carbon atoms are probably consumed via the slow combustion with oxygen, hence giving increasing porous properties. Increasing oxidation time from 240 to 1440 min had virtually no effect on all porous properties. Nevertheless, on increasing the time from 1440 to 4320 min, the porous properties decreased. One possible explanation to this behaviour is that longer oxidation time could allow pore enlargement by the combustion, producing a larger average pore size.

For activated carbon produced from carbonized char at 500°C and 90 min, the opposite results were observed as compared to the case of carbonized char at 400°C and 90 min. Porous properties of oxidized carbons were lower than that of the original carbon (AC950-90), except for the carbon sample oxidized for the longest time of 4320 min. As to the effect of oxidation time, there was a general tendency for the porous properties to slow increase when the oxidation time increased from 240 to 1440 min and significantly increase from 1440 to 4320 min. There is no sound explanation for these results, but it is probable that the resulting char structure after the carbonization process could affect the reactivity and distribution of active sites available for the subsequent oxidation reaction.

#### 4.4 Conclusions

Bamboo-based activated carbons were modified by air oxidation. The effect of oxidation time in the reactor and the type of original activated carbon samples were investigated. The textural properties of the oxidized samples are mostly unchanged, the BET specific area of the oxidized samples only changes in the range of less than 100 m<sup>2</sup>/g as compared to the original activated carbons. However, the percentage of mesopore of the oxidized samples increased with the increase of oxidation time. The amount of acidic functional groups increased with the increase of oxidation time, while the amount of basic functional groups decreased. The highest amount of acidic groups was 1.147 mmol/g, obtained from sample C5 OAC250-4320. The highest amount of basic groups was 1.146 mmol/g, obtained from sample C5 AC950-90. The carbonization temperature also influenced the amount of total surface functional groups, due principally to the amount and distribution of active sites in the original chars.



## 4.5 References

- Arafat, H. A., Franz, M., & Pinto, N. G. (1999). Effect of Salt on the Mechanism of Adsorption of Aromatics on Activated Carbon. *Langmuir*. 15(18): 5997-6003.
- Bandosz, T. J., Jagiello, J., & Schwarz, J. A. (1993). Effect of surface chemical groups on energetic heterogeneity of activated carbons. *Langmuir*. 9(10): 2518-2522.
- Bansal, R. C., Donnet, J. B., & Stoeckli, F. (1988). *Active Carbon*. New York City, New York: Marcel Dekker.
- Biniak, S., Pakuła, M., Szymański, G. S., & Świątkowski, A. (1999). Effect of Activated Carbon Surface Oxygen- and/or Nitrogen-Containing Groups on Adsorption of Copper(II) Ions from Aqueous Solution. *Langmuir*. 15(18): 6117-6122.
- Boehm, H. P. (1994). Some aspects of the surface chemistry of carbon blacks and other carbons. *Carbon*. 32(5): 759-769.
- Brunauer, S., Emmett, P. H., & Teller, E. (1938). Adsorption of Gases in Multimolecular Layers. *Journal of the American Chemical Society*. 60(2): 309-319.
- Coates, J. (2006). Interpretation of Infrared Spectra, A Practical Approach. In *Encyclopedia of Analytical Chemistry*: John Wiley & Sons.
- Contescu, A., Vass, M., Contescu, C., Putyera, K., & Schwarz, J. A. (1998). Acid buffering capacity of basic carbons revealed by their continuous pK distribution. *Carbon*. 36(3): 247-258.
- Dubinin, M. M. (1975). Physical Adsorption of Gases and Vapors in Micropores. In D. A. Cadenhead, J. F. Danielli, & M. D. Rosenberg (Eds.), *Progress in Surface and Membrane Science* (Vol. 9, pp. 1-70): Elsevier.
- El-Hendawy, A.-N. A. (2003). Influence of HNO<sub>3</sub> oxidation on the structure and adsorptive properties of corncob-based activated carbon. *Carbon*. 41(4): 713-722.
- Heo, Y.-J., & Park, S.-J. (2018). H<sub>2</sub>O<sub>2</sub>/steam activation as an eco-friendly and efficient top-down approach to enhancing porosity on carbonaceous materials: the effect of inevitable oxygen functionalities on CO<sub>2</sub> capture. *Green Chemistry*. 20(22): 5224-5234.

- Laine, N. R., Vastola, F. J., & Walker, P. L. (1963). THE IMPORTANCE OF ACTIVE SURFACE AREA IN THE CARBON-OXYGEN REACTION<sup>1,2</sup>. **The Journal of Physical Chemistry**. 67(10): 2030-2034.
- Liu, L., Liu, J., Zeng, Y., Tan, S. J., Do, D. D., & Nicholson, D. (2019). Formaldehyde adsorption in carbon nanopores – New insights from molecular simulation. **Chemical Engineering Journal**. 370: 866-874.
- Liu, L., Zeng, Y., Tan, S. J., Xu, H., Do, D. D., Nicholson, D., & Liu, J. (2019). On the mechanism of water adsorption in carbon micropores – A molecular simulation study. **Chemical Engineering Journal**. 357: 358-366.
- Liu, S. X., Chen, X., Chen, X. Y., Liu, Z. F., & Wang, H. L. (2007). Activated carbon with excellent chromium(VI) adsorption performance prepared by acid–base surface modification. **Journal of Hazardous Materials**. 141(1): 315-319.
- Marchon, B., Carrazza, J., Heinemann, H., & Somorjai, G. A. (1988). TPD and XPS studies of O<sub>2</sub>, CO<sub>2</sub>, and H<sub>2</sub>O adsorption on clean polycrystalline graphite. **Carbon**. 26(4): 507-514.
- Moreno-Castilla, C., López-Ramón, M. V., & Carrasco-Marín, F. (2000). Changes in surface chemistry of activated carbons by wet oxidation. **Carbon**. 38(14): 1995-2001.
- Ngernyen, Y. (2007). **Wood-Based Activated Carbon: Preparation, Surface Modification, and Adsorption Study**. Doctor of Philosophy. Suranaree University of Technology, Nakhon Ratchasima.
- Pradhan, B. K., & Sandle, N. K. (1999). Effect of different oxidizing agent treatments on the surface properties of activated carbons. **Carbon**. 37(8): 1323-1332.
- Puri, B. R., Myer, Y. P., & Sharma, L. R. (1956). Formation of oxygen complex on charcoal. **Journal of the Indian Chemical Society**. 33: 781.
- Rivera-Utrilla, J., & Sánchez-Polo, M. (2003). Adsorption of Cr(III) on ozonised activated carbon. Importance of  $\pi$ -cation interactions. **Water Research**. 37(14): 3335-3340.
- Santiago, M., Stüber, F., Fortuny, A., Fabregat, A., & Font, J. (2005). Modified activated carbons for catalytic wet air oxidation of phenol. **Carbon**. 43(10): 2134-2145.
- Sato, S., Yoshihara, K., Moriyama, K., Machida, M., & Tatsumoto, H. (2007). Influence of activated carbon surface acidity on adsorption of heavy metal ions and

- aromatics from aqueous solution. **Applied Surface Science**. 253(20): 8554-8559.
- Shafeeyan, M. S., Daud, W. M. A. W., Houshmand, A., & Shamiri, A. (2010). A review on surface modification of activated carbon for carbon dioxide adsorption. **Journal of Analytical and Applied Pyrolysis**. 89(2): 143-151.
- Tamon, H., & Okazaki, M. (1996). Influence of acidic surface oxides of activated carbon on gas adsorption characteristics. **Carbon**. 34(6): 741-746.
- Tangsathitkulchai, C., Ngernyen, Y., & Tangsathitkulchai, M. (2009). Surface modification and adsorption of eucalyptus wood-based activated carbons: Effects of oxidation treatment, carbon porous structure and activation method. **Korean Journal of Chemical Engineering**. 26(5): 1341-1352.
- Thommes, M., Kaneko, K., Neimark Alexander, V., Olivier James, P., Rodriguez-Reinoso, F., Rouquerol, J., & Sing Kenneth, S. W. (2015). Physisorption of gases, with special reference to the evaluation of surface area and pore size distribution (IUPAC Technical Report). In *Pure and Applied Chemistry* (Vol. 87, pp. 1051).
- Zhang, Y.-J., Xing, Z.-J., Duan, Z.-K., Meng, L., & Wang, Y. (2014). Effects of steam activation on the pore structure and surface chemistry of activated carbon derived from bamboo waste. **Applied Surface Science**. 315(Supplement C): 279-286.

## CHAPTER V

### WETTING TRANSITION OF ETHYLENE ON A PLANAR SUBSTRATE

#### Abstract

Two potential models of ethylene molecule with and without the quadrupole moment were employed to study the importance of partial charges in the ethylene molecule for their performance in describing the experimental data for vapour-liquid equilibria (VLE) and the adsorption isotherms. The potential model that consists of partial charges shows a good agreement with the vapour-liquid equilibria and the adsorption of ethylene on a graphite substrate. Then, this model was further applied to construct the parametric map of wetting of ethylene on planar substrates as a function of wetting temperature and substrate affinity. The presence of ethylene in the adsorbed phase presents three wetting zones on the wetting map, non-wetting, incomplete wetting, and complete wetting. The wetting modes of ethylene with different adsorption energies are governed by the temperature, adsorbate-adsorbate interactions, and isosteric heat at zero loading.

มหาวิทยาลัยเทคโนโลยีสุรนารี

## 5.1 Introduction

The adsorption of fluid on a substrate is one of the most common choices to separate valuable gases or liquids from the bulk stream in the industries because the operation is simple to handle and spends less power consumption. The examples of adsorption in the industries are separation of nitrogen from the air, dehydration of gaseous mixtures (Dabrowski, 2001) by a pressure swing adsorption, and recovery of ethylene from the ethylene/ethane mixture by a modified activated carbon (Zhou *et al.*, 2016). Generally, the significant parameters that should be considered in the adsorption process are solid substrate (*i.e.*, adsorbent), fluid (*i.e.*, adsorbate), temperature, and pressure. Since the adsorption behaviour of the concerning fluid depends on the mentioned parameters, it is important to choose the right conditions (*i.e.*, temperature and pressure) and a proper substrate (*i.e.*, the surface affinity of the adsorbent) that can adsorb the highest amount of the selected fluid on a substrate.

Adsorption of gases and vapours on graphitized thermal carbon black (GTCB) has been studied by a number of investigators both experimentally (Bär *et al.*, 1997; Beebe *et al.*, 1964; McDermot & Lawton, 1959; Millot, 1979) and theoretically (Do & Do, 2004, 2006; Hermosilla & Albesa, 2020; Sellers & Errington, 2008). To understand the physics of adsorption on GTCB, noble gases are usually employed as the adsorbates (De Boer *et al.*, 1972; Michels *et al.*, 1949) because of the fact that the operation is uncomplicated, the adsorbate is easy to handle, and is less harmful to human. The study also included the computer simulation using noble gases (Herrera *et al.*, 2021; Loi *et al.*, 2020; Luisa Prasetyo, Quang K. Loi, *et al.*, 2018).

Apart from using noble gases as the test molecules, physisorption of several different linear molecular fluids on a graphite substrate has been reported, *e.g.*, CO<sub>2</sub> (Deitz, 1967), N<sub>2</sub>O, C<sub>2</sub>N (Terlain & Larher, 1983), and N<sub>2</sub> (Grillet *et al.*, 1979; Volkmann & Knorr, 1991). Ethylene (C<sub>2</sub>H<sub>4</sub>) is also one of the linear molecules which consists of quadrupole moment (Borkman & Settle, 1971; Buckingham *et al.*, 1968). The physisorption of ethylene on graphite and activated carbon has also been studied experimentally (Hoory & Prausnitz, 1967; Menaucourt *et al.*, 1977; Reich *et al.*, 1980;

Specovius & Findenegg, 1980; Sutton *et al.*, 1983) using different techniques to describe its adsorption behaviour on the planar substrate.

Over the past few decades, the wetting/non-wetting behaviour of adsorbate on a substrate has been extensively studied (Bienfait, 1985; Bojan *et al.*, 1999; Cahn, 1977; Larese *et al.*, 1997; Nham & Hess, 1989; Yao & Ohmasa, 2001; Youn & Hess, 1990). Understanding this fundamental phenomenon can lead us to the development of an adsorbent that can be utilized effectively for the adsorption of the concerning fluid. Typically, in adsorption science, the wetting/non-wetting behaviour of fluid on a planar substrate can also be determined using adsorption isotherms as mentioned in Chapter II. There are comprehensive reviews of wetting behaviour of fluid on a solid substrate by Steele (Steele, 2008), Gatica and Cole (Gatica & Cole, 2009), and Saam (Saam, 2009) for the reader's interest. Generally, in adsorption science the wetting/non-wetting behaviour is dominated by adsorbate-adsorbate interactions (FF), adsorbent-adsorbate interactions (SF), and temperature of the system (de Gennes, 1985; Ulbricht *et al.*, 2006).

In 1977, Menaucourt, Thomy, and Duval (Menaucourt *et al.*, 1977) reported the adsorption isotherms of ethylene on graphite from 77 K to 105 K (bulk triple point temperature of ethylene is 104 K). The transition of isotherms from incomplete wetting to complete wetting can be observed, but the microscopic behaviour of adsorption during that transition cannot be determined. Specovius and Findenegg (Specovius & Findenegg, 1980) studied the ethylene adsorption on a graphite from the ambient temperature to the bulk critical temperature of ethylene and found that the complete wetting isotherm can be observed at the ambient temperature. While at the bulk critical temperatures, the surface excess decreases very sharply, due to a significant change of bulk gas density over a small change in pressure. Details of supercritical adsorption isotherms have been studied by Do and Do (Do & Do, 2005). Then in 1983, Sutton, Mochrie, and Birgeneau (Sutton *et al.*, 1983) performed the experiment of ethylene adsorption on graphite at several temperatures and used X-Ray diffraction to observe the layer-by-layer wetting. They reported the wetting temperature for each layer and discovered that the results are consistent with Specovius and Findenegg

(Specovius & Findenegg, 1980). Drir and co-workers (Drir *et al.*, 1986) reported the adsorption isotherm of ethylene on highly oriented pyrolytic graphite (HOPG) at different temperatures. The transition from partial wetting to complete wetting was observed, but they did not mention the roughening temperature (the roughening temperature,  $T_R$ , is the temperature that demarcates between incomplete wetting and complete wetting). Although the adsorption and wetting of ethylene on graphite have been widely studied, the physics and microscopic behaviour of ethylene in the adsorbed phase behind this phenomenon has not been examined thoroughly. It is therefore the purpose of the present work to study the microscopic mechanism of linear molecular fluid wetting on a planar substrate using a computer simulation.

To achieve this purpose, the Monte Carlo (MC) simulation in the grand canonical (GC) and the canonical (C) ensembles were employed to investigate the vapour-liquid equilibria (VLE) in the bulk fluid phase and the physisorption of ethylene on a planar substrate. Two potential models of ethylene were applied, they are the one without quadrupole moment, and the other which accounts for partial charges representing quadrupole moment in the molecules. First, the two potential models were compared using VLE data, then they were employed to describe the adsorption behaviour of ethylene on a graphite substrate and compared the results with the experimental data. Lastly, a selected model was used to construct the parametric map of wetting of ethylene on a planar substrate by presenting a relationship between wetting temperature vs surface affinity. The developed wetting map of ethylene was then compared with the reference adsorbate, *i.e.*, argon. The physics of adsorption using microscopic analyses was also investigated.

## 5.2 Simulation Model

### 5.2.1 Fluid-Fluid Potential

Ethylene was modelled as TraPPE UA and TraPPE UA2 models. The TraPPE UA2 is an improved model with partial charges that accounts for the quadrupole moment. These two models were proposed by Shah, Siepmann, and Tsapatsis (Shah *et al.*, 2017). The schematic representation of the two potential

models is shown in *Figure 5.1*. Values of the reduced well depth, partial charges, and collision diameter are listed in Chapter II.

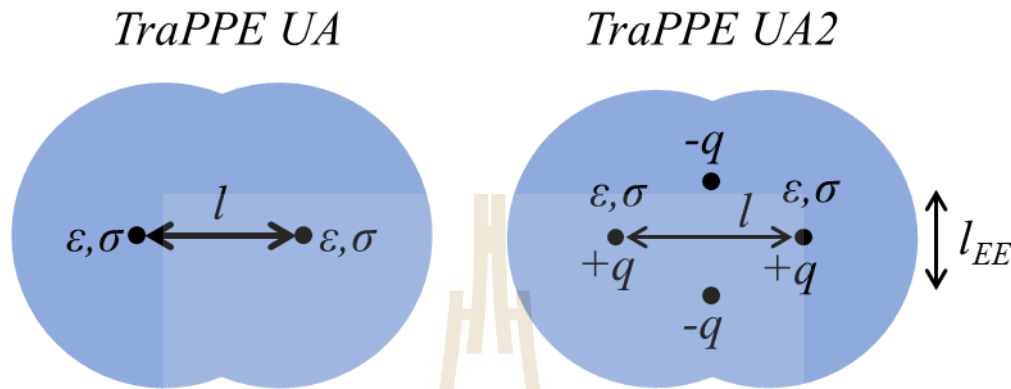


**Figure 5.1** Schematic drawing of two ethylene models.

### 5.2.2 Solid-Fluid Potential

The interaction energy between an ethylene molecule and graphite was calculated using Steele 10-4-3 equation (Steele, 1978). The molecular parameters of the carbon atom in the graphene layer are,  $\sigma_{ss} = 0.34$  nm, reduced well depth,  $\varepsilon_{ss}/k_B = 28$  K the interspacing between each graphene layer is,  $\Delta = 0.3354$  nm, and the density of carbon in graphene layer is,  $\rho_s = 38.2$  nm<sup>-2</sup>. To create the wetting map using different surface affinities, the  $\varepsilon_{ss}/k_B$  was merely varied. The cross-collision diameter and the cross well-depth were calculated using Lorentz-Berthelot (LB) mixing rule. The binary interaction parameter ( $k_{sf}$ ) between solid-fluid was introduced here to match the Henry constant from experimental data and the simulation. The LB mixing rule can be written as:  $\varepsilon^{s,f} = 1 - k_{sf} \sqrt{\varepsilon^{s,s} \varepsilon^{f,f}}$  with  $k_{sf} = 0.125$  (Do & Do, 2004).

The simulation was used to study the adsorption of ethylene on a planar substrate. The cut-off radius was five times of the first collision diameter of the fluid.  $2.5 \times 10^6$  cycles were used in the equilibration stage and the same number in the sampling stage. In each cycle, there were 1,000 moves of insertion, deletion, and displacement at equal probability. Periodic boundary conditions (PBC) were applied in the  $x$ - and  $y$ - direction. The dimensions of the simulation box were  $7.5 \times 7.5 \times 10.0$

$\text{nm}^3$  in the  $x$ -,  $y$ - and  $z$ -direction, respectively. The graphite substrate was placed at the bottom of the box, while the hard wall was placed at the top.

## 5.3 Results and Discussion

### 5.3.1 Comparison of Potential Models

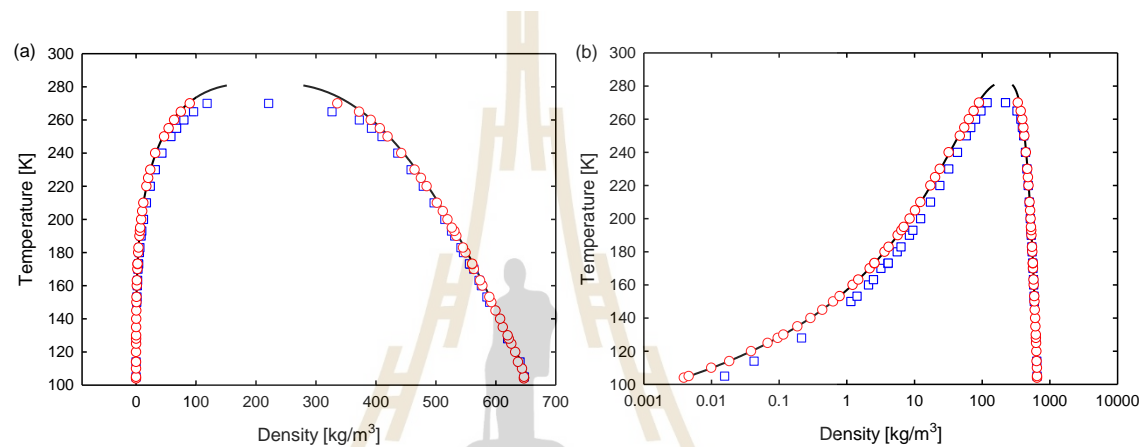


**Figure 5.2** Vapour-liquid coexistence densities curves for ethylene, blue squares represent TraPPE UA model, red circles are TraPPE UA2 model while the experimental data from NIST (Lemmon *et al.*, 2018) are shown as black solid lines. (a) Linear scale and (b) semi-log scale to emphasize at low-density region.

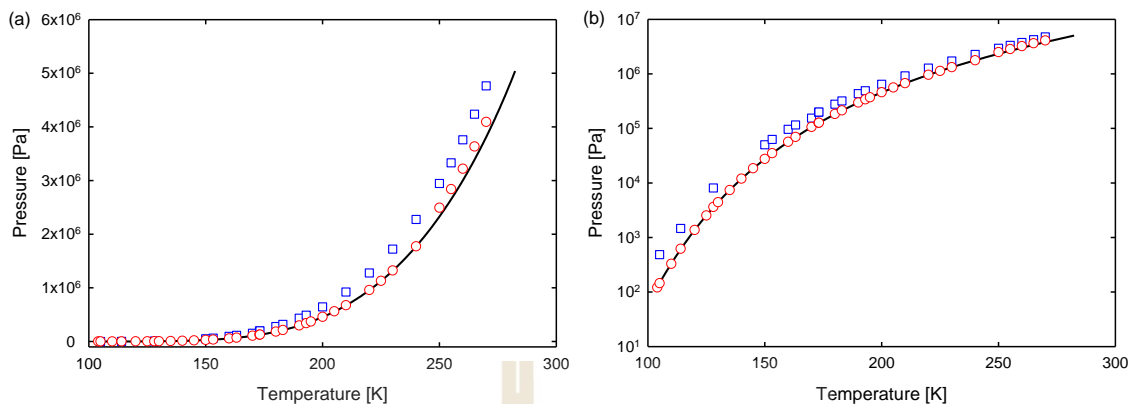


**Figure 5.3** Saturated vapour pressure or bulk coexistence pressure for ethylene, blue squares represent TraPPE UA model, red circles are TraPPE UA2 model while the experimental data from NIST (Lemmon *et al.*, 2018) are shown as black solid lines. (a) Linear scale and (b) semi-log scale to emphasize low-temperature region.

The vapour-liquid coexistence curves and bulk coexistence pressure of both potential models as a function of temperature are shown in *Figure 5.2* and *Figure 5.3*, respectively. They were calculated via canonical kMC simulation (Nguyen *et al.*, 2016). The TraPPE UA2 model gives slightly better agreement with the experimental data, because the molecular parameters are extracted from the fitting of the simulation results against the VLE experimental data. The partial charges in the TraPPE UA2 model also improve the adsorbate-adsorbate (FF) interactions in the bulk phase. The simulated heats of condensation for the temperatures above  $T_{tr}$  are also provided in Appendix A.

### 5.3.2 Adsorption on Graphite

The comparison between the two potential models shows that the model with partial charges gives a slightly better description of VLE, as previously noted. We now turn into the adsorption of ethylene on a homogeneous graphite substrate, which consists of adsorbed phase and bulk gas phase to investigate the role of the quadrupole moment of ethylene in the description of adsorption isotherm and isosteric heat of adsorption.

The simulation results of ethylene adsorption on graphite at 105 K (around the triple point temperature) from these models together with experimental data from Menaucourt *et al.* (Menaucourt *et al.*, 1977) are shown in *Figure 5.4*. For the adsorption isotherms, they are plotted against relative pressure, with the simulation results scaled against the bulk coexistence pressure.

Inspecting the simulation results, we see that the UA2 model generally describes the experimental data better than that of the UA model, suggesting the importance of quadrupole moment of ethylene in non-uniform adsorbed phase, with the UA2 model showing the better agreement at the onset of the first- and second-layer condensation. It is observed that the UA model fails to describe the onset of the second layer and the next layers. This failure is not due to the inherent problem with the potential models but rather results from the simplicity of the graphite model in the simulation. We note that after the first layer has been formed, the experimental isotherm exhibits a modest increase in the loading, while the simulation results show a constant in the adsorbed density. We would attribute this to the possible presence of fine gaps at the contacts between adjacent micro-crystallites (Franklin & Randall, 1951; Harris, 2001). Indeed, this is evident from the increase in the density of the experimental isotherm after each layer has been formed. This problem on the condensation of ethylene in the fine gaps has already been solved in recent work (Loi *et al.*, 2021).

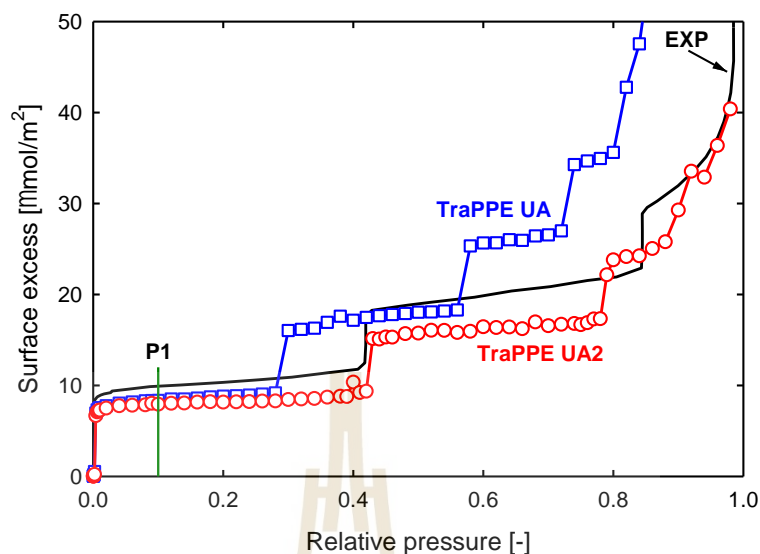


**Figure 5.4** The adsorption isotherms of ethylene at 105 K on graphite. Blue squares represent the TraPPE UA model, red circles are the TraPPE UA2 model, and the black solid line is the experimental data from Menaucourt *et al.* (Menaucourt *et al.*, 1977).

To reveal further the performance of two potential models, *Figure 5.5* shows the configuration snapshots of ethylene molecules at point P1 as marked in *Figure 5.4*, which is the point of the completion of the first molecular layer. As expected, most molecules orient parallel to the graphite surface, *i.e.*, laying down position (Groszek & Rideal, 1970) to maximize the interactions between Lennard-Jonesium (LJ) sites on ethylene molecules with graphite, and at the same time, they try to minimize the lateral repulsion as well (Bottani, 1999). Commonly, this alignment is observed before from the computer simulation of linear molecular adsorbates on graphite at very low temperatures (Fan *et al.*, 2013; Sordo *et al.*, 1990; Steele, 1996). This is also confirmed by the adsorption of hydrocarbon adsorbed on graphite (Hoory & Prausnitz, 1967).

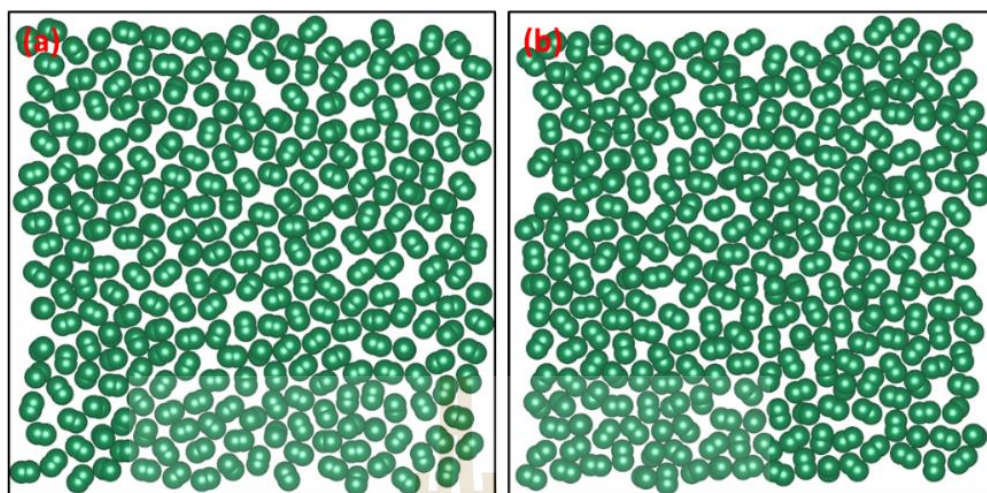


**Figure 5.5** The configurations of ethylene on graphite at 105 K, the pressure point is marked in *Figure 5.4* ( $P/P_0 = 0.1$ ). (a) TraPPE UA model and (b) TraPPE UA2 model.

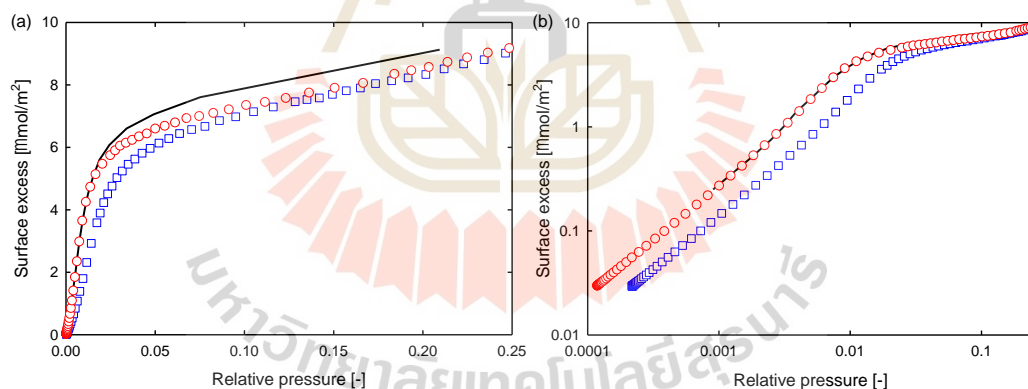


**Figure 5.6** The adsorption isotherms of ethylene at 193 K on graphite. (a) Plots are in linear scale and (b) log-log scale to emphasize Henry's law region. Blue squares represent the TraPPE UA model, red circles are the TraPPE UA2 model, and the black solid line is the experimental data from Avgul and Kiselev (Avgul & Kiselev, 1970).

To support the importance of quadrupole moment in the ethylene molecule, *Figure 5.6a* and *b* show the adsorption isotherms of ethylene on graphite at 193 K. A comparison between the experimental data and the two potential models is

displayed. In a very low-loading region (see *Figure 5.6b*), the UA2 model managed to capture a perfect Henry constant while the UA model failed to describe the low loading region. Then at  $P/P_0 = 0.01$  and higher pressures (see *Figure 5.6a*), the UA2 model still reproduces the experimental isotherm better than the UA, especially in the sub-monolayer density (less than  $8 \mu\text{mol}/\text{m}^2$ ). Now go back to the VLE for both potential models at 193 K, the UA gives  $P_0$  of 490.58 kPa while UA2 gives 340.71 kPa as compared to the experimental data at 338.09 kPa (Lemmon *et al.*, 2018). The data indicate that even in the bulk phase, the influence of quadrupole moment exists and results in the adsorbate-adsorbate (FF) interactions, giving the difference in the bulk coexistence pressure for each potential model. Once the  $P_0$  for each model is used to scale the relative pressure, this affects the shape and the adsorbed density of the isotherms as well.

To further substantiate what we have observed about the isotherms and the microscopic distributions, we show in *Figure 5.7* the simulated isosteric heats of adsorption versus loading for both potential models of ethylene at 105 K. The various contributions of isosteric heat from the adsorbent-adsorbate (SF) interactions, adsorbate-adsorbate (FF) interactions via dispersive force (LJ) and the electrostatic adsorbate-adsorbate (Charges) interactions are shown in *Figure 5.8*. Within the sub-monolayer coverage region (surface excess is less than  $8 \mu\text{mol}/\text{m}^2$ ), the isosteric heat is greater than the heat of condensation, resulting in the formation of the first layer. To show the role of quadrupole moment, the heat of adsorption released by the charges is about 2 kJ/mol within the sub-monolayer region (see *Figure 5.8*), then at the completion of the first layer the total isosteric heat reaches about 30 kJ/mol as predicted by the UA2 model (see *Figure 5.7b*), with a contribution from charges of about 5 kJ/mol (see *Figure 5.8*). While without considering the quadrupole moment, the simulated isosteric heat by the UA model at the completion of the monolayer is around 24 kJ/mol (see *Figure 5.7a*), with around 6 kJ/mol difference as compared with the UA2 model. This difference indicates that the quadrupolar moment arranges the adsorbate molecules to lay down on the graphite surface, as explained in the configuration figures (see *Figure 5.5*), to maximize the interactions.

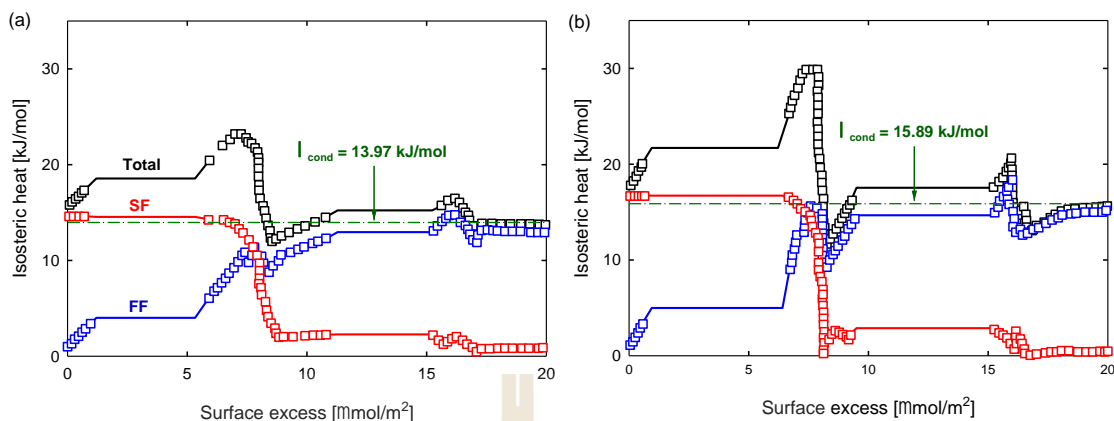


**Figure 5.7** The isosteric heat of adsorption of ethylene on graphite at 105 K. (a) TraPPE UA model and (b) TraPPE UA2 model. The solid lines represent the heats obtained from the canonical ensemble, which provides information on the transition during the first-order transition. The heats of condensation (green dash-dot lines) were obtained from the canonical kMC scheme (Nguyen *et al.*, 2016).

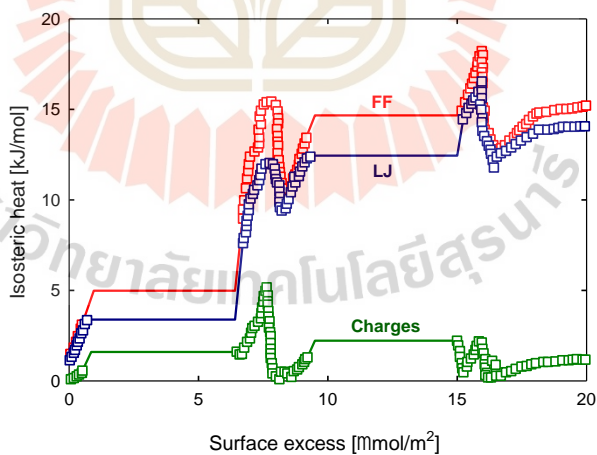


**Figure 5.8** The adsorbate-adsorbate (FF) contribution of isosteric heat and its dispersive (LJ) and electric interactions (Charges) contributions simulated with TraPPE UA2 model adsorption on graphite at 105 K.

The simple conclusions that can be drawn from the analysis of adsorption of ethylene on graphite are as follows: (1) the experimental isotherms can

be correctly reproduced with the potential model that consists of charges and (2) the molecules of ethylene usually lie flat to the graphite surface to maximize the interactions. However, there is no specific orientation for ethylene at a high temperature (105K).

### 5.3.3 Wetting Map

We first study the wetting map of argon on a planar substrate to understand the basic concept of the wetting map and then move to the wetting map of ethylene which shares almost the same pattern and features of the wetting map.

#### 5.3.3.1 Reference Adsorbate

The non-wetting/wetting behaviour of argon on the planar substrate has been extensively studied by Luisa *et al.* (L. Prasetyo *et al.*, 2018), and the results are summarized in *Figure 5.9a* showing the relationship between wetting temperature and surface affinity,  $D^*$ .  $D^*$  is the ratio between the surface attraction for the adsorbate and the cohesiveness of that adsorbate in the bulk phase. The  $D^*$  can be calculated using the depth of the solid-fluid (SF) potential energy profile to the depth of the fluid-fluid (FF) potential energy profile, the equation can be written as:

$$D^* = \frac{|u_{SF}|_{\min}}{|u_{FF}|_{\min}} \quad (5.1)$$

It should be noted that this equation is only valid at zero Kelvin (*i.e.*, in the absence of entropy).

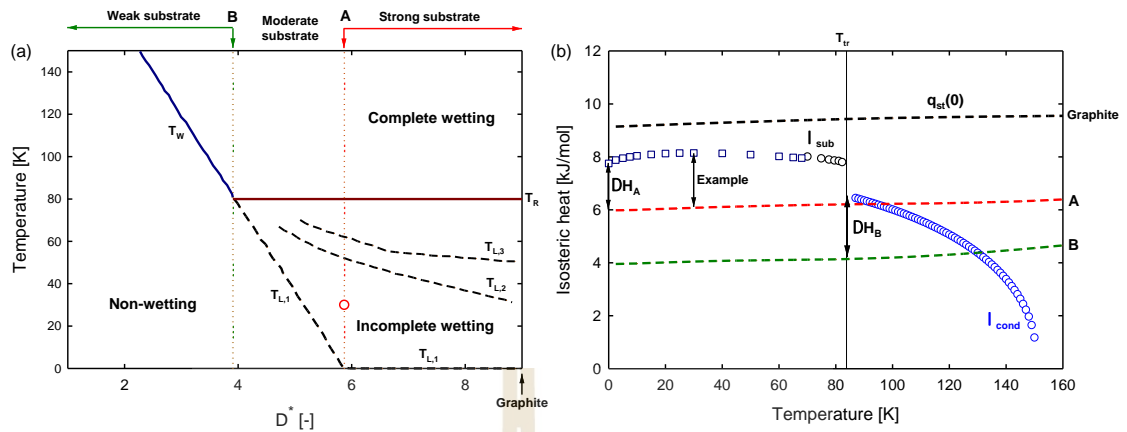


**Figure 5.9** (a) The parametric map of the wetting temperature of argon as a function of surface affinity,  $D^*$  and (b) the plots of heats of sublimation and condensation together with isosteric heats at zero loading calculated via Monte Carlo Integration (Do *et al.*, 2008) at different surface affinities.

In Figure 5.9a, the parametric map of wetting is separated into three regions: non-wetting, complete wetting, and incomplete wetting. The demarcating line between the non-wetting zone and the complete wetting zone (dark blue line) is the wetting temperature line ( $T_w$ ). This line is the boundary separating of two zones: one that has the clusters on the substrate at the bulk coexistence pressure,  $P_0$ , and the other exhibits infinite adsorbed loading as the pressure approaches  $P_0$ . The line separating the incomplete wetting zone and the complete wetting zone is the roughening temperature line ( $T_R$ , red solid line). Below this line, the interface separating the adsorbed film and the bulk gas is not corrugated enough to induce complete wetting at  $P_0$ , while in the zone above this line the complete wetting occurs at  $P_0$ . Because the surface is sufficiently corrugated such that incoming molecules have enough number of neighbouring molecules at the interface to induce the wetting. Finally, within the incomplete wetting region, there are further divisions that display the demarcation between zones of a different number of layers at  $P_0$ . For example, in the zone below  $T_{L,2}$  there is one layer formed on the substrate with  $T_{L,2}$  being the temperature at which the second layer is formed at  $P_0$ . Similarly, in the zone between  $T_{L,2}$  and  $T_{L,3}$  there are two adsorbed layers on the substrate at  $P_0$ . Usually, the layering

temperature for the second layer and higher, the temperature will be  $T_{L,n+1} > T_{L,n}$  where  $n$  is the number of layer  $n$ .

Apart from the three regions in the wetting map as shown in *Figure 5.9a*, we also distinguish two planar substrates to illustrate a strong substrate (denoted by **Substrate A**) and a weak substrate (denoted by **Substrate B**). The details of the microscopic behaviour of adsorption of fluid on each substrate are discussed in the next paragraph.

In *Figure 5.9b*, we show the heat of sublimation,  $\lambda_{sub}$ , for temperature below  $T_{tr}$ , black circles obtained from the simulation by Chen *et al.* (Chen *et al.*, 2001) while dark blue squares obtained from the experimental data by Ferreira and Lobo (Ferreira & Lobo, 2008) since there is no simulated data available at low temperature. The heat of condensation,  $\lambda_{cond}$ , for temperature above  $T_{tr}$  was obtained from the canonical kMC scheme (Nguyen *et al.*, 2016). The isosteric heat at zero loading,  $q_{st}^0$ , of argon on graphite, **Substrate A**, and **Substrate B**, which are shown in black, red, and green dash lines obtained from Monte Carlo Integration (Do *et al.*, 2008).

To distinguish the wetting behaviour between **Substrate A** (and higher surface affinity than **A**) and **Substrate B** (and lower surface affinity than **B**), the relationship between the heat of sublimation/condensation and isosteric heat at zero loading from Chapter II is presented in Equation (5.2):

$$\Omega = \frac{q_{st}^0 + Q_{FF}}{\lambda_{sub/cond}} \quad (5.2)$$

As previously mentioned in Chapter II, to measure the wetting of the system, the isosteric heat at zero loading should be higher than the heat of sublimation or condensation at a given temperature. However, if the ratio between  $q_{st}^0 / \lambda_{sub/cond}$  is less than one, it does not mean that the system cannot wet. By using the heat contributes by adsorbate-adsorbate ( $Q_{FF}$ ) interactions during the course of adsorption, the numerator can be easily compensated and resulting in  $\Omega \geq 1$ .

We note that when  $\Omega$  is more than one, wetting occurs at a given temperature (it starts with incomplete wetting at the temperature below  $T_R$  and then complete wetting occurs when the temperature is above  $T_R$  for the strong substrate). The heat contributed from adsorbate-adsorbate (FF) interactions is indicated as  $Q_{FF}$ , this parameter will be further used to clarify how wetting occurs when the  $q_{st}^0$  is lower than the  $\lambda_{sub/cond}$ . Next, we move to the analysis of **Substrates A** and **B**.

**Substrate A:** The isosteric heats at zero loading,  $q_{st}^0$  of substrate **A** are shown in *Figure 5.9b* presented in red dash line, for a temperature around 0 K and up to about triple point temperature of argon,  $q_{st}^0$  is less than the heat of sublimation, while the temperatures around the triple point and up to 150 K. The  $q_{st}^0$  is always larger than the heat of condensation. In this case, wetting can occur at 0 K and higher temperatures. The next paragraph clarifies how wetting occurs.

The estimation of the difference of the heat,  $\Delta H_A$  between  $q_{st}^0$  and  $\lambda_{sub}$  at 0 K is about 1.77 kJ/mol (see *Figure 5.9b*). This quantity can be made up by the heat contributing from adsorbate-adsorbate ( $Q_{FF}$ ) interactions, hence the formation of the first layer can be observed. So, the layering temperature ( $T_{L,1}$ ) of argon on substrate **A** is 0 K. Once the temperature is great enough and crosses  $T_R$ , then the complete wetting occurs, this is due to  $q_{st}^0$  (also together with  $Q_{FF}$  in the system) being greater than the heat of condensation from the temperature around  $T_t$  and up to 150 K (see *Figure 5.9b*).

Take this example to clarify the incomplete wetting at low temperature, the substrate **A** with  $D^*$  of 5.869, we show the adsorption isotherms of argon (in canonical and grand canonical ensembles) on this substrate at 30 K together with isosteric heat of adsorption in *Figure 5.10* below. The point of this adsorption temperature and surface energy is marked in the wetting map, as shown in *Figure 5.9a*.

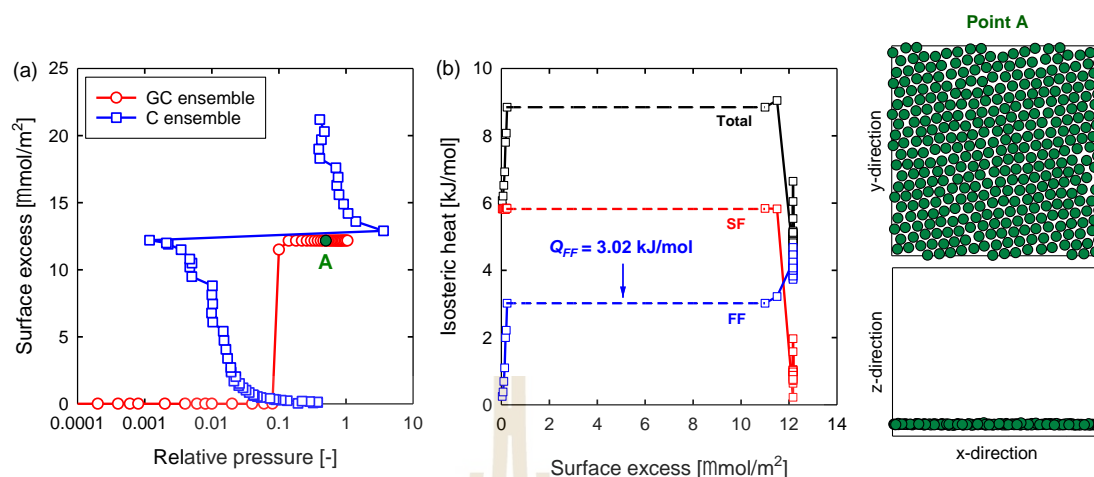


**Figure 5.10** (a) Adsorption isotherms of argon on substrate **A** at 30 K that has  $D^*$  of 5.869 and (b) isosteric heat of adsorption with the contributions from adsorbate-adsorbate (FF) interactions and adsorbent-adsorbate (SF) interactions. The dash lines in heat plots are obtained from the canonical ensemble to provide the evolution of heats during the first-order transition.

The difference between  $q_{st}^0$  and  $\lambda_{sub}$  at 30 K is about 2.07 kJ/mol to induce the wetting on this substrate (see *Figure 5.9b*). While the  $Q_{FF} = 3.02$  kJ/mol, this is the heat contributed by the adsorbate-adsorbate interactions (see *Figure 5.10b*), which is more than enough to make up the isosteric heat at zero loading. This would result in wetting of the first layer which is supported by the adsorption isotherms in *Figure 5.10a*, where the monolayer density of argon at  $12 \mu\text{mol}/\text{m}^2$  on this substrate can be observed. The snapshot of configuration in *Figure 5.10* also shows the full coverage of the monolayer of argon on substrate **A** to support that there is always at least one argon layer on this substrate at 30 K, where this system falls into an incomplete wetting region as marked in *Figure 5.9a*.

Take the next example, on a graphite substrate, the  $D^*$  is 8.996 for argon/graphite system as marked in *Figure 5.9a*. This substrate has a surface affinity that is greater than substrate **A**. In *Figure 5.9b*, the isosteric heat at zero loading of argon/graphite system is always greater than the heat of sublimation and heat of condensation for all temperatures. This indicates that the layering temperature of the

first layer ( $T_{L,1}$ ) of argon on graphite is always 0 K, then between  $T_{L,1}$  to  $T_R$  the incomplete wetting occurs. Once the temperature crosses  $T_R$ , complete wetting occurs by the thermal fluctuation and the interface between adsorbed film and bulk gas phase is undulated enough to induce the complete wetting. We use *Figure 5.11* to present the complete wetting where it can be seen for argon adsorption on a graphite substrate at 87 K. This is substantiated by the snapshot of argon at  $P/P_0 \sim 0.995$  showing multilayer adsorption (*i.e.*, complete wetting).

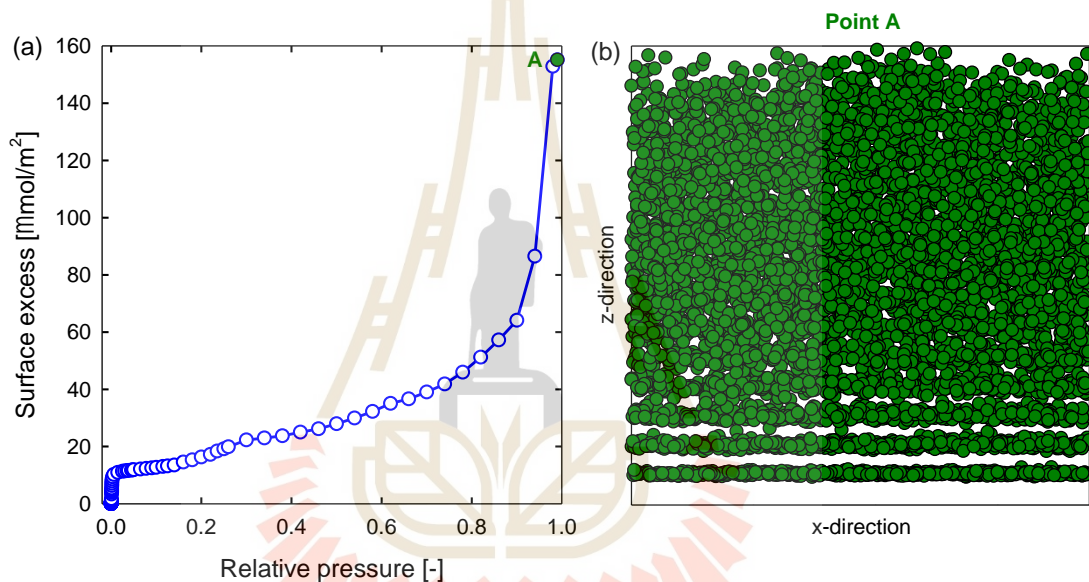


**Figure 5.11** (a) Adsorption isotherm of argon on a graphite substrate ( $D^*$  of 8.996) at 87 K and (b) snapshot of argon at 87 K and  $P/P_0 \sim 0.995$ .

**Substrate B:** This substrate exhibits differently from **Substrate A**. This substrate shows the same first layering temperature, wetting temperature, and roughening temperature or  $T_{L,1} = T_W = T_R$  (see *Figure 5.9a*). The  $q_{st}^0$  of substrate **B** is less than the heat of sublimation for the temperature at 0 K to around triple point temperature. Once again, Equation (5.1) is employed here. At the bulk triple point temperature,  $\Delta H_B$  is around 2.2 kJ/mol (see *Figure 5.9b*) and this heat value can be easily compensated by  $Q_{FF}$ . So, at this temperature, the system transforms from the clustering of argon molecules on the substrate at  $P_0$  to the complete wetting at the

temperature above  $T_R$ . This substrate is too weak to influence the wetting except the system reaches a very high temperature, so there is enough thermal fluctuation to induce the complete wetting (Xu *et al.*, 2021). Then for any substrate that has surface affinity less than substrate **B**, the wetting temperature will be even higher. The system will rely on thermal fluctuation to encounter wetting (see *Figure 5.9a* at very low surface affinity).

### 5.3.3.2 Ethylene

For ethylene adsorption, we employed the TraPPE UA2 model to construct the parametric map of wetting of ethylene on the planar substrate. An extensive number of computer simulations were carried out by varying surface affinities denoted by  $D^*$ . For ethylene adsorption on graphite, the  $D^*$  is 4.822 which results in a strong substrate.

The selection of bulk coexistence pressure,  $P_0$ , is a very significant step that is used to determine whether the system is wetting or not. Here we utilized  $P_0$  for temperatures above  $T_{tr}$  from the canonical KMC (Nguyen *et al.*, 2016) scheme for vapour-liquid equilibria (VLE). While the temperatures below  $T_{tr}$ , we used the sublimation pressures obtained from the experimental data by Smukala *et al.* (Smukala *et al.*, 2000), since there are no available simulation results. The sublimation pressures and heats of sublimation for ethylene are given in Appendix A.

*Figure 5.12a* and *b* show the wetting map of ethylene of the wetting temperature as a function of surface affinity together with the plots of the heat of sublimation ( $\lambda_{sub}$ ) and condensation ( $\lambda_{cond}$ ) compared to the isosteric heat at zero loading,  $q_{st}^0$ , at different substrate energies. from the plots consist of graphite substrate, **Substrate A**, and **B**. The wetting map of ethylene shares the same pattern as the wetting map of argon, all the wetting regions discussed in the previous section. In the ethylene system, the roughening temperature,  $T_R$  was found to be at 105 K in the simulation. Which is close to the values that were observed experimentally at 104.5 K (Meichel *et al.*, 1990) and 104 K (Arakawa *et al.*, 1988).

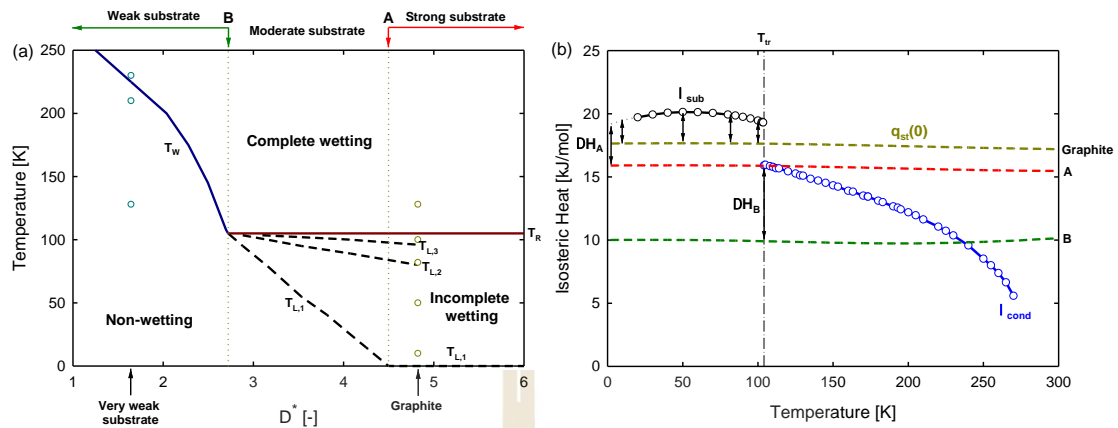


**Figure 5.12** (a) The parametric map of the wetting temperature of ethylene as a function of surface affinity,  $D^*$  and (b) the plots of heats of sublimation and condensation together with isosteric heats at zero loading calculated via Monte Carlo Integration (Do *et al.*, 2008) at different surface affinities.

To explore how wetting occurs on **Substrate A** and **B** for ethylene, the definition of  $\Delta H(T)$  in the previous section is employed here.

**Substrate A:** The red dot line that indicates substrate **A** on the wetting map of ethylene is marked in *Figure 5.12a*, this is the lowest limit of the strong substrate for the ethylene system. We used a heat map in *Figure 5.12b* to demonstrate the wetting behaviour on this substrate. At the temperature very close to 0 K (see *Figure 5.12b*) the  $\Delta H_A$  is around 3.3 kJ/mol to induce the wetting on this substrate, the  $q_{st}^0$  can be simply made up by  $Q_{FF}$ , so the layering temperature of the first layer is 0 K for this substrate and also for graphite substrate.

For example, the ethylene adsorption on graphite substrate has  $D^*$  of 4.822, where we plot a family of isotherms at various temperatures from 10 K to 128 K as displayed in *Figure 5.13*. When the temperature is increased from 10 K to 100 K, the isotherms show one, two, and three layers, respectively. Once the temperature is high enough above the roughening temperature,  $T_R$ , the system displays complete wetting at 128K where the trend of adsorbed density goes to infinity as the pressure approaches  $P_0$ . This is consistent with the finding of Mochrie *et al.* and Sutton *et al.*

(Mochrie *et al.*, 1984; Sutton *et al.*, 1983), they used X-Ray diffraction to observe the layer-by-layer wetting of ethylene on graphite. They reported the existence of ethylene in the adsorbed phase on a graphite substrate with one, two, and three layers at 56.7 K, 85.1 K, and 100 K, respectively.

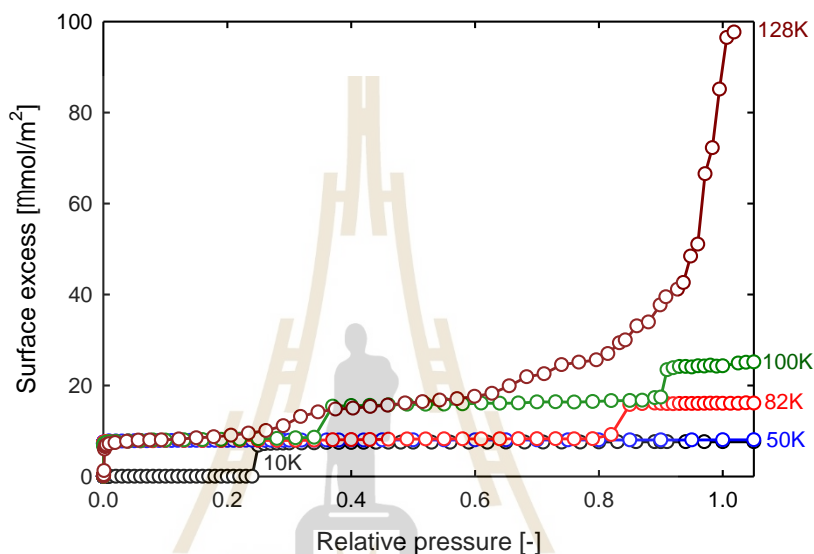


**Figure 5.13** Simulated adsorption isotherms of ethylene on graphite at various temperatures.

The evidence to support the formation of ethylene on graphite at various temperatures and  $P_0$  are shown in *Figure 5.14a* to *d*, which are the snapshots of the centre of mass (COM) of ethylene molecules. At the temperature of 10 K and 50 K only one layer is formed, while at the temperature of 82 K and 100 K, the second and third layers can be detected. Eventually, at the temperature of 128 K, the complete wetting can be observed because of the sufficiently corrugated interface between the adsorbed phase and the gas phase.

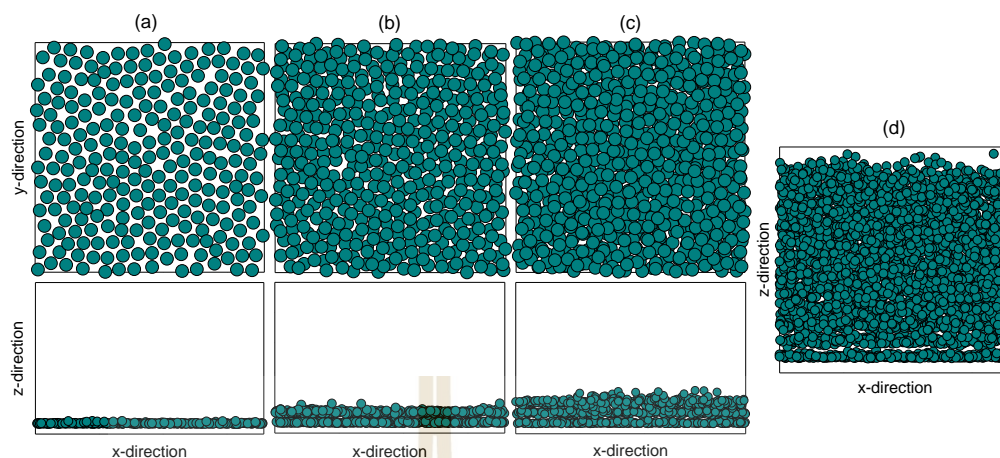


**Figure 5.14** The configurations snapshots of ethylene molecules on graphite at  $P_0$ , the plots using the centre of mass (COM) of ethylene molecules for temperatures (a) 50 K, (b) 82 K, (c) 100 K, and (d) 128 K.

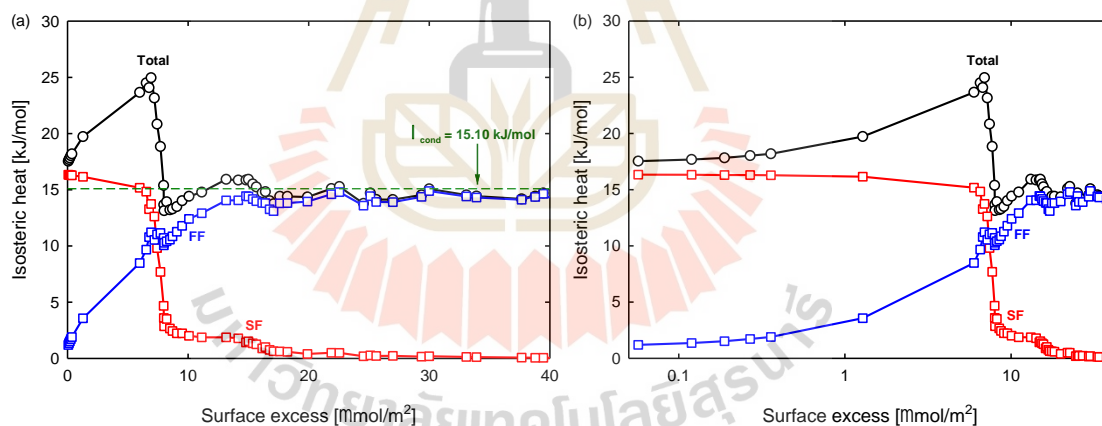


**Figure 5.15** (a) Isotherm of adsorption of ethylene on graphite at 128 K, it is decomposed into adsorbate-adsorbate (FF) and adsorbent-adsorbate (SF) interactions. (b) Plots of heats in semi-log scale to emphasize the low loading region. The green dash line is the heat of condensation at 128 K, calculated by the canonical kMC scheme (Nguyen *et al.*, 2016).

We confirm the formation of layers by considering the plot of isosteric heat of adsorption versus loading for ethylene at 128 K, as shown in *Figure 5.15*. For the sub-monolayer region, the interactions energy between graphite and ethylene (SF) is very

strong as indicated by the heat of adsorption at very low loading being higher than the heat of condensation, therefore one layer is entirely formed on graphite. Once the first layer has been completely formed, the isosteric heat decreases below the heat of condensation, signifying molecules beginning to enter the second layer and they only interact with three neighbouring molecules in the first layer. As more molecules adsorb to build up the second layer, the isosteric heat increases again due to the contribution from the interactions between adsorbate-adsorbate (FF) while the SF is very small due to the adsorption in the second layer being far apart from the graphite surface. Once there are enough molecules within the second layer, the isosteric heat becomes greater than the heat of condensation again, leading to the completion of the second layer, and so on. Then the process keeps on repeating until the simulation box is full (see *Figure 5.14d*).

**Substrate B:** The  $\Delta H_B$  at 104 K ( $T_{tr}$  of ethylene) is around 7.72 kJ/mol to change the system from non-wetting to complete wetting at around  $T_{tr}$  of ethylene. The wetting process is identical to substrate **B** of the argon system. Once the temperature is high enough, the clusters of ethylene on this substrate will coalesce and the adsorbed film will be developed. On this substrate, there is no layering temperature (layer-by-layer wetting) to transform the system from incomplete wetting to complete wetting. We show the example of a very weak substrate (much weaker than substrate **B**) to demonstrate the non-wetting to complete wetting transition in *Figure 5.16*.

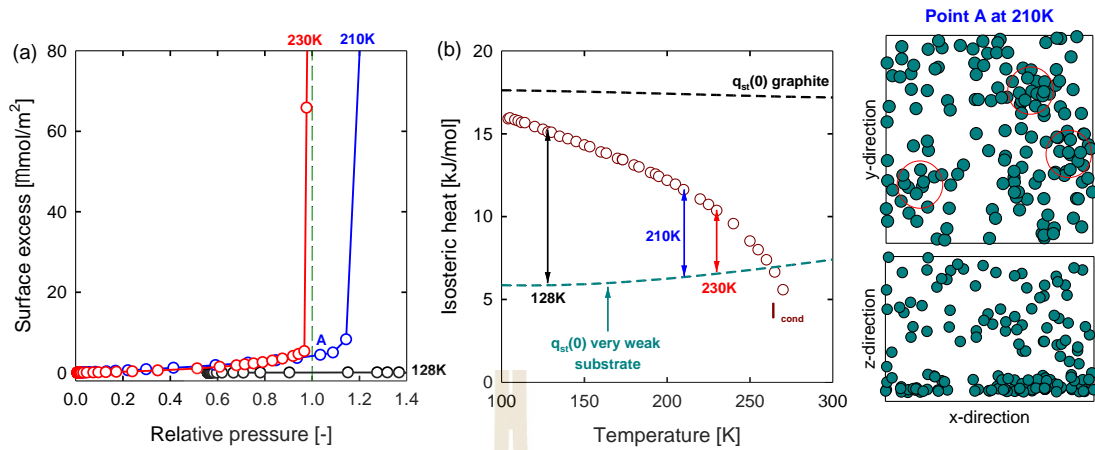


**Figure 5.16** (a) Adsorption isotherms of ethylene on a very weak substrate having  $D^*$  of 1.643 and (b) the plots of heats of sublimation and condensation together with isosteric heat at zero loading calculated via Monte Carlo Integration (Do *et al.*, 2008) at different surface affinities.

From *Figure 5.16a*, the isotherms at temperatures of 128 K and 210 K exhibit a non-wetting system. The isotherm cuts  $P_0$  at loading about  $0 \mu\text{mol}/\text{m}^2$  at 128 K, this implies that non-wetting of ethylene on this substrate is observed. When the temperature is increased to 210 K, the ethylene clusters have sparsely covered the surface at  $P_0$  (see snapshots in *Figure 5.16*). The non-wetting of ethylene on this substrate can be observed at 128 K and 210 K, which the strength of this substrate is too weak to induce the wetting at  $P_0$ . This is because the  $\Delta H$  at 128 K and 210 K are too high to be compensated by  $q_{st}^0$  and  $Q_{FF}$  (see *Figure 5.16b*). When the temperature increases to 230 K we observed the complete wetting, this system is discussed in the next paragraph.

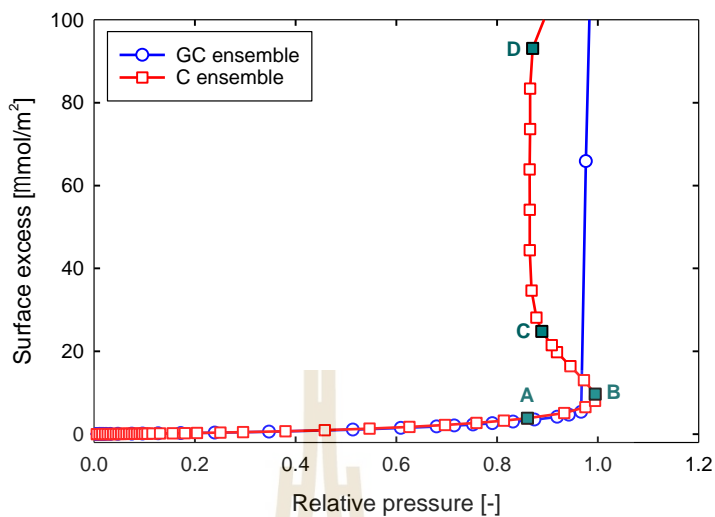


**Figure 5.17** Adsorption isotherms of ethylene at 230 K on a substrate having  $D^*$  of 1.643. The canonical isotherm gives the information during the transition from molecular clustering to adsorbed film on the substrate.

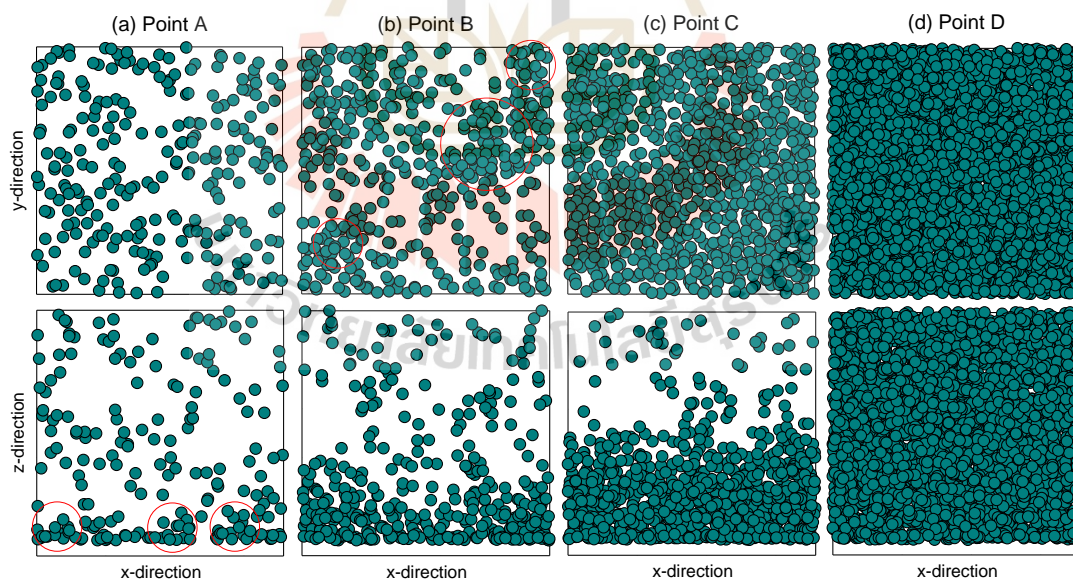


**Figure 5.18** The configuration snapshots of ethylene molecules on a very weak substrate at points A to D as marked in the canonical isotherm in *Figure 5.17*. The plots use the centre of mass (COM) of ethylene molecules.

To explore the course of adsorption of ethylene at the temperature on very low substrate energy, we do the microscopic analysis using snapshots at various points in the canonical (C) isotherm in *Figure 5.17* as follows:

- Point A: At loading around  $3.84 \mu\text{mol}/\text{m}^2$  where the mobile clusters of ethylene can be observed, the ethylene molecules exchange between clusters and the bulk gas phase. This is due to the competition between FF and SF interactions because the surface affinity is very weak.
- Point B: At the spinodal point in the canonical isotherm, the loading at  $9.65 \mu\text{mol}/\text{m}^2$  is higher than the monolayer coverage of ethylene at  $8.0 \mu\text{mol}/\text{m}^2$ . However, from the snapshot, the uncovered parts of the surface can be seen, this is due to the clusters of ethylene coalesce and increasing vertically but not reclining to cover the substrate.
- Point C: At this point, where the clusters keep agglomerating and form a thin adsorbed film on the surface. From the isotherm, lower pressure is required to equilibrate larger clusters (Luisa Prasetyo, Shiliang Tan, *et al.*, 2018).
- Point D: The adsorbed film on the surface fully exists, the interface between adsorbed film and bulk gas phase is undulated enough to build up a higher layer and the system becomes complete wetting.

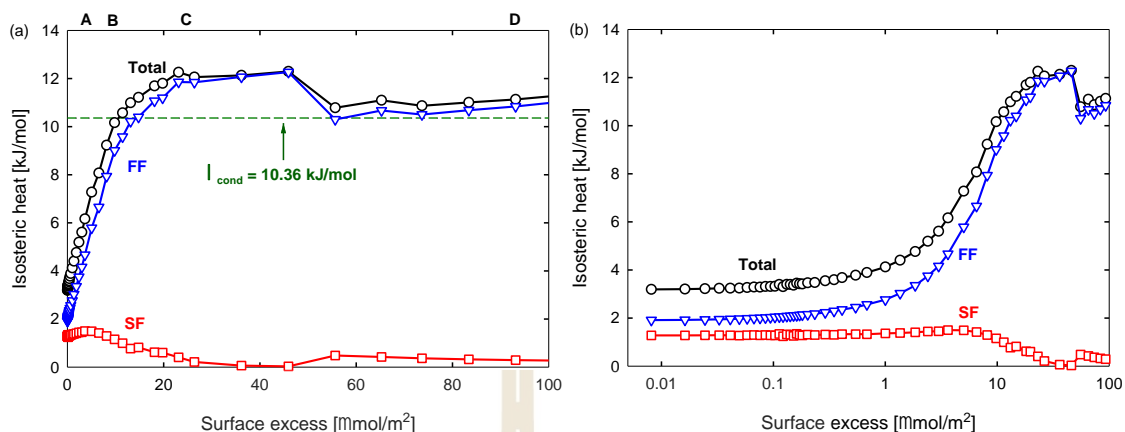


**Figure 5.19** (a) Isosteric heat of adsorption of ethylene on a very weak substrate at 230 K, it is decomposed into adsorbate-adsorbate (FF) and adsorbent-adsorbate (SF) interactions. (b) Plots of heats in semi-log scale to emphasize the low loading region. The green dash line is the heat of condensation at 230 K, calculated by the canonical kMC scheme (Nguyen *et al.*, 2016).

We substantiate the complete wetting at 230 K for ethylene on a very weak substrate using the isosteric heat profile during the course of adsorption. *Figure 5.19* presents the isosteric heat of adsorption of ethylene at 230 K on a very weak substrate with the contribution of heats from adsorbate-adsorbate (FF) and adsorbent-adsorbate (SF) interactions. At this temperature, the  $q_{st}^0$  is lower than the heat of condensation as seen in *Figure 5.16b* and it is confirmed by SF (red line with square symbols) at very low loading in *Figure 5.19b*. The incoming molecules from the bulk gas phase only form clusters on the substrate, and 60% of the heat contributes from FF interactions while the rest is SF, resulting in forming of the ethylene islands on the substrate (at low loading to point A). As the pressure increases, these molecules interact with clusters and then the clusters coalesce to form larger clusters. The heat curves show that there is a linear increase in FF at a very low loading up to point B, this is due to the new incoming molecules from the bulk gas phase interacting with the clusters of ethylene rather than forming an adsorbed film on the substrate. This is supported by the decrease in SF when the adsorbed density increases, where the ethylene

molecules merge on the clusters with fewer molecules interacting with the surface. Then from point C to D in the heat curve, the isosteric heat decreases to about  $\lambda_{cond}$ , this confirms that the adsorbed film behaves like a liquid state of the bulk (where the adsorbed film exists).

The last substrate that we have not mentioned before is a moderate substrate. This system falls between two extremes, a weak substrate, and a strong substrate (see *Figure 5.12a*). This substrate is initially non-wetting, passing through a transition to incomplete wetting and finally complete wetting. The distinction between non-wetting and incomplete wetting regions is the non-zero Kelvin layering temperature of the first layer, and the distinction between incomplete wetting and complete wetting is the roughening temperature. Therefore, the wetting transition is non-wetting, incomplete wetting, and complete wetting, at a fixed surface affinity with the increase of temperature.

### 5.3.3.3 Further Use of Wetting Map

The relationship between the wetting temperature and the substrate strength of the wetting map provides a useful piece of information in designing improved adsorbents for capturing fluids of concern. Typically, the minimum potential energy between solid-fluid and fluid-fluid can be determined from the simulation, which can be further employed to determine the  $D^*$  of the system. The difference in  $D^*$  can lead us to the difference in the adsorption behaviour of fluids on a substrate. For example, the transition from non-wetting to complete wetting can only be observed in the systems that have low  $D^*$ . On the other hand, the transition from incomplete wetting to complete wetting can be detected in the systems that have high  $D^*$ . Once the  $D^*$  of the system is calculated, it can be used as a guideline to predict the adsorption behaviour of the fluid of concern on an adsorbent.

## 5.4 Conclusions

Two potential models of ethylene were compared using VLE and adsorption on a graphite substrate by computer simulations. It was found that the model accounting for partial charges is acceptable for the VLE and adsorption studies, while the model without partial charges is inadequate in the description of VLE and adsorbed phase. Then the model with partial charges was employed to construct the wetting map of ethylene on a planar substrate. Ethylene in the adsorbed phase shows similar wetting modes to argon, which exhibits the non-wetting, incomplete wetting, and complete wetting. It was also observed that the wetting behaviour of ethylene on different substrates is dominated by the heat of vaporization/condensation in the bulk phase. In addition, the heat of adsorption contributed by the adsorbate-adsorbate interactions and the isosteric heat at zero loading are the important parameters to dominate the wetting transition of ethylene on a planar substrate.

## 5.5 References

- Arakawa, I., Koga, Y., & Morrison, J. A. (1988). Wetting Transition of Ethylene Adsorbed on Graphite. In J. D. Embury & G. R. Purdy (Eds.), *Advances in Phase Transitions* (pp. 145-150). Oxford: Pergamon.
- Avgul, N. N., & Kiselev, A. V. (1970). Physical Adsorption of Gases and Vapors on Graphitized Carbon Blacks. **Chemistry and Physics of Carbon**. 6: 1-124.
- Bär, T., Burns, T., & Knorr, K. (1997). Growth kinetics of Ar monolayers physisorbed on graphite (001). **Surface Science**. 383(2): 362-369.
- Beebe, R. A., Kiselev, A. V., Kovaleva, N., Tyson, R., & Holmes, J. (1964). Adsorption and state of carbon dioxide, sulfur hexafluoride and ammonia on a graphitized carbon surface. I. Adsorption Isotherms. **Russian J. Phys. Chem.**: 372-378.
- Bienfait, M. (1985). Wetting and multilayer adsorption. **Surface Science**. 162(1): 411-420.
- Bojan, M. J., Stan, G., Curtarolo, S., Steele, W. A., & Cole, M. W. (1999). Wetting transitions of Ne. **Physical Review E - Statistical Physics, Plasmas, Fluids, and Related Interdisciplinary Topics**. 59(1): 864-873.
- Borkman, R. F., & Settle, F. A. (1971). Bond orders and electric quadrupole moments for ethane, ethylene, and acetylene from a point-charge model. **Journal of the American Chemical Society**. 93(22): 5640-5644.
- Bottani, E. J. (1999). Computer simulation of ethylene physisorption on graphite. **Langmuir**. 15(17): 5574-5577.
- Buckingham, A. D., Disch, R. L., & Dunmur, D. A. (1968). Quadrupole moments of some simple molecules. **Journal of the American Chemical Society**. 90(12): 3104-3107.
- Cahn, J. W. (1977). Critical point wetting. **The Journal of Chemical Physics**. 66(8): 3667-3672.
- Chen, B., Siepmann, J. I., & Klein, M. L. (2001). Direct Gibbs Ensemble Monte Carlo Simulations for Solid-Vapor Phase Equilibria: Applications to Lennard-Jonesium and Carbon Dioxide. **The Journal of Physical Chemistry B**. 105(40): 9840-9848.

- Dabrowski, A. (2001). Adsorption — from theory to practice. **Advances in Colloid and Interface Science**. 93(1): 135-224.
- De Boer, J. H., Kaspersma, J. H., Van Dongen, R. H., & Broekhoff, J. C. P. (1972). The adsorption curve for physical adsorption at high relative pressures. **Journal of Colloid and Interface Science**. 38(1): 97-100.
- de Gennes, P. G. (1985). Wetting: statics and dynamics. **Reviews of Modern Physics**. 57(3): 827-863.
- Deitz, V. R. (1967). The adsorption of carbon dioxide on carbon solids. I. Graphite and diamond at 0.degree. **The Journal of Physical Chemistry**. 71(4): 830-837.
- Do, D. D., & Do, H. D. (2004). Adsorption of Ethylene on Graphitized Thermal Carbon Black and in Slit Pores: A Computer Simulation Study. **Langmuir**. 20(17): 7103-7116.
- Do, D. D., & Do, H. D. (2005). Adsorption of argon from sub- to supercritical conditions on graphitized thermal carbon black and in graphitic slit pores: A grand canonical Monte Carlo simulation study. **The Journal of Chemical Physics**. 123(8): 084701.
- Do, D. D., & Do, H. D. (2006). Modeling of Adsorption on Nongraphitized Carbon Surface: GCMC Simulation Studies and Comparison with Experimental Data. **The Journal of Physical Chemistry B**. 110(35): 17531-17538.
- Do, D. D., Nicholson, D., & Do, H. D. (2008). On the Henry constant and isosteric heat at zero loading in gas phase adsorption. **Journal of Colloid and Interface Science**. 324(1): 15-24.
- Drir, M., Nham, H. S., & Hess, G. B. (1986). Multilayer adsorption and wetting: Ethylene on graphite. **Physical Review B**. 33(7): 5145-5148.
- Fan, C., Do, D. D., Nicholson, D., Jagiello, J., Kevlin, J., & Puzan, M. (2013). Monte Carlo simulation and experimental studies on the low temperature characterization of nitrogen adsorption on graphite. **Carbon**. 52: 158-170.
- Ferreira, A. G. M., & Lobo, L. Q. (2008). The sublimation of argon, krypton, and xenon. **The Journal of Chemical Thermodynamics**. 40(12): 1621-1626.
- Franklin, R. E., & Randall, J. T. (1951). Crystallite growth in graphitizing and non-graphitizing carbons. 209(1097): 196-218.

- Gatica, S. M., & Cole, M. W. (2009). To Wet or Not to Wet: That Is the Question. **Journal of Low Temperature Physics**. 157(3): 111.
- Grillet, Y., Rouquerol, F., & Rouquerol, J. (1979). Two-dimensional freezing of nitrogen or argon on differently graphitized carbons. **Journal of Colloid and Interface Science**. 70(2): 239-244.
- Groszek, A. J., & Rideal, E. K. (1970). Selective adsorption at graphite/hydrocarbon interfaces. **Proceedings of the Royal Society of London. A. Mathematical and Physical Sciences**. 314(1519): 473-498.
- Harris, P. J. F. (2001). Rosalind Franklin's work on coal, carbon, and graphite. **Interdisciplinary Science Reviews**. 26(3): 204-210.
- Hermosilla, M. E. F., & Albesa, A. G. (2020). Monte Carlo simulations of simple gases adsorbed onto graphite and molecular models of activated carbon. **Adsorption**. 26(8): 1301-1322.
- Herrera, L., Loi, Q. K., Prasetyo, L., & Do, D. D. (2021). Evolution of adsorption isotherm and isosteric heat from sub-triple to super-critical points. **Adsorption**.
- Hoory, S. E., & Prausnitz, J. M. (1967). Adsorption of hydrocarbons on graphitized carbon. **Transactions of the Faraday Society**. 63(0): 455-460.
- Larese, J. Z., Lee, M. Y., & Lee, M. Y. (1997). Combined Neutron Diffraction and Adsorption Isotherm Study of the Anomalous Wetting Properties of NH<sub>3</sub> on Graphite. **Physical Review Letters**. 79(4): 689-692.
- Lemmon, E. W., McLinden, M. O., & Friend, D. G. (2018). **NIST Chemistry WebBook, SRD 69**. Gaithersburg, MD: National Institute of Standards and Technology.
- Loi, Q. K., Phothong, K., Do, D. D., & Nicholson, D. (2021). Effects of crystallite stacking on adsorption of ethylene on graphitized thermal carbon black. **Microporous and Mesoporous Materials**. 323: 111202.
- Loi, Q. K., Prasetyo, L., Tan, S., Do, D. D., & Nicholson, D. (2020). Order-disorder transition of an argon adsorbate in graphitic wedge pores. **Chemical Engineering Journal**. 384: 123286.
- McDermot, H. L., & Lawton, B. E. (1959). THE ADSORPTION OF SULPHUR DIOXIDE BY GRAPHITE. **Canadian Journal of Chemistry**. 37(3): 637-640.

- Meichel, T., Dawson, P. T., Morrison, J. A., Sullivan, D. E., & Koga, Y. (1990). Adsorption of ethylene on graphite near saturation: wetting transition/capillary condensation. *Langmuir*. 6(10): 1579-1584.
- Menaucourt, J., Thomy, A., & Duval, X. (1977). Variation in temperature function of the number of adsorbed ethylene layers on the cleavage faces of graphite. *Journal de Physique Colloques*. 38(C4): C4-195 - C194-200.
- Michels, A., Wijker, H., & Wijker, H. (1949). Isotherms of argon between 0°C and 150°C and pressures up to 2900 atmospheres. *Physica*. 15(7): 627-633.
- Millot, F. (1979). Adsorption of the first layer of argon on graphite. *J. Physique Lett.* 40(1): 9-10.
- Mochrie, S. G. J., Sutton, M., Birgeneau, R. J., Moncton, D. E., & Horn, P. M. (1984). Multilayer adsorption of ethylene on graphite: Layering, prewetting, and wetting. *Physical Review B*. 30(1): 263-273.
- Nguyen, V. T., Tan, S. J., Do, D. D., & Nicholson, D. (2016). Application of kinetic Monte Carlo method to the vapour-liquid equilibria of associating fluids and their mixtures. *Molecular Simulation*. 42(8): 642-654.
- Nham, H. S., & Hess, G. B. (1989). Ellipsometric study of krypton, methane, and argon films on graphite: how complete is wetting? *Langmuir*. 5(3): 575-582.
- Prasetyo, L., Loi, Q. K., Tan, S., Do, D. D., & Nicholson, D. (2018). The role of adsorbate size on adsorption of Ne and Xe on graphite. *Journal of Colloid and Interface Science*. 524: 490-503.
- Prasetyo, L., Loi, Q. K., Tan, S. J., Do, D. D., & Nicholson, D. (2018). Effects of temperature on the transition from clustering to layering for argon adsorption on substrates of different strength - Parametric map of wetting, pre-wetting and non-wetting. *Microporous and Mesoporous Materials*.
- Prasetyo, L., Tan, S., Akram, A., Do, D. D., & Nicholson, D. (2018). Cluster growth and coalescence of argon on weakly adsorbing substrates: The origin of the thin-to-thick film transition. *Colloids and Surfaces A: Physicochemical and Engineering Aspects*. 554: 169-179.
- Reich, R., Ziegler, W. T., & Rogers, K. A. (1980). Adsorption of Methane, Ethane, and Ethylene Gases and Their Binary and Ternary Mixtures and Carbon Dioxide on

- Activated Carbon at 212-301 K and Pressures to 35 Atmospheres. **Industrial & Engineering Chemistry Process Design and Development**. 19(3): 336-344.
- Saam, W. F. (2009). Wetting, Capillary Condensation and More. **Journal of Low Temperature Physics**. 157(3): 77-100.
- Sellers, M. S., & Errington, J. R. (2008). Influence of Substrate Strength on Wetting Behavior. **The Journal of Physical Chemistry C**. 112(33): 12905-12913.
- Shah, M. S., Siepmann, J. I., & Tsapatsis, M. (2017). Transferable potentials for phase equilibria. Improved united-atom description of ethane and ethylene. **AIChE Journal**. 63(11): 5098-5110.
- Smukala, J., Span, R., & Wagner, W. (2000). New Equation of State for Ethylene Covering the Fluid Region for Temperatures From the Melting Line to 450 K at Pressures up to 300 MPa. 29(5): 1053-1121.
- Sordo, T. L., Sordo, J. A., & Flórez, R. (1990). Theoretical study of adsorption of hydrocarbons on graphite. **Journal of Computational Chemistry**. 11(3): 291-296.
- Specovius, J., & Findenegg, G. H. (1980). Study of a Fluid/Solid Interface over a Wide Density Range Including the Critical Region. I. Surface Excess of Ethylene/Graphite. 84(7): 690-696.
- Steele, W. A. (1978). The interaction of rare gas atoms with graphitized carbon black. **The Journal of Physical Chemistry**. 82(7): 817-821.
- Steele, W. A. (1996). Monolayers of Linear Molecules Adsorbed on the Graphite Basal Plane: Structures and Intermolecular Interactions. **Langmuir**. 12(1): 145-153.
- Steele, W. A. (2008). Chapter Eight - Wetting Phenomena. In E. J. Bottani & J. M.D. Tascón (Eds.), *Adsorption by Carbons* (pp. 167-185). Amsterdam: Elsevier.
- Sutton, M., Mochrie, S. G. J., & Birgeneau, R. J. (1983). Direct Observation of Layer-by-Layer Wetting of Graphite by Ethylene. **Physical Review Letters**. 51(5): 407-410.
- Terlain, A., & Larher, Y. (1983). Phase diagrams of films of linear molecules with large quadrupole moments (CO<sub>2</sub>, N<sub>2</sub>O, C<sub>2</sub>N<sub>2</sub>) adsorbed on graphite. **Surface Science**. 125(1): 304-311.

- Ulbricht, H., Zacharia, R., Cindir, N., & Hertel, T. (2006). Thermal desorption of gases and solvents from graphite and carbon nanotube surfaces. **Carbon**. 44(14): 2931-2942.
- Volkman, U. G., & Knorr, K. (1991). Multilayer growth and wetting behavior of nitrogen physisorbed on graphite. **Physical Review Letters**. 66(4): 473-476.
- Xu, H., Phothong, K., Do, D. D., & Nicholson, D. (2021). Wetting/non-wetting behaviour of quadrupolar molecules (N<sub>2</sub>, C<sub>2</sub>H<sub>4</sub>, CO<sub>2</sub>) on planar substrates. **Chemical Engineering Journal**. 419: 129502.
- Yao, M., & Ohmasa, Y. (2001). Wetting phenomena for mercury on sapphire. **Journal of Physics: Condensed Matter**. 13(15): R297-R319.
- Youn, H. S., & Hess, G. B. (1990). Wetting and melting behavior of oxygen films on graphite. **Physical Review Letters**. 64(4): 443-446.
- Zhou, X., Feng, M., Niu, H., Song, Y., Li, C., & Zhong, D. (2016). Adsorptive recovery of ethylene by CuCl<sub>2</sub> loaded activated carbon via  $\pi$ -complexation. **Adsorption Science & Technology**. 34(6): 355-367.



## CHAPTER VI

### INCOMPLETE WETTING OF ETHANOL ON A GRAPHITE SUBSTRATE

#### Abstract

Extensive computer simulations for ethanol adsorption on a graphite were carried out to investigate the transition from incomplete wetting of bilayer adsorption to beyond bilayer adsorption over the temperature range from 190 K to 298 K. Then the simulation results were compared against the high-resolution experimental data of ethanol adsorption on a highly graphitized thermal carbon black (GTCB). At 190 K, we observed incomplete wetting at the bulk coexistence pressure,  $P_0$ , at which the adsorbed film consists of only 1.4 times of the statistical monolayer density even this temperature is 32 K above the bulk triple point temperature. Molecules in the first layer have their ethyl groups essentially lying flat on the graphite surface to maximize the dispersive interactions while the OH groups point away from the surface to facilitate hydrogen bonding with the OH groups of molecules in the second layer. This results in only the ethyl groups exposing to molecules in the gas phase, and therefore, hydrogen bonding is essentially absent in the interactions between molecules in the gas phase and the bilayer adsorbed film, which even persists at the bulk coexistence pressure. The wetting beyond bilayer was found at 298 K, observed with experimental data and computer simulation results. At this temperature, the thermal fluctuations are significant, and therefore the OH groups of molecules in the second layer do not have a preferential orientation enabling the formation of the third layer, which in turn induces the formation of higher layers, once again due to the non-preferential orientation of OH groups.

## 6.1 Introduction

The wetting/incomplete wetting/non-wetting of adsorbate on surfaces has attracted research interests over the last few decades due to its importance in many applications such as biomaterials (Wu *et al.*, 2010), coating on nanomaterial, sensor (Reisch *et al.*, 2009) as well as microparticle production (Sung *et al.*, 2008). As a result, wetting/non-wetting phenomena have also been studied experimentally and theoretically (Bojan *et al.*, 1999; Cheng *et al.*, 1991; Dietrich & Schick, 1986; Drir *et al.*, 1986; Patra *et al.*, 2015; Rutledge & Taborrek, 1992), and comprehensive reviews on this topic have been reported by Saam (Saam, 2009) and Gatica and Cole (Gatica & Cole, 2009). In colloidal sciences, the wettability is commonly characterized by the contact angle (Steele, 2008) while in adsorption sciences, the non-wetting/wetting behaviour of adsorbate on solid substrates is determined by analyzing adsorption isotherms for a range of temperature at the bulk coexistence pressure (Steele, 2008). For systems that exhibit a complete wetting behaviour, the thickness of the adsorbed layer increases with pressure and tends to infinity when the pressure approaches the bulk coexistence pressure,  $P_0$ . An incomplete (or partial) wetting occurs when the adsorption isotherm crosses the bulk coexistence pressure at a finite adsorbed density (*i.e.*, a finite number of adsorbate layers on the substrate), typically observed for moderately weak adsorbing systems. As the temperature is increased, the transition from incomplete wetting to complete wetting occurs. For non-wetting systems, only small clusters of adsorbate molecules are formed on the substrate at  $P_0$ , at which the overall adsorbed density is less than the statistical monolayer density. In the absence of strong sites in the system, these clusters grow under supersaturation conditions (*i.e.*, pressure greater than  $P_0$ ), up to the point when these clusters coalesce. A non-wetting system can become either complete wetting or incomplete wetting as the temperature increases. The temperature for the transition from non-wetting to complete wetting is called the wetting temperature,  $T_w$ , defined as the temperature at which the adsorbed density tends to infinity at  $P_0$ . The temperature, at which the transition from non-wetting to incomplete wetting is called the layering temperature for the first layer ( $T_{L,1}$ ) because only one layer is formed at  $P_0$ . As the temperature is further increased beyond  $T_{L,1}$  there are two possible situations: (1) there are transitions to form additional layers,

one layer at a time, and the temperatures for these transitions are  $T_{L,n}$ , and when the temperature has reached the roughening temperature,  $T_R$ , complete wetting occurs, e.g., argon adsorption on planar substrates (Prasetyo *et al.*, 2020), and (2) the system remains incomplete wetting with no clear layering of higher layers and when the  $T_R$  has been reached, complete wetting occurs, e.g., carbon dioxide adsorption on graphite (Xu *et al.*, 2019).

A measure of wetting/non-wetting phenomena is the parameter  $D^*$  (we use the same terminology from the previous chapter), defined as the ratio of the minimum of the molecular solid-fluid potential ( $u_{SF}$ ) energy to the minimum if the molecular fluid-fluid potential ( $u_{FF}$ ) energy:

$$D^* = |u_{SF}|_{\min} / |u_{FF}|_{\min} \quad (6.1)$$

A system with a large  $D^*$  is a strongly adsorbing system for which a behaviour of either incomplete wetting or complete wetting is expected due to the strong interaction between adsorbate and adsorbent. An example for this system in argon adsorption on graphite for which  $D^* = 9$  (Prasetyo *et al.*, 2020). On the other hand, a system having small value of  $D^*$  exhibits non-wetting system because of the weak interactions between adsorbate and adsorbent. For systems having intermediate values of  $D^*$ , they exhibit non-wetting behaviour at low temperatures, and incomplete wetting and complete wetting occurs as the temperature is increased. An example for this is the carbon dioxide adsorption on graphite system (Terlain & Larher, 1983; Xu *et al.*, 2019), whose  $D^*$  is 3.3. Carbon dioxide does not wet the graphite for temperature less than 90 K, and incomplete wetting of less than two statistical layers occurs for temperature between 90 K to 195 K and complete wetting occurs for temperatures beyond the bulk triple point temperature. Another example of this category is ammonia adsorption on graphite (Loi *et al.*, 2019). The methanol adsorption on graphite with  $D^*$  of 0.53 shows an interesting transition from an incomplete wetting of bilayer adsorbed film to complete wetting as the temperature is increased. At 190 K, methanol forms two layers on graphite substrate at  $P_0$ , and when the temperature is increased to 283 K, the system displays complete wetting at  $P_0$ . The behaviour of either incomplete

wetting or complete wetting rests with the orientation of the OH groups of methanol molecules in the first layer (Prasetyo *et al.*, 2019).

The parameter  $D^*$  is only valid at zero Kelvin as it does not account for the thermal fluctuations and the increasing interactions among adsorbed molecules with the progress of adsorption. To better understanding the wetting behaviour, a parameter  $\Omega$  which is a measure of the isosteric heat of adsorption  $q_{st}$  relative to the heat of phase change (condensation or sublimation),  $\lambda_{cond/sub}$ , suggested by Liu *et al.* (Liu, Liu, *et al.*, 2019), Loi *et al.* (Loi *et al.*, 2019), and Prasetyo *et al.* (L. Prasetyo *et al.*, 2018):

$$\Omega = \frac{q_{st}}{\lambda_{cond/sub}} \quad (6.2)$$

In this work, we carried out Monte Carlo (MC) simulation with the grand canonical (GC) ensemble to investigate the wetting transition behaviour for ethanol adsorption on graphite. The experimental data are used to support the validity of the molecular model and to provide credibility of the derivation of the adsorption isotherms. We also point out the possible parameters that influence the adsorption behaviour of ethanol adsorption on homogeneous substrate in the simulation. Since ethanol is one of the associating fluids, a normal scheme of the simulation could not describe the experimental data very well. So, we expect a new and improved scheme of MC simulation could be used to duplicate the experimental data.

## 6.2 Simulation Model

### 6.2.1 Fluid-Fluid Potential

The TraPPE UA Force Field of ethanol by Chen, Potoff, and Siepmann (B. Chen *et al.*, 2001) is employed here to study the vapor-liquid equilibria (VLE) and adsorption of ethanol on graphite substrate. The origin point of the model is  $\text{CH}_2$  group which comes with charge, while  $\text{CH}_3$  has no charge. The oxygen atom carries negative charge, and the rest of positive charge is on H atom. The H atom has no collision diameter, only charge exists. Details of reduced well depth, collision diameter, and

partial charge are listed in Chapter II. Please see a schematic drawing of the potential model in *Figure 6.1*.

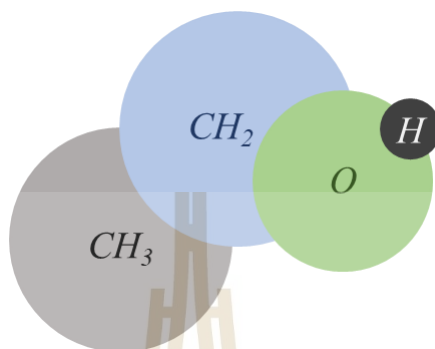


**Figure 6.1** Schematic drawing of the TraPPE UA ethanol molecule.

### 6.2.2 Solid-Fluid Potential

The graphite surface was modelled using Steele 10-4-3 solid (Steele, 1978), the details are similar to the previous chapter for the wetting of ethylene on planar substrate. However, from the LB mixing rule, the binary interactions parameter ( $k_{sf}$ ) is zero for the ethanol adsorption on graphite substrate.

The MC simulation was carried out to study the adsorption of ethanol on graphite,  $5.0 \times 10^6$  cycles were utilized in the equilibration stage and the same number of cycles were used in the production stage. This is due to ethanol is large molecule with dipole moment, the high number of cycles is to make sure system has reached equilibrium. In the equilibration stage, the maximum displacement length was initially set as 2.0 nm and adjusted at the end of each cycle to give an acceptance of 20% (Mountain & Thirumalai, 1994) and kept constant in the sampling stage. In each cycle, there are 1,000 moves of displacement, deletion or insertion moves, and sigma bond rotation of molecules chosen with equal probability. The cut off radius was 10 times of the collision diameter of the  $\text{CH}_3$  group. The Periodic Boundary Conditions (PBC) were applied in the x- and y-direction. The dimensions of simulation box were  $7.5 \times 7.5 \times 10.0 \text{ nm}^3$ . The homogeneous graphite surface was placed at the bottom of the simulation box, while the top of the box was a hard wall. The chemical potential

as a given temperature and pressure was calculated using the equation of state (EoS) by Johnson *et al.* (Johnson *et al.*, 1993), this was used as input in the MC simulation.

### 6.2.3 Adsorption Measurement

A highly graphitized thermal carbon black, Carbopack F (Supelco, USA), was used as an adsorbent. Its properties have been presented elsewhere (Horikawa, Takenouchi, *et al.*, 2015; Horikawa, Zeng, *et al.*, 2015). Carbopack F consists of polyhedral particles with homogeneous graphene layers on the faces of each polyhedron, with no micropores detected. Ethanol adsorption isotherms on Carbopack F were obtained using a high-resolution volumetric adsorption apparatus (BELSORP-max, MicrotracBEL, Japan) equipped with a cryostat system (BELCryo, MicrotracBEL, Japan). The studied temperatures are 190 K, 250 K, and 298 K. Before each measurement, the Carbopack F was outgassed at 573 K for 6 hours under a high vacuum of less than 0.1 mPa to eliminate any adsorbed substances on the adsorbent.

## 6.3 Results and Discussion

We first calculate the ratio of  $D^*$  using Equation (6.1) to determine how strong is it for the adsorption of ethanol on graphite substrate. *Figure 6.2* shows the potential energy of the ethanol molecule interacting with graphite, and the intermolecular potential energy. This system gives  $D^*$  of 0.75, so the ethanol adsorption on graphite system is weak adsorbing substrate.

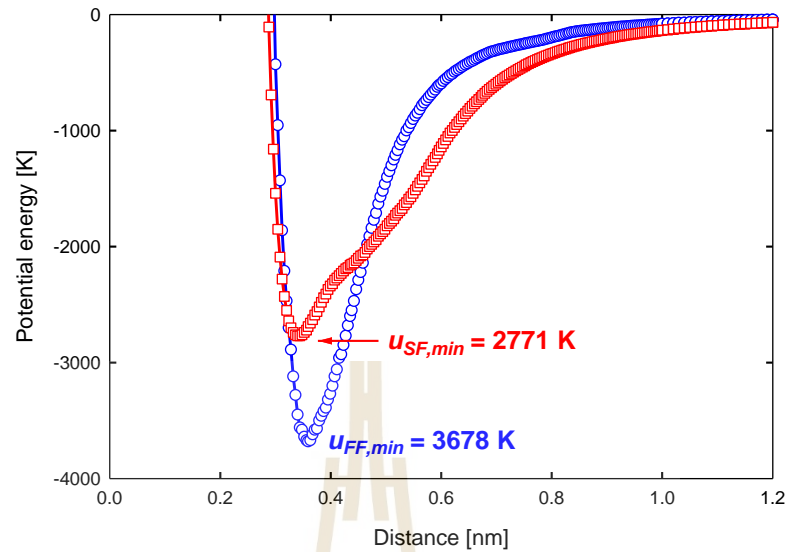


**Figure 6.2** The potential energy between ethanol, optimally oriented, and graphite as a function of the separation distance between the centre of geometry of ethanol and graphite (red squares), and the intermolecular potential energy as a function of the distance between the centres of geometry of two ethanol molecules, both of which are optimally oriented to maximize the interaction (blue circles).

Equation (6.2) is the ratio between isosteric heat,  $q_{st}$ , to the heat of phase change,  $\lambda_{cond/sub}$ , both of which are function of temperature. The heat of phase change decreases with temperature while the isosteric heat is a complex function of temperature and the loading, and this makes the analysis of wetting an interesting problem to deal with (Do *et al.*, 2008). The heat of phase change describes the cohesiveness of the adsorbate while the isosteric heat is a measure of the adhesiveness of the adsorbed film. Hence if  $\Omega$  is less than unity, the system would favour the bulk phase and non-wetting is expected to occur, and when  $\Omega > 1$  the system would favour wetting. *Figure 6.3a* shows the isosteric heat at zero loading and the heat of phase change as a function of temperature, and the plot of  $\Omega^0$  is shown in *Figure 6.3b*. One point that we would like to stress at this point is that even at temperature at which  $\Omega^0$  is less than unity it does not mean that wetting does not occur because this parameter is at zero loading, as the loading is increased, the contribution from the

adsorbate-adsorbate (FF) interactions can make the parameter  $\Omega$  greater than unity, hence wetting is resulted.

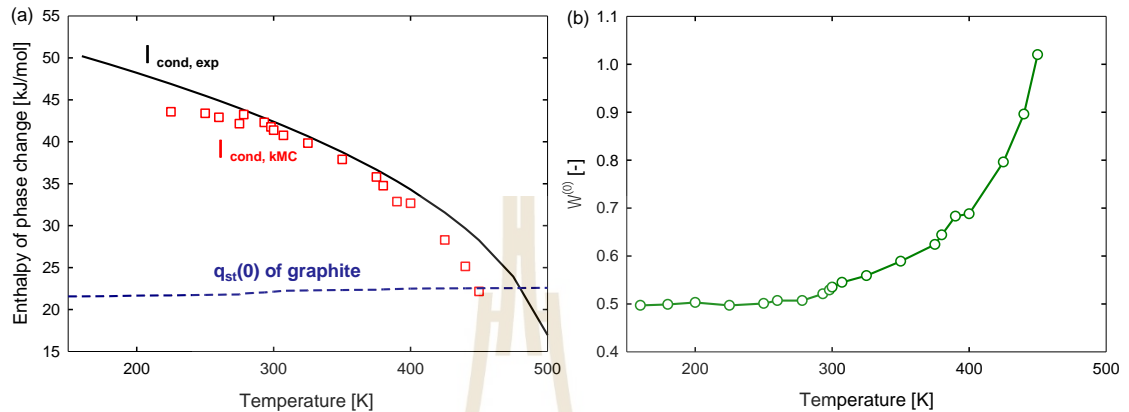


**Figure 6.3** (a) The isosteric heat of adsorption at zero loading,  $q_{st}^0$ , obtained via Monte Carlo Integration (MCI) (Do *et al.*, 2008) for ethanol on graphite substrate (blue dash line) as a function of temperature. The simulated heat of condensation obtained from the canonical kMC scheme (Nguyen *et al.*, 2016) is also plotted on the same figure (red squares). (b) The ratio between  $q_{st}^0$  and  $\lambda_{cond}$  as a function of temperature.

To properly assess the wetting behaviour of the system at the bulk coexistence pressure,  $P_\theta$ , its determination must be correctly calculated. The bulk coexistence pressure above the bulk triple point temperature were determined with the canonical kinetic Monte Carlo (kMC) scheme (Nguyen *et al.*, 2016), and the results are in good agreement with the experimental data (Green & Southard, 2019) as presented in *Table 6.1*.

**Table 6.1** Exact values of temperature and bulk coexistence pressure used in the simulation.

Temperature (K)	Experimental $P_0$ (Pa)	Simulated $P_0$ (Pa)
190.82	0.2388	0.2353
199.35	0.8731	0.8638
249.236	242.6	252.3
283.15	3152	3170
298.15	7927	7936

The canonical ensemble in kMC scheme also gives the vapour-liquid coexistence density of ethanol. *Figure 6.4* shows the experimental data of vapour-liquid coexistence density of ethanol (Green & Southard, 2019) (black dashed line) and the simulation results obtained via canonical kMC scheme (Nguyen *et al.*, 2016). The vapour-liquid coexistence curves from simulation are in good agreement with experimental data at high temperature, which comes as no surprised, because the potential parameters of ethanol were extracted from VLE at high temperature, between 300 K to 495 K (Bin Chen *et al.*, 2001; Eggimann *et al.*, 2020). While the potential model fails to describe the liquid density of ethanol at low temperature.

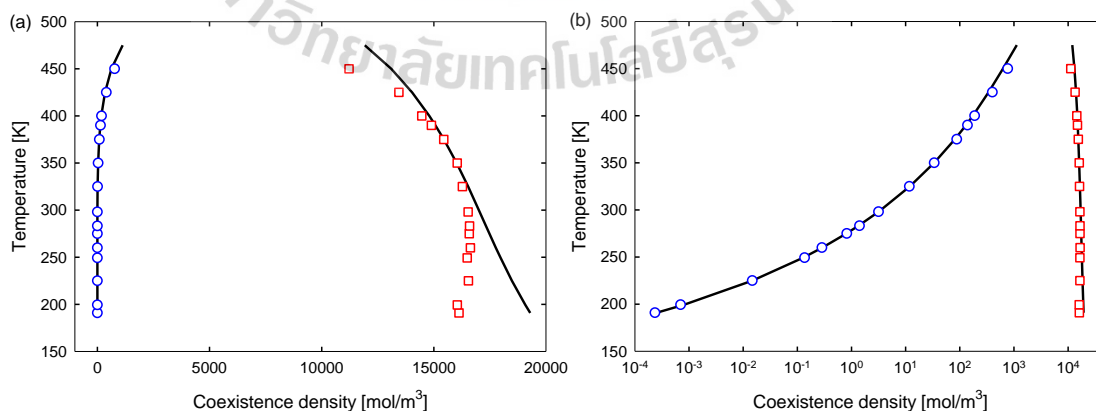


**Figure 6.4** (a) The simulated coexistence density of ethanol (blue circles and red squares) obtained from VLE simulation and experimental data are in black dash line. (b) Plots are in semi-log scale to emphasize low density region.

### 6.3.1 Possible Parameters that Influence Adsorption Behaviour

Firstly, we would like to point out the possible parameters in the simulation that influence the adsorption behaviour of ethanol on a graphite substrate. In this work, we use Steele 10-4-3 homogeneous graphite surface as a reference in the simulation (Steele, 1978). The experimental isotherm of ethanol adsorption on Carbpacck F compared with the simulated isotherm from simulation at 190 K (well above the bulk triple point temperature of 150 K) are shown in *Figure 6.5*. The results show that the isotherm from simulation not only cannot describe the monolayer density of ethanol on graphite, but also fails to describe the formation of a second layer as well.

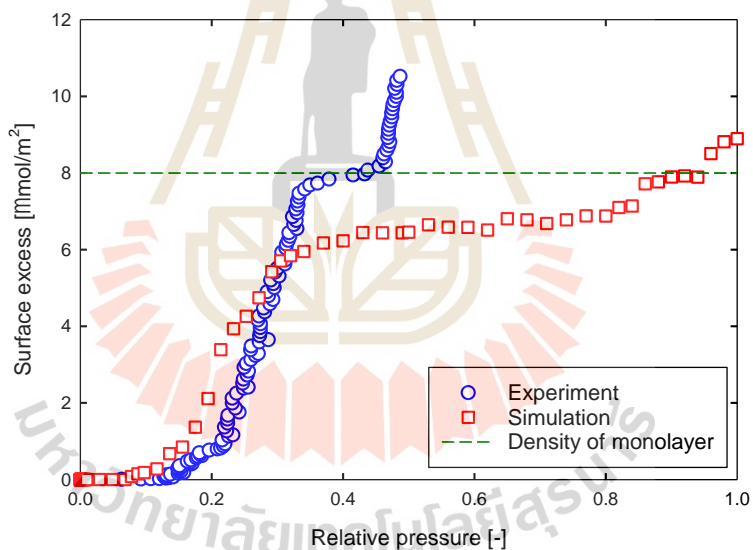


**Figure 6.5** Experimental and simulated adsorption isotherms of ethanol on homogeneous graphite surface at 190 K. Experimental data are in blue circles, while red squares are the simulated data. The green dash line is used to represent the statistical monolayer density of ethanol from the experimental data.

The issue that is facing us is the failure in the description of the experimental monolayer density of  $8.0 \mu\text{mol}/\text{m}^2$ , this is comparable with the experimental data of Avgul *et al.* in 1961 that they reported the monolayer density of

ethanol adsorption on highly graphitized thermal carbon black (GTCB) at  $7.5 \mu\text{mol}/\text{m}^2$  (Avgul *et al.*, 1961). Nonetheless, the simulation only gives  $6.4 \mu\text{mol}/\text{m}^2$ . This has a consequence in the description of the second layer formation, and it is the underprediction of the first layer that leads to the smaller affinity for the second layer to form. As a result, the simulation fails to describe the formation of the second layer. What to follow are the various issues that we will discuss to determine the possible failure of the simulation.

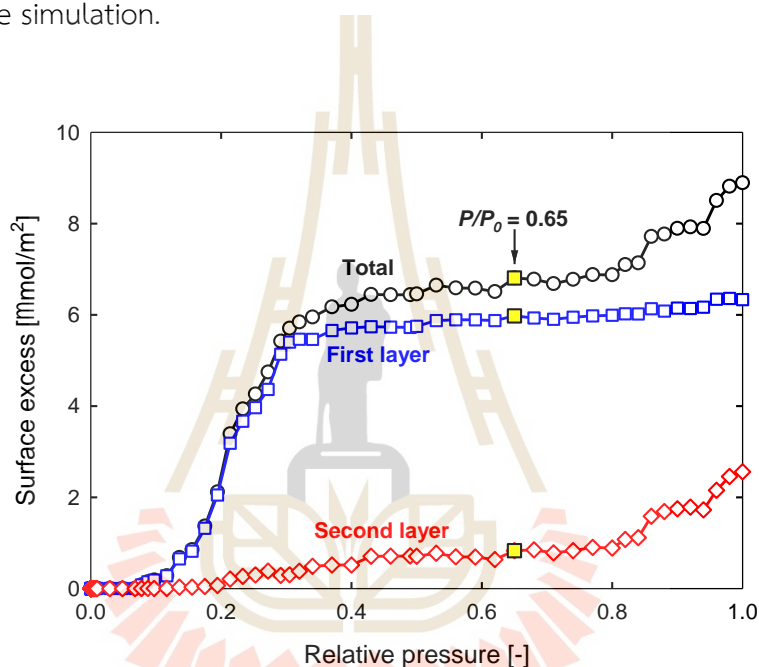


**Figure 6.6** Simulated adsorption isotherms of ethanol adsorption on graphite surface at 190 K, showing the contributions from first- (blue squares) and second layer (red diamonds) and total isotherm in black circles.

In *Figure 6.6*, the first layer seems to be completely dense at a relative pressure of 0.65, and the onset of the initial adsorption of the second layer starts at  $P/P_0 \sim 0.2$ , well before the first layer is completed. The snapshot of molecular configurations at this point is shown in *Figure 6.7*, where we see the first layer is, in fact, not completely dense as there are vacancies on the graphite surface. These vacancies are not sufficiently large for ethanol molecules to squeeze into, and if they agglomerate to form larger vacancies whose size are large enough to accommodate more ethanol molecules to enter the first layer. One possible reason is the size of the

graphite used in the simulation because as discussed above the initial adsorption has led to the formation of clusters of tetramer and pentamer and they act as large quasi molecules on the surface. With this large size of quasi-molecules, the surface dimension of  $7.5 \times 7.5 \text{ nm}^2$  is not large enough for clusters to displace and coalesce and at the same time large vacancies are created for the insertion of ethanol molecules. This might be the one of the reasons that the monolayer density obtained by simulation is wrong. We substantiate this assertion by considering methanol adsorption on graphite that was studied earlier. With the same dimension of graphite of  $7.5 \times 7.5 \text{ nm}^2$ , it was able to describe the experimental data very well, including the bilayer adsorption at  $P_0$  and 190 K. This is because methanol molecule is smaller than ethanol, and the clusters of tetramer and pentamer are small and when they coalesce, vacancies are created and they sufficiently large enough for methanol to squeeze into the first layer. Consequently, the isotherms were able to describe very well, including the correct description of the monolayer density (Prasetyo *et al.*, 2019). Thus, we concluded that the graphite dimension is one of the possible reasons. Another possible reason is the shape of graphite. Is it possible that ethanol clusters coalesce and create greater vacancies when the graphite takes a rectangular shape. Thus, more ethanol molecules can compress into the vacancies. However, larger surface dimension can lead to consumption of long computation time due to the huge number of molecules in the system, this is illustrated in the next paragraph.

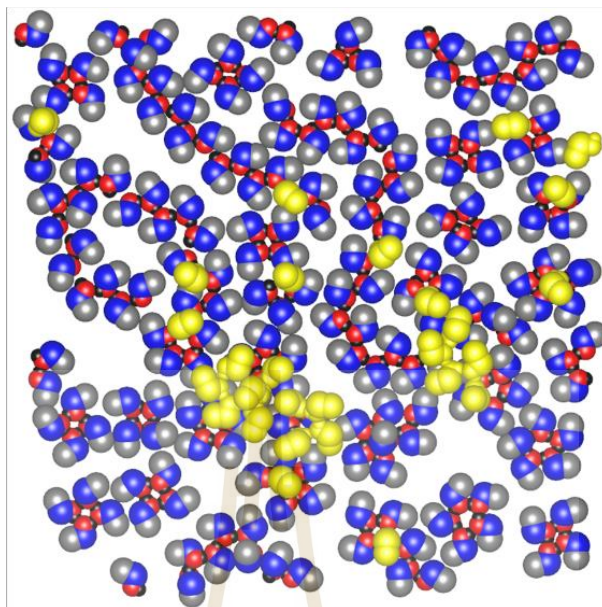


**Figure 6.7** Snapshot of ethanol adsorption on graphite at 190 K, at  $P/P_0 = 0.65$  as marked in *Figure 6.6*, where blue, grey, red, and black represent  $\text{CH}_2$ ,  $\text{CH}_3$ , O, and H atoms. The yellow molecules show ethanol in second layer.

Another reason is the length of the simulations. Ethanol is a large molecule with direction bonding of molecule, long simulation is required. We test this reason with the plots of control charts of the number of molecules and the system configuration energy as a function of cycle with 1,000 of trial moves in each cycle. They are shown in *Figure 6.8*.

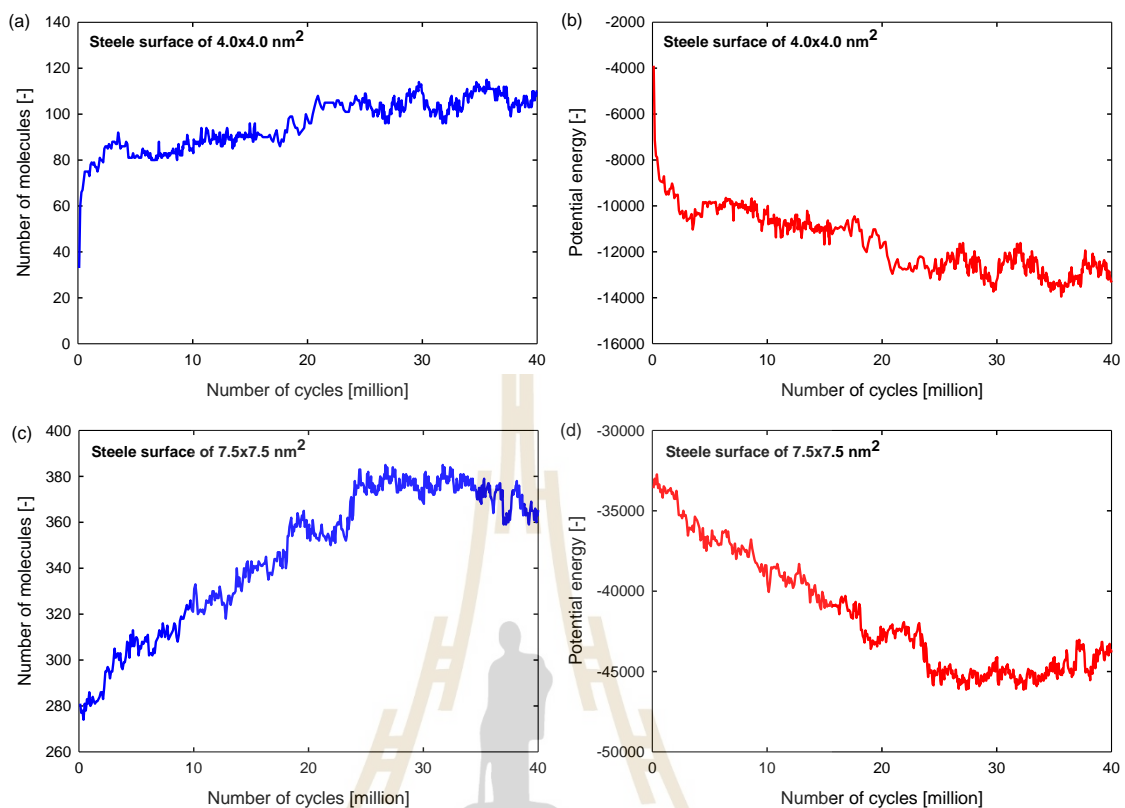


**Figure 6.8** Control charts of ethanol adsorption on graphite at 190 K and bulk coexistence pressure. (a) and (b) for graphite dimension of 4.0×4.0 nm<sup>2</sup>, while (c) and (d) for graphite dimension of 7.5×7.5 nm<sup>2</sup>.

Even with the smallest graphite surface at 4.0×4.0 nm<sup>2</sup> (see *Figure 6.8a* and *b*), the number of molecules required to form a monolayer is lowest, compared to other systems, equilibrium is not reached after 40 billion configurations have been executed. As seen in the progressive increase in the number of molecules and the progressive decrease of the potential energy. The same is true for graphite dimension of 7.5×7.5 nm<sup>2</sup> (see *Figure 6.8c* and *d*). Therefore, extremely long simulations are required for ethanol to reach equilibrium. Direction bonding is an issue that leads to the requirement of long simulation to achieve equilibrium. This is indeed also true for water adsorption of surface or in pore because of its greater extend of direction bonding despite of its small size compared to ethanol (Liu, Zeng, *et al.*, 2019).

As mentioned in the previous paragraph, the direction bonding is also an issue in the simulation. This could be resolved by applying new scheme in the MC simulation. Usually in the GC ensemble, there are three main trial moves which are, displacement, insertion, and deletion of the molecules in the simulation during the equilibration stage. We come up with the new idea of move, which is the rotation of bond between OH and CH<sub>3</sub> groups in ethanol molecule. Perhaps, this could allow ethanol molecule to rotate their bond freely, consequently, once the bond is in the optimum position, the ethanol molecules can compress themselves into the vacancies between clusters of ethanol in the first layer. This new scheme in the simulation could solve the issue of monolayer density and lead us to the correction of the adsorption behaviour of ethanol in the simulation.

Before we turn into the discussion of ethanol adsorption on graphite, a short conclusion can be drawn at this point that the *size* and *shape of graphite* also the *length of simulation* are critical in the convergence to equilibrium. Subject to the practical availability of the supercomputer time, a judicious choice of these variables and parameters is of paramount importance.

### 6.3.2 Adsorption of Ethanol on Graphite

#### 6.3.2.1 Henry's Law Region

We first consider the simulated results at low loading (Henry's law region). The simulated adsorption isotherms of ethanol on graphite are shown in *Figure 6.9* for a wide range of temperatures from 160 K to 400 K. For a given reduced pressure, the adsorbed density of ethanol increases with temperature in the Henry law region. This is simply due to the fact that the parameter  $\Omega^\circ$  is less than unity for temperatures less than 450 K (see *Figure 6.3*), and this behaviour was also observed with methanol adsorption on graphite (Prasetyo *et al.*, 2019). It contrasts with noble gases adsorption on graphite (L. Prasetyo *et al.*, 2018; Luisa Prasetyo *et al.*, 2018; Zeng *et al.*, 2017), where parameter  $\Omega^\circ$  is greater than unity, resulting in the adsorbed density always decreases with temperature for a given reduced pressure.

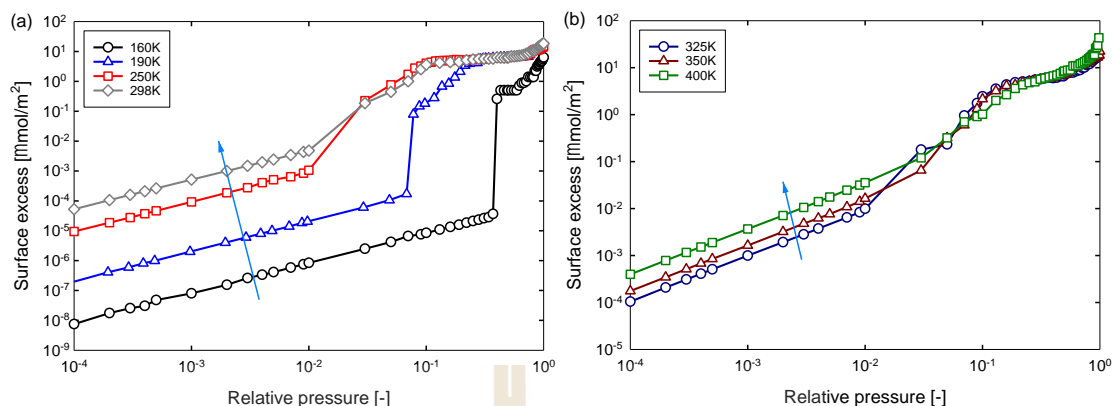


**Figure 6.9** Simulated adsorption isotherms for ethanol adsorption on graphite, plotted in terms of the surface excess density versus the reduced pressure; (a) 160 K to 298 K and (b) 325 K to 400 K.

The first order transition is also captured for the ethanol adsorption at low temperature, e.g., 160 K and 190 K. This is certainly due to the ethanol molecules on graphite surface form clusters of tetramers or pentamers since adsorbate-adsorbate (FF) interactions are very strong as compared to the adsorbate-adsorbent (SF) interactions, this will be further discussed in the isosteric heat of adsorption.

### 6.3.2.2 High Loadings

To show the behaviour of adsorption at high loadings (beyond the Henry's law region), we plotted the simulated adsorption isotherms with respect to the reduced pressure in linear scales in *Figure 6.10*. Isotherms for temperatures greater than 250 K show Type III behaviour for low loadings and becomes Type II at high loadings according to the IUPAC isotherm classification (Thommes *et al.*, 2015). For temperature less than 375 K, incomplete wetting is observed as evidenced in *Figure 6.10b*, where the isotherms crossing the  $P_0$  axis at finite loading which increases with temperature, and complete wetting occurs for temperatures greater than 400 K, suggesting that the roughening (Larher & Angerand, 1988; Tan *et al.*, 2019) temperature is between 375 K and 400 K. This complete wetting temperature is much greater than the bulk triple point temperature of 158 K. It is distinctly different from simple gases for which wetting occurs for temperatures greater than the bulk triple point

temperature, and this highlights the role of hydrogen bonding in associating fluids that makes them to behave in an interesting manner.

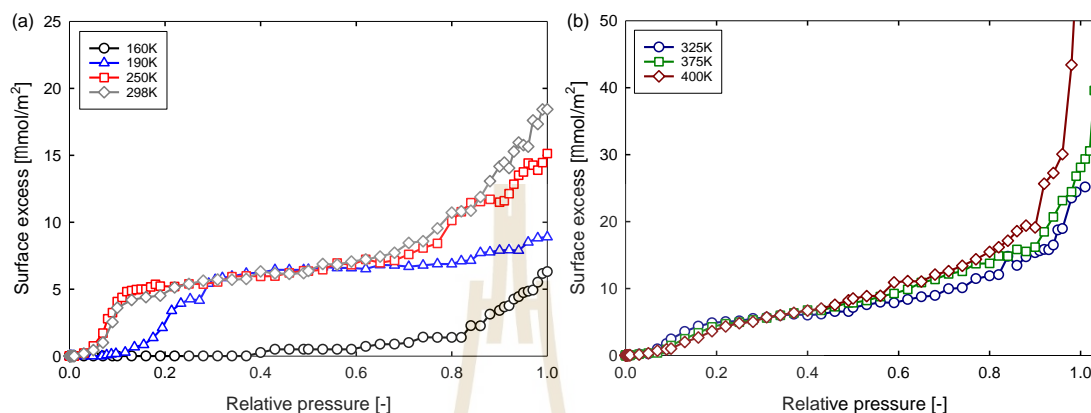


**Figure 6.10** Simulated adsorption isotherms for ethanol adsorption on graphite, plotted in terms of the surface excess versus the reduced pressure in linear scales to highlight the high loading region, for a range of temperatures from (a) 160 K to 298 K and (b) from 325 K to 400 K.

We take 160 K as an example of incomplete wetting (see *Figure 6.10a*), its isotherm crosses the  $P_0$  axis at a loading close to the statistical monolayer density (this does not mean that a monolayer is formed on the surface, but rather the total number of molecules in the form of clusters scattering on the surface is the same number required to form a monolayer), indicating an incomplete wetting behaviour. As the temperature is increased, but less than the wetting temperature, the adsorbed density at  $P_0$  increases with temperature, and this is due to the thermal fluctuations such that the interface between the adsorbed film and the bulk gas is undulating, providing strong adsorption sites that facilitate the formation of more layers. For temperature greater than 298 K, the isotherms have Type III behaviour, and the onset of the adsorption occurs at a reduced pressure of  $\sim 0.1$ , beyond which the isotherms exhibit Type II behaviour, and complete wetting occurs at temperature of 400 K and greater.

### 6.3.2.3 Ethanol Adsorption on Carbopack F

The experimental isotherms for ethanol adsorption on Carbopack F at various temperatures are presented in *Figure 6.11a*, and the simulated isotherms are displayed in *Figure 6.11b*. At 190 K, the onset of the experimental isotherm occurs at reduced pressure of 0.25 and the isotherm crosses the bulk coexistence pressure at a loading about  $16 \mu\text{mol}/\text{m}^2$ , exhibiting an incomplete wetting. For 298 K, the onset of the isotherm occurs at  $P/P_0 \sim 0.1$  and the adsorbed amount tends to infinity as the pressure approaches the bulk coexistence pressure, a feature of complete wetting which is not observed in our simulation results. In fact, as mentioned in the last section, simulation results predict wetting to occur only for temperatures at 400 K and greater. We already discussed the possible parameters in the simulation that influence the results in section 6.3.1. However, the simulated adsorption isotherms are in qualitative agreement with the experimental data, especially the incomplete wetting behaviour is correctly described even at temperatures above the bulk triple point temperature. Lastly, we believe that the simulated results are adequately reliable to explain the basic adsorption mechanism of ethanol on graphite.

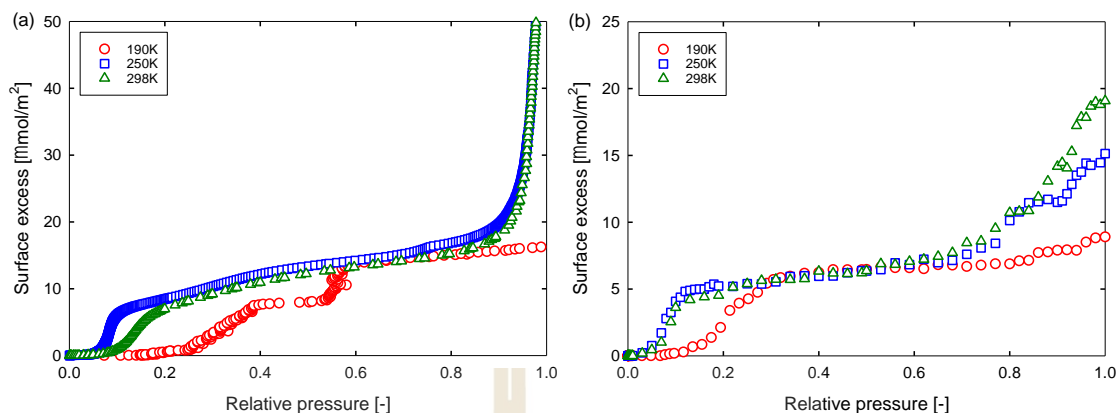


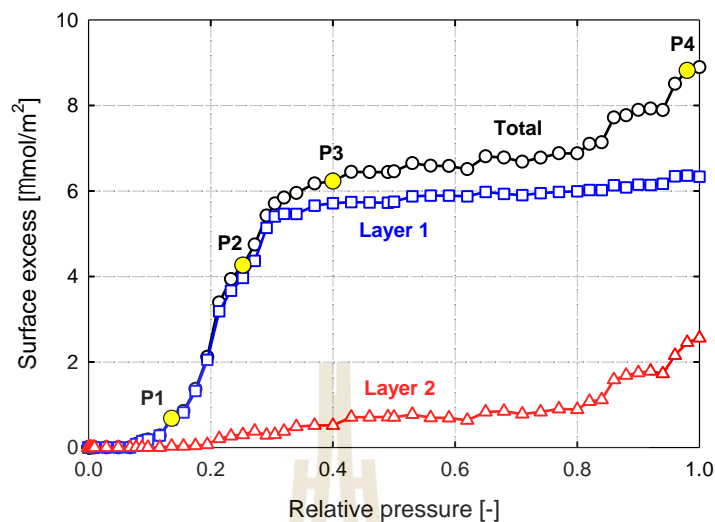
**Figure 6.11** (a) Experimental adsorption isotherms for ethanol on Carbopack F at various temperatures and (b) simulated adsorption isotherms for ethanol on graphite at various temperatures from 190 K to 298 K.

### 6.3.3 Wetting Transition

To understand the microscopic reasons behind the incomplete wetting, we investigated the isotherms, molecular configurations, local density distributions as well as the isosteric heat of adsorption of adsorbate for 190 K and 298 K to reveal the features of bilayer adsorbed film and the orientations of OH groups of ethanol molecules in these two layers.

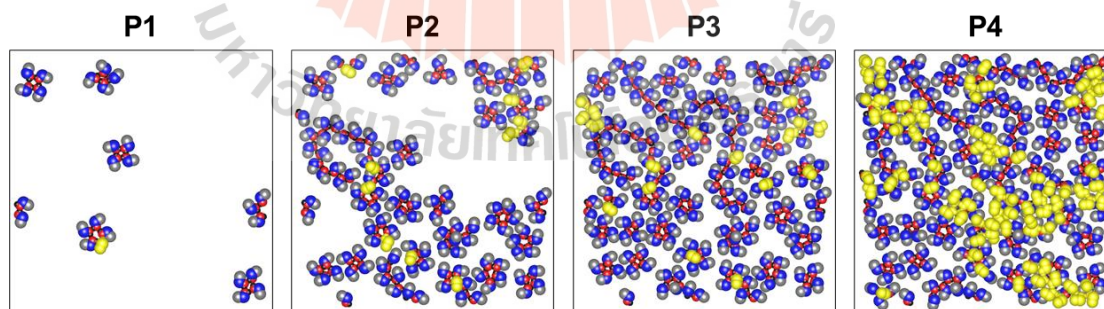
#### 6.3.3.1 Incomplete Wetting at 190 K

Figure 6.12 shows the simulated isotherm for ethanol adsorption on graphite at 190 K (32 K above the bulk triple point temperature) and its contributions from the first two molecular layers. The demarcation of these layers is done with the analysis of the local density distribution. This isotherm crosses the bulk coexistence pressure,  $P_0$ , at a loading of  $8.9 \mu\text{mol}/\text{m}^2$  which is about 1.4 times of the statistical monolayer coverage of  $6.4 \mu\text{mol}/\text{m}^2$  (according to the simulation results). This incomplete wetting behaviour is due to the lack of energetic sites between the adsorbed film and the gas phase to facilitate adsorption of further molecules to complete the second layer and to build up higher layers as the pressure has approached  $P_0$ .



**Figure 6.12** Simulated isotherms and its contributions from the first and second layers for ethanol adsorption on graphite at 190 K.

The microscopic configurations of ethanol molecules on graphite in the form of snapshots at various points as marked in *Figure 6.12* are shown in *Figure 6.13*, and the local density distribution of the various sites (CH<sub>3</sub>, CH<sub>2</sub>, O and H) on ethanol molecule (LDDs) are shown in *Figure 6.14*.



**Figure 6.13** The configurations snapshots of ethanol molecules on graphite at 190 K (not to scale) for points P1, P2, P3, and P4 as marked in *Figure 6.12*. The black, red, blue, and grey circles refer to H atom, O atom, CH<sub>2</sub> group, and CH<sub>3</sub> group, respectively, for molecules in the first layer, the yellow circles refer to molecules in the second layer.

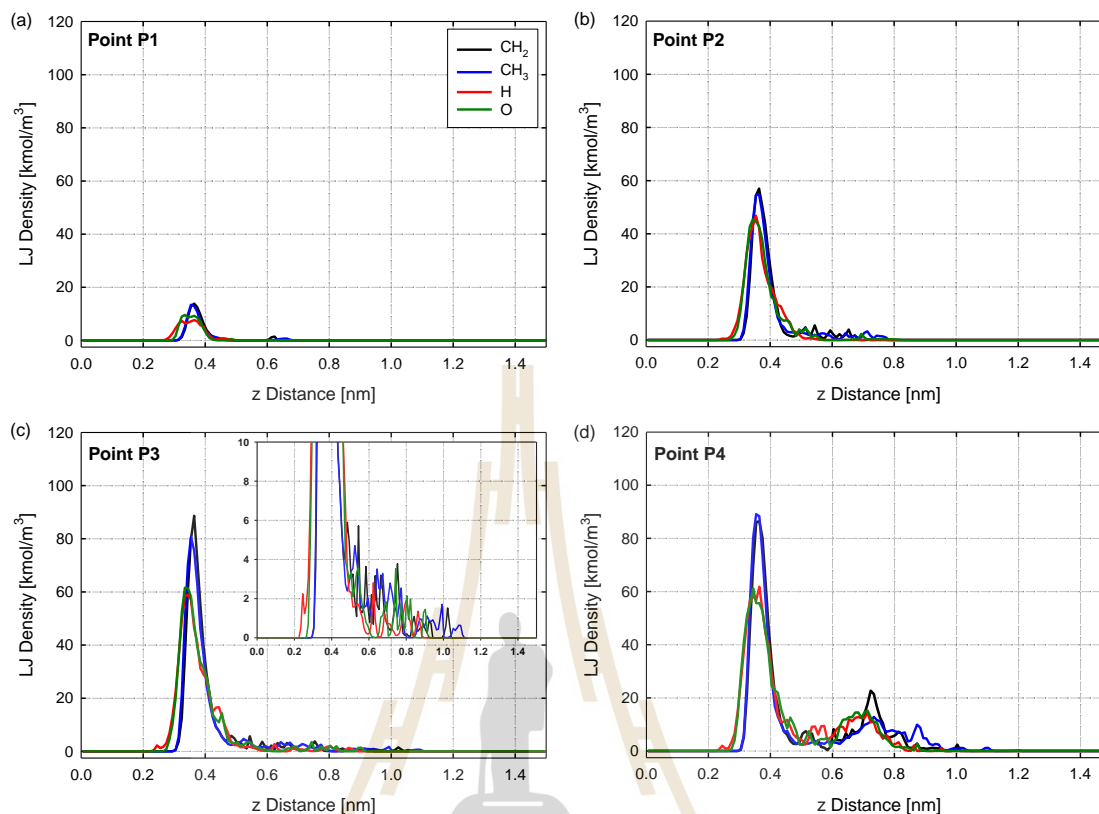


**Figure 6.14** Local density distribution (LDDs) of various sites in ethanol molecule on graphite at 190 K at points P1, P2, P3, and P4 as marked in *Figure 6.12*. The black, blue, red, and green solid lines represent CH<sub>2</sub>, CH<sub>3</sub>, H and O sites, respectively.

The characteristics of adsorption for various points are summarized below:

- Point P1 (in the sub-monolayer region,  $P/P_0 = 0.14$ ): This is the onset of the isotherm, ethanol molecule form 2D-clusters on the graphite surface with each cluster having a ring structure consisting of four or five ethanol molecules (tetramer or pentamer) to maximize the hydrogen bonding among the OH groups in a ring cluster (see *Figure 6.13*). These molecules lie flat on the surface as evidenced in the peaks of all sites on ethanol molecule at the same distance of about 0.36 nm from the surface (see *Figure 6.14a*).
- Point P2 (about 65% of the monolayer coverage,  $P/P_0 = 0.25$ ): As the loading is increased, the clusters are broken to form “zigzag” chains of ethanol

molecules because of the increasing interactions between ring clusters (see *Figure 6.13*), which is in agreement with the neutron and x-ray diffraction experiments (Herwig & Trouw, 1992; Morishige, 1992). This molecular structure is also observed experimentally (Morishige *et al.*, 1990) and by simulation (Dilokekunakul *et al.*, 2019; Prasetyo *et al.*, 2019) of the methanol adsorption on graphite as well, as methanol is one of the associating fluids. While the first layer has not been completed, ethanol molecules begin to adsorb on top of the first layer as evidenced in the isotherm in *Figure 6.12* and the snapshot in *Figure 6.13*. It is confirmed by the LDDs in *Figure 6.14b* where the appearance of the shoulder of the O and H sites lie between height of 0.4 nm to 0.6 nm from the surface, the results show that there are hydrogen bondings between first and second layers.

- Point P3 (the plateau of the first layer,  $P/P_0 = 0.40$ ): At this point, the first molecular layer is relatively dense, although not completely filled with ethanol molecules, 90% of the loading is contributed by the first layer and 10% from the second layer. The LDDs in *Figure 6.14c* also show the first peaks, while the second peaks (corresponding to the second layer) is building between the  $z$  distance of 0.6 nm to 0.8 nm. To support this, the snapshot at this reduced pressure is provided in *Figure 6.13* with the molecules in the second layer are plotted in yellow.
- Point P4 (at  $P/P_0 = 0.98$ ): As the pressure approaches the bulk coexistence pressure,  $P_0$ , the adsorbed density reached a plateau and then crossed  $P_0$  at a finite surface density of  $8.9 \mu\text{mol}/\text{m}^2$ , indicating incomplete wetting of ethanol adsorption on graphite at 190K (see *Figure 6.12*). The LDDs in *Figure 6.14d* show two distinct peaks of  $\text{CH}_2$  and  $\text{CH}_3$  groups, suggesting that adsorbate molecules form only two layers on the surface. The minor peaks for H- and O- atoms nestled between the two peaks of  $\text{CH}_2$  and  $\text{CH}_3$  indicate the presence of hydrogen bonding between molecules in the first against the second layer as illustrated in *Figure 6.15*.

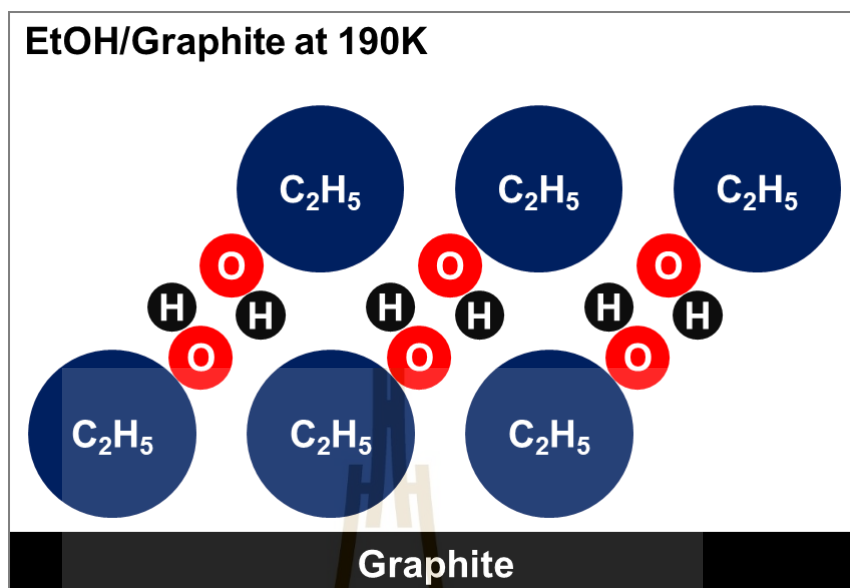


**Figure 6.15** Illustration of ethanol configuration on graphite surface at 190 K. The configuration shows hydrogen bonding between first and second layer.

To supplement the analyses of molecular configurations and LDDs, we showed in *Figure 6.16* the isosteric heat versus loading and its contributions from the adsorbate-adsorbent (SF) interactions and the adsorbate-adsorbate (FF) interactions. Since the parameter,  $\Omega^0$ , at zero loading is less than unity at 190 K, adsorption is not favourable at low loading by relying only on the SF interactions. As adsorption proceeds, the isosteric heat increases as adsorbed molecules interact with more neighbours leading to an increase in FF contributions up to point P1, at which the total isosteric heat exceeds the heat of condensation,  $\lambda_{cond}$ . Beyond P1 up to point P3 (loading less than the statistical monolayer density), the isosteric heat and its contributions from the FF and SF interactions are essentially constant, suggesting molecules lying flat on the surface and the growth of clusters by way of boundary growth (also the clusters are broken and form zigzag chains). From point P3 to point P4, the SF interactions decrease as molecules adsorb away from the surface but at the same time the FF interactions increase due to hydrogen bonding between the OH groups pointing upward from the first adsorbate layer and the OH groups of the molecules in the second layer. The total heat decreases due to the larger decrease

in SF interactions compared to the gain from the formation of hydrogen bond. Beyond point P4, the SF contribution decreases as molecules continue building on the second layer while the FF contribution remains relatively constant, approaching the heat of condensation.

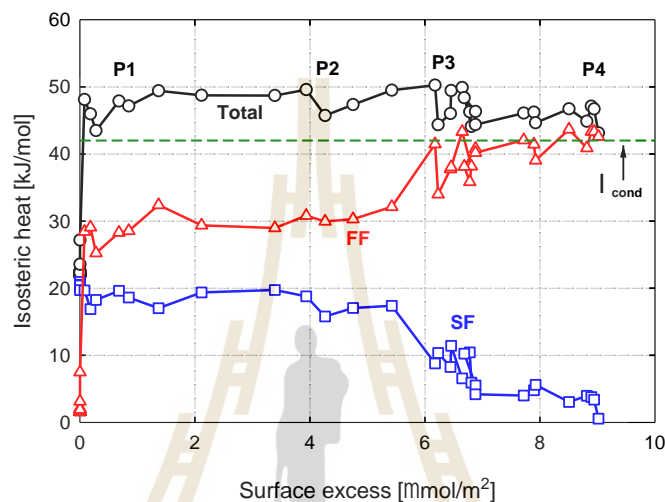


**Figure 6.16** The simulated isosteric heat and its contributions from the adsorbate-adsorbate (FF) interactions and the adsorbent-adsorbate (SF) interactions for ethanol adsorption on graphite at 190 K. The horizontal dash line is the simulated heat of condensation from the canonical kMC scheme (Nguyen *et al.*, 2016).

### 6.3.3.2 Loading Beyond Bilayer at 298 K

At 298 K, ethanol forms more than two statistical monolayers on the surface as shown in *Figure 6.17*. The isotherm shows a second order transition at a reduced pressure of about 0.1, beyond which the adsorbed density increases smoothly with increasing pressure and reaches a finite loading at  $P_0$  corresponding to approximately three statistical monolayers. For higher temperature such as 298 K, ethanol can form more than two adsorbed layers on the surface due to the entropic effect where the interactions between the layers are maximized because the adsorbed molecules have more freedom to arrange their OH sites as explained in the later sections.

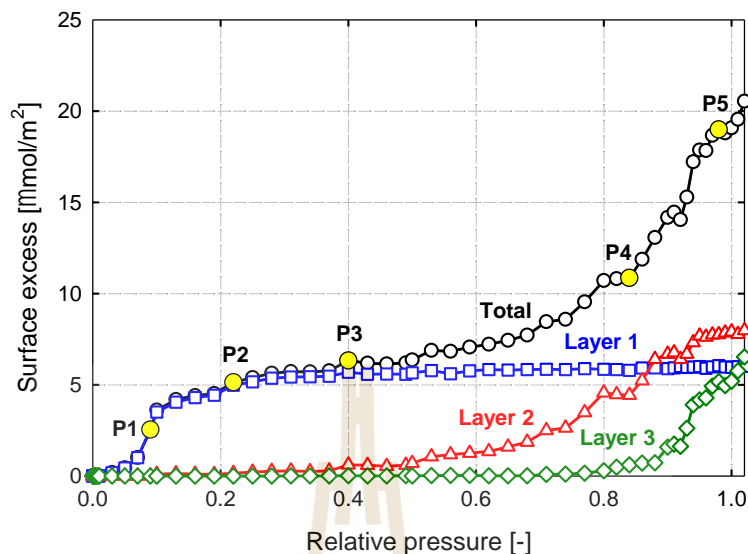


**Figure 6.17** Simulated isotherm and its contributions from the first and second layers for ethanol adsorption on graphite at 298 K.

The configurations snapshots of ethanol molecules on graphite for various points as marked on the simulated isotherm in *Figure 6.17* are shown in *Figure 6.18* and *Figure 6.19*, respectively. The results show that the microscopic structure of the adsorbed phase is quite different for ethanol adsorption at 298 K compared to 190 K. For loading at point P1 and P2 (sub-monolayer region), the ethanol molecules formed the ring clusters of four or five molecules by pointing  $\text{CH}_3$  and  $\text{CH}_2$  groups outward, while the OH groups point inward and anchor together to maximize the hydrogen bonding. This is similar to the observation at 190 K at loading below monolayer coverage. Notably, as the monolayer is forming, the “zigzag” chain configurations are absent at 298 K as opposed to 190 K due to thermal fluctuation that allows ethanol molecules to move independently. When the pressure is further increased to point P3 ( $P/P_0 = 0.40$ ), where the onset of the second layer occurs (see *Figure 6.17*) and at the same time, the first layer is almost full of ethanol molecules that lie flat on the graphite substrate as evidenced in *Figure 6.18*. This coplanar arrangement of the LJ sites is confirmed by the peaks at the same position as shown by the LDDs in *Figure 6.20a* and *b*, for the point P1 and P3.

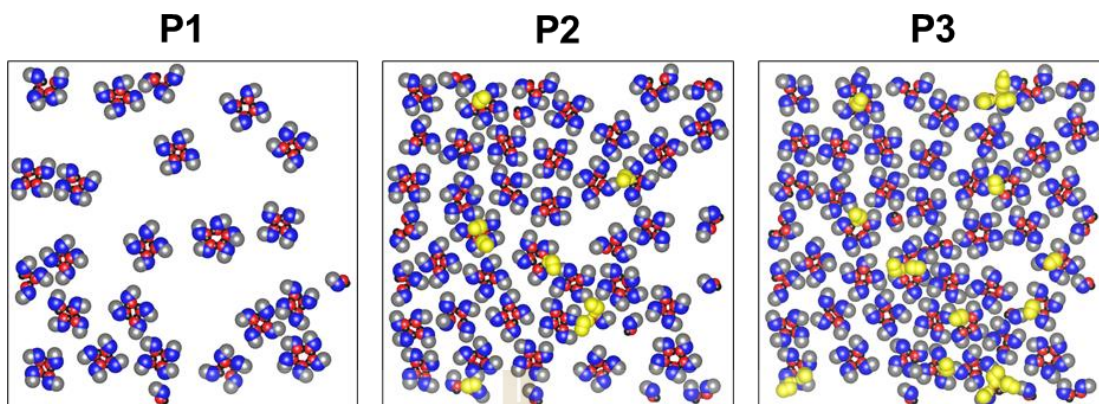


**Figure 6.18** The configurations snapshots of ethanol molecules on graphite at 298 K (not to scale) for points P1, P2, and P3 as marked in *Figure 6.17*. The black, red, blue, and grey circles refer to H atom, O atom, CH<sub>2</sub> group, and CH<sub>3</sub> group, respectively, for molecules in the first layer, the yellow circles refer to molecules in the second layer.

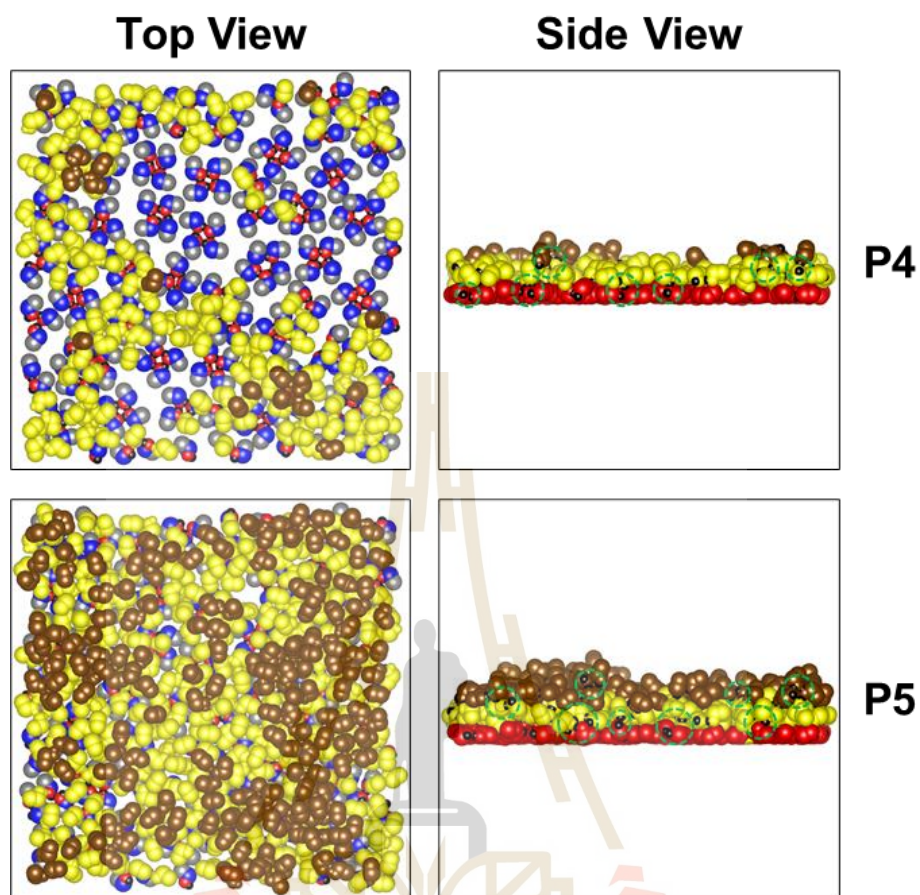


**Figure 6.19** The configurations snapshots of ethanol molecules on graphite at 298 K (not to scale) for points P4 and P5 as marked in *Figure 6.17*. The black, red, blue, and grey circles refer to H atom, O atom, CH<sub>2</sub> group, and CH<sub>3</sub> group, respectively. For side view, we divided first, second, and third molecular layers using red, yellow, and brown molecules, respectively. The green dash circles are used to emphasize the hydrogen bonding between each layer.

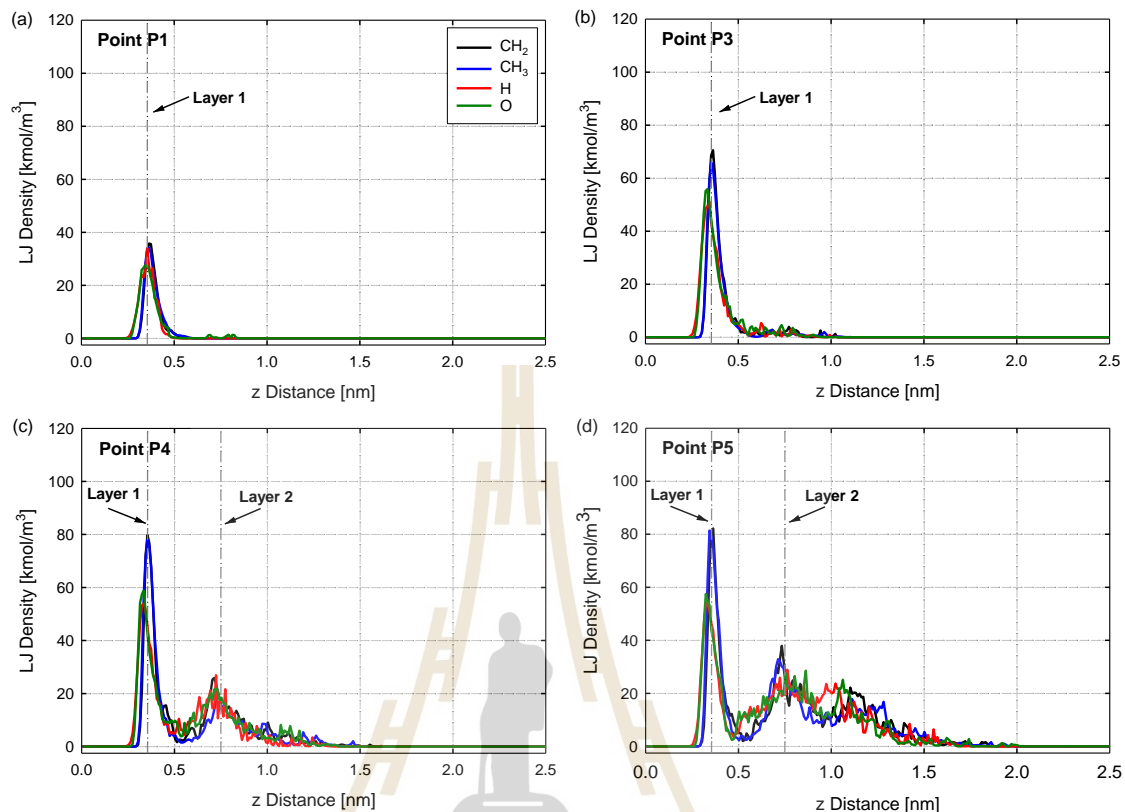


**Figure 6.20** Local density distributions (LDDs) of various sites in ethanol molecules on graphite at 298 K at point P1, P3, P4, and P5 as marked in *Figure 6.17*. The black, blue, red, and green solid lines represent CH<sub>2</sub>, CH<sub>3</sub>, H and O sites, respectively.

From the point P4 to P5, we observe the onset of the third layer as indicated in *Figure 6.17*, the first layer is completed (technically is not, there are vacancies on graphite), the loading from the second layer contributes about 45% while the third layer contributes about 5% to the total adsorbed density. This proves that the adsorption of ethanol on graphite surface beyond the bilayer is possible, we shall discuss points P4 and P5 with the snapshots in *Figure 6.19* and LDDs in *Figure 6.20* as follows.

- Point P4 ( $P/P_0 = 0.84$ ): This is in agreement with the previous observation, the OH groups point away from the surface to maximize hydrogen bonding between layers as shown by the presence of O and H atoms in the region between the peaks of CH<sub>3</sub> and CH<sub>2</sub> groups in *Figure 6.20c*. The density of CH<sub>3</sub>

and CH<sub>2</sub> groups is higher than the O and H atoms, indicating that the completion of the first layer (see *Figure 6.17* for the full monolayer coverage). Focusing on the distribution of O and H atoms, their distribution around the second peaks of CH<sub>3</sub> and CH<sub>2</sub> groups (*i.e.*,  $z \sim 0.75$  nm) are broader in both directions toward and away from the surface, indicating that molecules in the second layer are arranging such that hydrogen bondings are formed both with the first layer and the third layer.

- Point P5 ( $P/P_0 = 0.99$ ): As pressure approaches  $P_0$ , molecules continue to adsorb on the third layer as shown by the peaks of CH<sub>3</sub> and CH<sub>2</sub> groups, O and H atoms around  $z = 1.1$  nm in *Figure 6.20d*. The first peaks are of the same density as observed in point P4 suggesting the first layer was already completed while the second and third layers continue to form. As seen the peaks of O and H atoms in point P4 and P5, it is clearly observed that hydrogen bondings are formed between different layers as highlighted by the circled region in the side view in *Figure 6.19*. The freedom rotation of ethanol molecules is illustrated in *Figure 6.21*, showing that O and H atoms orienting in such a way to maximize hydrogen bonding and facilitate formation of higher layers. The broader peaks of O and H atoms beyond  $z = 1.25$  nm (see *Figure 6.20d*) from the graphite surface suggests that higher layers can form, initiated by the hydrogen bonding with the OH groups in the third layer pointing toward the gas phase.

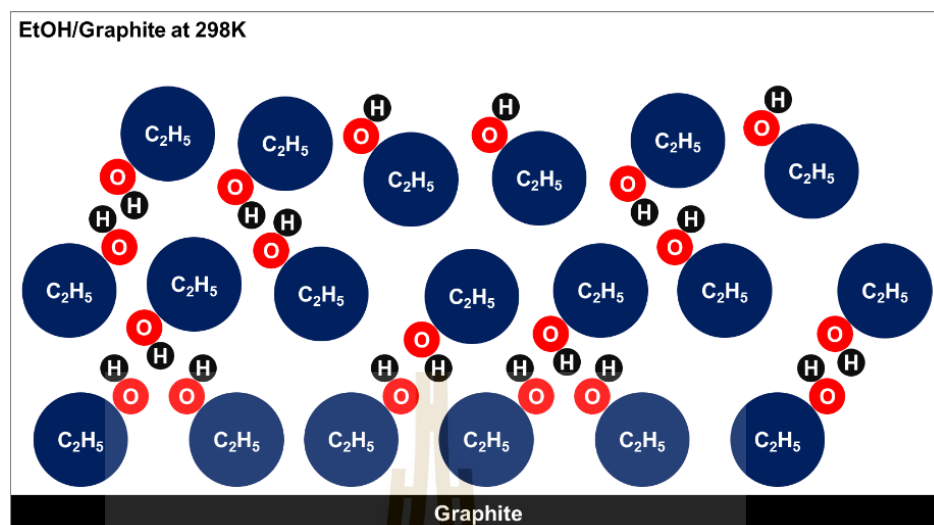


**Figure 6.21** Illustration of ethanol configuration on graphite surface at 298 K. The configuration shows random rotation of ethanol molecules in second and third layers due to thermal fluctuation. The O and H atoms are pointing away from graphite surface, encourages the adsorption of ethanol beyond second layer.

To explain the course of adsorption of ethanol on graphite from bilayer and beyond that, we utilized the isosteric heat and its contributions from the FF and SF interactions at 298 K as seen in *Figure 6.22*. In the Henry's law region, the isosteric heat at zero loading is less than the heat of condensation  $\Omega^0 < 1$  but it does not mean the adsorption cannot occur. We consider the low loading region to point P1 using FF interactions (see *Figure 6.22b*), there is a sharp jump that contributes heat about 22 kJ/mol together with the heat from SF interactions, resulting in total heat greater than the heat of condensation  $\lambda_{cond}$ . So, the onset of adsorption isotherm occurs before point P1 (see *Figure 6.17*). From the snapshot at point P1 in *Figure 6.18*, the ethanol molecules interact together by forming clusters using hydrogen bonding, therefore causing a sudden rise in the heat of adsorption as mentioned early. From point P1 and onward, the total isosteric heat remains almost constant and drops to around heat of condensation at point P3, the FF is increasing since the formation of clusters and the onset of the second layer at point P3 as well. While the SF slowly

decreases due to the first layer is full. Beyond point P3 and onwards, the FF keeps on increasing due to the interactions energy between fluid molecules which building second layer and higher, while the SF slowly decreases again and becomes almost negligible since the ethanol molecules adsorbed further away from graphite surface. From point P4 and onwards, the FF interaction energy now contributes almost 100% to the total heat, this causes by the interaction energy of the fluid molecules in the multilayer adsorption. Ultimately, the total isosteric heat of adsorption approaches the heat of condensation due to the adsorbed ethanol molecules behave like liquid in this state.

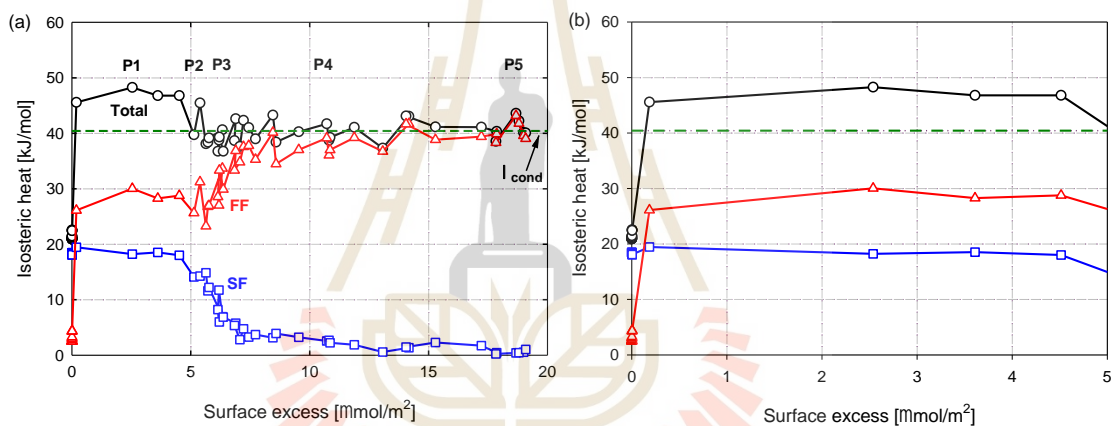


**Figure 6.22** (a) The isosteric heat and its contributions from the adsorbate-adsorbate (FF) interactions and adsorbent-adsorbate (SF) interactions and (b) the simulated isosteric heat at low loading for ethanol adsorption on graphite at 298 K. The horizontal dash line is the simulated heat of condensation from the canonical kMC scheme (Nguyen *et al.*, 2016).

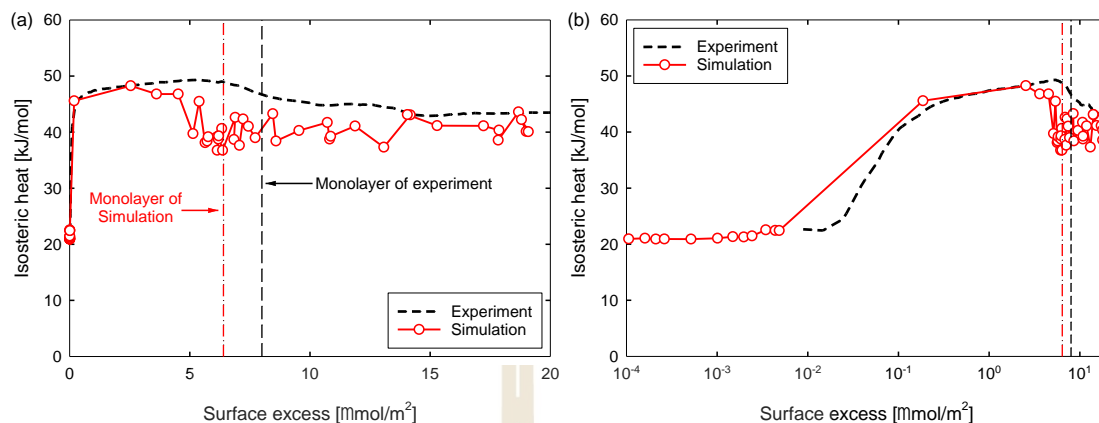


**Figure 6.23** (a) The isosteric heat of adsorption of ethanol on Carbopack F and (b) plots are in semi-log scale to highlight low loading region.

To substantiate the simulated data, we employ the isosteric heat of adsorption of ethanol on Carbopack F, which derived from the adsorption data of ethanol on Carbopack F at 283 K and 298 K. The results are shown in *Figure 6.23*. The pattern of the heat curve from the simulation is in qualitative agreement with the experimental data, where the heat at zero loading of the simulated data shows about 21.5 kJ/mol (the red solid line in *Figure 6.23b*) while the experimental data gives about 22 kJ/mol (the black dash line in *Figure 6.23b*). As the course of adsorption proceeds, the heat of adsorption slowly increases while ethanol molecules are building up the monolayer and reaches the maximum at about 49 kJ/mol and maintains almost constant at this level until the monolayer is completed (between loading of 6.5 to 8.0  $\mu\text{mol}/\text{m}^2$ ). Then the adsorption occurs on the second and higher layers, the isosteric heat approaches the heat of liquefaction about 43.5 kJ/mol which is in agreement with the heat of vaporization of ethanol at 298 K (Green & Southard, 2019).

### 6.3.4 Effect of Surface Affinity and Wetting Map

To illustrate the effect of the substrate strength from weaker than graphite and increasing towards graphite, we have carried out an extensive number of simulations by varying substrate affinities denoted by  $D^*$  as stated in Equation (6.1). The wetting map of ethanol on a variety of surface affinities is summarized in *Figure 6.24*, we plotted temperature as a function of substrate strength. The wetting map

consists of non-wetting, incomplete (partial) wetting and complete wetting regions as highlighted by grey, light cyan and dark cyan, respectively. The region between non-wetting and complete wetting is separated by the blue solid line, which is the wetting temperature,  $T_W$ . The black dashed line below is used to demarcate the non-wetting and incomplete wetting regions. Within the incomplete wetting region, there are more black dashed lines representing the layering temperatures, for example, the zone between  $T_{L,1}$  and  $T_{L,2}$  there is one layer formed on the substrate and if the temperature is increased (by keeping  $D^*$  constant) across  $T_{L,2}$ , the second layer is formed at the bulk coexistence vapour pressure,  $P_0$ . Lastly, the red solid line demarcates the incomplete wetting and complete wetting zone representing the roughening temperature line, denoted as  $T_R$  (Larher & Angerand, 1988).

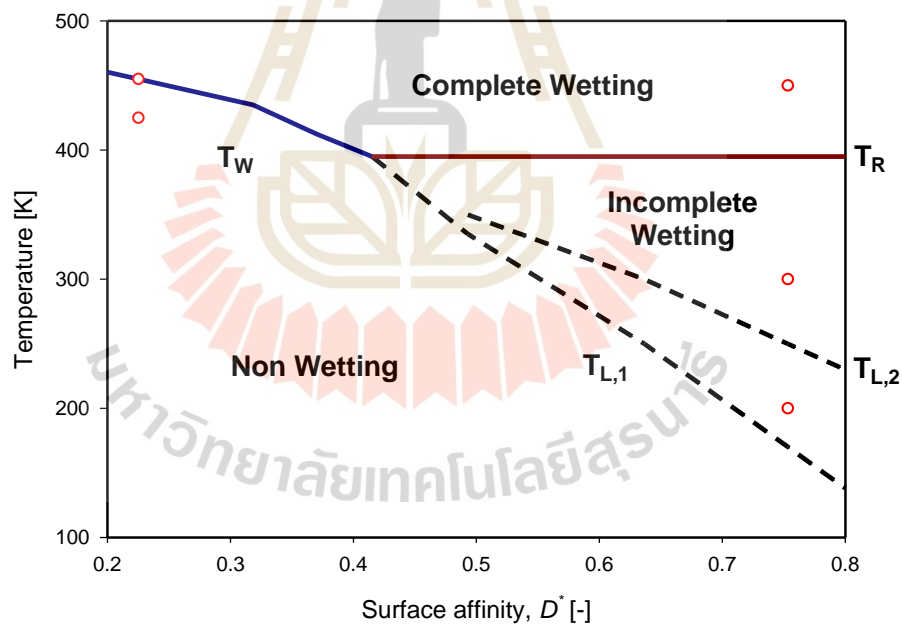


**Figure 6.24** The wetting map for ethanol as a function of temperature and surface affinity,  $D^*$ .

In order to show the transition between non-wetting to complete wetting regions as temperature is increased, we present the adsorption isotherms on a weak surface affinity ( $D^*$  of 0.23) as marked in *Figure 6.24*. When the temperature is

increased, at 425 K the isotherm falls in the non-wetting region as illustrated in *Figure 6.25a*, where the isotherm cuts  $P_0$  at a finite loading of  $2.4 \mu\text{mol}/\text{m}^2$  which is lower than the statistical monolayer coverage of  $6.4 \mu\text{mol}/\text{m}^2$ . When the temperature is increased to 455 K, the system is in the complete wetting region and the adsorption isotherm shows a transition in the adsorbed density. The snapshots at 455 K are shown in *Figure 6.26*, before a sharp transition, the ethanol molecules are lightly adsorbed on the surface without “zigzag” chain or cluster configurations that found on the graphite surface. Most of the ethanol molecules adsorbed on the surface and loosely connected in the gas phase above the surface, since on the low surface affinity (much weaker than graphite) they preferred to anchor together by hydrogen bonding. When the pressure approaches  $P_0$  and reached the transition, the ethanol molecules filled up the simulation box without any layering behaviour.

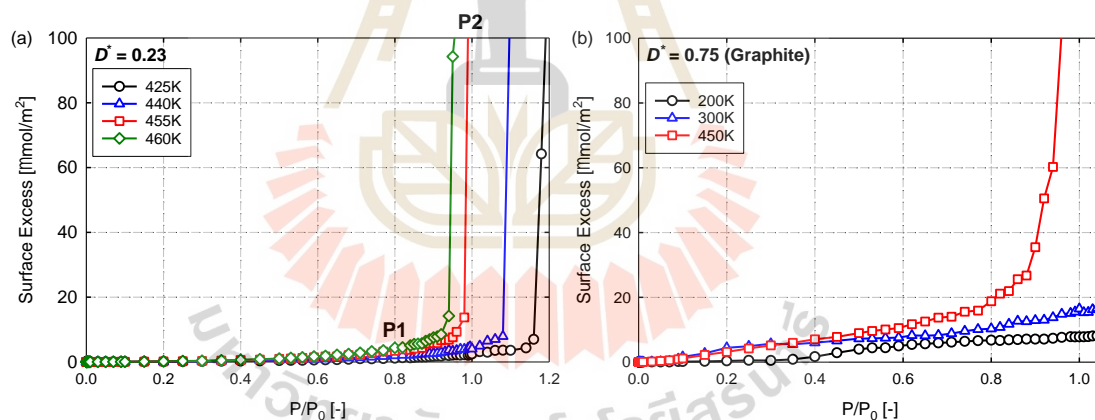


**Figure 6.25** Adsorption isotherms for ethanol on: (a) weak substrate having  $D^*$  of 0.23 and (b) graphite substrate.

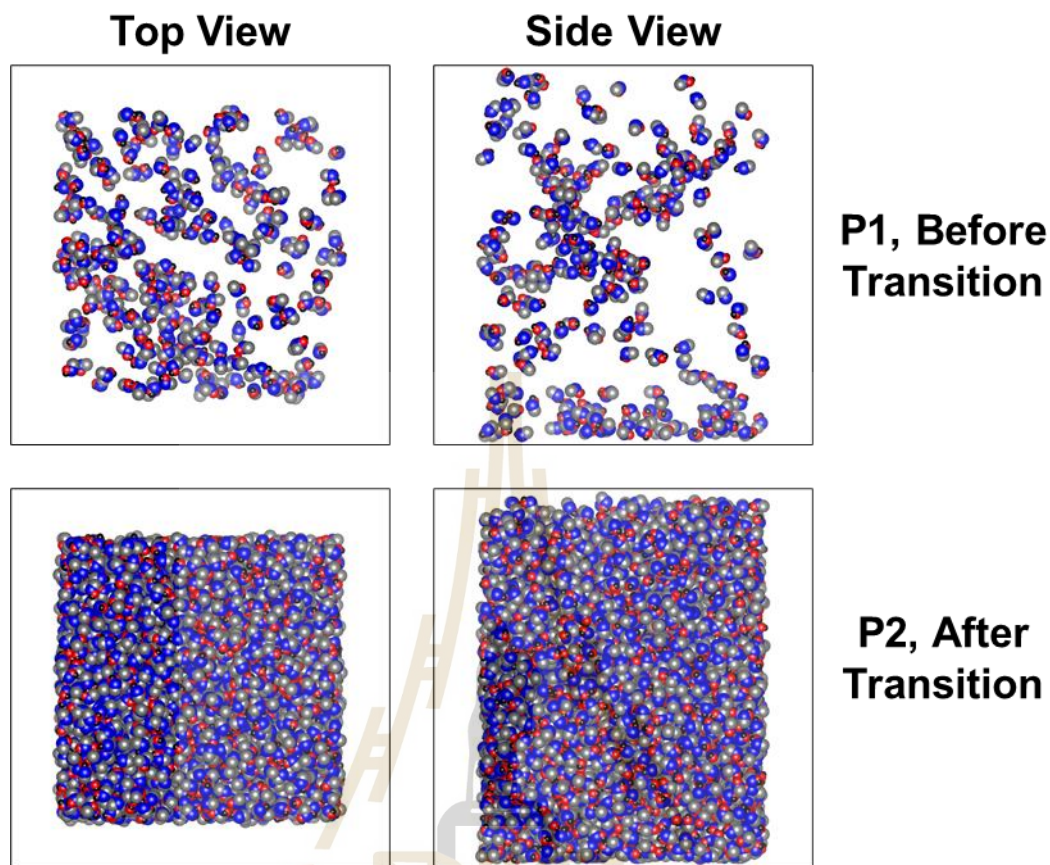


**Figure 6.26** The configurations snapshots of ethanol molecules on the weak substrate having  $D^*$  of 0.23 at 455 K. The pressure points before and after the transition are marked in *Figure 6.25a*.

Take the next example for  $D^*$  of 0.75 as indicated in *Figure 6.24* or ethanol adsorption on graphite surface, the transition between regions are non-wetting, incomplete wetting, and then complete wetting. For the temperature of 200 K, this falls between  $T_{L,1}$  and  $T_{L,2}$  region, the adsorption isotherm in *Figure 6.25b* shows that there is one layer formed before the isotherm crosses the  $P_0$ . As the temperature is increased to 300 K, the system is above the  $T_{L,2}$  but below the  $T_R$  line, the adsorbed density is about  $15.4 \mu\text{mol}/\text{m}^2$  at  $P_0$ , indicating that there are two and a half layers formed on the graphite surface. Finally, when the temperature is increased to 450 K, which is in the complete wetting region, the loading of ethanol tends to infinity as the bulk coexistence pressure approaches the unity (see *Figure 6.25b*). To support the wetting transition of ethanol on graphite surface, we presented the corresponding

snapshots of ethanol molecules adsorbed on graphite surface at  $P_0$  for various temperatures in Appendix A.

## 6.4 Conclusions

We have presented the extensive number of computer simulation for ethanol adsorption on graphite using grand canonical Monte Carlo simulation and the experimental study of ethanol adsorption on Carbopack F to investigate the wetting transition of ethanol when the temperature is varied. The ethanol adsorption on graphite surface shows incomplete wetting at 190 K with loading about 1.4 times of the statistical monolayer coverage at the bulk coexistence pressure, while at 298 K the adsorbed density beyond bilayer can be observed. By analyzing the microscopic mechanism, at 190 K the ethanol molecules in second layer preferred to point their OH sites to graphite surface and created hydrogen bonding between ethanol molecules in the first layer, thus the system is unable to form higher layer. While at high temperature, the system can build up the molecular layer beyond the second layer due to entropy that allowed ethanol molecules to rotate randomly and balance the hydrogen bonding between second, third, and higher layers.

## 6.5 References

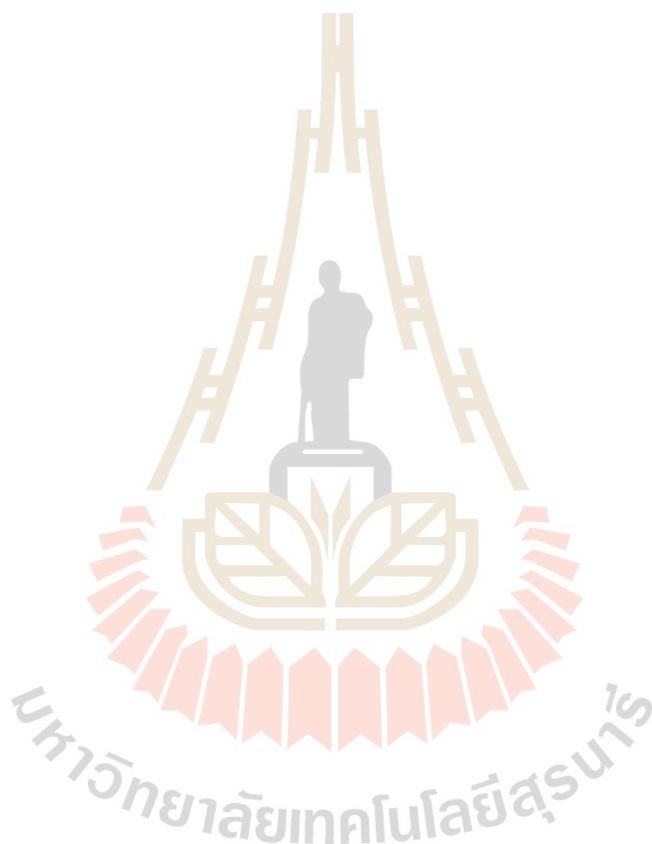
- Avgul, N. N., Berezin, G. I., Kiselev, A. V., & Lygina, I. A. (1961). The adsorption and heat of adsorption of normal alcohols on graphitized carbon black. **Bulletin of the Academy of Sciences of the USSR, Division of chemical science**. 10(2): 186-193.
- Bojan, M. J., Stan, G., Curtarolo, S., Steele, W. A., & Cole, M. W. (1999). Wetting transitions of Ne. **Physical Review E**. 59(1): 864-873.
- Chen, B., J. Potoff, J., & Siepmann, J. I. (2001). Monte Carlo Calculations for Alcohols and Their Mixtures with Alkanes. Transferable Potentials for Phase Equilibria. 5. United-Atom Description of Primary, Secondary, and Tertiary Alcohols. **The Journal of Physical Chemistry B**. 105: 3093-3104.
- Chen, B., Potoff, J. J., & Siepmann, J. I. (2001). Monte Carlo Calculations for Alcohols and Their Mixtures with Alkanes. Transferable Potentials for Phase Equilibria. 5. United-Atom Description of Primary, Secondary, and Tertiary Alcohols. **The Journal of Physical Chemistry B**. 105(15): 3093-3104.
- Cheng, E., Cole, M. W., Saam, W. F., & Treiner, J. (1991). Helium prewetting and nonwetting on weak-binding substrates. **Physical Review Letters**. 67(8): 1007-1010.
- Dietrich, S., & Schick, M. (1986). Order of wetting transitions. **Physical Review B**. 33(7): 4952-4968.
- Dilokekunakul, W., Klomklang, N., Sakdaronnarong, C., Chaemchuen, S., Do, D. D., & Nicholson, D. (2019). Structure of methanol sub-monolayer on functionalized graphite at temperatures below the triple point. **Colloids and Surfaces A: Physicochemical and Engineering Aspects**. 577: 110-117.
- Do, D. D., Nicholson, D., & Do, H. D. (2008). On the Henry constant and isosteric heat at zero loading in gas phase adsorption. **Journal of Colloid and Interface Science**. 324(1): 15-24.
- Drir, M., Nham, H. S., & Hess, G. B. (1986). Multilayer adsorption and wetting: Ethylene on graphite. **Physical Review B**. 33(7): 5145-5148.
- Eggimann, B. L., Sun, Y., DeJaco, R. F., Singh, R., Ahsan, M., Josephson, T. R., & Siepmann, J. I. (2020). Assessing the Quality of Molecular Simulations for Vapor-Liquid

- Equilibria: An Analysis of the TraPPE Database. **Journal of Chemical & Engineering Data**. 65(3): 1330-1344.
- Gatica, S. M., & Cole, M. W. (2009). To Wet or Not to Wet: That Is the Question. **Journal of Low Temperature Physics**. 157(3): 111.
- Green, D. W., & Southard, M. Z. (2019). **Perry's Chemical Engineers' Handbook** (9th Edition ed.). New York: McGraw-Hill Education.
- Herwig, K. W., & Trow, F. R. (1992). Ethanol on graphite: The influence of hydrogen bonding on surface melting. **Physical Review Letters**. 69(1): 89-92.
- Horikawa, T., Takenouchi, M., Do, D. D., Sotowa, K.-I., Alcántara-Avila, J. R., & Nicholson, D. (2015). Adsorption of Water and Methanol on Highly Graphitized Thermal Carbon Black and Activated Carbon Fibre %J Australian Journal of Chemistry. 68(9): 1336-1341.
- Horikawa, T., Zeng, Y., Do, D. D., Sotowa, K.-I., & Alcántara Avila, J. R. (2015). On the isosteric heat of adsorption of non-polar and polar fluids on highly graphitized carbon black. **Journal of Colloid and Interface Science**. 439: 1-6.
- Johnson, J. K., Zollweg, J. A., & Gubbins, K. E. (1993). The Lennard-Jones equation of state revisited. **Molecular Physics**. 78(3): 591-618.
- Larher, Y., & Angerand, F. (1988). The Roughening Temperature of the Densest Crystal Face of Ar, Kr, CO and CH<sub>4</sub> Derived from Multilayer Adsorption Studies. **Europhysics Letters (EPL)**. 7(5): 447-451.
- Liu, L., Liu, J., Zeng, Y., Tan, S. J., Do, D. D., & Nicholson, D. (2019). Formaldehyde adsorption in carbon nanopores – New insights from molecular simulation. **Chemical Engineering Journal**. 370: 866-874.
- Liu, L., Zeng, Y., Tan, S. J., Xu, H., Do, D. D., Nicholson, D., & Liu, J. (2019). On the mechanism of water adsorption in carbon micropores – A molecular simulation study. **Chemical Engineering Journal**. 357: 358-366.
- Loi, Q. K., Prasetyo, L., Tan, S., Do, D. D., & Nicholson, D. (2019). Nonwetting/Prewetting/Wetting Transition of Ammonia on Graphite. **Langmuir**. 35(3): 641-652.
- Morishige, K. (1992). Structure and melting of a monolayer ethanol film on graphite. 97(3): 2084-2089.

- Morishige, K., Kawamura, K., & Kose, A. (1990). X-ray diffraction study of the structure of a monolayer methanol film adsorbed on graphite. *93*(7): 5267-5270.
- Mountain, R. D., & Thirumalai, D. (1994). Quantative measure of efficiency of Monte Carlo simulations. **Physica A: Statistical Mechanics and its Applications**. *210*(3): 453-460.
- Nguyen, V. T., Tan, S. J., Do, D. D., & Nicholson, D. (2016). Application of kinetic Monte Carlo method to the vapour-liquid equilibria of associating fluids and their mixtures. **Molecular Simulation**. *42*(8): 642-654.
- Patra, T. K., Khan, S., Srivastava, R., & Singh, J. K. (2015). Understanding Wetting Transitions Using Molecular Simulation. In Y. M. Joshi & S. Khandekar (Eds.), *Nanoscale and Microscale Phenomena: Fundamentals and Applications* (pp. 139-166). New Delhi: Springer India.
- Prasetyo, L., Horikawa, T., Takashima, N., Do, D. D., & Nicholson, D. (2019). On the transition from partial wetting to complete wetting of methanol on graphite. **Physical Chemistry Chemical Physics**. *21*(47): 26219-26231.
- Prasetyo, L., Loi, Q. K., Tan, S. J., Do, D. D., & Nicholson, D. (2018). Effects of temperature on the transition from clustering to layering for argon adsorption on substrates of different strength - Parametric map of wetting, pre-wetting and non-wetting. **Microporous and Mesoporous Materials**.
- Prasetyo, L., Loi, Q. K., Tan, S. J., Do, D. D., & Nicholson, D. (2020). Effects of temperature on the transition from clustering to layering for argon adsorption on substrates of different strength - Parametric map of wetting, pre-wetting and non-wetting. **Microporous and Mesoporous Materials**. *304*: 109239.
- Prasetyo, L., Tan, S., Akram, A., Do, D. D., & Nicholson, D. (2018). Cluster growth and coalescence of argon on weakly adsorbing substrates: The origin of the thin-to-thick film transition. **Colloids and Surfaces A: Physicochemical and Engineering Aspects**. *554*: 169-179.
- Reisch, A., Voegel, J.-C., Gonthier, E., Decher, G., Senger, B., Schaaf, P., & Mésini, P. J. (2009). Polyelectrolyte Multilayers Capped with Polyelectrolytes Bearing Phosphorylcholine and Triethylene Glycol Groups: Parameters Influencing Antifouling Properties. **Langmuir**. *25*(6): 3610-3617.

- Rutledge, J. E., & Taborek, P. (1992). Prewetting phase diagram of 4-He on cesium. **Physical Review Letters**. 69(6): 937-940.
- Saam, W. F. (2009). Wetting, Capillary Condensation and More. **Journal of Low Temperature Physics**. 157(3): 77-100.
- Steele, W. A. (1978). The interaction of rare gas atoms with graphitized carbon black. **The Journal of Physical Chemistry**. 82(7): 817-821.
- Steele, W. A. (2008). Chapter Eight - Wetting Phenomena. In E. J. Bottani & J. M.D. Tascón (Eds.), *Adsorption by Carbons* (pp. 167-185). Amsterdam: Elsevier.
- Sung, K. E., Vanapalli, S. A., Mukhija, D., McKay, H. A., Mirecki Millunchick, J., Burns, M. A., & Solomon, M. J. (2008). Programmable Fluidic Production of Microparticles with Configurable Anisotropy. **Journal of the American Chemical Society**. 130(4): 1335-1340.
- Tan, S. J., Prasetyo, L., Do, D. D., & Nicholson, D. (2019). Interplay between Wetting and Filling of Argon Adsorption in Slit Pores with Different Surface Energies Transition from Filling in Micropores to Capillary Condensation in Mesopores. **Industrial & Engineering Chemistry Research**. 58(51): 23294-23303.
- Terlain, A., & Larher, Y. (1983). Phase diagrams of films of linear molecules with large quadrupole moments (CO<sub>2</sub>, N<sub>2</sub>O, C<sub>2</sub>N<sub>2</sub>) adsorbed on graphite. **Surface Science**. 125(1): 304-311.
- Thommes, M., Kaneko, K., Neimark Alexander, V., Olivier James, P., Rodriguez-Reinoso, F., Rouquerol, J., & Sing Kenneth, S. W. (2015). Physisorption of gases, with special reference to the evaluation of surface area and pore size distribution (IUPAC Technical Report). In *Pure and Applied Chemistry* (Vol. 87, pp. 1051).
- Wu, C., Chen, M., & Xing, C. (2010). Molecular Understanding of Conformational Dynamics of a Fibronectin Module on Rutile (110) Surface. **Langmuir**. 26(20): 15972-15981.
- Xu, H., Zeng, Y., Do, D. D., & Nicholson, D. (2019). On the Nonwetting/Wetting Behavior of Carbon Dioxide on Graphite. **The Journal of Physical Chemistry C**. 123(14): 9112-9120.
- Zeng, Y., Horio, K., Horikawa, T., Nakai, K., Do, D. D., & Nicholson, D. (2017). On the evolution of the heat spike in the isosteric heat versus loading for argon

adsorption on graphite-A new molecular model for graphite & reconciliation between experiment and computer simulation. **Carbon**. 122: 622-634.



## CHAPTER VII

### CONCLUSIONS AND RECOMMENDATIONS

#### 7.1 Conclusions

The primary purpose of the present work was to investigate the development of porosity and the formation of surface functional groups of activated carbon during the activation of bamboo chars using CO<sub>2</sub> as the activating agent under various process conditions of carbonization temperature, activation temperature, and activation time. Empirical equations were proposed to correlate the porous properties and the amounts of surface functional groups with the previously mentioned parametric conditions. The work was further supplemented by the study of increasing surface functional groups concentration by oxidation of the selected prepared activated carbons with air. This work also incorporated the fundamental study of the wetting behaviour of polar and non-polar fluids on a planar graphite substrate using a computer simulation technique. Results from these studies have led to the following conclusions.

1. Increasing activation conditions appeared to increase the porous properties of the produced activated carbon, however, at a relatively high degree of burn-off tended to decrease the porous properties. The prepared activated carbon contained mostly micropore, *i.e.*, more than 85% by volume. The maximum BET specific area of 907 m<sup>2</sup>/g and a total pore volume of 0.446 cm<sup>3</sup>/g were obtained at a carbonization temperature of 400°C and 90 min, activation temperature of 900°C and 120 min. The activated carbons derived from char carbonized at 400°C and 90 min yielded the highest porous properties as compared to the samples derived from char carbonized at 500°C and 600°C, possibly due its higher number of active sites for CO<sub>2</sub> gasification.

Empirical equations were proposed and correlated to describe the development of textural properties of the obtained activated carbons as functions of carbonization temperature, activation temperature, and activation time. The equations can be used to predict the development of textural properties of the prepared activated carbon with reasonable accuracy.

2. It was found that the surface functional groups were formed during the carbonization process and the gasification process under  $\text{CO}_2$  along with the formation of pores. The amount of acidic groups appeared to decrease with the increase of carbonization temperature. While in the activation process, the amount of acidic and basic groups increased with the increase of activation temperature. The amounts of acidic groups obtained from the prepared activated carbons are in the range of 0.2152 to 0.5069 mmol/g, while the basic groups are 0.6264 to 1.1459 mmol/g. Empirical correlations were proposed and correlated to describe the development of the amount of surface functional groups of the obtained activated carbons as functions of carbonization temperature, activation temperature, and activation time. The obtained empirical correlations are in good agreement with the experimental data with the coefficient of determination of 0.8210 and 0.9254, for acidic and basic groups, respectively.

3. For the air oxidation process, the porous properties of the oxidized activated carbon are mostly unchanged. The BET specific area of the oxidized activated carbon only changes in the range of 50 to 100  $\text{m}^2/\text{g}$ . The percentage of mesopore volumes increased with the increase of oxidation time by about 12%, this was due to the enlargement of the pores created by the slow combustion between air and the carbon surfaces even at a low oxidation temperature. The amount of acidic groups increased by 200% for the sample derived from the char carbonized at  $400^\circ\text{C}$  and 90 min (C4 OAC250-4320). The amount of acidic groups increased by 320% for the sample obtained from char carbonized at  $500^\circ\text{C}$  and 90 min (C5 OAC250-4320), as compared to the original activated carbon. This could be attributed to the difference of the number and distribution of active sites in the original chars.

4. Two potential models of ethylene were compared based on the comparison of vapour-liquid equilibria (VLE) and the adsorption of ethylene on a

graphite substrate. It was found that the model with partial charges could better describe the VLE and the adsorption of ethylene on a graphite substrate as compared with the model without partial charges. This should result from the existence of quadrupole moment in the real ethylene molecules. Then, the model with partial charges was utilized to construct the parametric map of wetting of ethylene on a planar carbon substrate. The wetting map of ethylene shows similar wetting behaviour to the wetting map of argon (reference adsorbate). The wetting map is separated into three zones, which are non-wetting, incomplete wetting, and complete wetting. Each wetting zone in the wetting map is governed by the three important parameters, temperature, adsorbate-adsorbate interaction, and adsorbate-adsorbent interaction. The layering temperature of ethylene on a graphite substrate was found to be at 0 K, and the roughening temperature ( $T_R$ ) is 104 K. The roughening temperature is identical to the triple point temperature of ethylene in the bulk phase. These two parameters are similar to the wetting map of the argon system, this was due to ethylene being a linear quadrupolar molecule sharing the same features to argon and nitrogen system.

5. For incomplete wetting of ethanol on a graphite substrate, the potential model of ethanol was able to describe VLE correctly, but it failed to duplicate the experimental adsorption isotherms of ethanol on a graphite substrate. This could be due to the simulation of the ethanol system requiring an extremely long time and the simplicity of the graphite substrate in the simulation. Then the potential model was employed to investigate the effect of temperature on the wetting transition of ethanol on a graphite substrate. At 190 K, the adsorption of ethanol on a graphite substrate only showed the density of 1.5 times the monolayer coverage at the bulk coexistence pressure ( $P_0$ ). Once the temperature was increased to 298 K, the adsorption of ethanol beyond 2 layers can be observed at  $P_0$ . This was due to the thermal fluctuation allowing the ethanol molecules in the adsorbed phase to rotate freely, resulting in the connection of hydrogen bonding between the first- and second layer, and the second layer to higher layer. Thus, the wetting transition of ethanol on graphite substrate heavily relies on a thermal fluctuation. Another reason is the interaction between adsorbate-adsorbate is much higher than that of adsorbate-adsorbent interaction. These results indicate that complete wetting can occur only at high temperatures.

## 7.2 Recommendations

Although interesting results have been produced from this thesis work, there remains several research works that could be further investigated as follows:

### 7.2.1 Extension Study of Development of Pore and Formation of Surface Groups by Char Reactivity and the Distributed Activation Energy Model (DAEM)

The analysis of the development of porosity and formation of surface functional groups during CO<sub>2</sub> activation has been completed. The kinetic of the pyrolysis and activation processes involving many thermochemical reactions should be studied further. Thus, the DAEM and the concept of char reactivity can be employed to investigate the change in activation energy during the gasification. This could be helpful to describe more accurately the development of pores during the course of char activation.

### 7.2.2 Further Work to Investigate the Increase of Surface Functional Groups in Activated Carbon

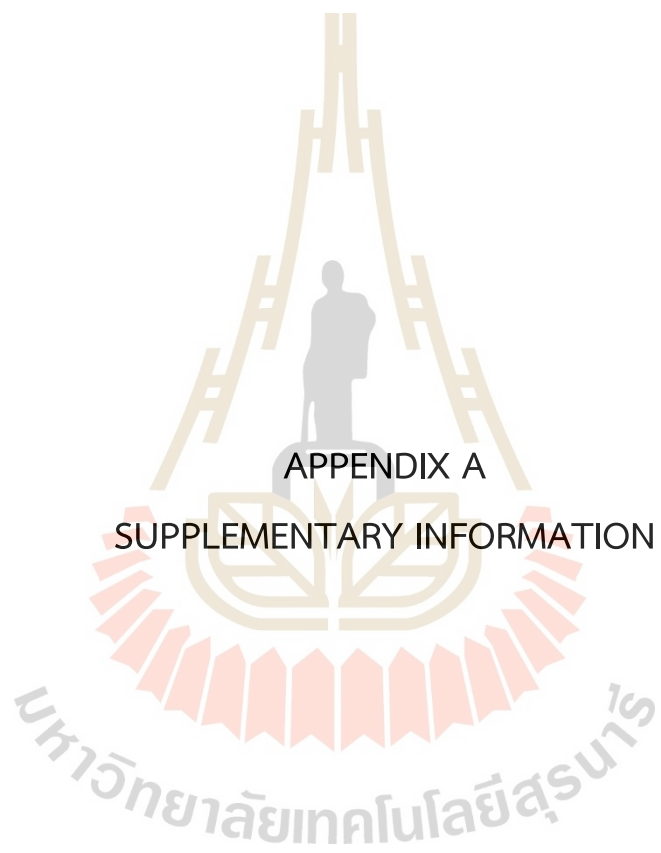
The work in Chapter IV concentrated mainly on the formation and destruction of functional groups on activated carbon surfaces using air oxidation. It should be helpful to extend to the study to other different oxidizing agents such as H<sub>2</sub>O<sub>2</sub>, steam, and NH<sub>3</sub> to better understand the mechanism of functional groups formation on surfaces of activated carbon. In addition, a quantitative and more precise measurement of the amount of surface functional groups should be employed such as the Temperature Programmed Desorption (TPD). This method will allow one to follow the change in the amount of surface functional groups during the surface functional groups formation.

### 7.2.3 Wetting Transition of Fluids on a Planar Substrate

In Chapter V, the wetting transition behaviour of ethylene on a planar and homogeneous substrate can be achieved. This work could be a reference adsorbate for the understanding of wetting of the linear molecules on a homogeneous substrate. However, most of the solid substrates in the industries are amorphous and

they exhibit the wetting behaviour which has not been fully understood to date. Therefore, it is worthwhile to investigate the wetting transition of the concerning fluids on a nonhomogeneous planar substrate. This also could be extended to the pore filling of the fluids when the adsorbents are amorphous, the adsorbate could also be large molecules of hydrocarbons such as propane, n-butane, and aromatic compounds.

In Chapter VI, the wetting transition of ethanol in the presence of adsorbed phase on a graphite substrate has been achieved. However, the experimental data have not been fully described by the simulation results. This is due to the simplicity of the potential model and the graphite substrate used in the simulation, as well as the number of the computation cycles. The problem could be resolved by modifying the Monte Carlo algorithm, and by accounting for the sigma-bond rotation of ethanol molecule around a reference axis in the simulation. Moreover, using ethanol adsorption on a graphite substrate should be extended to the study of the wetting transition of the larger chemical compounds in the alcohol series such as *tert*-butanol and isopropanol.



APPENDIX A

SUPPLEMENTARY INFORMATION

CHAPTER III – THE ANALYSIS OF PORE DEVELOPMENT AND SURFACE FUNCTIONAL GROUPS FORMATION DURING CO<sub>2</sub> ACTIVATION OF BAMBOO-BASED ACTIVATED CARBON

Table S1 Porous properties of the prepared activated carbons.

Run no.	Sample	$S_{BET}$ (m <sup>2</sup> /g)	$V_{mic}$ (cm <sup>3</sup> /g)	$V_{mes}$ (cm <sup>3</sup> /g)	$V_{tot}$ (cm <sup>3</sup> /g)	$D_{avg}$ (nm)	Burn-off (%)
from C400-90							
1	AC850-60	584	0.2432 (95.8%)	0.0107 (4.2%)	0.2539	1.74	32.9
2	AC900-60	666	0.2879 (90.5%)	0.0302 (9.5%)	0.3181	1.91	39.2
3	AC950-60	728	0.3145 (87.7%)	0.0441 (12.3%)	0.3586	1.93	44.7
4	AC1000-60	693	0.2980 (88.3%)	0.0393 (11.7%)	0.3373	1.95	49.4
5	AC850-90	621	0.2691 (94.4%)	0.0160 (5.6%)	0.2851	1.84	36.5
6	AC900-90	753	0.3265 (90.3%)	0.0351 (9.7%)	0.3616	1.92	44.5
7	AC950-90	810	0.3498 (87.8%)	0.0488 (12.2%)	0.3986	1.97	53.6
8	AC1000-90	787	0.3377 (84.7%)	0.0611 (15.3%)	0.3988	2.02	60.7
9	AC850-120	654	0.2830 (90.0%)	0.0315 (10.0%)	0.3145	1.92	35.7
10	AC900-120	907	0.3943 (88.4%)	0.0515 (11.6%)	0.4458	1.97	46.2
11	AC950-120	884	0.3811 (83.8%)	0.0735 (16.2%)	0.4546	2.06	58.9
12	AC1000-120	749	0.3182 (82.8%)	0.0663 (17.2%)	0.3845	2.05	65.1
from C500-90							
13	AC850-60	513	0.2221 (95.0%)	0.0116 (5.0%)	0.2337	1.82	20.7
14	AC900-60	628	0.2716 (92.4%)	0.0224 (7.6%)	0.294	1.87	29.0
15	AC950-60	685	0.2956 (89.5%)	0.0346 (10.5%)	0.3302	1.93	34.4
16	AC1000-60	614	0.2644 (89.2%)	0.0320 (10.8%)	0.2964	1.93	37.9
17	AC850-90	585	0.2532 (93.0%)	0.0190 (7.0%)	0.2722	1.86	24.2
18	AC900-90	684	0.2956 (90.1%)	0.0323 (9.9%)	0.3279	1.92	31.1
19	AC950-90	786	0.3405 (86.5%)	0.0531 (13.5%)	0.3936	2.00	44.5
20	AC1000-90	666	0.2870 (87.4%)	0.0414 (12.6%)	0.3284	1.97	50.5
21	AC850-120	627	0.2716 (94.1%)	0.0169 (5.9%)	0.2885	1.84	27.8
22	AC900-120	764	0.3299 (90.5%)	0.0347 (9.5%)	0.3646	1.90	39.8
23	AC950-120	782	0.3352 (87.7%)	0.0471 (12.3%)	0.3823	1.96	47.2
24	AC1000-120	665	0.2848 (84.9%)	0.0505 (15.1%)	0.3353	2.02	58.3
from C600-90							
25	AC850-60	518	0.2243 (96.3%)	0.0085 (3.7%)	0.2328	1.80	16.1
26	AC900-60	614	0.2662 (93.0%)	0.0201 (7.0%)	0.2863	1.86	22.7
27	AC950-60	660	0.2859 (90.4%)	0.0305 (9.6%)	0.3164	1.92	29.3
28	AC1000-60	529	0.2265 (90.6%)	0.0236 (9.4%)	0.2501	1.89	33.0
29	AC850-90	594	0.2577 (97.0%)	0.0079 (3.0%)	0.2656	1.79	20.5
30	AC900-90	734	0.3185 (91.2%)	0.0307 (8.8%)	0.3492	1.90	31.8
31	AC950-90	709	0.3053 (89.7%)	0.0351 (10.3%)	0.3404	1.92	38.7
32	AC1000-90	642	0.2748 (86.5%)	0.0430 (13.5%)	0.3178	1.98	47.4
33	AC850-120	660	0.2854 (94.1%)	0.0180 (5.9%)	0.3034	1.84	26.0
34	AC900-120	776	0.3359 (89.0%)	0.0417 (11.0%)	0.3776	1.95	36.3
35	AC950-120	803	0.3461 (85.4%)	0.0593 (14.6%)	0.4054	2.02	48.4
36	AC1000-120	708	0.3018 (84.2%)	0.0566 (15.8%)	0.3584	2.02	57.5

Examples of calculations of  $S_{BET}$ ,  $V_{tot}$ ,  $V_{mic}$ , and  $D_{avg}$  from adsorption isotherm of  $N_2$  at 77.4 K using activated carbon sample AC950-90 derived from char sample C400-90.

**Table S2** Adsorption isotherm of  $N_2$  at 77.4 K obtained from activated carbon sample C400-90 AC950-90, bamboo precursor was used in this work.

$P/P_0$	Volume adsorbed, $V$ (cm <sup>3</sup> at STP/g)	$\frac{P/P_0}{V(1-P/P_0)}$
0.050719	210.6808	0.000254
0.054942	211.6169	0.000275
0.060669	212.7513	0.000304
0.065378	213.6072	0.000327
0.07143	214.5985	0.000358
0.075922	215.2763	0.000382
0.082278	216.1532	0.000415
0.087151	216.7767	0.00044
0.09351	217.5302	0.000474
0.100747	218.3189	0.000513
0.145742	222.0417	0.000768

The linear BET equation can be written in the relative pressure form as follows:

$$\frac{P/P_0}{V(1-P/P_0)} = \frac{1}{cV_m} + \frac{c-1}{cV_m} \frac{P}{P_0} \quad (S.1)$$

Where the slope and y-intercept from Equation (S.1) are:

$$\text{Slope} = \frac{c-1}{cV_m} \quad (S.2)$$

$$\text{y-intercept} = \frac{1}{cV_m} \quad (S.3)$$

The BET plot is shown in *Figure S1*.

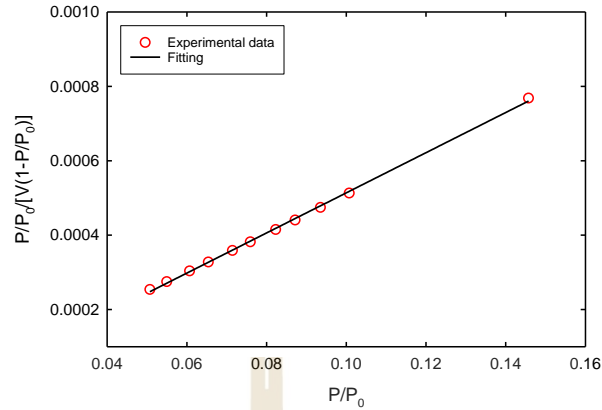


**Figure S1** The linear plot of BET to determine slope and y-intercept from N<sub>2</sub> adsorption isotherm at 77.4 K.

The slope and y-intercept can be obtained from *Figure S1*, and they are  $5.3984 \times 10^{-3}$  and  $2.5998 \times 10^{-5}$ , respectively. By solving Equations (S.2) and (S.3), the  $c$  and  $V_m$  are  $-206.65$  and  $186.14 \text{ cm}^3$  at STP/g, respectively.

The  $S_{BET}$  can be determined by the following equation:

$$S_{BET} = V_m N_A a_m \quad (\text{S.4})$$

where  $N_A$  is the Avogadro's number,  $6.02214076 \times 10^{23}$  molecules/mol, and  $a_m$  is the projection area of a N<sub>2</sub> molecule, that is  $16.2 \times 10^{-20} \text{ m}^2/\text{molecule}$ . Finally, the  $S_{BET}$  can be obtained as follows:

$$S_{BET} = \frac{186.14 \text{ cm}^3 \text{ STP}}{\text{g}} \times \frac{1 \text{ mol}}{22,400 \text{ cm}^3 \text{ STP}} \times \frac{6.02214076 \times 10^{23} \text{ molecules}}{\text{mol}} \times \frac{16.2 \text{ m}^2}{\text{molecule}} \quad (\text{S.5})$$

$$S_{BET} = 810 \text{ m}^2/\text{g} \quad (\text{S.6})$$

The total pore volume,  $V_{tot}$ , was determined at a relative pressure of 0.9886. At this pressure, the plateau can be observed for the adsorbed amount of N<sub>2</sub>. This implies that the pores are completely filled by N<sub>2</sub>. Equation (S.7) was employed to determine total pore volume.

$$V_{tot} = V_{adsorbed} \left[ \frac{\rho_{N_2,STP}}{\rho_{N_2,liquid}} \right] \quad (\text{S.7})$$

where  $V_{adsorbed}$  is the volume of  $N_2$  adsorbed at a relative pressure of  $\sim 0.99$ ,  $\rho_{N_2,STP}$  is the density of  $N_2$  at STP, and  $\rho_{N_2,liquid}$  is the density of  $N_2$  in the liquid state at 77.4 K.

$$\rho_{N_2,STP} = \frac{28 \text{ g/mol}}{22,400 \text{ cm}^3/\text{mol}} = 1.25 \times 10^{-3} \text{ g/cm}^3 \quad (\text{S.8})$$

And the density of  $N_2$  in the liquid state at 77.4 K is 0.8077 g/cm<sup>3</sup>, taken from NIST (Lemmon *et al.*, 2018). Thus, the  $V_{tot}$  of sample C400-90 AC950-90 is:

$$V_{tot} = \frac{257.668 \text{ cm}^3}{g} \times \frac{1.25 \times 10^{-3} \text{ g/cm}^3}{0.8077 \text{ g/cm}^3} = 0.3987 \text{ cm}^3/g \quad (\text{S.9})$$

Next, the Dubinin-Radushkevich (DR) equation was employed to determine the micropore volume,  $V_{mic}$ , from the adsorption isotherm of  $N_2$  at 77.4 K. The adsorption isotherm is tabulated in *Table S3*.

**Table S3** The adsorption isotherm of  $N_2$  at 77.4 K obtained from activated carbon sample C400-90 AC950-90.

$P/P_0$	Volume adsorbed, $V$ (cm <sup>3</sup> at STP/g)	$\log(V)$	$\log^2(P_0/P)$
0.002867	174.9746	2.242975	6.464557
0.004771	181.1646	2.258073	5.388791
0.00685	185.5879	2.26855	4.684103
0.008857	188.8269	2.276064	4.213536
0.010194	190.6223	2.280174	3.966765
0.015919	196.2788	2.292873	3.233096
0.01972	199.0091	2.298873	2.907323
0.025091	202.0685	2.305499	2.561534
0.030398	204.4785	2.310648	2.301757
0.035346	206.3421	2.314588	2.107307
0.039916	207.8279	2.317704	1.956775
0.045815	209.48	2.321143	1.792907
0.050719	210.6808	2.323625	1.676594
0.054942	211.6169	2.32555	1.587837
0.060669	212.7513	2.327872	1.481174
0.065378	213.6072	2.329616	1.403201
0.07143	214.5985	2.331627	1.313583
0.075922	215.2763	2.332996	1.253573
0.082278	216.1532	2.334762	1.176606
0.087151	216.7767	2.336013	1.123025
0.09351	217.5302	2.33752	1.059131
0.100747	218.3189	2.339091	0.993545

The linear form of DR equation can be written as:

$$\log V = \log V_0 - 2.303 \left[ \frac{RT}{\beta E_0} \right]^2 \log^2 \left( \frac{P_0}{P} \right) \quad (\text{S.10})$$

Where  $V_0$  is the micropore volume which can be determined from y-intercept of the plot between  $\log(V)$  and  $\log^2(P_0/P)$ . The plot is shown in *Figure S2*.

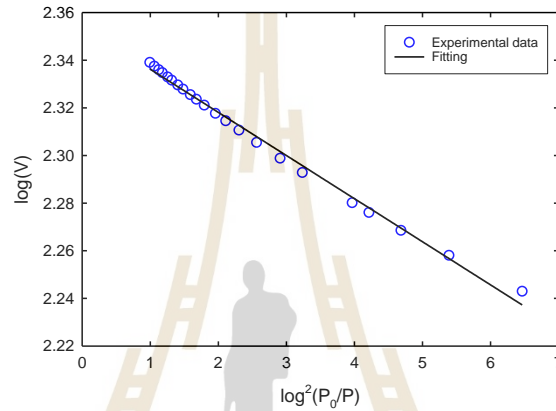


**Figure S2** DR-plot for  $N_2$  adsorption at 77.4 K on C400-90 AC950-90 sample.

The y-intercept is 2.3543, obtained from *Figure S2*. From Equation (S.10),  $V_0$  can be determined as follows:

$$\log V_0 = 2.3543 \quad (\text{S.11})$$

$$V_0 = 226.12 \text{ cm}^3 \text{ at STP/g} \quad (\text{S.12})$$

Then, the weight of adsorbed  $N_2$  in carbon sample is

$$N_2 = \frac{226.12 \text{ cm}^3 \text{ at STP}}{g} \times \frac{1 \text{ mol}}{22,400 \text{ cm}^3 \text{ at STP}} \times \frac{28 \text{ g}}{\text{mol}} = 0.2826 \frac{g \text{ N}_2}{g \text{ carbon}} \quad (\text{S.13})$$

The density of  $N_2$  in the liquid state at 77.4 K was employed again to convert weight of  $N_2$  to volume.

$$V_{mic} = \frac{0.2826 \text{ g N}_2}{g \text{ carbon}} \times \frac{\text{cm}^3 \text{ N}_2}{0.8077 \text{ g N}_2} = 0.349 \text{ cm}^3/g \quad (\text{S.14})$$

Finally, the  $D_{avg}$  can be calculated from equation, by assuming cylindrical pore:

$$D_{avg} = 4V_{tot}/S_{BET} \quad (S.15)$$

The  $D_{avg}$  of sample C400-90 AC950-90 is:

$$D_{avg} = \frac{4 \times 0.3987 \text{ cm}^3}{g} \times \frac{1 \text{ g}}{810 \text{ m}^2} = 1.969 \text{ nm} \quad (S.16)$$

**Table S4** Saturated properties of a single Lennard-Jones  $N_2$  model proposed by Neimark *et al.* (Ravikovitch *et al.*, 2000) used in the Monte Carlo simulation to determine pore size distribution. These properties were obtained from the canonical kMC scheme (Nguyen *et al.*, 2016). While the experimental data were taken from NIST (Lemmon *et al.*, 2018).

T (K)	$P_{0,exp}$ (Pa)	$P_{0,sim}$ (Pa)	$\rho_{l,exp}$ (kmol/m <sup>3</sup> )	$\rho_{l,sim}$ (kmol/m <sup>3</sup> )	$\rho_{g,exp}$ (kmol/m <sup>3</sup> )	$\rho_{g,sim}$ (kmol/m <sup>3</sup> )	$\Delta H_{exp}$ (kJ/mol)	$\Delta H_{sim}$ (kJ/mol)
77	97,152	91,553	28.83	28.45	0.1584	0.1482	5.592	5.425
87	276,261	253,028	27.14	26.80	0.4185	0.3776	5.194	5.076
100	778,275	697,320	24.61	24.50	1.1409	0.9861	4.509	4.520

Kinetic Monte Carlo (kMC) in the canonical ensemble (C) was employed to calculate the saturated properties of the  $N_2$ , this step is very important in the simulation for its reproducing the filling pressure of  $N_2$  in slit pores. The vapour-liquid equilibria (VLE) in the C-kMC program consists of one simulation box, with a dimension of  $4 \times 4 \times 16 \text{ nm}^3$  and 1,000 molecules of  $N_2$  in the box.  $5.0 \times 10^8$  configurations in the C-kMC program were executed in the equilibration stage, and the same number of configurations were used in the sampling stage to obtain the average outputs. The C-kMC algorithm only involves one type of move, where a selected molecule is moved to a random position in the simulation box and the molecule is also free to make a random orientation. Moreover, the molecules in the C-kMC algorithm that have positive molecular energies (*i.e.*, high mobility rate) are more possibly to be selected to move (Nguyen *et al.*, 2016).

The saturated properties obtained from the simulation are shown in *Table S4*, the properties of  $N_2$  are in good agreement with the experimental values taken from

the National Institute of Standards and Technology (NIST) (Lemmon *et al.*, 2018). Thus, this model is validated and reliable to represent  $N_2$  in adsorbed phase. Moreover, the simulated data of  $N_2$  in the bulk phase are shown in *Figure S3*, where the plots of vapour density as a function of pressure are presented.

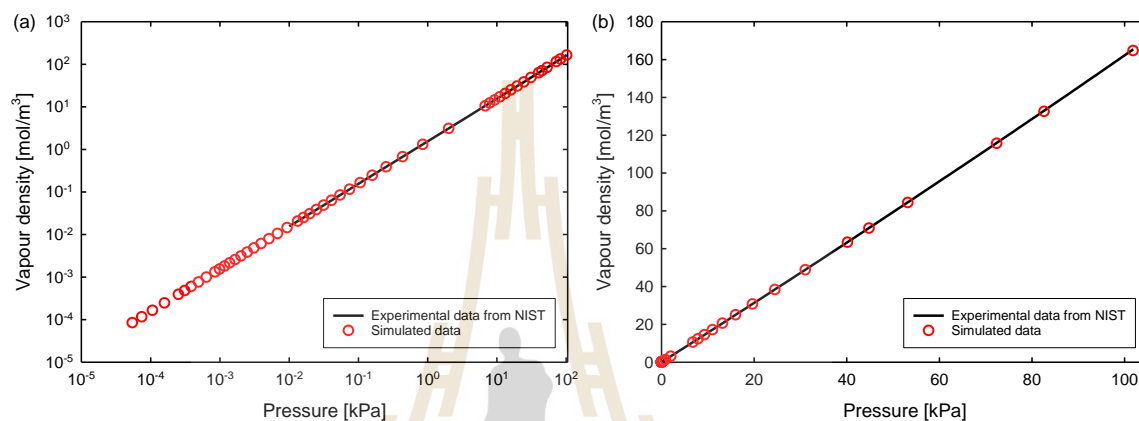


**Figure S3** The simulated bulk properties of  $N_2$  at 77.4 K. The red circles are the simulated data, obtained from the canonical kMC (Nguyen *et al.*, 2016) scheme. The black dash line is the experimental data, taken from NIST (Lemmon *et al.*, 2018). (a) The plots are in log-log scale to highlight the low-pressure regions, while (b) is shown in linear scale.

The simulated vapour density of  $N_2$  shows a linear behaviour and they correctly match the experimental data. This implies that the  $N_2$  potential model has an ideal behaviour on pressure, thus the  $N_2$  potential model is credible to simulate the adsorption in pores. The consistency with these results is of paramount importance to the validation of the method used in this research.

Next, the simulated adsorption isotherms of  $N_2$  by Monte Carlo (MC) simulation in the grand canonical (GC) ensemble are shown in *Figure S4*. Each isotherm contains 46 pressure points, from 1 Pa to  $10^5$  Pa, covering the micropore region to the packing of pores at high pressure. The pressures from the simulation at a given temperature were scaled with  $P_0$  obtained from C-kMC simulation at 77.4 K, resulting in plots of the amount of adsorbed versus relative pressure ( $P/P_0$ ).

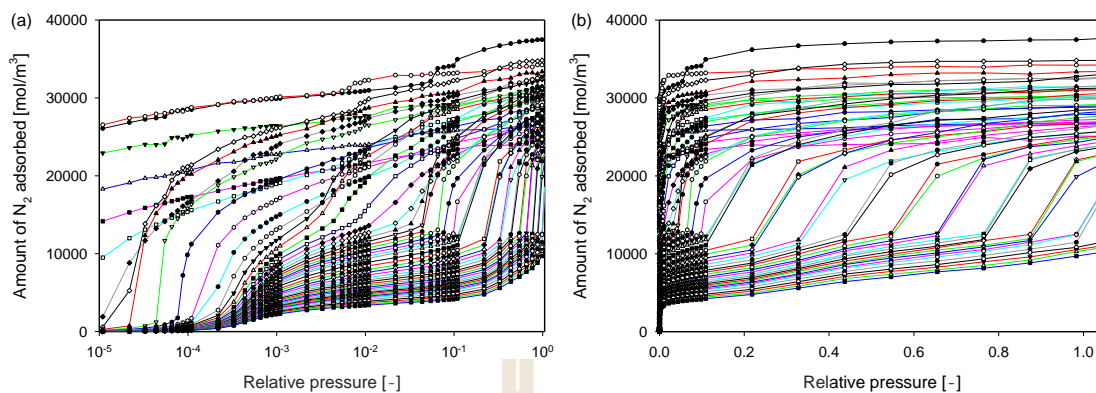


**Figure S4** Simulated isotherms of  $N_2$  in carbon slit pores at 77.4 K. Ranging from pore width,  $H$ , of 0.65 nm to 5 nm. Plots in (a) are presented in semi-log scale to highlight the adsorbed amount at the low-pressure region, while (b) are in linear scale.

#### CHAPTER IV – PRELIMINARY STUDY ON THE FORMATION OF OXYGEN FUNCTIONAL GROUPS IN BAMBOO-BASED ACTIVATED CARBON BY AIR OXIDATION

In spectrophotometry, absorbance and transmittance have been used to tell how much energy can be absorbed by the sample at several wavelengths of light. This technique is very useful to identify the unknown chemical substances on the sample, moreover, using this technique with a set of standards, the concentration of a substance in the sample can be also determined.

In Fourier Transform Infrared Spectroscopy (FTIR), there is a family of correlations used to calculate transmittance and absorbance. These equations are in the following forms:

$$T = I/I_0 \quad (\text{S.17})$$

$$A = 2 - \log \%T \quad (\text{S.18})$$

$$A = \log \left[ \frac{I_0}{I} \right] \quad (\text{S.19})$$

Where transmittance (T) means the amount of light that successfully passes through the sample and comes out to the detector on the other side.  $I$  is the “output” light obtained by the detector,  $I_0$  is the “input” light. Equation (S.17) represents either fraction or percentage of transmittance.

On the other hand, absorbance (A), represents how much the light that sample can absorb. It is also called optical density. The correlations to convert transmittance to absorbance are shown in Equations (S.18) and (S.19).

An example set of values that correlate between transmittance and absorbance is shown in *Table S5*.

**Table S5** Example of transmittance to absorbance values.

Transmittance (%)	Absorbance (a.u.)
100	0
99	0.004
98	0.009
97	0.013
96	0.018
95	0.022
90	0.046
85	0.071
80	0.097
75	0.125
70	0.155
60	0.222
50	0.301
40	0.398
30	0.523
20	0.699
10	1
5	1.301
1	2

## CHAPTER V – WETTING TRANSITION OF ETHYLENE ON A PLANAR SUBSTRATE

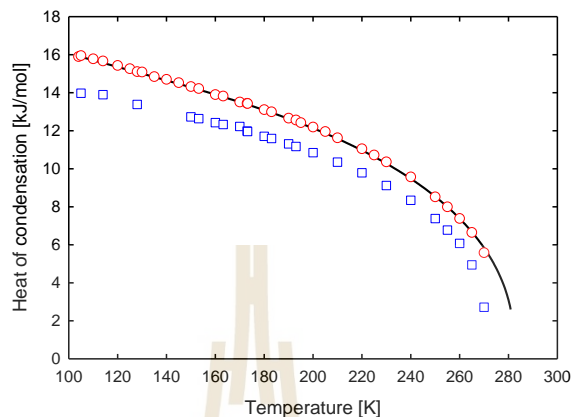


**Figure S5** The heat of vaporization/condensation for the temperatures between  $T_{tr}$  and  $T_c$  of ethylene for both potential models, obtained from the canonical kMC scheme (Nguyen *et al.*, 2016). The solid line is the experimental data obtained from NIST (Lemmon *et al.*, 2018), while red circles represent the TraPPE UA2 (Shah *et al.*, 2017) model and blue squares are the TraPPE UA (Wick *et al.*, 2000) model.

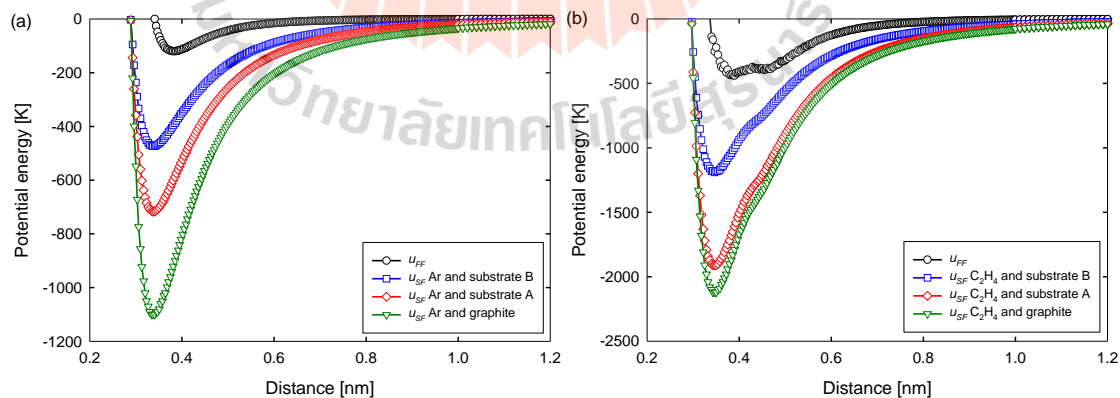


**Figure S6** The potential profiles of adsorbate-adsorbate interactions and adsorbate-adsorbent interactions for various surface affinities, (a) argon (Michels *et al.*, 1949) and (b) ethylene TraPPE UA2 (Bin *et al.*, 2001) model.

**Table S6** Sublimation pressure ( $P_0$ ) of argon at a temperature below  $T_{tr}$  taken from VSE simulation by Chen *et al.* (Chen *et al.*, 2001), they are presented above the dash line. While the simulated bulk coexistence pressure of argon at 87 K was obtained from the canonical kMC scheme (Nguyen *et al.*, 2016). The experimental data of sublimation pressure were taken from Ferreira and Lobo (Ferreira & Lobo, 2008), while the saturation pressure of argon at 87 K was obtained from NIST (Lemmon *et al.*, 2018).

Temperature (K)	$P_0$ (Pa)	Experimental data (Pa)
30	$6.3590 \times 10^{-5}$	$6.3785 \times 10^{-5}$
40	$2.0452 \times 10^{-1}$	$2.5269 \times 10^{-1}$
87	88,911	98,131

**Table S7** Sublimation pressure of ethylene at a temperature below  $T_{tr}$  obtained from the experimental data by Smukala *et al.* (Smukala *et al.*, 2000).

Temperature (K)	$P_0$ (Pa)
50	$3.6369 \times 10^{-9}$
82	$2.9792 \times 10^{-1}$
100	50.0884

**Table S8** Bulk coexistence pressures ( $P_0$ ) of ethylene for both potential models, obtained from canonical kMC scheme (Nguyen *et al.*, 2016). While the experimental data was obtained from NIST (Lemmon *et al.*, 2018).

Temperature (K)	Experiment (Pa)	TraPPE UA (Pa)	TraPPE UA2 (Pa)
105	145.68	458.96	151.16
128	3,557.14	8,096.08	3,618.61
193	338,095	490,570	340,708
210	672,307	921,475	674,168
230	1,319,598	1,722,793	1,323,753

**Table S9** Surface affinity ( $D^*$ ) of argon (Michels *et al.*, 1949) and ethylene (Shah *et al.*, 2017) at various substrates.

Substrate	Argon	Ethylene (TraPPE UA2)
Very weak	–	1.643
B	3.873	2.734
A	5.869	4.346
Graphite	8.996	4.822

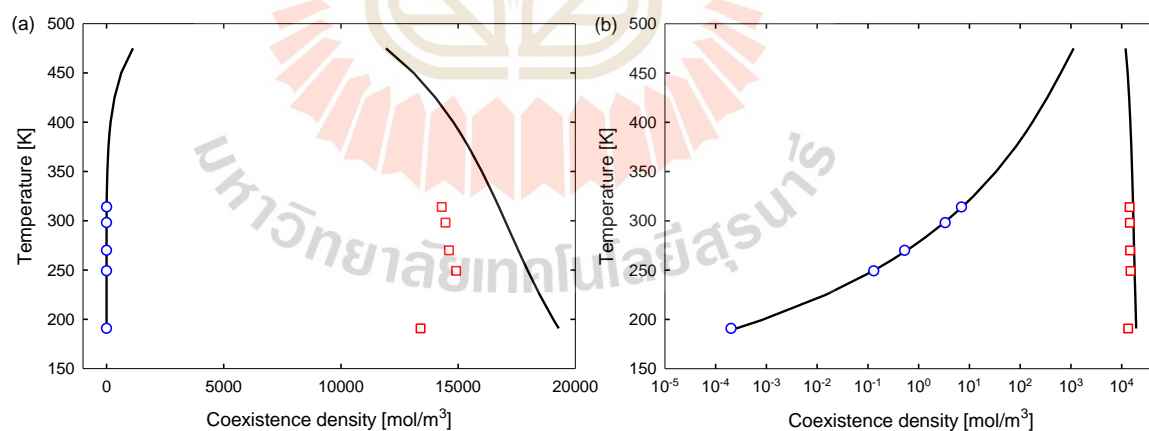
**Table S10** Heats of sublimation of ethylene at the temperature below  $T_{tr}$  were obtained from Brown and Ziegler (Brown & Ziegler, 1980).

Temperature (K)	$\Delta H_{Sublimation}$ (kJ/mol)
50	20.13
82	19.90
100	19.45

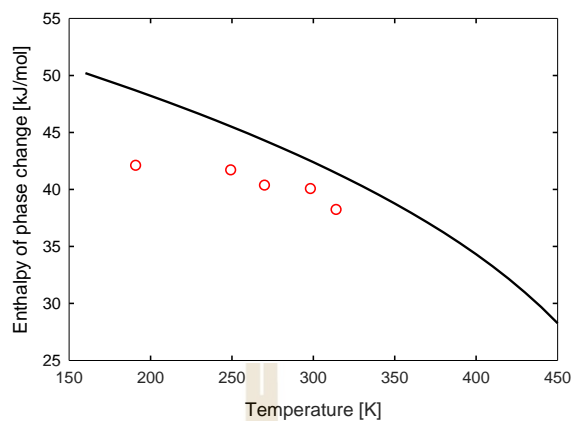
## CHAPTER VI – INCOMPLETE WETTING OF ETHANOL ON A GRAPHITE SUBSTRATE

**Table S11** Bulk coexistence pressure ( $P_0$ ) of ethanol for TraPPE UA model (Bin *et al.*, 2001) and a rigid molecular model (Schnabel *et al.*, 2005), obtained from the canonical kMC scheme (Nguyen *et al.*, 2016). While the experimental data were obtained from Perry's Chemical Engineers' Handbook (Green & Southard, 2019).

Temperature (K)	Experimental $P_0$ (Pa)	TraPPE UA (Pa)	Rigid model (Pa)
190.82	0.2388	0.2353	0.2407
199.35	0.8731	0.8638	–
249.236	242.6	252.3	240.0
270	1273	–	1179
283.15	3152	3170	–
298.15	7927	7936	7947
314	18806	–	18924

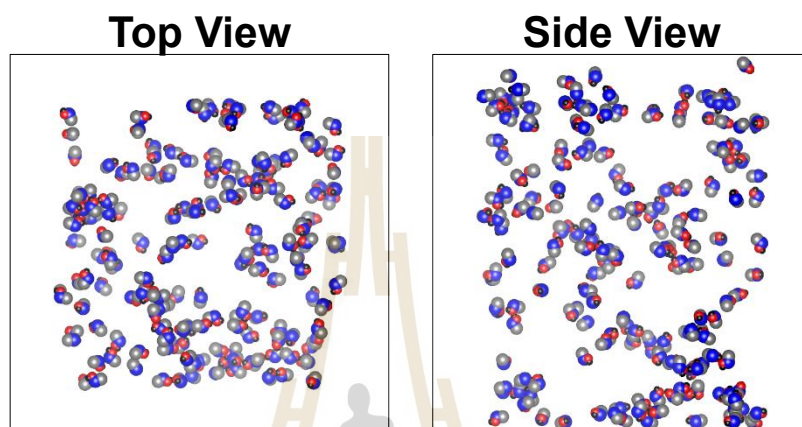


**Figure S7** (a) The simulated coexistence density of the rigid model ethanol (Schnabel *et al.*, 2005) obtained from VLE simulation via the canonical kMC scheme (Nguyen *et al.*, 2016). Blue circles represent gas density, red squares are liquid density while the black solid lines are experimental data (Green & Southard, 2019). (b) Plots are in semi-log scale to emphasize low-density regions.



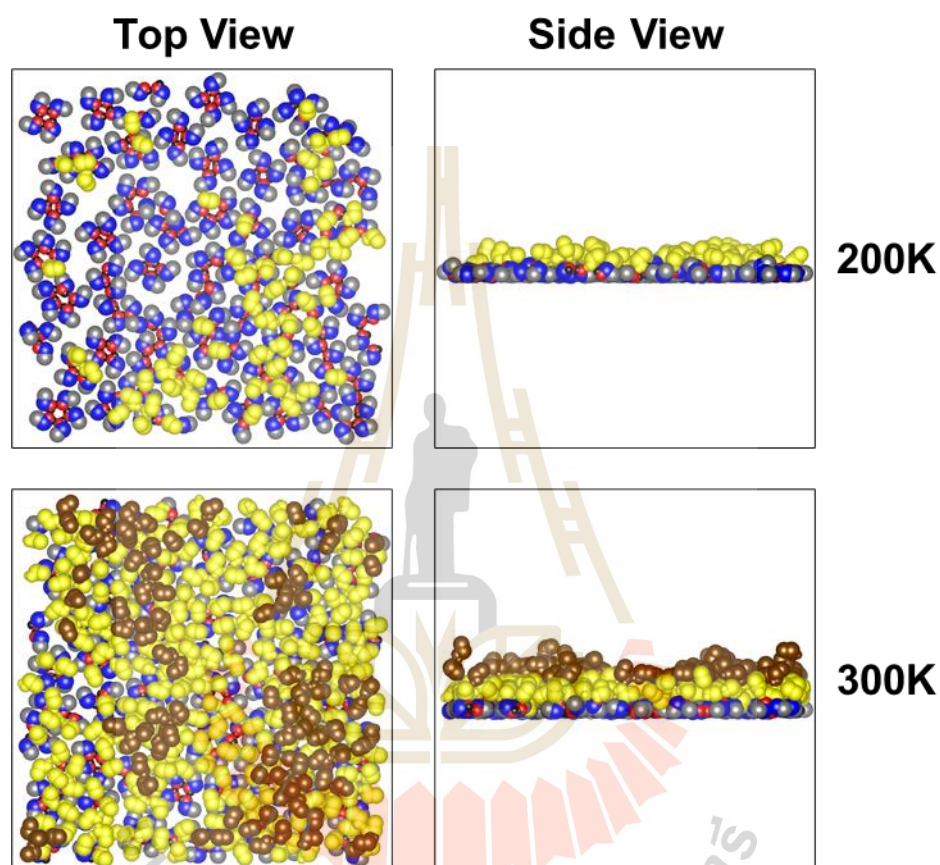
**Figure S8** The heats of vaporization/condensation for the temperatures between  $T_{tr}$  and  $T_c$  of the rigid model ethanol (Schnabel *et al.*, 2005) obtained from VLE simulation via the canonical kMC scheme (Nguyen *et al.*, 2016). Red circles represent simulated data while the black solid line is experimental data (Green & Southard, 2019).

The configurations of ethanol molecules on a planar substrate with a substrate affinity,  $D^*$  of 0.23 at 425 K and  $P_0$ . Some of the ethanol molecules show random rotation on the substrate, while the remainders are connected above the substrate.



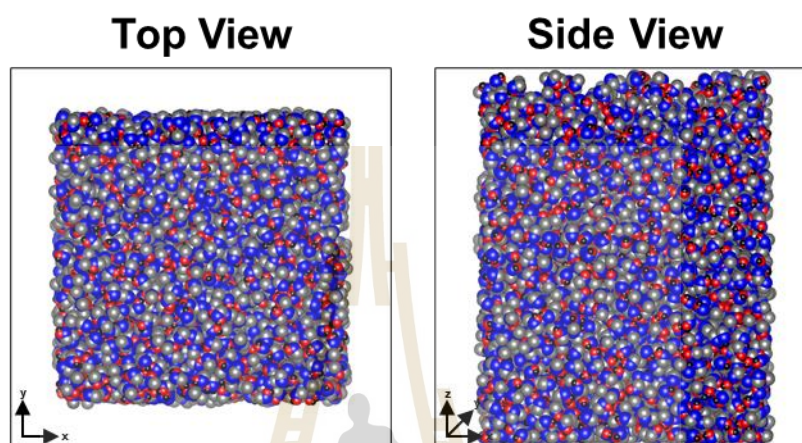
**Figure S9** The configurations snapshot of ethanol molecules on the weak substrate having  $D^*$  of 0.23 at 425 K for the pressure at  $P_0$ . The black, red, blue, and grey circles refer to the H atom, O atom, CH<sub>2</sub> group, and CH<sub>3</sub> group, respectively. The data was obtained from the ethanol TraPPE UA model.

The configurations of ethanol molecules on graphite surface ( $D^*$  of 0.75) at 200 K and 300 K for the pressure at  $P_0$ . The configurations show incomplete wetting at 200 K and 300 K, we only see second- and third layers at  $P_0$ , respectively.

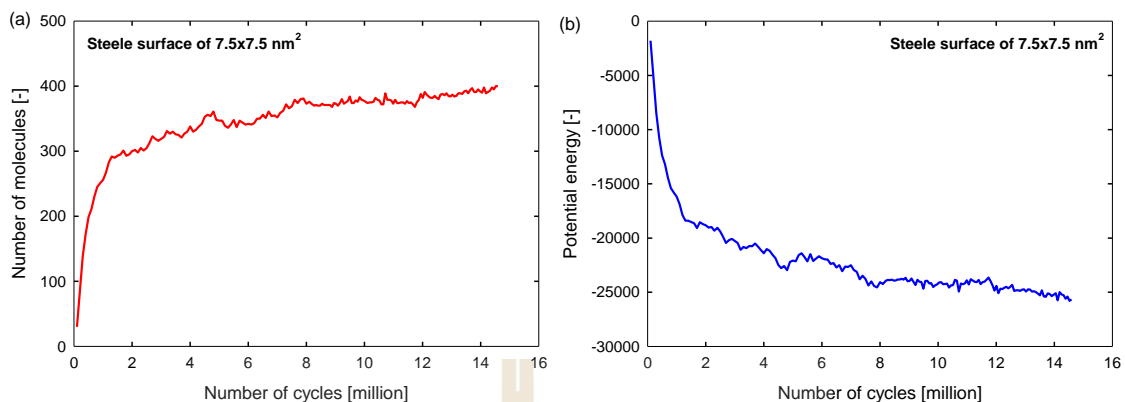


**Figure S10** The configurations snapshot of ethanol molecules on graphite at 200 K and 300 K for the pressure at  $P_0$ . The black, red, blue, and grey circles refer to H atom, O atom, CH<sub>2</sub> group, and CH<sub>3</sub> groups, respectively, for the molecules in the first layer. While the yellow and brown molecules represent the second- and third molecular layers, respectively. The data was obtained from the ethanol TraPPE UA model.

The configurations of ethanol molecules on graphite surface ( $D^*$  of 0.75) at 450 K for the pressure at  $P_0$ . Ethanol molecules have filled the simulation box, showing complete wetting at these conditions.

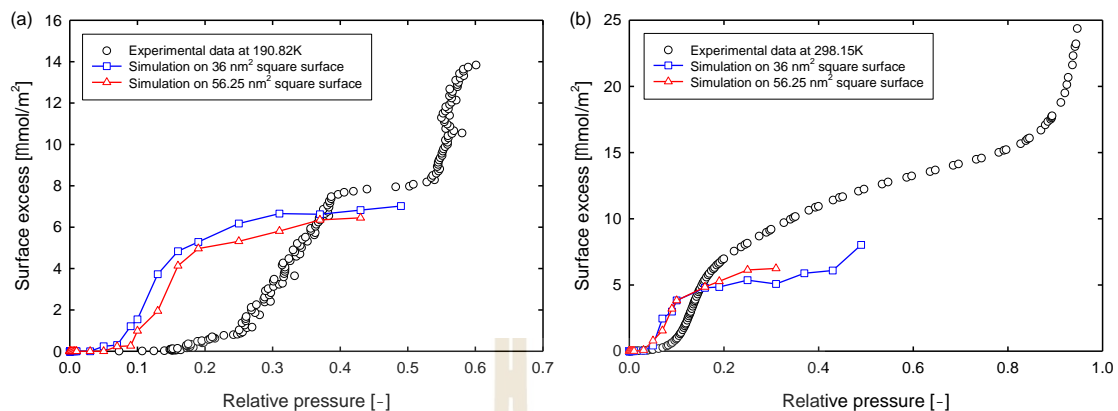


**Figure S11** The configurations snapshot of ethanol molecules on graphite at 450 K for the pressure at  $P_0$ . The black, red, blue, and grey circles refer to the H atom, O atom, CH<sub>2</sub> group, and CH<sub>3</sub> groups, respectively. The data was obtained from the ethanol TraPPE UA model.



**Figure S12** Control charts of ethanol adsorption on a graphite surface at 190.82 K and bulk coexistence pressure. (a) The plot shows the number of molecules in the simulation box, while (b) shows the potential energy of the system. The data were obtained from the rigid ethanol model (Schnabel *et al.*, 2005), while the control charts of the ethanol TraPPE UA model are in Chapter VI.

From *Figure S12*, even 15 million cycles (or 15 billion configurations) have been executed, the progressive increase in the number of molecules in the simulation box is observed. Moreover, the potential energy of the system is still decreasing without any signs to achieve equilibrium. This implies that the rigid ethanol model also required an extremely long simulation for the system to reach equilibrium, probably much longer than the simulation of water in carbon slit pore (Liu *et al.*, 2019). According to the experimental data, we presume to see the number of molecules at about 550 molecules on the 7.5x7.5 nm<sup>2</sup> surface ( $\sim 16.2 \mu\text{mol}/\text{m}^2$ ) to achieve fully developed two molecular layers on graphite at 190.82 K and  $P_0$ . Nevertheless, only about 400 molecules have been achieved on this surface ( $\sim 11.8 \mu\text{mol}/\text{m}^2$ ) so far.



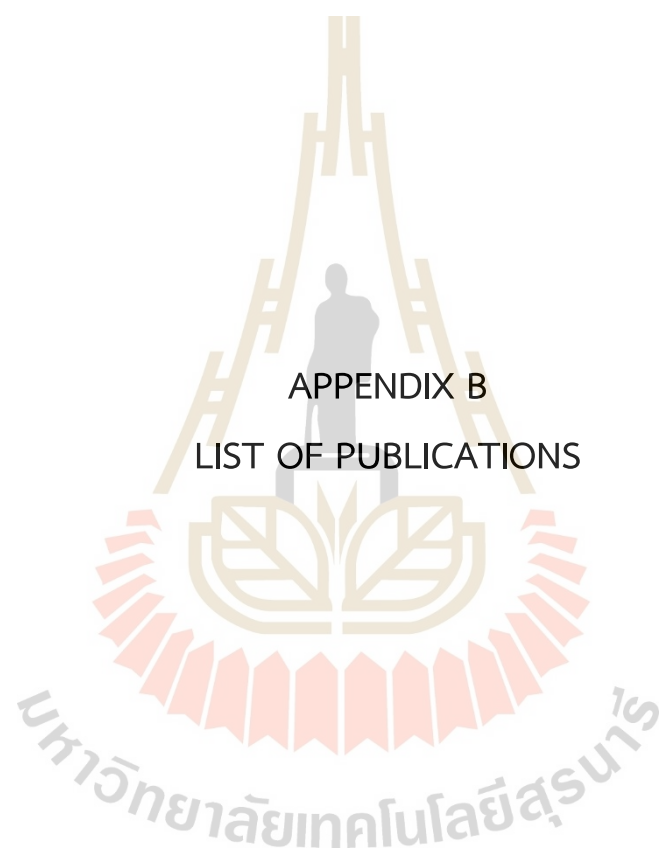
**Figure S13** The adsorptions isotherms of ethanol on a graphite substrate at (a) 190.82 K and (b) 298.15 K.

Figure S13 shows the adsorption isotherm of ethanol on a graphite substrate at 190.82 K and 298.15 K. The experimental data are in black circles, while the simulated data are in blue squares and red triangles. The potential model of ethanol used in this simulation is the rigid model (Schnabel *et al.*, 2005).

## References

- Bin, C., Potoff, J. J., & Siepmann, J. I. (2001). Monte Carlo Calculations for Alcohols and Their Mixtures with Alkanes. Transferable Potentials for Phase Equilibria. 5. United-Atom Description of Primary, Secondary, and Tertiary Alcohols. **The Journal of Physical Chemistry B**. 105(15): 3093-3104.
- Brown, G. N., & Ziegler, W. T. (1980). Vapor Pressure and Heats of Vaporization and Sublimation of Liquids and Solids of Interest in Cryogenics below 1-atm Pressure. In K. D. Timmerhaus & H. A. Snyder (Eds.), *Advances in Cryogenic Engineering* (pp. 662-670). Boston, MA: Springer US.
- Chen, B., Siepmann, J. I., & Klein, M. L. (2001). Direct Gibbs Ensemble Monte Carlo Simulations for Solid-Vapor Phase Equilibria: Applications to Lennard-Jonesium and Carbon Dioxide. **The Journal of Physical Chemistry B**. 105(40): 9840-9848.
- Ferreira, A. G. M., & Lobo, L. Q. (2008). The sublimation of argon, krypton, and xenon. **The Journal of Chemical Thermodynamics**. 40(12): 1621-1626.
- Green, D. W., & Southard, M. Z. (2019). **Perry's Chemical Engineers' Handbook** (9th Edition ed.). New York: McGraw-Hill Education.
- Lemmon, E. W., McLinden, M. O., & Friend, D. G. (2018). **Thermophysical Properties of Fluid Systems in NIST Chemistry WebBook, NIST Standard Reference Database Number 69**. Gaithersburg, MD: National Institute of Standards and Technology.
- Liu, L., Zeng, Y., Tan, S. J., Xu, H., Do, D. D., Nicholson, D., & Liu, J. (2019). On the mechanism of water adsorption in carbon micropores – A molecular simulation study. **Chemical Engineering Journal**. 357: 358-366.
- Michels, A., Wijker, H., & Wijker, H. (1949). Isotherms of argon between 0°C and 150°C and pressures up to 2900 atmospheres. **Physica**. 15(7): 627-633.

- Nguyen, V. T., Tan, S. J., Do, D. D., & Nicholson, D. (2016). Application of kinetic Monte Carlo method to the vapour–liquid equilibria of associating fluids and their mixtures. **Molecular Simulation**. 42(8): 642-654.
- Ravikovitch, P. I., Vishnyakov, A., Russo, R., & Neimark, A. V. (2000). Unified approach to pore size characterization of microporous carbonaceous materials from N<sub>2</sub>, Ar, and CO<sub>2</sub> adsorption isotherms. **Langmuir**. 16(5): 2311-2320.
- Schnabel, T., Vrabec, J., & Hasse, H. (2005). Henry's law constants of methane, nitrogen, oxygen and carbon dioxide in ethanol from 273 to 498 K: Prediction from molecular simulation. **Fluid Phase Equilibria**. 233(2): 134-143.
- Shah, M. S., Siepmann, J. I., & Tsepatis, M. (2017). Transferable potentials for phase equilibria. Improved united-atom description of ethane and ethylene. **AIChE Journal**. 63(11): 5098-5110.
- Smukala, J., Span, R., & Wagner, W. (2000). New Equation of State for Ethylene Covering the Fluid Region for Temperatures From the Melting Line to 450 K at Pressures up to 300 MPa. **Journal of Physical and Chemical Reference Data**. 29(5): 1053-1121.
- Wick, C. D., Martin, M. G., & Siepmann, J. I. (2000). Transferable Potentials for Phase Equilibria. 4. United-Atom Description of Linear and Branched Alkenes and Alkylbenzenes. **The Journal of Physical Chemistry B**. 104(33): 8008-8016.



APPENDIX B  
LIST OF PUBLICATIONS

## LIST OF PUBLICATIONS

### 1. International Publications

Loi, Q.K., **Phothong, K.**, Do, D.D. and Nicholson, D. (2021). Effects of crystallite stacking on adsorption of ethylene on graphitized thermal carbon black.

**Microporous and Mesoporous Materials.** 323: 111202.

Xu, H., **Phothong, K.**, Do, D.D. and Nicholson, D. (2021). Wetting/non-wetting behaviour of quadrupolar molecules ( $N_2$ ,  $C_2H_4$ ,  $CO_2$ ) on planar substrates.

**Chemical Engineering Journal.** 419: 129502.

**Phothong, K.**, Tangsathitkulchai, C. and Lawtae, P. (2021). The analysis of pore development and formation of surface functional groups in bamboo-based activated carbon during  $CO_2$  activation. **Molecules.** 26(18): 5641.

### 2. National Publication

**Phothong, K.**, Janseedar, C., Tangsathitkulchai, C. and Wongkoblap, A. (2018). Study for adsorption of gas mixture in activated carbon by Grand Canonical Monte Carlo simulation. **The Journal of KMUTNB.** 28(2): 333-340.

### 3. Conference Abstract

**Phothong, K.** and C., Tangsathitkulchai. (2019). Development of pore structure and surface functional groups in bamboo-based activated carbon during  $CO_2$  activation. **The 1<sup>st</sup> Thailand Biorefinery Conference.** Nakhon Ratchasima, Thailand.

## VITA

Krittamet Phothong was born on the 19<sup>th</sup> of April 1992 to Praphasri Phothong in Si Racha, Chonburi, Thailand. In 1998, the family then moved to the township of Nakhon Ratchasima. After graduating from Surathampitak School in 2010, he attended a university in Nakhon Ratchasima at Suranaree University of Technology (SUT). After receiving a bachelor's degree of Engineering in Chemical Engineering in July 2014, he performed a job as a mathematics tutor at SAM Singapore Maths Thailand (Nakhon Ratchasima branch). Then in July 2015, he left SAM Singapore Maths Thailand to attend graduate school in the School of Chemical Engineering, SUT by earning the Royal Golden Jubilee (RGJ) scholarship program under the Thailand Research Fund (TRF). With Prof. Dr. Chaiyot Tangsathitkulchai's kind willingness, he joined the Carbon and Adsorption Research (CAR) group in August 2015 to pursue his degree in Doctor of Philosophy (Ph.D.). During his Ph.D. years, he had spent fifteen months (August 2019 to November 2020) in the School of Chemical Engineering, The University of Queensland (UQ), Australia, doing research about the fundamental of adsorption via computer simulation under the supervision of Prof. Dr. Duong D. Do. He successfully defended his dissertation for a Ph.D. in Chemical Engineering with a concentration in porous materials and molecular simulation in March 2022.